Stirling/magnetic cryocooler

by

Greg Nellis

B.S., Mechanical Engineering
University of Wisconsin at Madison, 1992

M.S., Mechanical Engineering
Massachusetts Institute of Technology, 1995

Submitted to the Department of Mechanical Engineering
in Partial Fulfillment of the Requirements for the Degree of

Doctor of Philosophy

at the
Massachusetts Institute of Technology
February, 1997

Signature of Author......... ....
Department of Mechanical Engineering
February, 1997

Certified by.. ....
Joseph L. Smith, Jr.
Thesis Supervisor

Accepted by.. ....
Ain A. Sonin, Chairman
Departmental Graduate Committee
Department of Mechanical Engineering

STIRLING/MAGNETIC CRYOCOOLER

by
Greg Nellis

Submitted to the Department of Mechanical Engineering
on January 30, 1997 in Partial Fulfillment of the Requirements for the Degree of
Doctor of Philosophy in Mechanical Engineering

ABSTRACT

This thesis describes the design and construction of an experimental prototype of a new type of cryocooler. The cycle employed by the device (subsequently referred to as a Stirling/magnetic cycle) uses two thermodynamically active substances : a compressible gas (helium) and a paramagnetic solid (Gadolinium Gallium Garnet or GGG). The two substances alternately regenerate one another, thereby overcoming the low temperature thermal saturation associated with a Stirling cycle while producing more refrigeration than a simple magnetic cycle.

The experimental prototype ultimately reached a no load temperature of 4.5 K while rejecting heat at 10.9 K. The prototype could supply 0.36 W of refrigeration at 6 K while rejecting heat at 15.4 K. The prototype clearly shows that the Stirling/magnetic cycle is an effective refrigeration cycle below 10 K. Furthermore, the results of the experimental prototype agree very well with the predictions of models of this type of cycle which had been developed previously.

Thesis supervisor :	Professor Joseph L. Smith, Jr.
Title :	Collins Professor of Mechanical Engineering

ACKNOWLEDGMENTS

The last four years have been some of the most enjoyable in my life due to the exceptional group of people at the Cryolab. It has been a privelege to work for Professor Smith. I have gained a tremendous amount of theoretical and practical knowledge from him. I will miss working for him.

I would like to thank Professor Brisson for repeatedly coming to my rescue. In particular, I appreciate his help as I struggled to master the art of transferring liquid helium. Professor Lienhard contributed constructive suggestions and comments while serving on my committee and taught the best course I took at MIT.

Doris has kept a watchful eye on me, always encouraging me and making sure I didn't forget anything important. When I first arrived at MIT, Lisa went out of her way to help me become acclimated and feel comfortable.

The technicians at the Cryolab have helped me over and over again. In particular, Bob was an invaluable resource in learning the basics of machining and Mike spent a lot of time with me when I needed advice, regardless of how busy he was with other projects. Don was always willing to help me and talk about baseball. I probably would not have graduated with all of my fingers if it weren't for them.

Finally, the other graduate students have all been willing to lend a hand or an ear when I needed one. In particular, Ed Ognibene always managed to make me laugh, regardless of how frustrated I was. Brian Bowers has helped me on numerous occasions when two sets of hands were needed. I also would like to thank Ashok , Sankar , Hua, and Hayung.

I have been blessed with a wonderful family and much of the credit for anything I accomplish should go to them. My father has given me the stubbornness and my mother the optimism required to tackle challenging problems. The Pick family has also continued to support and encourage me, even as their daughter slaved away to put me through (even more) school.

My deepest thanks and love go to my wife, Jill, for her patience, love, and support.

TABLE OF CONTENTS

LIST OF FIGURES AND TABLES

Chapter 1

Chapter 2

Chapter 3

Chapter 4

NOMENCLATURE

Whenever appropriate, typical units are indicated in square brackets and the specific section is indicated in parenthesis.

a	specific area [m^2/m^3]
A_c	cross sectional area [m^2]
A_S	total surface area [m^2]
B	Biot number [-] (2.3.5)
c	specific heat capacity [J/kgK]
C	Curie constant [K]
C	total heat capacity [J/K]
c_H	specific heat capacity at constant applied field [J/kgK]
$c_{H=0}$	specific heat capacity at zero magnetic field [J/kgK]
c_P	specific heat capacity at constant pressure [J/kgK]
D	diameter [m]
D_h	hydraulic diameter [m]
FOM	figure of merit [W/K]
h	enthalpy [J/kg]
$\overline{h}$	mass average enthalpy [J/kg]
H	total enthalpy [J]
H	applied field [A/m]
i	square root of negative one [-]
I	current [A]
k	ratio of specific heat capacities [-]
k	thermal conductivity [W/mK]
$\overline{k}$	dimensionless thermal conductivity [-]
L	length [m]
L	inductance [H]
m	mass flow rate [kg/s]
mr	primary mass ratio [-]
M	magnetization [A/m]
M	total mass [kg]
ME	magnetic effect [J]
MM	molar mass [kg/kgmol]
MR	mass ratio [-]
N	number [-]
NTU	number of transfer units [-]
Nu	Nusselt number [-]
P	pressure [N/m^2]
P	power [J/s]
pe	wetted perimeter [m]
Pr	Prandtl number [-]
PR	pressure ratio [-]

Q	total heat transfer [J] or heat transfer rate [W]
R	ideal gas constant [Nm/kgK]
R	radius [m]
R°	universal gas constant [8314.5 Nm/kgmolK]
Re	Reynolds number [-]
s	specific entropy [J/kgK]
$\bar{s}$	mass average specific entropy [-]
S	sensitivity of sensor [ohm/K]
S	total entropy [J/K]
S	displacer stroke [m]
S_{gen}	entropy generated by irreversibility [J/K]
t	time [s]
T	temperature [K]
TR	temperature ratio [-]
TRP	total refrigeration potential [J]
u	specific internal energy [J/kg]
U	total internal energy [J]
U	total conductance or heat transfer coefficient [W/m^{2}K]
v	specific volume [m^3/kg]
V	total volume [m^3]
V	voltage [V]
v_o	velocity based on unfilled regenerator tube [m/s]
VF	volumetric flow rate [m^3/s]
VR	volume ratio [-]
w	dimensionless temperature used to set up complex temperature [-] (2.3.5)
W	total work transfer [J]
x	position [m]
f	friction factor [-]
α	attenuation [-] (2.4.2)
α	thermal diffusivity [m^2/s]
α	effectiveness [-] (2.3.3)
α	dimensionless shuttle heat transfer rate [-] (2.3.5)
α	dimensionless heat leak through magnet leads [-] (2.3.6)
β	dimensionless entropy [-] (1.3.4)
β	dimensionless stroke [-] (2.3.5)
β	generation to conduction ratio [-] (2.3.6)
χ	convection to conduction ratio [-] (2.3.6)
δ	thickness [m]
δ	penetration depth [m]
$\Delta\Pi$	dimensionless pressure variation [-] (2.4.2)
$\Delta\Theta$	dimensionless temperature variation [-] (2.4.2)
ζ	dimensionless time [-]

ε	dimensionless position [-]
ε	porosity [-]
Γ	sensible heat capacity ratio [-]
η	efficiency [-]
λ	ratio of mass storage to pressure gradient effects [-] (2.4.2)
λ	magnetic capacity ratio [-] (1.3.4)
λ	dimensionless time constant [-] (2.3.5)
μ_o	permeability of free space, 4πe-7 H/m
π	pi, 3.1416
Π	dimensionless pressure [-] (2.4.2)
σ	dimensionless mass flow rate [-] (2.4.2)
σ	dimensionless applied field [-] (1.3.4)
Θ	dimensionless temperature [-]
ϕ	phase shift [radians]
ϕ	shape factor [-]
ϕ	magnetic flux [Wb]
μ	viscosity [Ns/m^2]
ρ	density [kg/m^3]
ρ_e	electrical resistivity [ohm m]
$\bar{\rho}_e$	dimensionless electrical resistivity [-]
τ	half-cycle time [s]
ω	angular frequency [rad/s]
Ω	dimensionless lost refrigeration [-] (2.4.2)
Ψ	dimensionless refrigeration [-] (1.3.4)
Ψ	complex dimensionless temperature [-] (2.3.5)

Subscripts

across	in one dimension (of two dimensional array)
baffle	baffle
bo	boil off
c	coolant stream
C	cold space, cold
carnot	carnot
center	center-to-center distance
chx	cold heat exchanger
cold	coldest temperature seen by device
com	compression/demagnetization process
D	Debye
dead	non-swept volume
dis	displacer
exp	expansion/magnetization process
f	compressible fluid
flux	through-flow of entropy or enthalpy

gen	generated by magnet operation
G	GGG
gg	gas gap
h	helium
H	hot space, hot
i	inner
ia	inactive
in	hot-to-cold blow/demagnetization process
l	lead
Lhe	liquid helium
mag	magnetic stage
max	maximum seen within a cycle
mech	mechanical
min	minimum seen within a cycle
ml	magnet lead
o	outer
out	cold-to-hot blow/magnetization process
p	particle
pack	packing
Pb	lead
ph	phenolic
r	regenerator
run	experimental run
rm	room temperature
sc	sub-cool
sh	super-heat
shuttle	shuttle heat transfer
ss	stainless steel
str	associated with structural members
tube	tube
us	upper stage
w	working fluid
wr	between the working fluid and regenerator
wc	between the working fluid and coolant

Superscripts

'	per unit length

Overbar - mass or time average

FUNDAMENTALS OF A STIRLING/MAGNETIC CYCLE

This chapter is divided into three sections. In the first section, the Stirling/magnetic cycle is introduced. The motivation for the development of this type of cycle is described and its advantages and disadvantages relative to other types of refrigeration cycles in the temperature range below 12 K are examined. The second section describes the magnetocaloric effect exhibited by paramagnetic solids. The method used to develop a thermodynamically consistent set of properties for a paramagnetic substance is explained and illustrated using the Curie-Weiss equation of state. The final section investigates the Stirling/magnetic cycle. A first-order model is developed and used to examine how the magnetic effect must be coupled to the mechanical effect in order to achieve an effective Stirling/magnetic cycle. A set of dimensionless curves are developed which can aid in the preliminary design of future cryocoolers based on the Stirling/magnetic cycle.

1.1 Introduction

There are many applications which must be kept at very low temperatures. The most important of these are superconducting devices which must be kept at or near 4.2 K in order to remain in their superconducting state. These devices typically are cooled by immersion in a liquid helium bath. While this technique is reliable, it is inefficient and inconvenient for remotely operating devices [1].

In order to provide the required cooling at 4.2 K without relying on liquid helium boiling, several types of closed cycle cryocoolers have been developed. The most important of these include Stirling-type cryocoolers and Joule-Thomson type cryocoolers [2]. Both of these techniques fail to reliably provide significant refrigeration at temperatures below 15 K. Cryocoolers which employ a Joule-Thomson expansion valve suffer from poor reliability [3] and Stirling-type cycles suffer from regenerator thermal saturation [4].

The thermal and magnetic properties of some paramagnetic substances are highly coupled in this temperature range, making them attractive alternative low temperature refrigerants. Several cryocoolers based upon the concept of pumping heat via a magnetic work input (i.e. a magnetic cycle) have been developed [5]. These cryocoolers have taken many different forms including: reciprocating magnetic material, rotating magnetic material, and magnetic regenerator matrix. These devices have successfully overcome many of the limitations associated with Stirling and Joule-Thomson cycles.

Unfortunately, magnetic cycle cryocoolers do not exploit the fact that there are two thermodynamic substances present in these devices, each with significant refrigeration potentials even below 15 K (i.e. the helium and the paramagnetic material). Magnetic cycle cryocoolers use isobaric helium as a heat transfer medium for the paramagnetic substance without taking advantage of the refrigeration potential of the helium. It has been shown computationally that a cryocooler in which both the pressure and applied magnetic field are appropriately controlled should achieve 50% more refrigeration than either a Stirling or magnetic cryocooler [6,7]. Furthermore, the pressure ratio at which such a cryocooler (subsequently referred to as a Stirling/magnetic cryocooler) operates most effectively is on the same order as the pressure ratio employed by a Stirling device. Therefore, a Stirling/magnetic cryocooler is ideally suited for the lowest temperature stage of a conventional cryocooler, extending its temperature range and increasing its refrigeration power.

1.2 Magneto-caloric Effect

This section is divided into two subsections. In the first subsection the magneto-caloric effect is described. The appropriate differential first law for a paramagnetic material is derived and analogies between a compressible substance and a paramagnetic substance are made. The second subsection describes the procedure used to derive a set of thermodynamically consistent properties for a paramagnetic substance. The procedure is demonstrated using the Curie-Weiss equation of state. The method by which the thermodynamic properties of GGG were obtained from experimental measurements of the magnetic equation of state is described.

1.2.1 Description of the magneto-caloric effect

A differential energy balance on a simple thermodynamic substance represents the fact that its internal energy may be changed through either a heat transfer or a work transfer [8].

$$dU = T \cdot dS - dW \tag{1.1}$$

For the compressible substances typically considered, the differential work transfer can be written as pressure multiplied by a volume change. However, a paramagnetic material undergoes a magnetic work transfer. The magnetic work transfer is associated with the alignment of individual dipoles within the material. These dipoles can be thought of as tiny torsional springs. As a magnetic field is applied to the material, the dipoles tend to align along the axis of the magnetic field. The alignment of the dipoles takes place against a force and therefore requires a work transfer to the material.

Electromagnetic theory is required to show that the differential work transfer for a non-hysteretic paramagnetic substance is given by equation 1.2 [9,10].

$$dW_{mag} = \mu_0 H \cdot d(V \cdot M) \tag{1.2}$$

The permeability of free space multiplied by the magnetic field ($\mu_o H$) is the applied magnetic field measured in units of Tesla. This quantity can be thought of as the magnetic equivalent of pressure. The applied field forces the alignment of the dipoles just as pressure forces the organization of molecules in a compressible substance. As the dipoles align, the total magnetic moment of the substance (VM) increases. The negative total magnetic moment can be thought of as the magnetic equivalent of volume.

The volume of a compressible substance decreases as pressure is applied. It requires a negative work transfer to accomplish this process. The entropy of a compressible substance tends to decrease as the volume decreases. Similarly, the magnetic moment of a paramagnetic substance increases as applied field is applied. It requires a negative work transfer to accomplish this process. The entropy of a paramagnetic substance tends to decrease as the magnetic moment increases.

Substituting equation 1.2 into equation 1.1 yields the differential first law for a paramagnetic substance.

$$dU = T \cdot dS + \mu_0 H \cdot d(VM) \tag{1.3}$$

On a mass specific basis, the differential first law is given by equation 1.4.

$$du = T \cdot ds + \mu_0 H \cdot d(vM) \tag{1.4}$$

In contrast to a ferromagnetic material, the dipoles of a paramagnetic substance are sufficiently isolated so that thermal agitation significantly reduces the overall alignment. A paramagnetic substance is therefore a coupled thermodynamic system with a significant cross-influence between its thermal and magnetic properties.

Using the analogies developed above, all of the thermodynamic results derived for substances which undergo only mechanical work interactions (i.e. compressible substances) may be applied to paramagnetic materials which undergo only magnetic work interactions. Therefore, the equation of state for a paramagnetic substances is the specific magnetization as a function of temperature and applied field.

$$vM = \Im(T, \mu_0 H) \tag{1.5}$$

Furthermore, all of the Maxwell relations associated with a compressible substance may be extended to paramagnetic substances. These relations are listed in equations 1.6 through 1.9.

$$\left(\frac{\partial s}{\partial \mu_0 H}\right)_{vM} = \left(\frac{\partial vM}{\partial T}\right)_s \tag{1.6}$$

$$-\left(\frac{\partial s}{\partial vM}\right)_T = \left(\frac{\partial \mu_0 H}{\partial T}\right)_{vM} \tag{1.7}$$

$$\left(\frac{\partial s}{\partial \mu_0 H}\right)_T = \left(\frac{\partial vM}{\partial T}\right)_{\mu_0 H} \tag{1.8}$$

$$-\left(\frac{\partial s}{\partial vM}\right)_{\mu_0 H} = \left(\frac{\partial \mu_0 H}{\partial T}\right)_s \tag{1.9}$$

1.2.2 Determination of the thermodynamic properties of a paramagnetic substance

A set of thermodynamically consistent properties may be derived for a paramagnetic substance from its equation of state and zero-field heat capacity ($c_{H=0}$). The Curie-Weiss law is an approximate equation of state for a paramagnetic substance at temperatures which are not too low (i.e. sufficiently above the Curie temperature) and at magnetic fields which are not too high (i.e. sufficiently below magnetic saturation). This equation of state is given in equation 1.10, where C is the Curie constant for the material under consideration.

$$M = C \cdot \frac{H}{T} \tag{1.10}$$

The entropy of the paramagnetic substance may be written as a function of temperature and applied field.

$$ds = \left(\frac{\partial s}{\partial T}\right)_{\mu_0 H} dT + \left(\frac{\partial s}{\partial \mu_0 H}\right)_T d\mu_0 H \tag{1.11}$$

The partial derivative with respect to temperature can be expressed in terms of the heat capacity at constant applied field and the partial derivative with respect to applied field can be expressed using the Maxwell relation given in equation 1.8.

$$ds = \frac{c_H}{T} \cdot dT + \left(\frac{\partial vM}{\partial T}\right)_{\mu_0 H} d\mu_0 H \tag{1.12}$$

An arbitrary reference entropy is defined as zero at a reference state of 1 K and 0 Tesla. Equation 1.12 is integrated to the desired state first along a line of constant zero applied field and then along a line of constant temperature.

$$s(T, \mu_0 H) = \int_{1K}^{T} \frac{c_{H=0}}{T} \cdot dT + \int_{0\,T}^{\mu_0 H} \left(\frac{\partial vM}{\partial T}\right)_{\mu_0 H} (T, \mu_0 H) \cdot d\mu_0 H \tag{1.13}$$

Equation 1.10 is used to evaluate the partial derivative of specific magnetization with respect to temperature at constant applied field for a substance obeying the Curie-Weiss equation of state.

$$\left(\frac{\partial\, vM}{\partial\, T}\right)_{\mu_0 H} = -\frac{C}{\mu_0 \cdot \rho} \cdot \frac{\mu_0 H}{T^2} \tag{1.14}$$

Equation 1.14 indicates that as temperature increases, the specific magnetization must decrease when the applied field is held constant. This is due to the increasing thermal agitation disrupting the magnetic alignment of the individual dipoles. Equation 1.14 is substituted into equation 1.13 and the resulting entropy function and its first partial derivatives are given below (assuming a constant specific heat capacity at zero applied field).

$$s(T,\mu_o H) = c_{H=0} \cdot \ln(T) - \frac{1}{2} \cdot \frac{C}{\mu_o \cdot \rho} \cdot \frac{(\mu_o H)^2}{T^2} \tag{1.15}$$

$$\left(\frac{\partial s}{\partial T}\right)_{\mu_o H} = \frac{c_{H=0}}{T} + \frac{C}{\mu_o \cdot \rho} \cdot \frac{(\mu_o H)^2}{T^3} \tag{1.16}$$

$$\left(\frac{\partial s}{\partial \mu_o H}\right)_T = -\frac{C}{\mu_o \cdot \rho} \cdot \frac{\mu_o H}{T^2} \tag{1.17}$$

The partial derivative of entropy with respect to temperature at constant applied field is directly proportional to the specific heat capacity of the substance at constant applied field. Equation 1.16 indicates that the specific heat capacity of a paramagnetic substance must increase with applied field. This effect is the basis for magnetically activated regenerators (i.e. paramagnetic regenerators in which a constant magnetic field is applied).

The partial derivative of entropy with respect to applied field at constant temperature is negative, indicating that as applied field increases entropy will decrease. This effect is the basis of magnetic cooling - a paramagnetic substance demagnetized in the presence of a heat sink it will absorb entropy.

Gadolinium Gallium Garnet (GGG) is the paramagnetic material used to construct the magnetic regenerator for the experimental prototype. The thermodynamic properties of GGG were derived by Greg Gallagher [11]. These properties were obtained using an equation of state based on experimental observations of the specific magnetization as a function of temperature and applied field which was reported by Brodale et. al. [12-14] and by Hashimoto. This equation of state is illustrated in Figure 1-1. The thermodynamic coupling is evident in the fact that each of the constant applied field lines have a significantly negative slope with temperature. In other words, it requires an increasing applied field to maintain a constant level of specific magnetization as temperature increases.

The entropy function for GGG was generated using the equation of state illustrated in Figure 1-1 and the experimentally determined zero field specific heat capacity of GGG [15]. The entropy function for GGG is illustrated in Figure1-2. The temperature-entropy diagram behaves qualitatively like the temperature-entropy diagram for a compressible substance. Isobars are replaced by isofield lines and isochors are replaced by isomagnetic

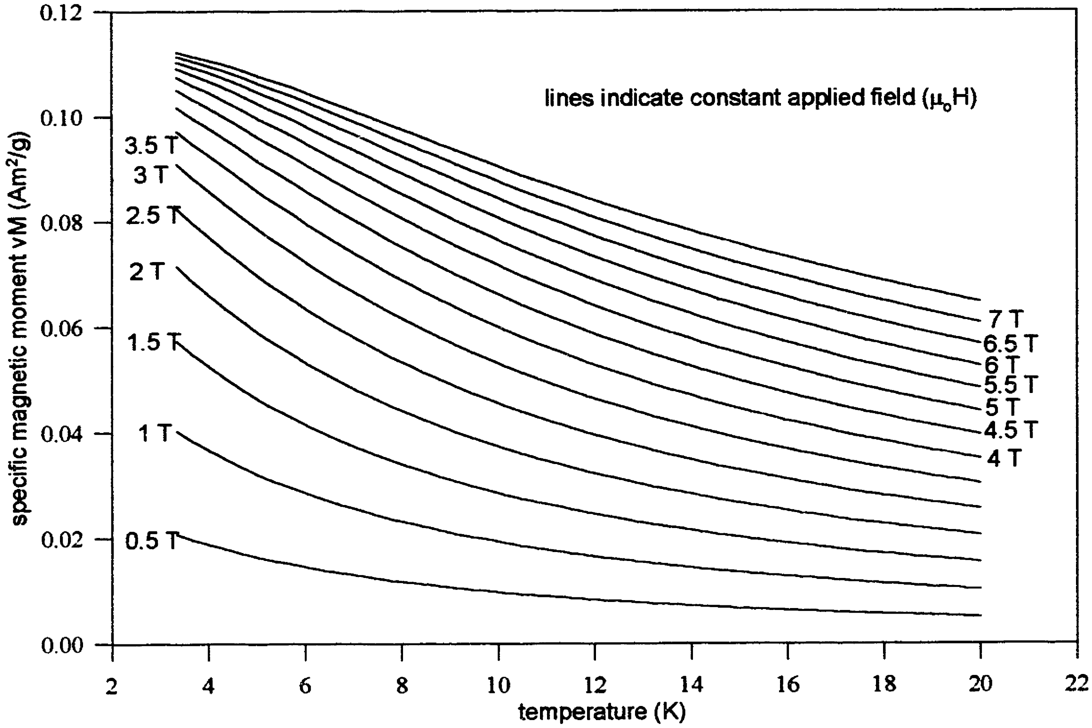

Figure 1-1. Equation of state for Gadolinium Gallium Garnet

moment lines. The computer code used to calculate the entropy of GGG and its first partial derivatives as functions of applied field and temperature is listed in appendix A.1.

1.3 Stirling/magnetic cycle

This section is divided into four subsections. In the first three sections the Stirling cycle, the magnetic cycle, and the Stirling/magnetic cycle are qualitatively described. The Stirling/magnetic cycle is shown to be the superposition of the Stirling cycle on the regenerative magnetic cycle and, for a very idealized cycle, the total refrigeration can be thought of as the sum of the refrigeration which would be obtained from these two cycles. In the fourth subsection, a first order model of the Stirling/magnetic cycle is developed. This model is subsequently used to investigate some of the important effects associated with the design of a Stirling/magnetic device. In particular, the dimensionless quantities which govern this type of a device are determined and a set of curves are developed to aid in the preliminary design of future Stirling/magnetic devices.

1.3.1 Description of Stirling cycle

The Stirling cycle (or the very similar Gifford McMahon cycle) is widely used to provide low temperature refrigeration [16]. This type of cycle utilizes the thermodynamic coupling which is present in a single-phase compressible substance.

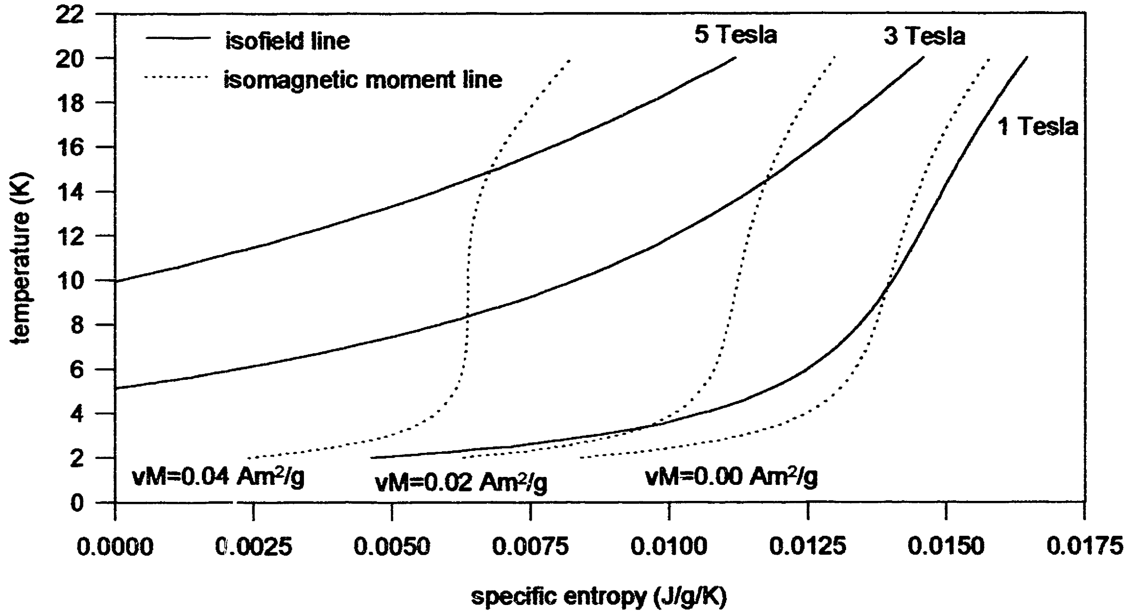

Figure 1-2. Entropy function for Gadolinium Gallium Garnet

An idealized version of a device used to implement a Stirling cycle is illustrated in Figure 1-3. The device consists of a cylinder which contains two opposing pistons. A regenerator lies between the pistons and the system is filled with a compressible substance. The regenerator is a matrix of material with a large heat capacity that is used to alternately absorb and release energy to the gas.

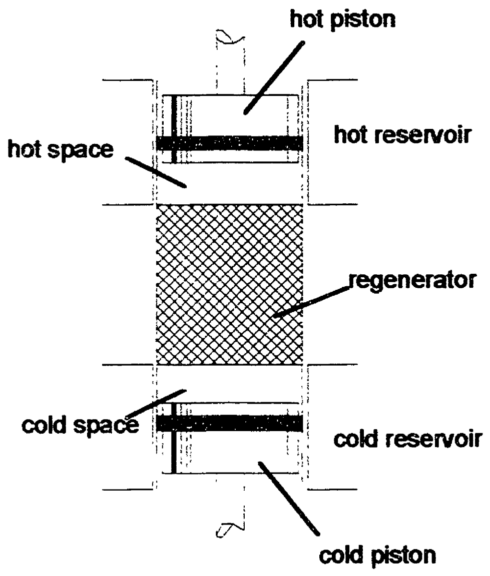

Figure 1-3. Stirling device

The space above the regenerator is called the hot space and is maintained at a high temperature (T_H) through contact with the hot reservoir. The space below the regenerator is called the cold space and is maintained at a low temperature (T_C) through contact with the cold reservoir.

Figure 1-4 illustrates the sequence of four processes which make up an ideal Stirling cycle [17]. These processes are described below.

compression

During the compression process, all of the gas is contained in the hot space of the device. The volume of the hot space is initially the maximum volume seen by the system (V_{max}). The hot piston is moved downwards until the system volume reaches the minimum volume seen by the system (V_{min}). In the limit of perfect thermal contact between the hot space and the hot reservoir, the gas remains at a constant temperature throughout the process.

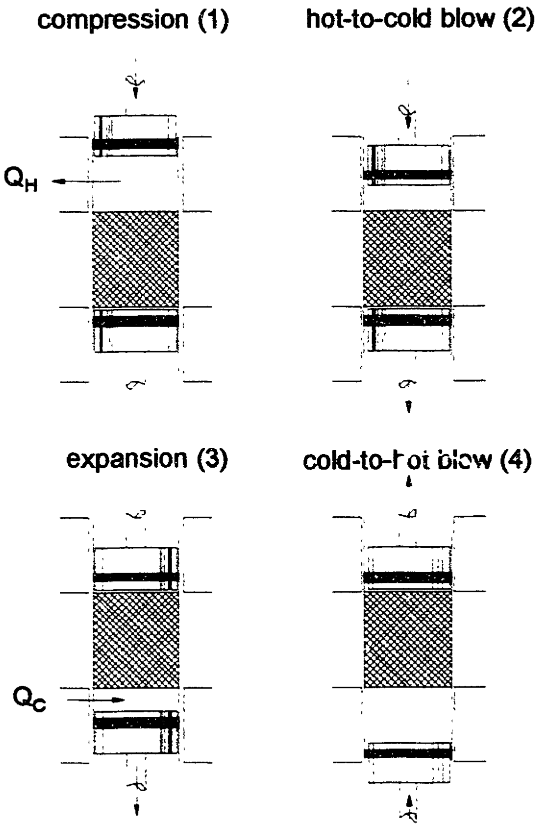

compression (1)

hot-to-cold blow (2)

expansion (3)

cold-to-hot blow (4)

Figure 1-4. Stirling cycle

The pressure rises as the volume decreases and a heat transfer is induced from the gas to the hot reservoir. A simple energy balance on the hot space shows that, for an ideal gas under these conditions, the heat rejection is given by equation 1.18 (where M_f is the total mass of fluid contained in the device and R is the ideal gas constant).

$$Q_H = M_f \cdot R \cdot T_H \cdot \ln\left(\frac{V_{max}}{V_{min}}\right) \quad \textbf{(1.18)}$$

hot-to-cold blow

During the hot-to-cold blow process, the hot and cold pistons move together, pushing gas from the hot space, through the regenerator, into the cold space. This process occurs at constant system volume. The regenerator will absorb entropy from the gas in order to reduce the temperature of the gas. Provided the regenerator heat capacity is sufficiently large, the temperature of the regenerator will not increase significantly during this process. In the limit of a perfect regenerator (i.e. infinite heat capacity and perfect thermal contact between the gas and the regenerator) the gas will reach the cold space at precisely the cold reservoir temperature. A real regenerator will deliver the gas to the cold space at a temperature somewhat above the cold reservoir temperature.

expansion

During the expansion process, all of the gas is contained in the cold space of the device. The volume of the cold space is initially the minimum volume seen by the system. The cold piston is moved downwards until the system volume reaches the maximum volume seen by the system. In the limit of perfect thermal contact between the cold space and the cold reservoir, the gas remains at a constant temperature throughout the process. The pressure drops as the volume increases and a heat transfer is induced from the cold reservoir to the gas. A simple energy balance on the cold space shows that, for an ideal gas under these conditions, the refrigeration is given by:

$$Q_C = M_f \cdot R \cdot T_C \cdot \ln\left(\frac{V_{max}}{V_{min}}\right) \quad \textbf{(1.19)}$$

cold-to-hot blow

During the cold-to-hot blow process, the hot and cold pistons move together, pushing gas from the cold space, through the regenerator, into the hot space. This process occurs at constant system volume. The regenerator will release entropy to the gas in order to increase the temperature of the gas.

The volume of the hot and cold spaces are illustrated in Figure 1-5. The net effect of a Stirling cycle is to pump entropy from the cold reservoir to the warm reservoir via a mechanical work transfer. In order for the Stirling cycle to operate effectively, the

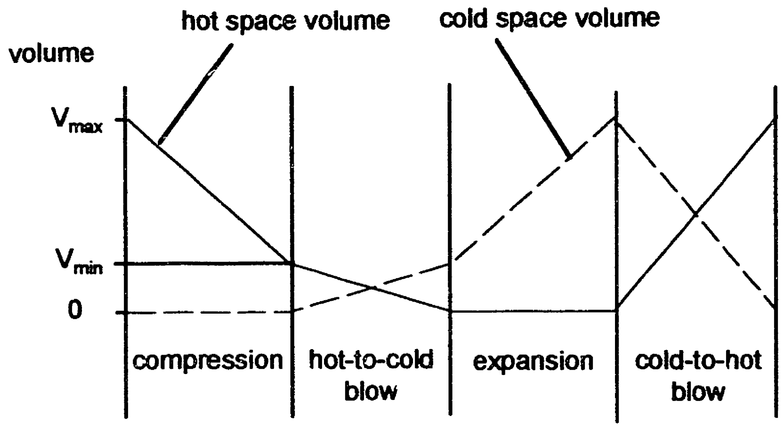

Figure 1-5. Volume of hot and cold spaces during Stirling cycle

regenerator must be capable of absorbing and releasing entropy from the compressible fluid with only a slight temperature change. At temperatures below 15 K, the specific heat capacity of conventional regenerator materials decreases very quickly, as illustrated in Figure 1-6. This effect is called thermal saturation and limits the temperature range of Stirling cycles. In order to efficiently produce refrigeration below 15 K, researchers have developed cryocoolers which use a paramagnetic substance as the thermodynamic working fluid and do not thermodynamically cycle a compressible fluid. This type of cycle is called a magnetic cycle and is explored in the next subsection.

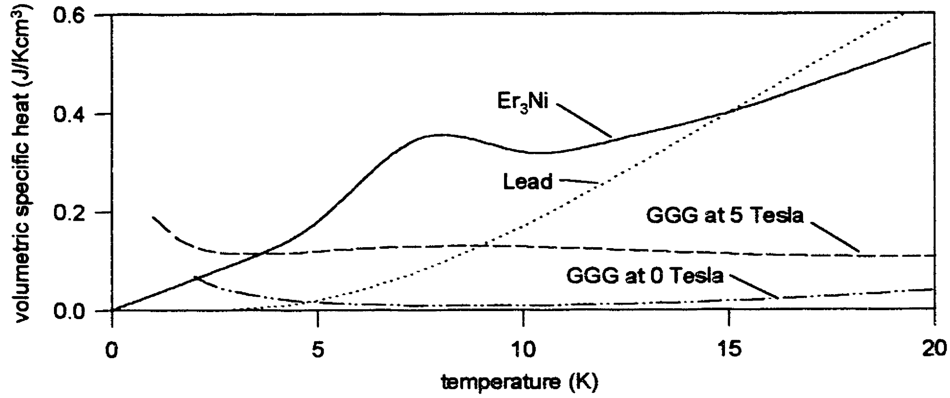

Figure 1-6. Volumetric heat capacity of common regenerator materials

1.3.2 Description of magnetic cycle

This subsection is divided into two parts corresponding to the two general ways that a paramagnetic material can be configured in order to produce refrigeration. The first part describes a 'rotating wheel' type magnetic cycle which is thermodynamically equivalent to a 'reciprocating' type magnetic cycle. In this type of magnetic cycle, the paramagnetic

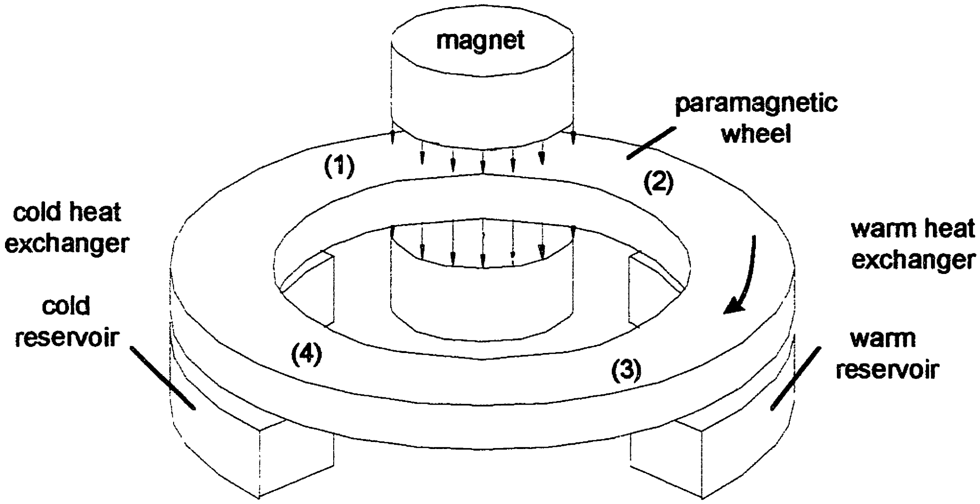

Figure 1-7. 'Rotating wheel' type magnetic refrigerator

material is physically moved into and out of an applied magnetic field. The second part describes a regenerative magnetic cycle.

1.3.2.1 Description of 'rotating wheel' type magnetic cycle

The 'rotating wheel' type device is illustrated in Figure 1-7. This type of device utilizes a constant magnetic field and two heat exchangers. The ideal thermodynamic cycle employed by this type of device is the magnetic equivalent of a Carnot cycle, as illustrated in Figure 1-8. The magnetic material moves through the magnetic field, causing its temperature rises (state 1 to state 2).

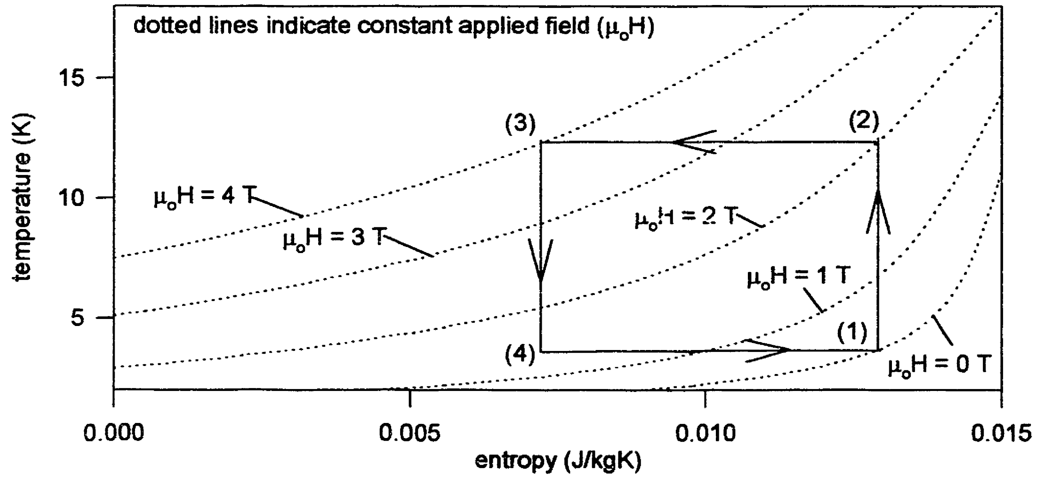

Figure 1-8. Magnetic equivalent of a Carnot cycle

Next, the material passes through the warm reservoir where it rejects heat and is further magnetized (state 2 to state 3). It is then demagnetized, causing its temperature to drop (state 3 to state 4). Finally, it accepts heat from the cold reservoir while it is further demagnetized (state 4 to state 1).

All of the paramagnetic material in a 'rotating wheel' type device undergoes the same thermodynamic cycle (albeit at different times). Therefore, the overall temperature range spanned by such a device is limited by the thermodynamic characteristics of the paramagnetic material. Also, it is very difficult to construct heat exchangers or thermal switches which can effectively transfer heat from the paramagnetic material to or from the associated thermal reservoirs. There have been several magnetic refrigerators built and tested which use some version of a 'rotating wheel' type magnetic cycle [18-26].

1.3.2.2 Description of regenerative magnetic cycle

A regenerative magnetic configuration overcomes the limitations outlined above. A regenerative magnetic device is illustrated in Figure 1-9. The device is similar to the Stirling device illustrated in Figure 1-3 except that the regenerator is composed of a paramagnetic substance which is surrounded by a solenoid. The solenoid can impose a controlled, time varying applied field on the paramagnetic matrix.

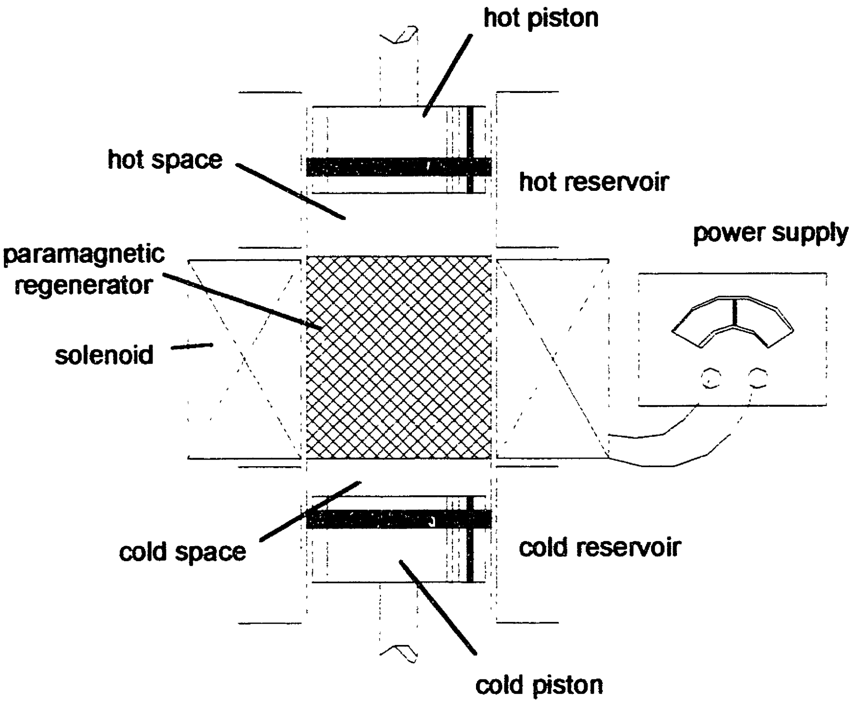

Figure 1-9. Regenerative magnetic device

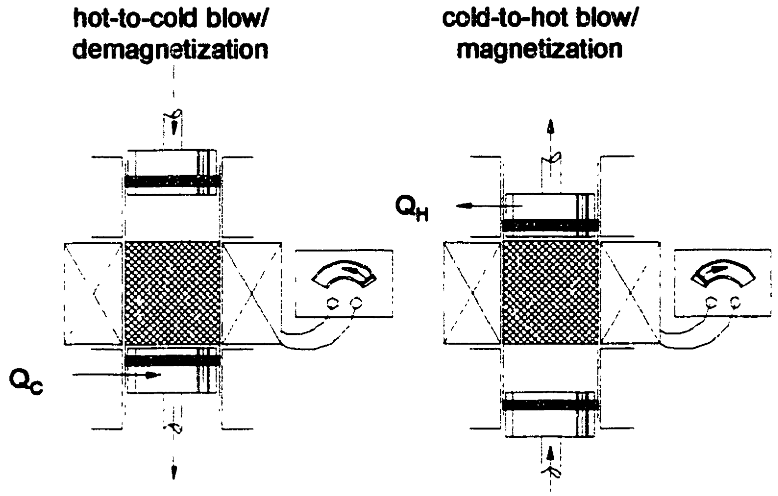

Figure 1-10. Regenerative magnetic cycle

All of the magnetically active regenerative devices currently being developed undergo some variation of the magnetic cycle described below and illustrated in Figure 1-10.

hot-to-cold blow/demagnetization

During the hot-to-cold blow/demagnetization process, the hot and cold pistons move together, pushing gas from the hot space, through the regenerator, into the cold space. This process occurs at constant system volume. The applied field in the paramagnetic regenerator goes from the maximum applied field seen by the cycle ($\mu_o H_{max}$) to zero. The regenerator absorbs entropy from the gas in order to reduce its temperature. Because the regenerator is being demagnetized, it can absorb this entropy even as its temperature decreases. Therefore, the fluid may be delivered to the cold space at a temperature *below* the temperature of the cold reservoir. This sub-cooled fluid produces the refrigeration associated with a regenerative magnetic cycle.

cold-to-hot blow/magnetization

During the cold-to-hot blow/magnetization process, the hot and cold pistons move together, pushing gas from the cold space, through the regenerator, into the hot space. This process occurs at constant system volume. The applied field in the paramagnetic regenerator goes from zero to the maximum applied field seen by the cycle. The regenerator releases entropy to the gas. Because the regenerator is being magnetized, it can release this entropy even as its temperature increases. Therefore, the fluid may be delivered to the cold space at a temperature above the temperature of the hot reservoir. This super-heated fluid causes heat to be rejected to the hot reservoir.

Many regenerative magnetic cycles also incorporate two adiabatic processes in which the applied field is varied without any flow through the regenerator. The resulting temperature change can increase the effectiveness of the overall cycle by increasing the net heat transfer to the magnetic regenerator.

The magnetic material undergoes a different thermodynamic cycle at each axial location. Consequently, this type of cryocooler can span a much larger temperature range than the 'rotating wheel' type magnetic device. The net result of a regenerative magnetic cycle is to pump entropy from the cold reservoir to the warm reservoir with a magnetic work transfer.

There have been several regenerative magnetic devices constructed and tested [27-32]. These devices have, to varying degrees, been successful. However, it is evident that the regenerative magnetic cycle uses a compressible fluid as the heat transfer medium without utilizing its ability to pump heat in addition to the paramagnetic substance. The Stirling/magnetic cycle described in the next subsection overcomes this limitation.

1.3.3 Description of Stirling/magnetic cycle

The regenerative magnetic devices use a purely magnetic cycle due to analytical and experimental convenience rather than any inherent advantage associated with this type of cycle. The interactions which occur between two thermodynamically active materials become highly complex, particularly when the properties of both substances are non-ideal.

The Stirling/magnetic cycle allows both the compressible fluid and the paramagnetic material to undergo thermodynamic cycles and pump heat. The applied field in a paramagnetic regenerator and the pressure within a compressible fluid are both cyclically varied. This is a fundamentally new type of refrigeration cycle which has not previously been tested. This type of cycle was first proposed by Jeong, et. al. [33] and subsequently analyzed by the author [34]. The results of this analysis indicate that a Stirling/magnetic cycle has the potential to be more effective than either a Stirling cycle or a regenerative magnetic cycle, particularly at low temperatures.

The device used to implement a Stirling/magnetic cycle is identical to the regenerative magnetic device illustrated in Figure 1-9. The Stirling/magnetic cycle is illustrated in Figure 1-11 and described below.

hot-to-cold blow/demagnetization

During the hot-to-cold blow/demagnetization process, the hot and cold pistons move together, pushing gas from the hot space, through the regenerator, into the cold space. This process occurs at constant minimum system volume (V_{min}). The applied field in the paramagnetic regenerator goes from the maximum value seen by the cycle ($\mu_o H_{max}$) to zero. The regenerator absorbs entropy from the gas in order to reduce its temperature. Because the regenerator is being demagnetized, it can absorb this entropy even as its temperature decreases. Therefore, the fluid may be delivered to the cold space at a temperature *below* the temperature of the cold reservoir. This sub-cooled fluid produces refrigeration in the same way as the

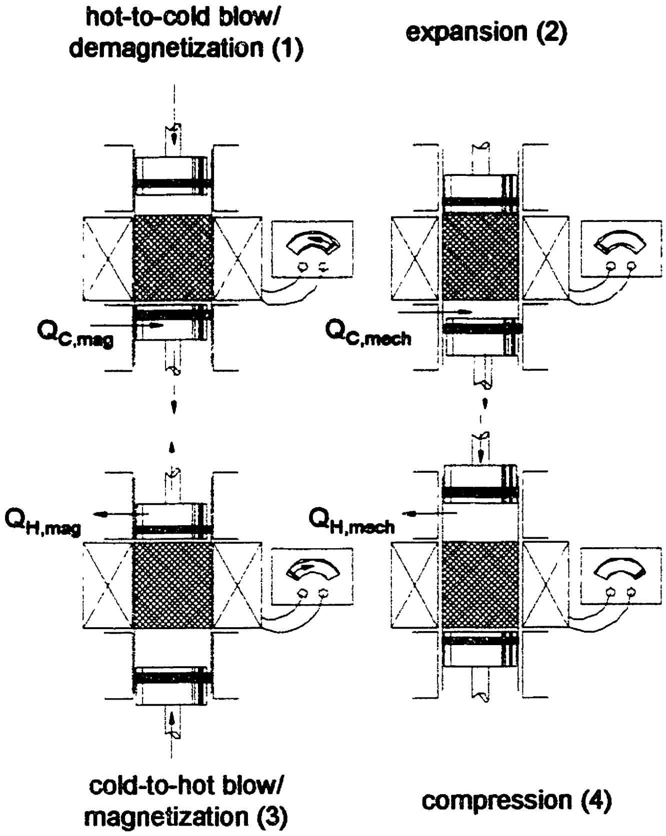

Figure 1-11. Stirling/magnetic cycle

regenerative magnetic cycle. For this idealized cycle, the refrigeration due to the flow of sub-cooled fluid into the cold space may be thought of as the 'magnetic' component of the total refrigeration ($Q_{C,mag}$).

expansion

During the expansion process, the hot piston is not moved so that all of the gas remains in the cold space of the device. The cold piston is moved downwards until the system volume reaches the maximum volume seen by the system (V_{max}). In the limit of perfect thermal contact between the cold space and the cold reservoir, the gas remains at a constant temperature throughout the process. The pressure drops as the volume increases and a heat transfer is induced from the cold reservoir to the gas, producing refrigeration in the same manner as a Stirling cycle. For this idealized cycle, the refrigeration associated with the expansion of the compressible fluid in the cold space may be thought of as the 'mechanical' component of the total refrigeration ($Q_{C,mech}$).

cold-to-hot blow/magnetization

During the cold-to-hot blow/magnetization process the hot and cold pistons move together, pushing gas from the cold space, through the regenerator, into the hot space. This process occurs at constant maximum system volume. The applied field in the paramagnetic regenerator goes from zero to the maximum applied field seen by the cycle ($\mu_o H_{max}$).

compression

During the compression process the cold piston is not moved so that all of the gas remains in the hot space of the device. The hot piston is moved downwards until the system volume reaches the minimum volume seen by the system.

During the Stirling/magnetic cycle, both the paramagnetic regenerator and the compressible fluid undergo thermodyamic cycles. Because both substances are used for thermal energy conversion, the refrigeration potential of the cycle is much larger than either the Stirling cycle or the regenerative magnetic cycle alone.

1.3.4 First order model of Stirling/magnetic cycle

This subsection is divided into three parts. The first part develops a first order model of a Stirling/magnetic device. This model is based on several simplifying assumptions and therefore is not a predictive model. Its value lies in its ability to illustrate the fundamental processes associated with a Stirling/magnetic cycle. The second part presents and interprets the results of the first order model. Because the first order model limits to a Stirling cycle and a regenerative magnetic cycle for certain input parameters, it can be used to compare the refrigeration potential of a typical Stirling cycle, regenerative magnetic cycle, and Stirling/magnetic cycle. This comparison is carried out in the final part.

1.3.4.1 Development of first order model.

This model assumes that there is no void volume within the regenerator. Therefore, the regenerator only influences the overall cycle during the hot-to-cold blow and cold-to-hot blow processes. Additional key assumptions include : ideal gas behavior of the compressible substance, Curie-Weiss behavior of the paramagnetic material, no axial conduction, no pressure drop due to flow resistance, and isothermal cold and hot spaces. These assumptions restrict the use of this first order model as a design tool. However the results are capable of illustrating the fundamental processes associated with a Stirling/magnetic cycle.

Figure 1-12 illustrates the control volume used to develop the governing equations for the hot-to-cold blow process ($0 < t \leq \tau$). Energy balances around a differential fluid passage and differential regenerator segment yield two partial differential equations (note that U in equation 1.20 represents the total conductance between the fluid and the regenerator).

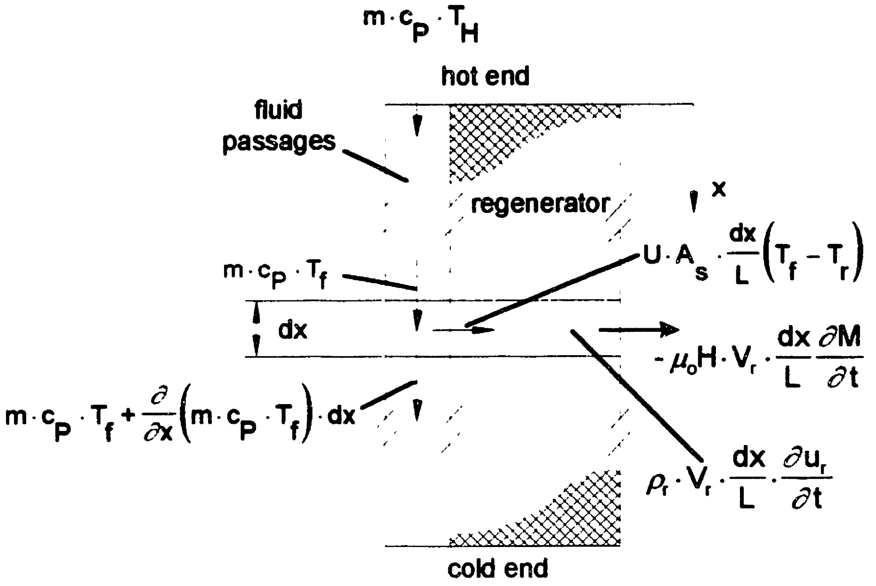

Figure 1-12. Control volume for Stirling/magnetic cycle governing equations

$$0 = U \cdot A_s \cdot \frac{dx}{L}(T_f - T_r) + \frac{\partial}{\partial x}(m \cdot c_p \cdot T_f) \cdot dx \tag{1.20}$$

An energy balance on the regenerator must include a magnetic work term as well as an energy storage term (note that M_r in equation 1.21 refers to the total magnetization of the regenerator material).

$$0 = U \cdot A_s \cdot \frac{dx}{L} \cdot (T_r - T_f) + \rho_r \cdot V_r \cdot \frac{dx}{L} \cdot \frac{\partial u_r}{\partial t} - \mu_o H \cdot V_r \cdot \frac{dx}{L} \cdot \frac{\partial M_r}{\partial t} \tag{1.21}$$

If linear piston motions are assumed, then the mass flow rate is constant throughout the hot-to-cold blow process and is equal to the total mass of fluid (M_f) divided by the flow process time (τ). Substituting this into equations 1.20 and 1.21 and simplifying yields the governing equations for the hot-to-cold blow process.

$$0 = \frac{U \cdot A_s}{L}(T_f - T_r) + \frac{M_f \cdot c_p}{\tau} \frac{\partial T_f}{\partial x} \tag{1.22}$$

$$0 = U \cdot A_s(T_r - T_f) + \rho_r \cdot V_r \left(\frac{\partial u_r}{\partial t} - \mu_o H \cdot \frac{\partial (vM)_r}{\partial t} \right) \tag{1.23}$$

If the regenerator material is assumed to undergo an internally reversible process, then the mass specific differential first law for a paramagnetic substance (equation 1.4) may be substituted into equation 1.23.

$$0 = U \cdot A_s\left(T_r - T_f\right) + \rho_r \cdot V_r \cdot T_r \cdot \frac{\partial s_r}{\partial t} \tag{1.24}$$

The entropy change of the paramagnetic material is divided into a temperature and an applied field driven component.

$$0 = U \cdot A_s\left(T_r - T_f\right) + \rho_r \cdot V_r \cdot T_r \cdot \left[\left(\frac{\partial s_r}{\partial T}\right)_{\mu_o H} \frac{\partial T_r}{\partial t} + \left(\frac{\partial s_r}{\partial \mu_o H}\right)_T \frac{d\mu_o H}{dt}\right] \tag{1.25}$$

The partial derivatives of entropy associated with the Curie-Weiss equation of state (equations 1.16 and 1.17) are substituted into equation 1.25.

$$0 = U \cdot A_s\left(T_r - T_f\right) + \left[c_{H=0} \cdot \rho_r \cdot V_r + \frac{C}{\mu_o} \cdot \frac{\left(\mu_o H\right)^2 \cdot V_r}{T_r^2}\right] \frac{\partial T_r}{\partial t} - \frac{C}{\mu_o} \cdot \frac{\mu_o H \cdot V_r}{T_r} \cdot \frac{d\mu_o H}{dt} \tag{1.26}$$

Equations 1.22 and 1.26 are the governing partial differential equations for the hot-to-cold blow/demagnetization portion of the Stirling/magnetic cycle. The temperature of the fluid entering the hot end of the device during this process is assumed to be the temperature of the hot reservoir.

$$T_f(0,t) = T_H \quad 0 < t \le \tau \tag{1.27}$$

The governing partial differential equations for the cold-to-hot blow/magnetization portion of the cycle are also equations 1.22 and 1.26 except that the sign of the second term in equation 1.22 is switched since the mass flow rate is in the opposite direction. The axial boundary condition associated with this process is that the temperature of the fluid entering the cold end of the regenerator is assumed to be at the cold reservoir temperature.

$$T_f(L,\ t) = T_C \quad \tau < t \le 2 \cdot \tau \tag{1.28}$$

The boundary condition required in time is that the cycle be steady state.

$$T_r(x,0) = T_r(x,\ 2 \cdot \tau) \tag{1.29}$$

In order to reduce the number of parameters required for a complete analysis and make the model more general, several nondimensional parameters are defined. The sensible heat capacity ratio (Γ) reflects the ratio of the sensible heat capacity of the regenerator matrix to the capacity of the compressible fluid. The number of transfer units (NTU) reflect the ratio of the conductance between the matrix and the compressible fluid to the capacity rate of the compressible fluid. These parameters are defined below.

$$\Gamma \equiv \frac{V_r \cdot \rho_r \cdot c_{H=0}}{M_f \cdot c_P} \tag{1.30}$$

$$NTU \equiv \frac{U \cdot A_s \cdot \tau}{M_f \cdot c_P} \tag{1.31}$$

The temperatures, position, and time are also made dimensionless.

$$\varepsilon \equiv \frac{x}{L} \tag{1.32}$$

$$\varsigma \equiv \frac{t}{\tau} \tag{1.33}$$

$$\Theta_f \equiv \frac{T_f}{T_C} \tag{1.34}$$

$$\Theta_r \equiv \frac{T_r}{T_C} \tag{1.35}$$

The volume ratio ($VR = V_{max}/V_{min}$), temperature ratio ($TR = T_H/T_C$), and ratio of specific heat capacities of the fluid ($k = c_P/c_V$) are also parameters used in this analysis.

In addition to the dimensionless parameters typically associated with a Stirling cycle analysis, several new parameters must be defined. The magneto-caloric effect is scaled with respect to the sensible heat capacity of the fluid and the result is called the magnetic capacity ratio (λ) which is defined below.

$$\lambda \equiv \frac{(\mu_o H_{max})^2 \cdot C \cdot V_r}{M_f \cdot c_P \cdot \mu_o \cdot T_C^2} \tag{1.36}$$

The dimensionless applied field (σ) is obtained by dividing the applied field by the maximum applied field seen by the cycle.

$$\sigma \equiv \frac{\mu_o H}{\mu_o H_{max}} \tag{1.37}$$

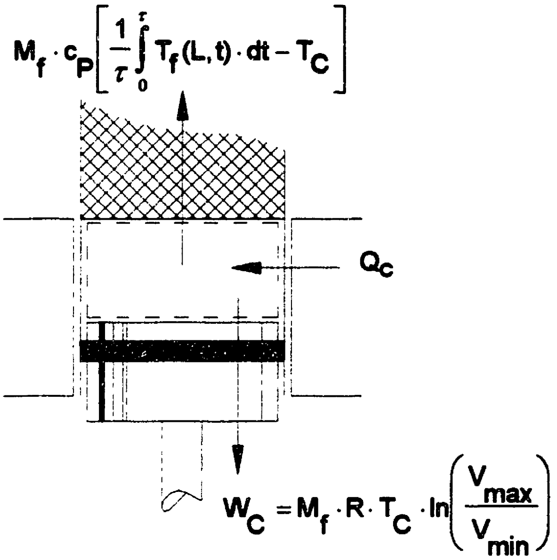

Figure 1-13. Control volume for refrigeration calculation

The nondimensional statement of the problem is given below.

$$\begin{gathered}
0 = NTU(\Theta_r - \Theta_f) + \left[\Gamma + \frac{\lambda\cdot\sigma^2}{\Theta_r^2}\right]\frac{\partial\Theta_r}{\partial\varsigma} - \frac{\lambda\cdot\sigma}{\Theta_r}\cdot\frac{d\sigma}{d\varsigma} \\
\sigma = (1-\varsigma) \quad \frac{d\sigma}{d\varsigma} = -1 \ \text{for } 0 < \varsigma \le 1 \\
\sigma = \varsigma \quad \frac{d\sigma}{d\varsigma} = 1 \ \text{for } 1 < \varsigma \le 2 \\
\Theta_r(\varepsilon,0) = \Theta_r(\varepsilon,2)
\end{gathered} \tag{1.38}$$

$$0 = NTU\left(\Theta_f - \Theta_r\right) + \frac{\partial\Theta_f}{\partial\varepsilon} \quad \Theta_f(0,\varsigma) = 1 \ \text{for } 0 < \varsigma \le 1 \tag{1.39}$$

$$0 = NTU\left(\Theta_f - \Theta_r\right) - \frac{\partial\Theta_f}{\partial\varepsilon} \quad \Theta_f(1,\varsigma) = 0 \ \text{for } 1 < \varsigma \le 2 \tag{1.40}$$

The total refrigeration associated with the Stirling/magnetic is obtained using a control volume which consists of the cold space of the device, as shown in Figure 1-13.

$$Q_C = M_f \cdot R \cdot T_C \cdot \ln\left(\frac{V_{max}}{V_{min}}\right) - M_f \cdot c_P \cdot \left[\frac{1}{\tau}\int_0^\tau T_f(L,t)\cdot dt - T_C\right] \tag{1.41}$$

The refrigeration is made nondimensional by comparing it to the refrigeration associated with an ideal (i.e. reversible) Stirling cycle. In such a cycle, the working fluid is delivered to the cold space at exactly the cold temperature and the refrigeration is the first term of equation 1.41. The dimensionless refrigeration is given by equation 1.42.

$$\Psi \equiv \frac{Q_C}{M_f \cdot R \cdot T_C \cdot \ln(VR)} = 1 - \frac{k}{(k-1) \cdot \ln(VR)} \int_0^1 \{\Theta_f(1,\varsigma) - 1\} \cdot d\varsigma \qquad (1.42)$$

It is also convenient to define a dimensionless entropy for use in examining the thermodynamic cycles undergone by the paramagnetic substance at each axial position. The dimensionless specific entropy is taken to be the entropy divided by the specific heat capacity at constant zero applied field.

$$\beta \equiv \frac{s}{c_{H=0}} = \ln(\Theta) - \frac{1}{2} \cdot \frac{\lambda}{\Gamma} \cdot \frac{\sigma^2}{\Theta^2} \qquad (1.43)$$

The ratio of the magnetic capacity ratio to the sensible heat capacity ratio (λ/Γ) which appears in equation 1.43 is a material property of the paramagnetic substance that reflects the strength of the magneto-caloric effect relative to its sensible heat capacity. This ratio will subsequently be referred to as the magnetic to thermal capacity ratio.

The dimensionless refrigeration defined in equation 1.42 has the functional dependence shown below.

$$\Psi = \Im(VR, TR, k, \Gamma, \lambda, NTU) \qquad (1.44)$$

The most relevant parameters with regards to understanding the fundamental processes associated with a Stirling/magnetic cycle are the sensible heat capacity ratio and the magnetic capacity ratio. The investigation of these parameters is the primary goal of the next subsection. The effect of the other parameters is also interesting but fairly unambiguous. Increasing the number of transfer units will always help the cycle, as will increasing the volume ratio. Decreasing the temperature ratio will tend to make the cycle more effective. The ratio of specific heats is a secondary parameter in this analysis.

1.3.4.2 Results of first order model

The set of nonlinear partial differential equations and boundary conditions given by equations 1.38 to 1.40 are solved using a full matrix inversion of the linearized equations. The resulting solution is used to recalculate the coefficients of the linearized equations, resulting in a Newton-Raphson iteration to the correct solution. The code used to solve these equations is listed in appendix A.2.

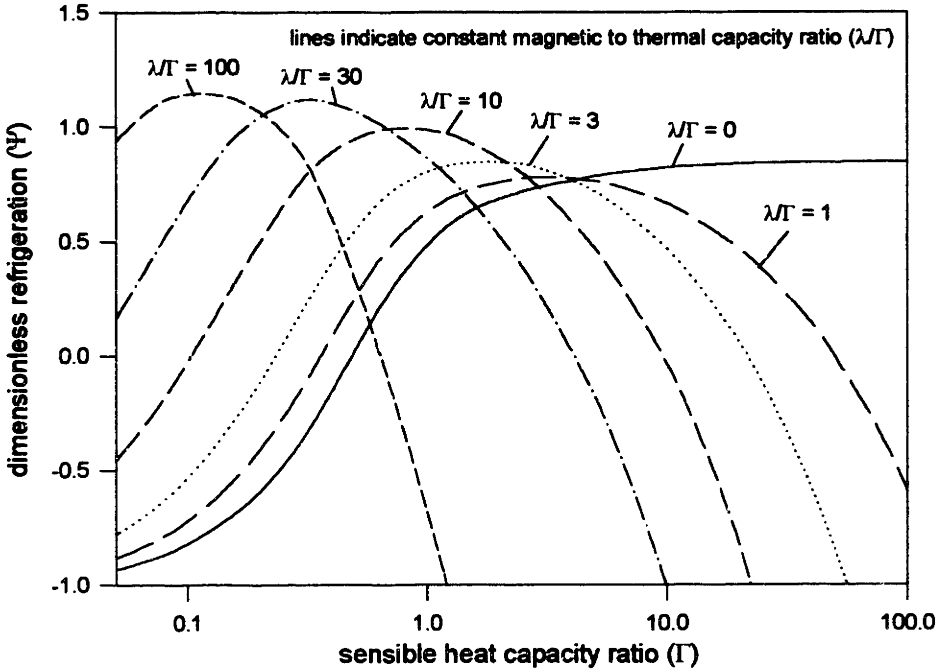

Figure 1-14. Dimensionless refrigeration as a function of sensible heat capacity ratio at various values of the magnetic to thermal capacity ratio ($k = 5/3$, $TR = 2$, $VR = 3$, $NTU = 25$)

Figure 1-14 illustrates the variation of the dimensionless refrigeration as a function of the sensible heat capacity ratio at several values of the magnetic to thermal capacity ratio. A magnetic to thermal capacity ratio of zero indicates a conventional regenerator material (i.e. no magneto-caloric effect) and corresponds to the performance of a Stirling device at the given capacity ratio and number of transfer units. This curve asymptotically approaches a constant value as the sensible heat capacity ratio increases. This occurs because the effectiveness of a conventional regenerator unambiguously increases as the heat capacity of the regenerator becomes larger relative to the heat capacity of the gas.

Figure 1-15 illustrates the temperature of the fluid at the cold end of the device as a function of time during the hot-to-cold blow/demagnetization process for a conventional regenerator (i.e. $\lambda/\Gamma = 0$). Various levels of the sensible heat capacity ratio are illustrated. For a low sensible heat capacity ratio, the capacity of the fluid overwhelms the capacity of the regenerator matrix resulting in a rush of warm fluid into the cold end. Consequently, the refrigeration suffers as the cold reservoir is required to cool the incoming fluid. This is the origin of the thermal saturation effect which limits the temperature range of devices with conventional regenerator materials.

As the magnetic to thermal capacity ratio is increased, the curves shown in Figure 1-14 become more bell-shaped. At low sensible heat capacity ratios, the increase in magnetic to thermal capacity increases the refrigeration. Figure 1-16 illustrates the temperature of the fluid entering the cold space as a function of time during the hot-to-cold

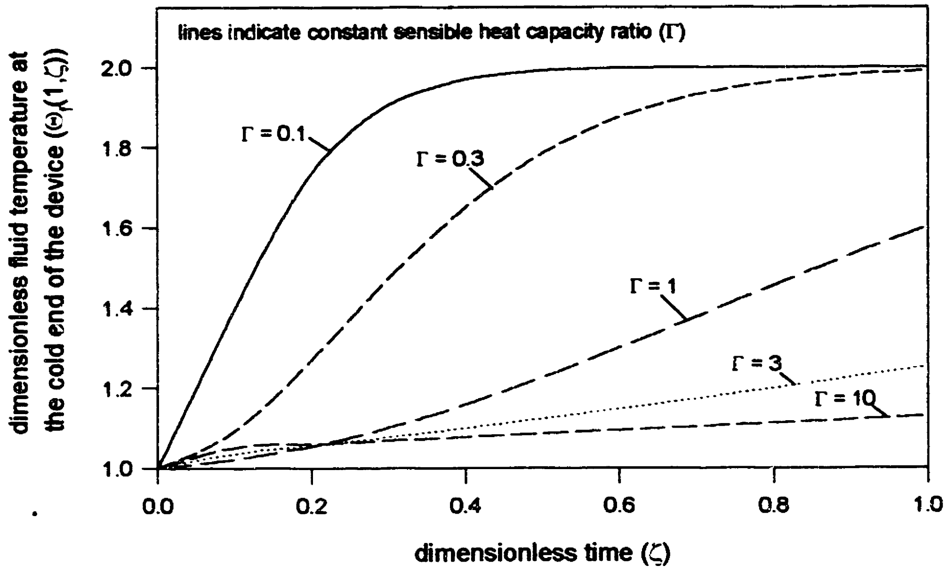

Figure 1-15. Variation of fluid temperature at cold end of device for conventional regenerator (λ=0) as a function of dimensionless time at various values of the sensible heat capacity ratio (k=5/3, TR = 2, VR = 3, NTU = 25)

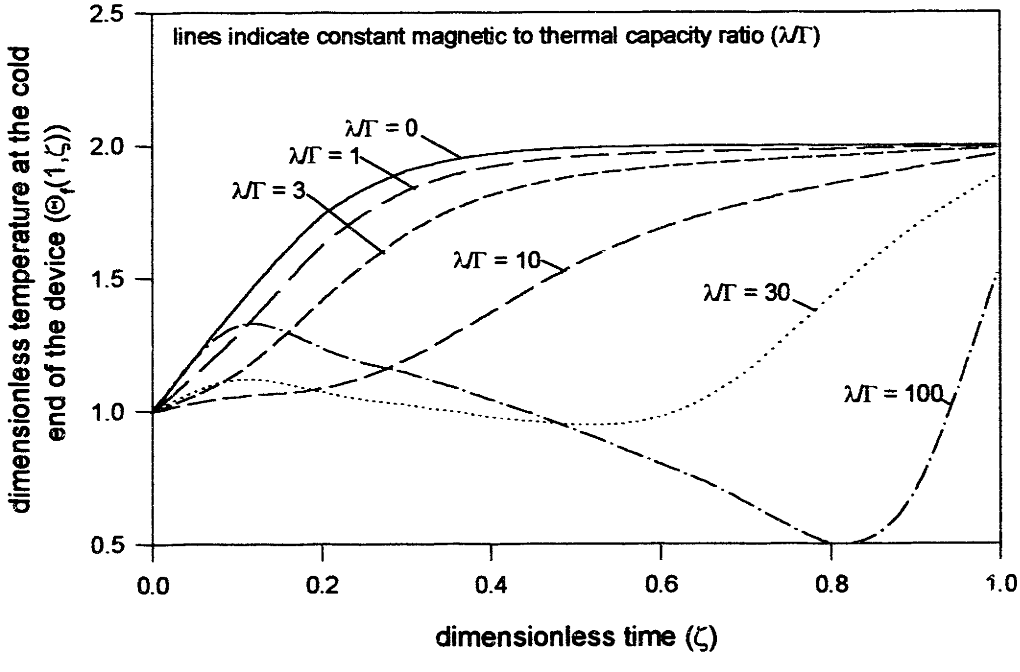

Figure 1-16. Variation of the fluid temperature at the cold end of the device as a function of dimensionless time for various values of magnetic to thermal capacity ratio (k = 5/3 , TR = 2 , VR = 3 , NTU = 25 , Γ = 0.1)

blow/demagnetization portion of the cycle for a low sensible heat capacity ratio ($\Gamma = 0.1$). Various values of the magnetic to thermal capacity ratio are illustrated. At $\lambda/\Gamma = 0$, the regenerator exhibits the thermal saturation effect discussed with regards to Figure 1-15. However, as the magneto-caloric effect of the regenerator is increased, the temperature at the cold end begins to decrease. The regenerator can absorb some entropy from the gas due to the demagnetization effect. Consequently, its temperature need not rise as dramatically and the fluid is delivered to the cold space at a colder temperature. At very high λ/Γ, the fluid becomes 'subcooled' - it flows into the cold space with a temperature less than the cold reservoir temperature ($\Theta_f(1,\zeta) < 1$). This is the manifestation of the magnetic refrigeration seen at the cold end. A regenerative magnetic cycle depends on this effect alone to produce refrigeration.

The behavior of the paramagnetic regenerator can be understood by examining the thermodynamic cycles undergone by the regenerator material at each axial position. Figure 1-17 illustrates the dimensionless temperature-entropy diagram for the regenerator material at the midpoint of the device for various values of magnetic to thermal capacity ratios. For $\lambda/\Gamma = 0$, the thermodynamic cycle undergone by the regenerator material falls on a single line (the material is an uncoupled substance). As the magneto-caloric effect is

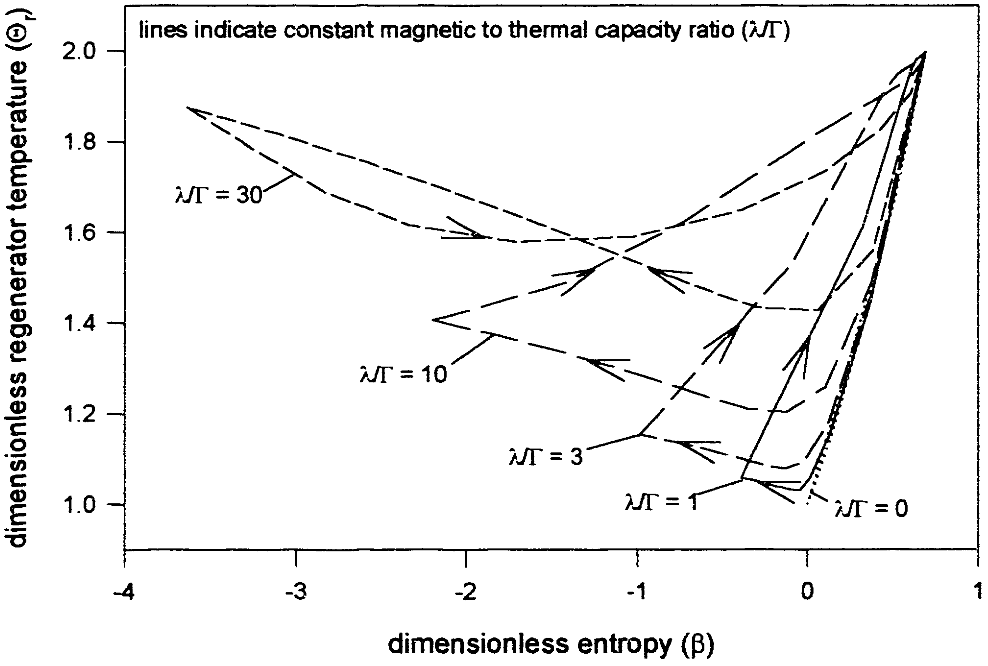

Figure 1-17. Thermodynamic cycles undergone by the paramagnetic material at the midpoint of the device ($\varepsilon = 0.5$) for various values of magnetic to thermal capacity ratio ($k = 5/3$, $TR = 2$, $VR = 3$, $NTU = 25$, $\Gamma = 0.1$)

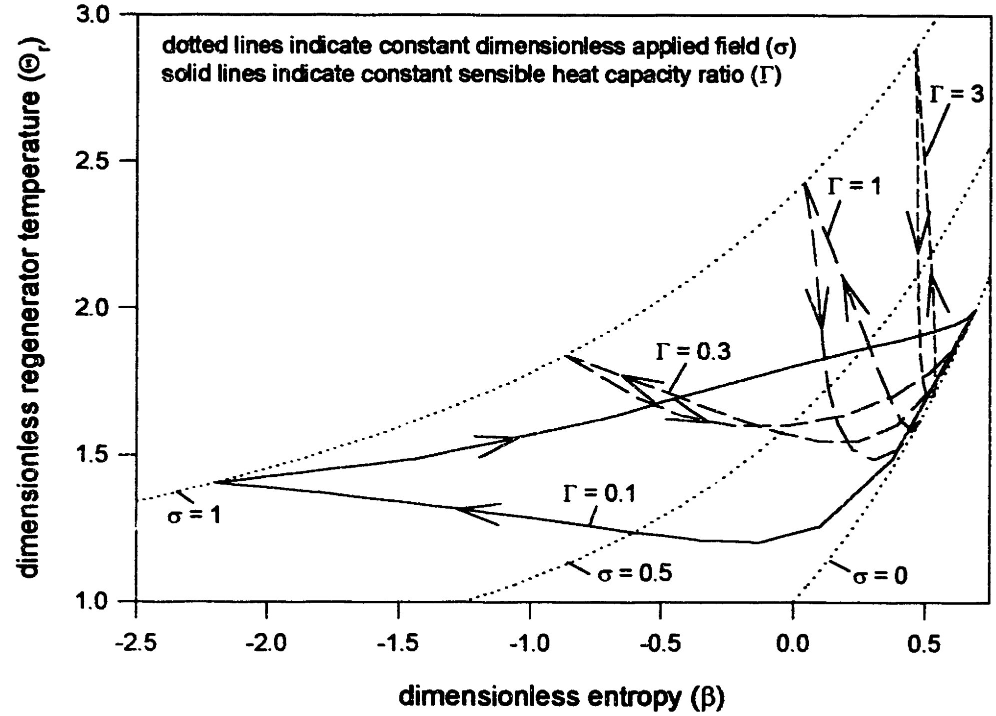

Figure 1-18. Thermodynamic cycles undergone by the paramagnetic material at the midpoint of the device ($\varepsilon = 0.5$) for various values of sensible heat capacity ratio ($k = 5/3$, $TR = 2$, $VR = 3$, $NTU = 25$, $\lambda/\Gamma = 10$)

increased, the area of the temperature entropy diagram increases. At high λ/Γ, the regenerator material actually becomes a differential refrigerator - the material absorbs heat at a low temperature and rejects it to a slightly higher temperature by virtue of a magnetic work transfer. As the magnetic field approaches zero, the magneto-caloric effect becomes small regardless of the magnetic to thermal capacity ratio. Consequently the temperature of the regenerator material starts to increase abruptly. It is for this reason that most regenerative magnetic cycles do not completely demagnetize the regenerator.

Figure 1-14 shows that for every sensible heat capacity ratio there is an optimal magnetic to thermal capacity ratio. This effect occurs because the magnetization during the cold-to-hot blow/magnetization process drives the temperature of the regenerator up an increasing amount as λ/Γ is increased. The optimal magnetic to thermal capacity ratio balances the increasing amount entropy absorption available during the hot-to-cold blow/demagnetization process with the increasing temperature elevation during the cold-to-hot blow/magnetization process.

Figure 1-14 also shows that for any nonzero λ/Γ there is a maximum dimensionless refrigeration as the sensible heat capacity ratio is varied. Figure 1-18 illustrates the thermodynamic cycles undergone by the regenerator material at the midpoint of the device for various values of sensible heat capacity ratio. At very high sensible heat capacity ratio, the capacity of the gas is small relative to the magnetocaloric effect. Consequently the temperature of the regenerator matrix decreases nearly adiabatically during the hot-to-cold

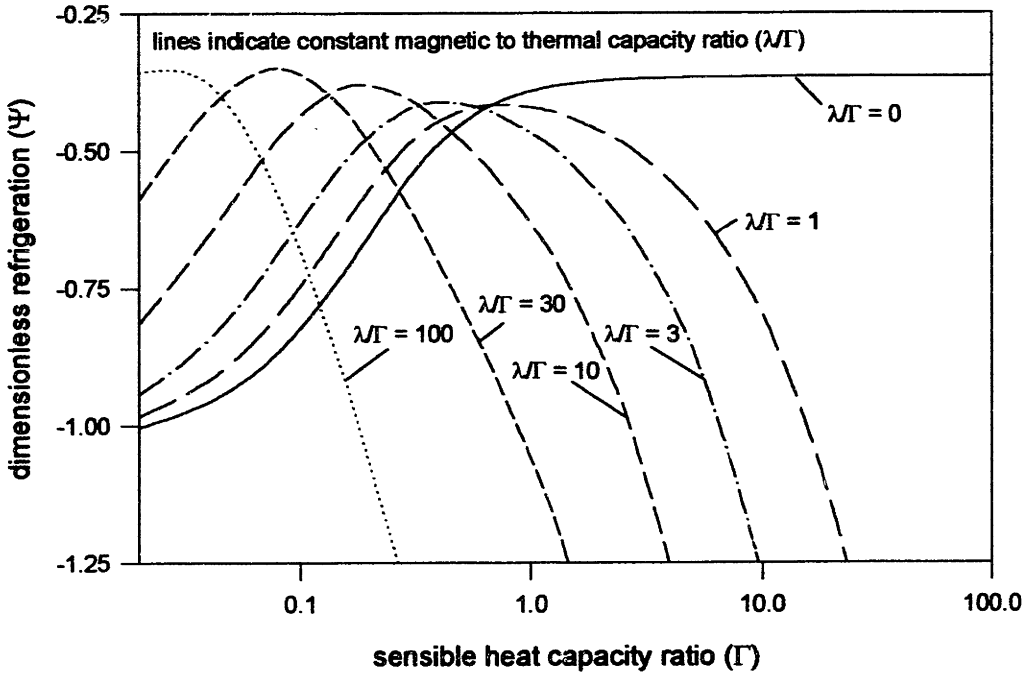

Figure 1-19. Dimensionless refrigeration as a function of sensible heat capacity ratio at various values of the magnetic to thermal capacity ratio (k=5/3 , TR = 2 VR = 3 , NTU = 1)

blow portion of the cycle and increases nearly adiabatically during the cold-to-hot blow portion of the cycle. However, no significant area is swept out by the thermodynamic cycle and the differential refrigeration is negligible. At very low sensible heat capacity ratio, the capacity of the gas overwhelms the magneto-caloric effect and the temperature rises during the cold-to-hot blow process resulting in a refrigeration loss at the cold end. The optimal sensible heat capacity ratio balances these two effects.

Figure 1-14 illustrates that the Stirling/magnetic cycle effectively overcomes the thermal saturation effect. At very low sensible heat capacity ratio (such as might occur at very low temperature) the Stirling cycle (i.e. λ/Γ = 0) becomes very ineffective. This is precisely the region where the Stirling/magnetic cycle becomes most effective.

Figures 1-19 and 1-20 illustrate the variation of the dimensionless refrigeration as a function of the sensible heat capacity ratio at several values of the magnetic to thermal capacity ratio. Each figure corresponds to a different number of transfer units (NTU = 1 and NTU = 10). As the number of transfer units are increased, the cycles become more effective but the shape of the curves do not qualitatively change.

The first order Stirling/magnetic model limits to a Stirling cycle when the magnetic to thermal capacity ratio is zero and limits to a regenerative magnetic cycle when the volume ratio is zero. Therefore, it can be used to effectively illustrate the advantages associated with a Stirling/magnetic cycle over either of the other two types of cycles. This is the goal of the next subsection.

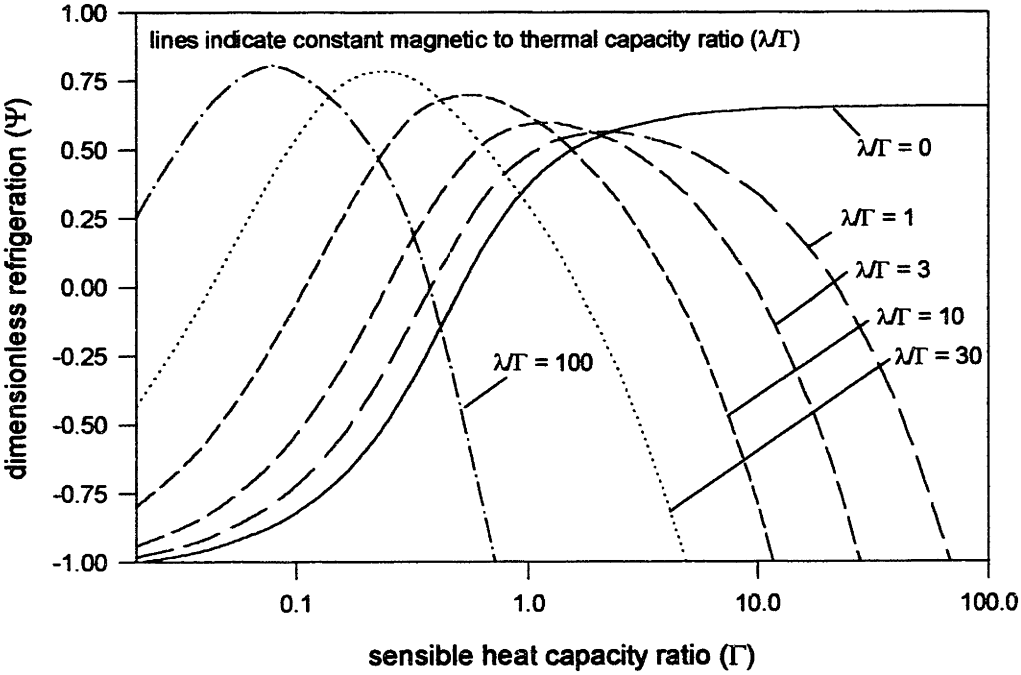

Figure 1-20. Dimensionless refrigeration as a function of sensible heat capacity ratio at various values of the magnetic to thermal capacity ratio (k=5/3 , TR = 2 VR = 3 , NTU = 10)

1.3.4.3 Comparison of Stirling cycle, regenerative magnetic cycle, and Stirling/magnetic cycle

In order to demonstrate the advantages associated with a Stirling/magnetic cycle relative to either a Stirling cycle or a regenerative magnetic cycle, the refrigeration potential of a typical device undergoing each of these cycles is examined. The characteristics of such a device are listed in Table 1-1. It is assumed that the Stirling device has a lead regenerator matrix since lead has a larger volumetric heat capacity than most paramagnetic materials even at low temperatures. Because the temperature range of interest (below 20 K) is much less than the Debye temperature for lead ($T_{D,Pb}$ = 88 K [35]), the specific heat capacity of lead can be modeled with the following equation [36].

$$c_{Pb}(T) \approx 3 \cdot R^{\circ} \cdot \frac{4 \cdot \pi^4}{5 \cdot MM_{Pb}} \cdot \left(\frac{T}{T_{D,Pb}} \right)^3 \qquad (1.45)$$

It is also assumed that the regenerative magnetic device and the Stirling/magnetic device have a regenerator composed of GGG behaving according to the Curie-Weiss law. The compressible fluid in all of the devices is taken to be helium-4 behaving as an ideal gas. The required property values are evaluated at the average of the warm and cold reservoir temperatures of the device.

Table 1-1. Characteristics of a typical regenerative cryocooler used to compare a Stirling cycle, regenerative magnetic cycle, and Stirling/magnetic cycle

Description	Value	Description	Value
bore diameter	5 cm	bore length	7 cm
area for heat transfer	1.6 m^2	regenerator volume	1.37e-4 m^3
molecular mass of lead	207.2 kg/kgmol	GGG specific heat capacity at constant zero applied field	2.95 J/kgK
Curie constant of GGG	1.9 K	Debye temperature of lead	88 K
maximum applied field	4 tesla	heat transfer coefficient	50 W/m^2K
universal gas constant	8314.5 J/kgmolK	ratio of specific heat capacities for helium-4	5/3
temperature ratio	2	volume ratio	3
specific heat capacity at constant pressure for helium-4	5231 J/kgK	density of lead	11300 kg/m^3
density of GGG	7140 kg/m^3	half cycle time	3 seconds

The number of transfer units (NTU) associated with these devices is a function of the helium charge mass, as illustrated in Figure 1-21. Also illustrated in Figure 1-21 is the sensible heat capacity ratio of the GGG regenerator. The sensible heat capacity ratio of the conventional regenerator is illustrated in Figure 1-22 as a function of helium charge mass and at several values of refrigeration temperature.

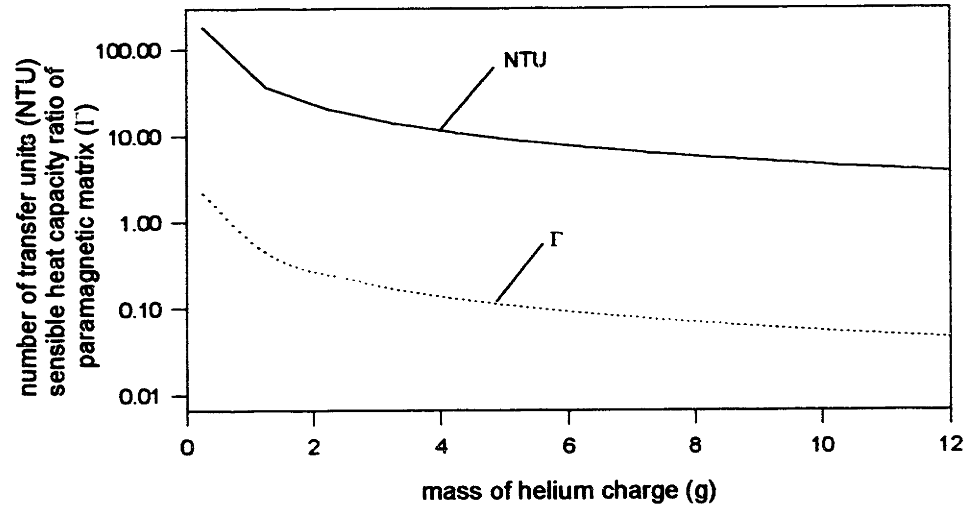

Figure 1-21. Number of transfer units associated with a typical regenerator (conventional or paramagnetic) and sensible heat capacity ratio associated with a typical paramagnetic regenerator as a function of helium charge mass (other values given in Table 1-1)

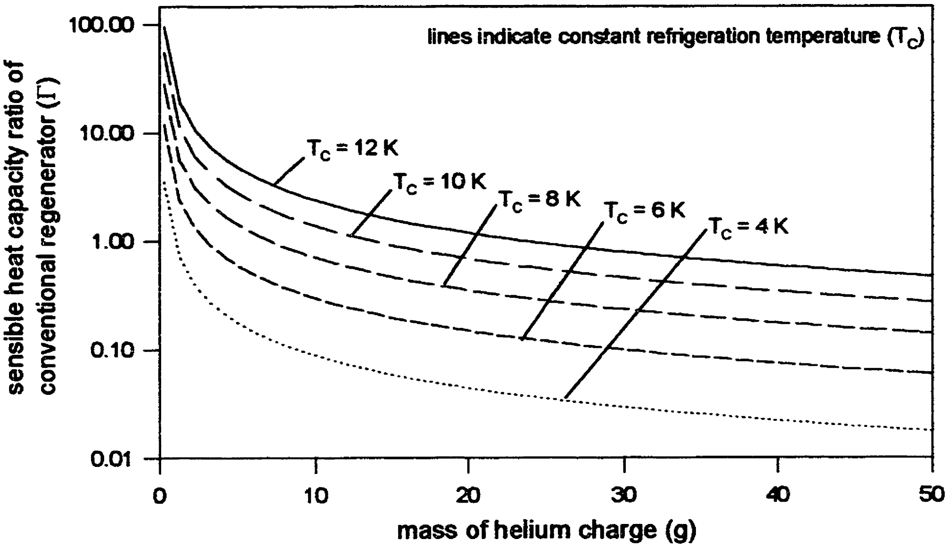

Figure 1-22. Sensible heat capacity ratio of a typical conventional regenerator as a function of helium mass charge for several values of refrigeration temperature (all other values given in Table 1-1)

The magnetic to thermal capacity ratio (λ/Γ) of the paramagnetic regenerator is a material property of the paramagnetic substance and therefore varies only with temperature. This variation is illustrated in Figure 1-23. As the temperature becomes lower, the magnetic effect becomes more pronounced. Therefore, in the temperature range where the Stirling device becomes less effective due to thermal saturation, the Stirling/magnetic type device

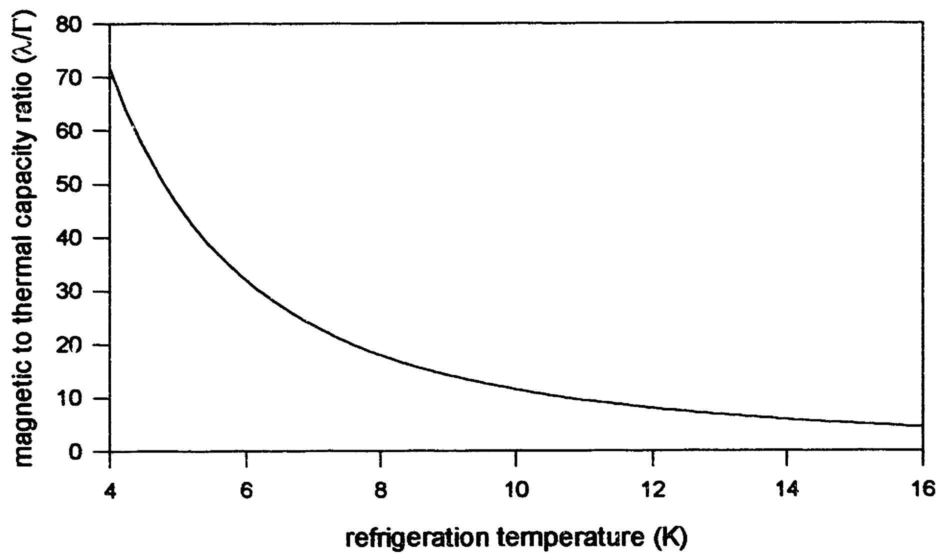

Figure 1-23. Magnetic to thermal capacity ratio of a typical paramagnetic regenerator as a function of refrigeration temperature (all other values given in Table 1-1)

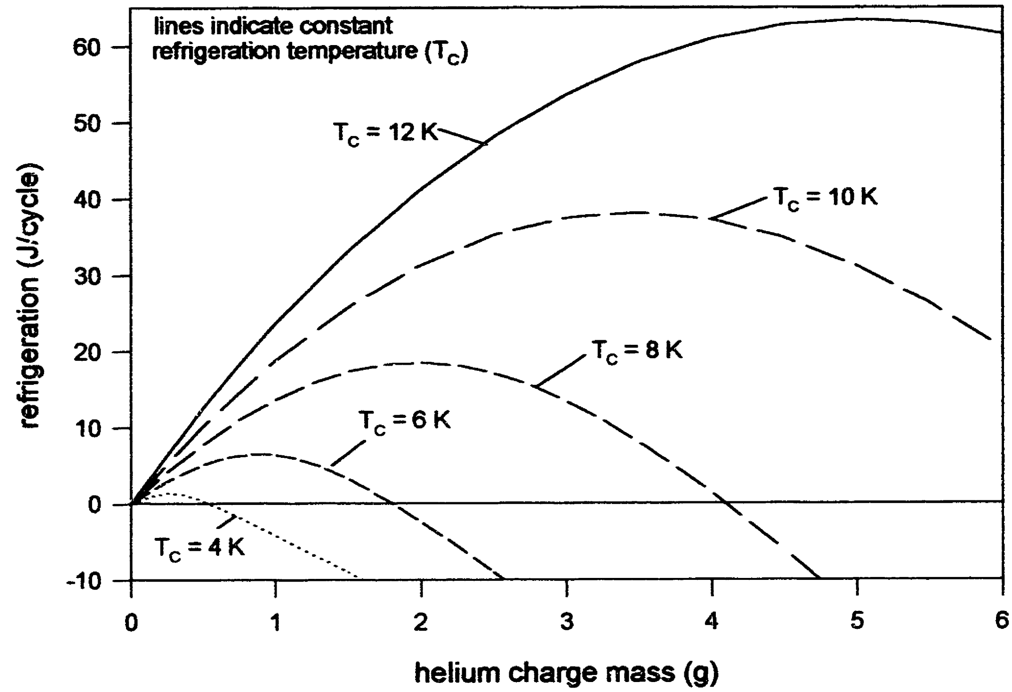

Figure 1-24. Cyclic refrigeration produced by a typical Stirling device as a function of helium charge mass at several values of refrigeration temperature (all other values given in Table 1-1)

becomes more effective due to a larger magneto-caloric effect. This is one of the reasons that the Stirling/magnetic cycle will be an effective low temperature stage of a conventional GM device.

Figure 1-24 illustrates the cyclic refrigeration produced by the Stirling device (according to the model developed in subsection 1.3.4.1) as a function of the helium charge mass for several values of refrigeration temperature. As the refrigeration temperature decreases, the specific heat capacity of lead goes down (proportional to the third power of temperature) and the Stirling cycle very quickly loses effectiveness. The optimal helium charge mass gets decreases as the regenerator capacity is reduced.

Figure 1-25 illustrates the cyclic refrigeration produced by the Stirling/magnetic device as a function of the helium charge mass for several values of refrigeration temperature. As the refrigeration temperature decreases, the magneto-caloric effect somewhat compensates for the decrease in the mechanical effect of expanding the helium. Therefore, the refrigeration potential of the cycle is not degraded to the extent of the Stirling device. The refrigeration associated with a regenerative magnetic device is obtained by subtracting the expansion refrigeration from the refrigeration associated with the Stirling/magnetic device.

Figure 1-26 illustrates the maximum refrigeration associated with the three types of cycles as a function of refrigeration temperature. The Stirling/magnetic cycle always produces more refrigeration than either the Stirling or the regenerative magnetic device in this temperature region. At very high temperatures the Stirling/magnetic device would limit to

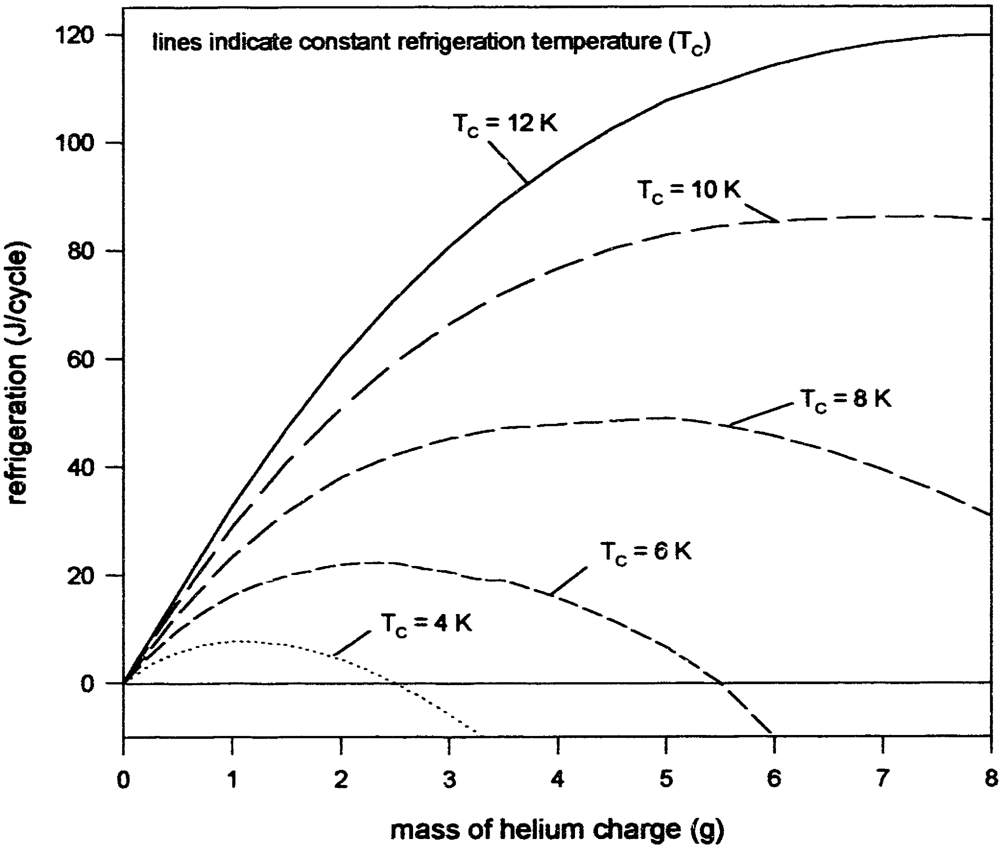

Figure 1-25 Cyclic refrigeration produced by a typical Stirling/magnetic device as a function of helium charge mass for several values of refrigeration temperature (all other values given in Table 1-1)

the Stirling device if they had the same regenerator material because the magneto-caloric effect becomes negligible. At very low temperatures the Stirling/magnetic device will limit to the regenerative magnetic device because the mechanical effect becomes negligible.

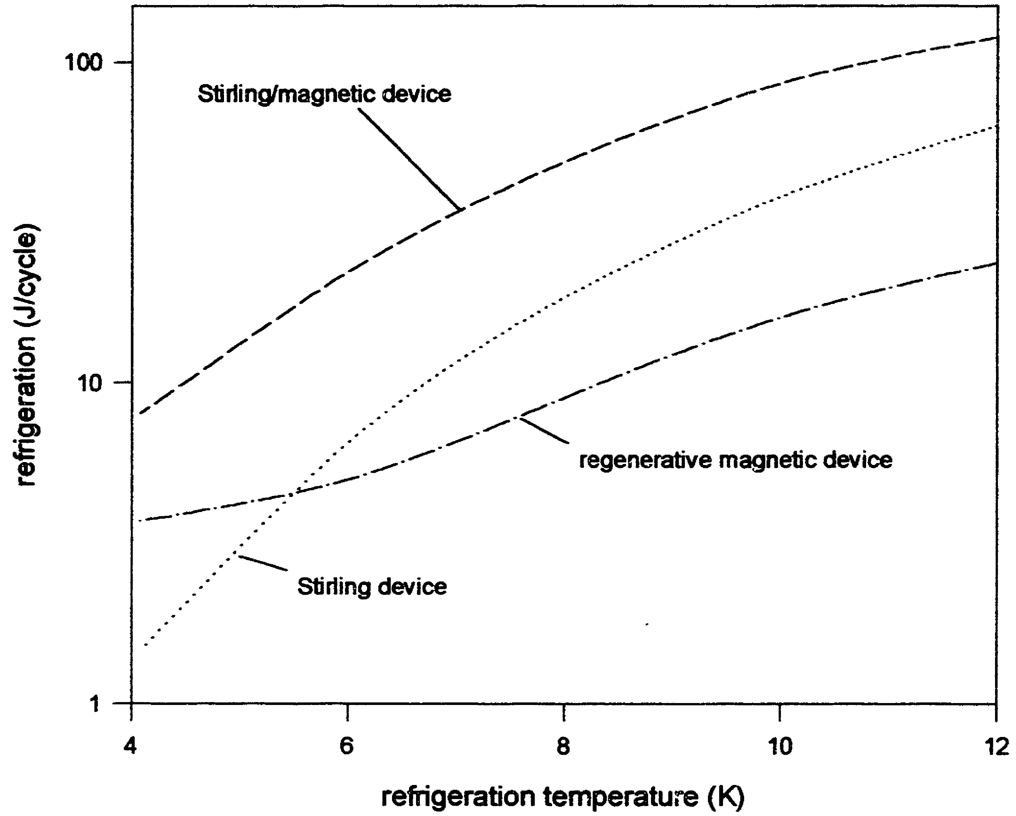

Figure 1-26. Cyclic refrigeration produced by a typical Stirling, regenerative magnetic, and Stirling/magnetic device as a function of refrigeration temperature (all other values given in Table 1-1)

EXPERIMENTAL APPARATUS DESIGN AND CONSTRUCTION

In order to experimentally investigate the properties of a GM/magnetic cycle, an experimental prototype has been designed and constructed. This chapter describes the design procedure and some of the more interesting fabrication techniques used during the construction of the experimental prototype. Several important models developed during the design process are also presented.

This chapter is divided into five sections. In the first section the predictive model of the GM/magnetic cycle is described. The results of this model are subsequently used in the design of the magnetic stage of the experimental apparatus. The second section gives an overview of the entire experimental apparatus and details how the different subsystems work together to generate a GM/magnetic cycle. The third section explains how each of the major subsystems associated with the apparatus are modeled, designed and constructed. The fourth subsection describes how the apparatus is instrumented for temperature and pressure measurements. In the final subsection, the control mechanisms used in the device are explained.

2.1 Predictive Model

This section explores the results of a predictive model of a GM/magnetic cycle which was developed previously in order to aid in the design of the experimental apparatus. The section is divided into two subsections. In the first subsection, the various features and limiting assumptions of the predictive model are described. The second subsection presents the most important results obtained from the predictive model and explains how they are used as a starting point for the design of the experimental apparatus.

2.1.1 Description of predictive model

Because the details and results of the predictive model of a GM/magnetic device have been reported elsewhere [37], only the most important features will be restated here. The predictive model relaxes three of the most limiting assumptions associated with the first order model developed in chapter 1. In particular, the properties of the GGG and helium are no longer assumed to be ideal and the entrainment of helium in the void volume is not neglected. The properties of GGG have been carefully constructed from experimental magnetization data by Ghallagher in his M.S. Thesis [38]. The properties of helium-4 are obtained using bicubic spline interpolation of tables of properties generated by the FORTRAN program *NBS Standard Reference Database 12* [39].

The set of governing differential equations solved by the predictive model are shown below. They include a mass balance on a differential piece of regenerator void volume, an energy balance on a differential piece of regenerator void volume, and an entropy balance on a differential piece of regenerator material.

$$\frac{\partial m_h}{\partial x} + A_c \cdot \varepsilon \cdot \left\{ \left(\frac{\partial \rho_h}{\partial P} \right)_T \frac{\partial P}{\partial t} + \left(\frac{\partial \rho_h}{\partial T} \right)_P \frac{\partial T_h}{\partial t} \right\} = 0 \tag{2.1}$$

$$\begin{aligned} m_h \cdot c_{P,h} \cdot \frac{\partial T_h}{\partial x} + m_h \cdot \left(\frac{\partial h_h}{\partial P} \right)_T \cdot \frac{\partial P}{\partial x} + A_c \cdot \varepsilon \cdot \left\{ \rho_h \cdot \left(\frac{\partial u_h}{\partial P} \right)_T - \frac{P}{\rho_h} \cdot \left(\frac{\partial \rho_h}{\partial P} \right)_T \right\} \cdot \frac{\partial P}{\partial t} \\ + A_c \cdot \varepsilon \cdot \left\{ \rho_h \cdot \left(\frac{\partial u_h}{\partial T} \right)_P - \frac{P}{\rho_h} \cdot \left(\frac{\partial \rho_h}{\partial T} \right)_P \right\} \cdot \frac{\partial T_h}{\partial t} + U \cdot a \cdot A_c \cdot (T_h - T_G) = 0 \end{aligned} \tag{2.2}$$

$$\begin{aligned} T_G \cdot (1-\varepsilon) \cdot A_c \cdot \rho_G \cdot \left(\frac{\partial s_G}{\partial \mu_o H} \right)_T \cdot \frac{d \mu_o H}{dt} + T_G \cdot (1-\varepsilon) \cdot A_c \cdot \rho_G \cdot \left(\frac{\partial s_G}{\partial T} \right)_{\mu_o H} \cdot \frac{\partial T_G}{\partial t} \\ + U \cdot a \cdot A_c \cdot (T_G - T_h) = 0 \end{aligned} \tag{2.3}$$

The heat transfer coefficient and axial pressure drop are calculated from correlations for the Nusselt number [40] and friction factor [41] associated with a packed bed. The local flow conditions are used in these calculations. Equations 2.1 through 2.3 imply two major assumptions: the GGG is modeled as undergoing an internally reversible process and the applied field is modeled as being spatially uniform. These two conditions are very nearly met in the experimental apparatus. The very small particle diameter of the GGG in the magnetic regenerator limits the temperature gradients within the magnetic material (Biot numbers are calculated to be less than 1/10). The magnet is constructed with compensating coils in order to limit the field non-uniformity within the bore.

The boundary conditions for the three partial differential equations are associated with the (assumed) isothermal heat exchangers, the requirement of a steady state cycle, an imposed warm end pressure variation, and a mass balance on the displacer. The imposed warm end pressure and displacer volume variation are assumed to be linear and discontinuous. This assumption and the assumption of isothermal heat exchangers prove to be problematic when the model is verified against experimental data, as explained in subsection 4.3.1.

The solution of these nonlinear partial differential equations is complicated by the fact that the properties of both substances tend to fluctuate dramatically over certain temperature ranges: the helium when it approaches the critical state and the GGG when it approaches the Curie temperature. Consequently, it is very difficult to obtain a solution which is thermodynamically consistent when checked against the second law. The method of entropy based modification [42] yields good results when applied to this problem. This technique forces second law satisfaction and makes the simulation more stable. The resulting program has been run on the MIT Cray XMP to yield the results discussed in section 2.1.2.

Table 2-1. Input parameters used to generate operating curves associated with predictive model

Parameter description	Symbol	Value	Units
compression/demag. process time	τ_{com}	0.5	second
hot-to-cold blow/demag. process time	τ_{in}	0.5	second
expansion/mag. process time	τ_{exp}	0.5	second
cold-to-hot blow/mag. process time	τ_{out}	0.5	second
maximum applied field	$\mu_o H_{max}$	5	Tesla
applied field after compression/demag.	$\mu_o H_{com}$	2	Tesla
minimum applied field	$\mu_o H_{min}$	1	Tesla
applied field after expansion/mag.	$\mu_o H_{exp}$	4	Tesla
minimum imposed pressure	P_{min}	304000	Pa
displacer area	$A_{c,dis}$	0.00096	m^2
regenerator length	L_r	0.121	m
regenerator area	$A_{c,r}$	0.00096	m^2
cold space dead volume	$V_{dead,chx}$	0	m^3
porosity of regenerator matrix	ε	0.35	-
particle diameter	D_p	0.00015	m
warm reservoir temperature	T_H	12	K
cold reservoir temperature	T_C	4.75	K

2.1.2 Results of predictive model

The predictive model was used to simulate a GM/magnetic cycle with a geometry similar to the what was anticipated for the experimental prototype. The cycle conditions which were held constant in order to generate the curves presented in this section are listed in Table 2-1. Many of these parameters do not apply to the experimental apparatus due to constraints which were unforeseen at the time the simulation was run. In particular, the cycle time associated with the experimental device is much longer than the cycle time used in the simulation. However, it is expected that the refrigeration per cycle predicted by the simulation will scale nearly linearly with cycle time since the major loss mechanism (pressurization of the void volume) scales directly with cycle time.

The displacer stroke and maximum imposed pressure were varied to generate the operating curves illustrated in Figure 2-1. These operating curves illustrate the dimensionless refrigeration as a function of the mass ratio and the pressure ratio. Here, the dimensionless refrigeration is defined relative to the magnetic effect available in the magnetic regenerator rather than the mechanical effect. This is because the magnetic effect dominates the mechanical effect in this temperature region. Also, for a fixed temperature range, geometry, and applied field variation the magnetic effect remains constant. This allows easier interpretation of Figure 2-1 relative to the design of the experimental apparatus. The

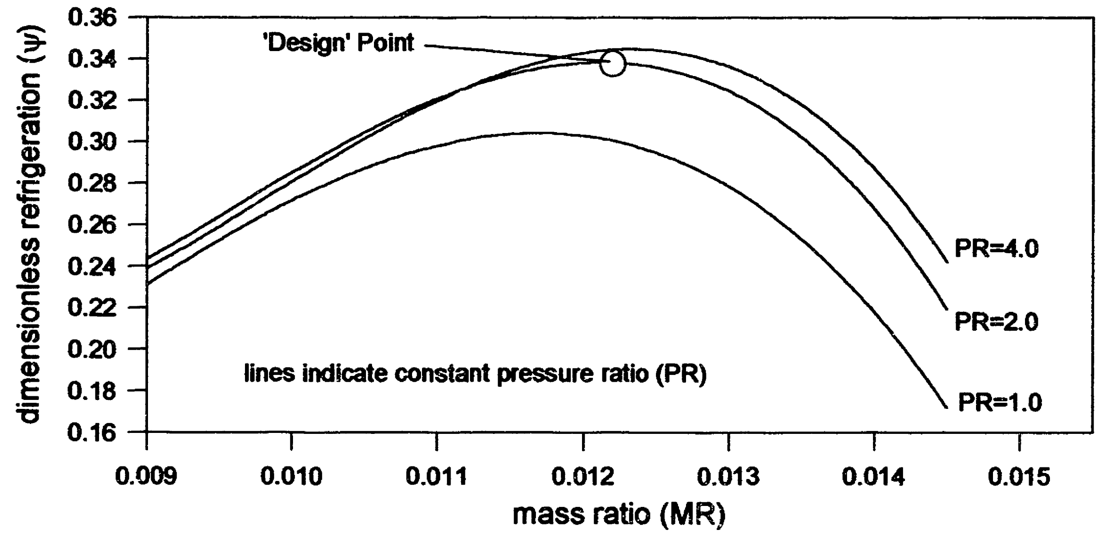

Figure 2-1. Dimensionless refrigeration as a function of primary mass ratio and pressure ratio obtained using predictive model (input parameters given in Table 2-1)

formal definition of the dimensionless refrigeration associated with Figure 2-1 is given below (where Q_C indicates the refrigeration and M_G indicates the mass of GGG).

$$\psi \equiv \frac{Q_C}{\frac{M_G}{(T_H - T_C)} \cdot \int_{T_C}^{T_H} T \cdot \left\{ s_G(\mu_o H_{min}, T) - s_G(\mu_o H_{max}, T) \right\} \cdot dT} \tag{2.4}$$

The mass ratio is defined as the ratio of the helium mass which passes through the warm end of the device to the mass of GGG. The mass of helium which enters the device at the warm end is quite different than the mass of helium which finally makes it into the cold space due to the 'breathing' effect associated with pressurization of the entrained helium in the regenerator matrix. However, the amount of helium entering the warm end of the magnetic stage is an important quantity for the design of the upper stage and a conservative value to use when designing the cold heat exchanger and displacer. The mass ratio and pressure ratio are defined below.

$$MR \equiv \frac{\int\limits_{\substack{\text{hot-to-cold blow/demag.}\\ \text{compression/demag.}}} m_h(0,t) \cdot dt}{M_G} \tag{2.5}$$

$$PR \equiv \frac{P_{max}}{P_{min}} \tag{2.6}$$

Table 2-2. Important results associated with design GM/magnetic cycle

Parameter description	Symbol	Value	Units
pressure ratio	PR	2	-
primary mass ratio	MR	0.0125	-
dimensionless refrigeration	Ψ	0.33	-
degree of warm end superheat	ΔT_{sh}	2	K

The 'design' point is illustrated on Figure 2-1. This is the set of operating conditions which is expected to yield an effective GM/magnetic cycle and are subsequently used during the design of the experimental apparatus. The important characteristics associated with the design point are reported in Table 2-2. The degree of warm end superheat (ΔT_{sh}) listed in Table 2-2 is an important design parameter for the upper stage device. The degree of superheat is approximately how far above the warm reservoir temperature the helium is when it leaves the warm end of the matrix during the cold-to-hot blow process. At the 'design' point, the helium leaves the magnetic regenerator at approximately 14 K and enters at 12 K.

Most of the design characteristics are reported in their dimensionless form despite the fact that they were derived using the specific geometry associated with Table 2-1. This is because the actual geometry of the experimental apparatus is somewhat different than the geometry used to optimize the predictive model and it is hoped that the dimensionless characteristics of the design GM/magnetic cycle will not change as much as their dimensional counterparts.

2.2 Description of the Experimental Apparatus

The overall system can be divided into several subsystems: the superconducting solenoid, the paramagnetic regenerator bed, the upper stage, the cold heat exchanger, the displacer, and the current leads. Additional components include the displacer drive control system, the pressure control system (i.e. the compressor and associated plumbing), and the magnet power supply. The apparatus was instrumented for temperature and pressure measurements. All of these subsystems are individually described in the remaining sections of this chapter. This section describes how these subsystems operate together to impose a GM/magnetic cycle on the magnetic stage of the apparatus.

The experimental prototype is illustrated schematically in Figure 2-2. There are only two distinct processes associated with the experimental apparatus - hot-to-cold blow/demagnetization and cold-to-hot blow/magnetization. The displacer moves sinusoidally. During the hot-to-cold blow/demagnetization process, the displacer moves upwards. The pressurization valve is open and high pressure helium is drawn into the apparatus. The warm helium flows first into the upper stage system. The upper stage system is basically a regenerative device which maintains the temperature at the warm end of the magnetic stage. The warm helium is cooled by the regenerator matrix and flows into

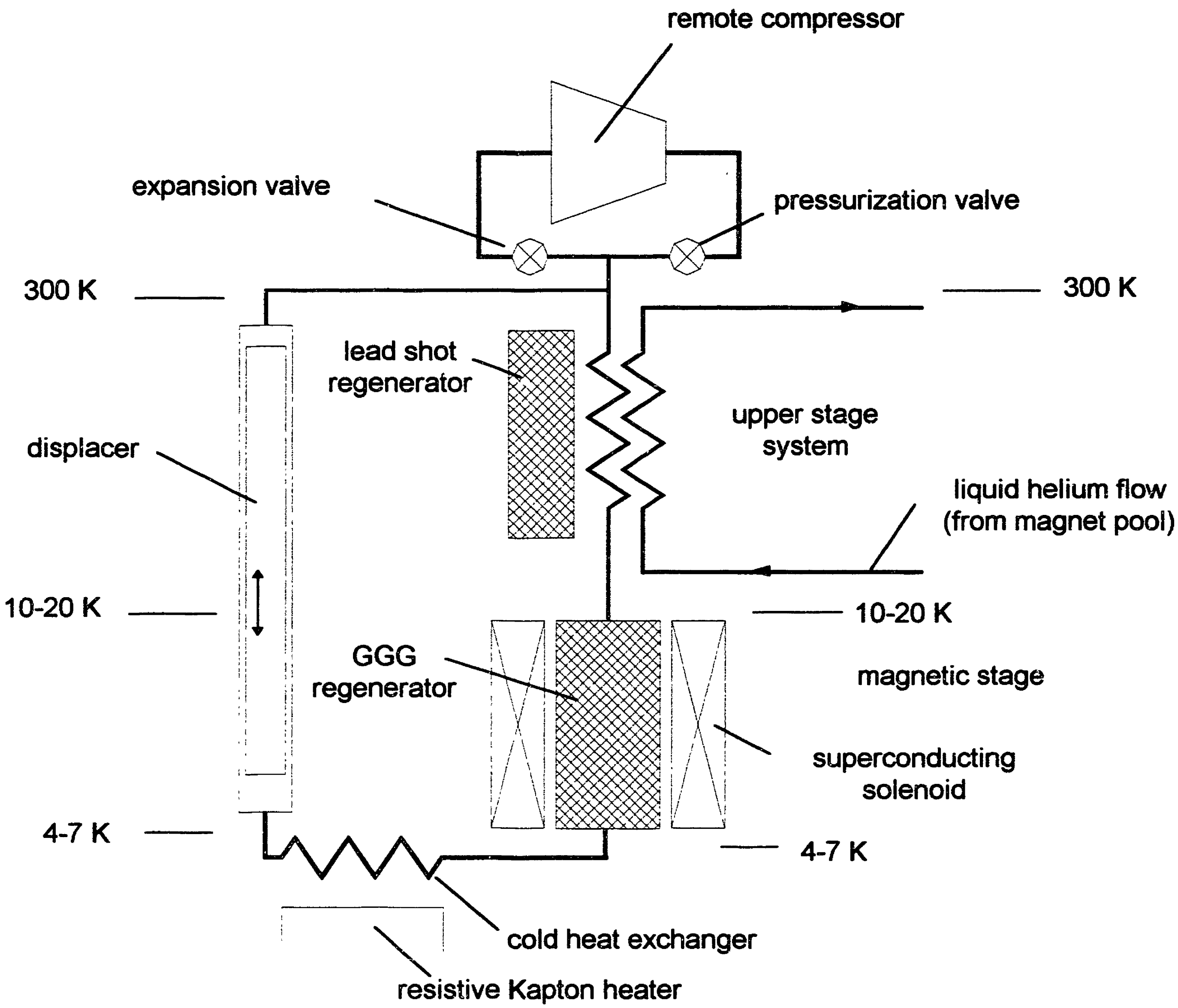

Figure 2-2. Schematic of experimental apparatus

the paramagnetic bed at 10 to 20 K. The regenerative upper stage is made more effective by a stream of cold helium vapor (boil-off from the superconducting magnet) which is forced to flow in close thermal contact with the regenerator material. The regenerator material of the upper stage is lead shot.

The paramagnetic regenerator matrix is a bed of crushed GGG particles contained inside a superconducting solenoid. The large specific area associated with the packed bed matrix creates good thermal contact between the helium working fluid and the GGG. The applied field within the GGG is controlled by varying the current within the superconducting solenoid. As the warm, high pressure helium flows into the GGG bed, the superconducting solenoid is demagnetized from some high value of applied field (in the 2.5 to 4 Tesla range) to 1 Tesla. The demagnetization induces the GGG to absorb entropy from the helium causing it to exit the cold end of the magnetic stage in the 4 to 7 K temperature range.

The helium next flows through the cold heat exchanger. The refrigeration load is generated by a resistive heater placed within the cold heat exchanger. This heat exchanger is affixed to the cold end of the magnetic regenerator bed. Finally, the helium enters the cold space created by the displacer motion.

The cold-to-hot blow/magnetization process starts when the displacer hits top-dead-center and begins to travel downwards. The pressurization valve is closed and the expansion valve opens. The temperature of the helium contained in the cold space drops as a consequence of the expansion process. The helium flow reverses. The helium flows through the cold heat exchanger and into the paramagnetic bed. The superconducting solenoid is magnetized from 1 Tesla back to the high level of applied field. This induces the GGG to release entropy to the helium which consequently exits the warm end of the GGG bed and enters the upper stage. The helium is heated to near room temperature by the upper stage regenerative matrix at which time it leaves the experimental apparatus and flows through the compressor to be pressurized for the next cycle.

The experimental apparatus is placed within a double vacuum jacketed dewar with a liquid nitrogen radiation shield constructed by Carl Taussig for an earlier regenerative magnetic refrigeration device [43]. The upper stage, magnetic stage, cold heat exchanger, and most of the displacer are vacuum insulated from the liquid helium pool cools the superconducting magnet. This ensures that the magnetic stage is thermally isolated from the 4.2 K reservoir.

2.3 Design and Construction of Experimental Apparatus

This section describes the individual subsystems associated with the experimental apparatus. In some cases, the subsystems were designed and built. In other cases, the subsystems were obtained from existing equipment. Some of the more interesting fabrication techniques are described as well as the most important design models.

Table 2-3. Some resources used during the construction of the experimental prototype

Description of product	Company name	phone number
power supply for superconducting magnet	Lakeshore Electronics	(614) 891-2243
gun drill fordisplacer	El Dorado	(800) 658-8855
stripper for de-epoxification of GGG	MillerStephenson	(203) 743-4447
lead shot for upper stage regenerator	Clad Metal Industries	(201) 337-1800
stainless steel tube for upper stage flow passages	Vita needle	(617) 444-8629
stainless steel tubing fordisplacer, regenerator, etc.	B & S Aircraft Alloys Inc.	(800) 645-2401
perforated metal for upper stage baffles	McNichols Company	(508) 692-4141
resistors for temperature measurement	Newark Electronics	(617) 935-8350

The section is divided into six subsections which describe: (1) the superconducting solenoid, (2) the paramagnetic regenerator bed, (3) the upper stage, (4) the cold heat exchanger, (5) the displacer, and (6) the current leads.

Table 2-3 lists some of the difficult to obtain products used to construct the experimental prototype.

2.3.1 Superconducting solenoid

This section describes the superconducting solenoid used in the experimental apparatus. The characteristics of the superconducting solenoid (an existing piece of equipment) are described. A plug used to fill the upper non-uniform field section of the solenoid while allowing helium flow is designed. Also, the eddy current generation associated with the regenerator tube is estimated.

The primary windings of the superconducting solenoid were constructed by Woodrow Chin [44]. The solenoid was subsequently modified by adding an extra set of windings which allowed the magnetic field to be axially varied in a controlled fashion [45]. The superconducting solenoid and some of its critical dimensions are illustrated in Figure 2-3. The most important characteristics of the superconducting solenoid are summarized in Table 2-4. A photograph of the superconducting solenoid is shown in Figure 2-4.

The solenoid is composed of two circuits (the primary circuit and the secondary circuit). Each circuit is composed of one main coil and two compensating coils. The primary circuits generates a uniform applied field within the bore and is the only circuit energized by the experimental apparatus. The primary main coil is uniformly wrapped around a 1.5 mm

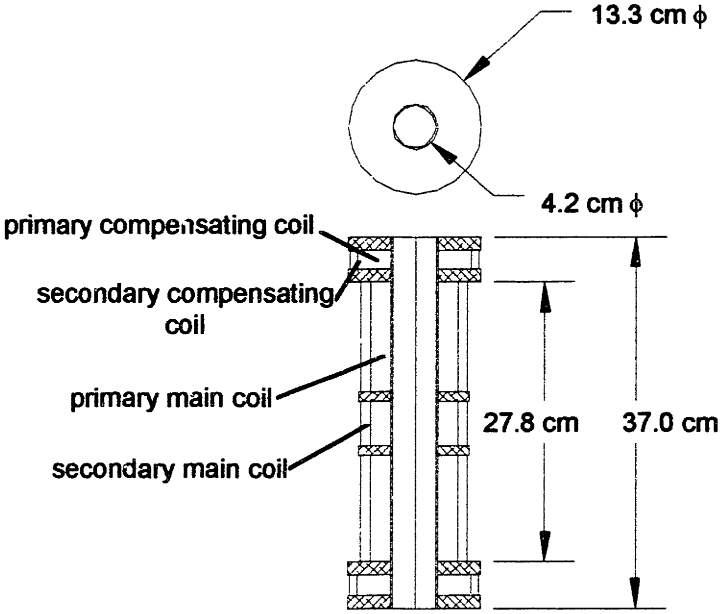

Figure 2-3. Superconducting solenoid drawing

Micarta coil form. The two compensating coils offset the end effects within the solenoid bore and create an applied field which is more nearly axially uniform. The structure of the solenoid is created with G10 disks and rods. These disks have been perforated in order to allow liquid helium to penetrate to the inner windings.

The applied field generated by the primary circuit is illustrated in Figure 2-5 [46]. The ends of the solenoid bore are characterized by a rapid decrease in the applied field. In regions where the magnetic field is low, the magnetic effect associated with the GGG quickly approaches zero. If the ramped field portions of the solenoid were filled with paramagnetic material, the cycle would be degraded by the additional void volume more than it would be

Table 2-4. Characteristics of the superconducting solenoid

Parameter description	Symbol	Value	Units
length of uniform magnetic field bore	L_{mag}	27.8	cm
diameter of regenerator bed	D_{mag}	3.16	cm
inductance	L	1	Henry
current per applied field	-	25	Amp/Tesla
approximate high applied field	$\mu_o H_{max}$	3.5	Tesla
low applied field	$\mu_o H_{min}$	1	tesla
approximate half-cycle time	τ	6.25	second
magnet voltage	V_{mag}	10	volt
approximate high current	I_{max}	87.5	amp
low current	I_{min}	25	amp

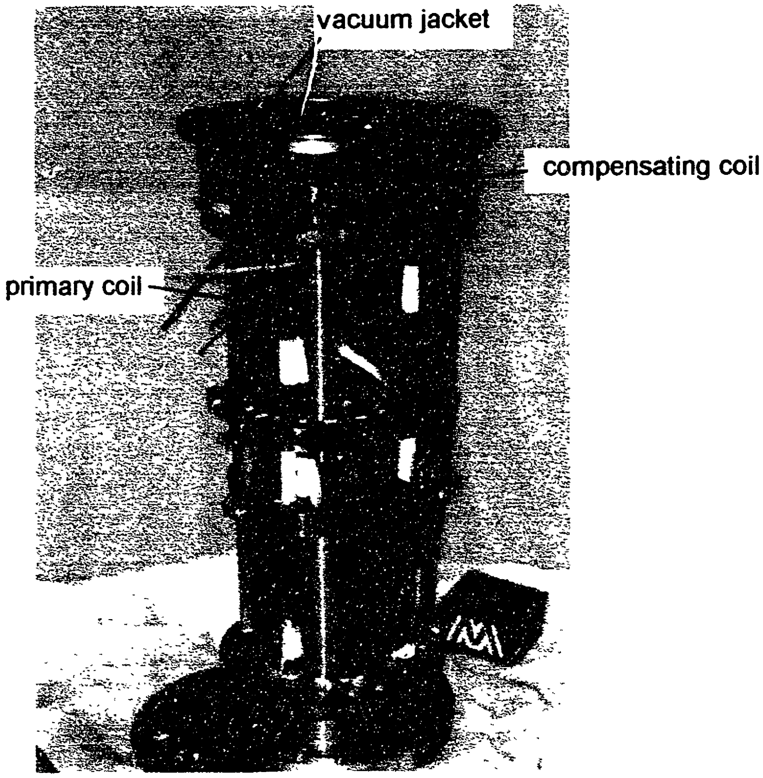

Figure 2-4. Superconducting solenoid

augmented by the added magnetic effect. Consequently, the upper end of the solenoid is filled with a phenolic cylindrical plug which occupies the ramped field section of the bore. The ramped field section on the cold end of the superconducting bore is filled with the cold heat exchanger.

The design of the phenolic plug is important to the overall performance of the magnetic stage because there can be no regenerative effect between the upper stage and the magnetic stage. The upper stage is specifically designed to have an effectiveness greater than unity

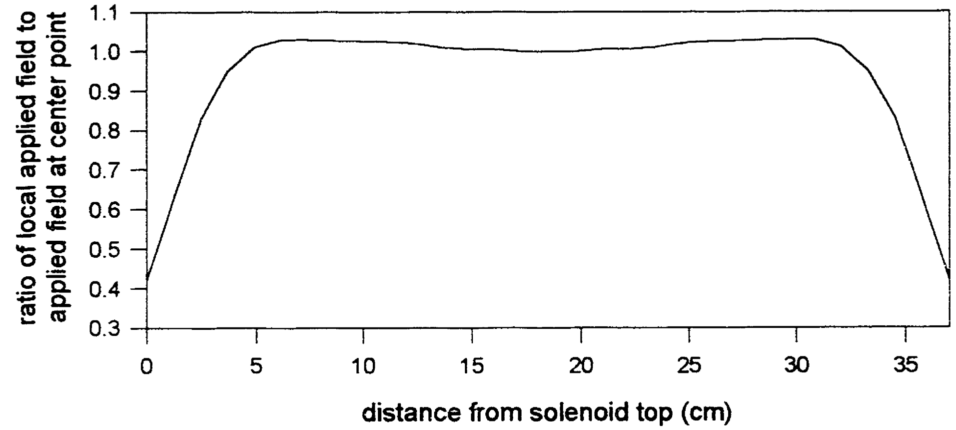

Figure 2-5. Axial variation of applied field in superconducting solenoid

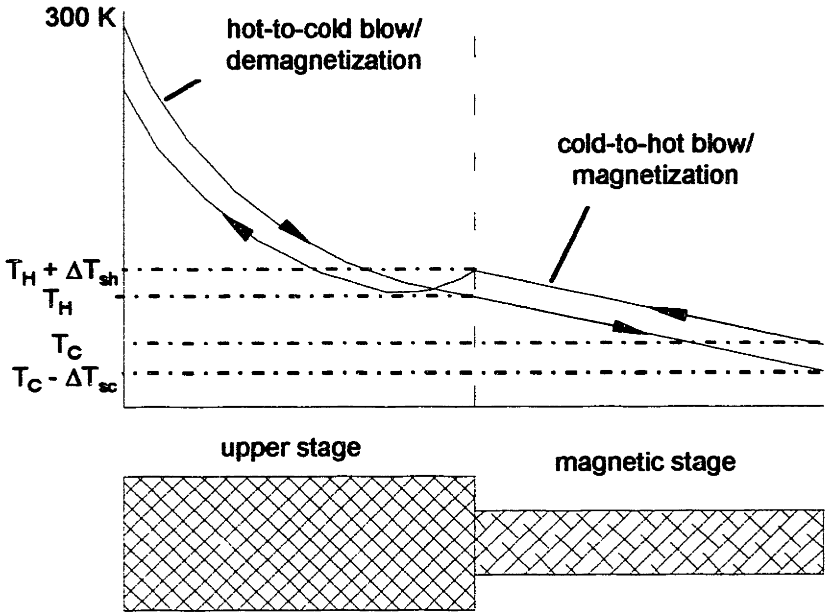

Figure 2-6. Qualitative temperature profiles which exist in the experimental apparatus with no regenerative between the upper stage and the magnetic stage

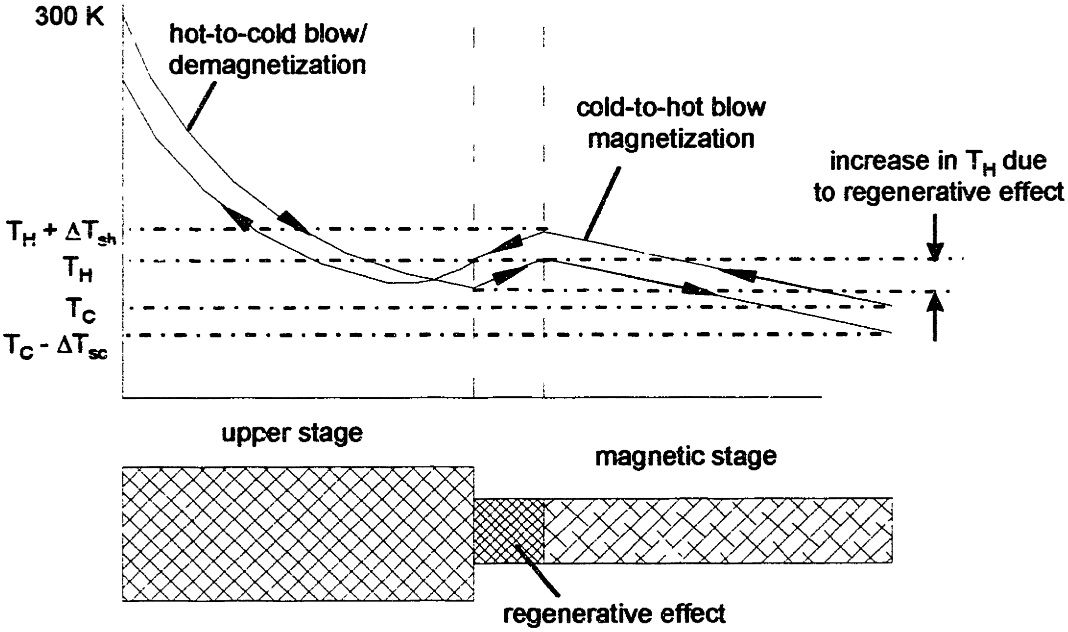

Figure 2-7. Qualitative temperature profiles which exist in the experimental apparatus with a regenerative effect between the upper stage and the magnetic stage

(this can be accomplished due to the coolant stream which flows in thermal contact with the regenerator material). In other words, the upper stage should deliver helium to the magnetic stage at a temperature *colder* than the magnetic stage delivers helium back to the upper stage (by an amount $\Delta T_{sh} \approx 2$ K as reported in Table 2-2). The magnetic stage tends to superheat the upflowing helium relative to the downflowing helium. This situation is illustrated qualitatively in Figure 2-6. This figure shows the temperature profile which exists within the upper stage and the magnetic stage during the hot-to-cold blow/demagnetization process in relation to the temperature profile which exists during the cold-to-hot blow/magnetization process. The required superheat (ΔT_{sh}) which exists between the upper stage and magnetic stage means that a regenerative effect between the two devices will tend to increase the warm reservoir temperature seen by the magnetic stage. This situation is illustrated in Figure 2-7. The regenerative effect between the two stages elevates the warm reservoir temperature because the superheat from the cold-to-hot blow/magnetization process tends to heat the fluid entering during the hot-to-cold blow/demagnetization process. This type of problem is an important issue related to effectively interfacing a GM/magnetic device with a conventional GM device.

For this experimental apparatus it is sufficient to simply minimize the regenerative effect while ensuring that the pressure drop through the phenolic plug does not grow too large. As the flow passages in the plug become smaller, the regenerative effect decreases and the pressure drop increases. The design of the plug is a trade-off between pressure drop and regenerative effect.

The phenolic plug allows helium to flow through several small circular flow passages. The regenerative effect is estimated by determining the heat capacity of the phenolic which is affected by the flowing fluid. The flowing helium is modeled as a sinusoidally varying temperature variation on the surface of a semi-infinite body, as illustrated in Figure 2-8. The temperature variation within the solid above the time average surface temperature is given below [47].

$$T = \frac{\Delta T_{sh}}{2} \cdot \exp\left(-x \cdot \left\{\frac{2 \cdot \pi}{\tau \cdot \alpha_{ph}}\right\}^{\frac{1}{2}}\right) \sin\left(\frac{\pi \cdot t}{\tau} - x \cdot \left\{\frac{2 \cdot \pi}{\tau \cdot \alpha_{ph}}\right\}^{\frac{1}{2}}\right) \tag{2.7}$$

Examination of equation 2.7 indicates that the approximate penetration depth can be expressed in terms of the cycle time and thermal diffusivity.

$$\text{penetration depth } \delta \approx \left\{\frac{\alpha_{ph} \cdot \tau}{\pi}\right\}^{\frac{1}{2}} \tag{2.8}$$

The amount of phenolic which is affected by the helium flow is proportional to the penetration depth. The effective heat capacity of the phenolic is given by equation 2.9. The diameter of the flow passage is indicated by D, the length by L, and the number of flow passages by N.

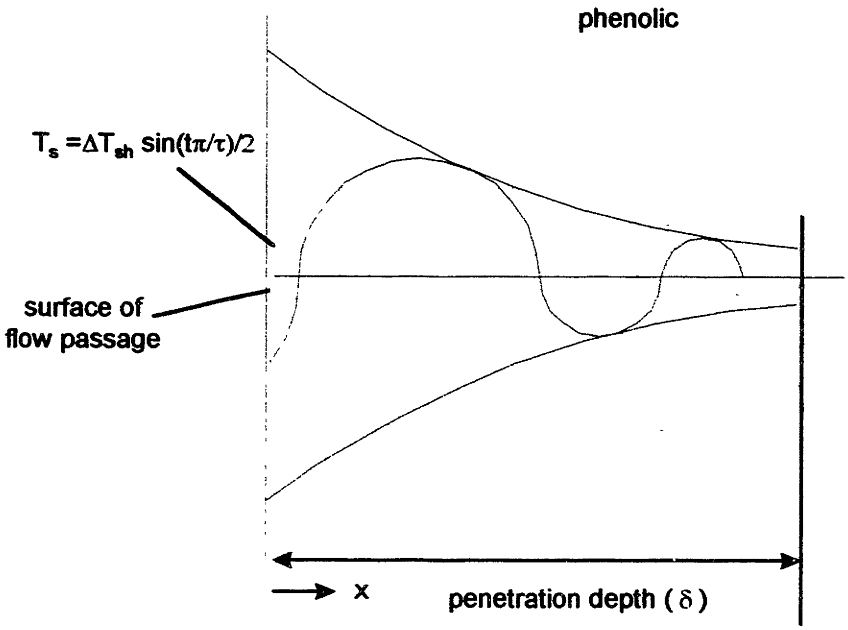

Figure 2-8. Model for estimation of effective phenolic plug heat capacity

$$C_{Ph} \approx N\cdot D\cdot\delta\cdot L\cdot\rho_{Ph}\cdot c_{Ph} = N\cdot D\cdot\left\{\frac{\alpha_{Ph}\cdot\tau}{\pi}\right\}^{\frac{1}{2}}\cdot L\cdot\rho_{Ph}\cdot c_{Ph} \qquad \textbf{(2.9)}$$

The ratio of the phenolic heat capacity to the helium heat capacity determines the magnitude of the regenerative effect.

$$CR_{Ph\text{-}h} = \frac{N\cdot D\cdot\left\{\frac{\alpha_{Ph}\cdot\tau}{\pi}\right\}^{\frac{1}{2}}\cdot L\cdot\rho_{Ph}\cdot c_{Ph}}{M_h\cdot c_{p,h}} \qquad \textbf{(2.10)}$$

The pressure drop across the phenolic plug must be small in relation to the pressure drop across the magnetic stage. The pressure drop across the phenolic plug can be estimated using a friction factor correlation for tubes.

$$\Delta P_{Ph} = \frac{f(Re)\cdot M_h^2\cdot 8\cdot L}{\tau^2\cdot\pi^2\cdot D^5\cdot\rho_h\cdot N^2} \qquad \textbf{(2.11)}$$

The Reynolds number of the helium flowing through the phenolic plug is given below.

$$Re = \frac{4\cdot M_h}{N\cdot\pi\cdot D\cdot\mu_h\cdot\tau} \qquad \textbf{(2.12)}$$

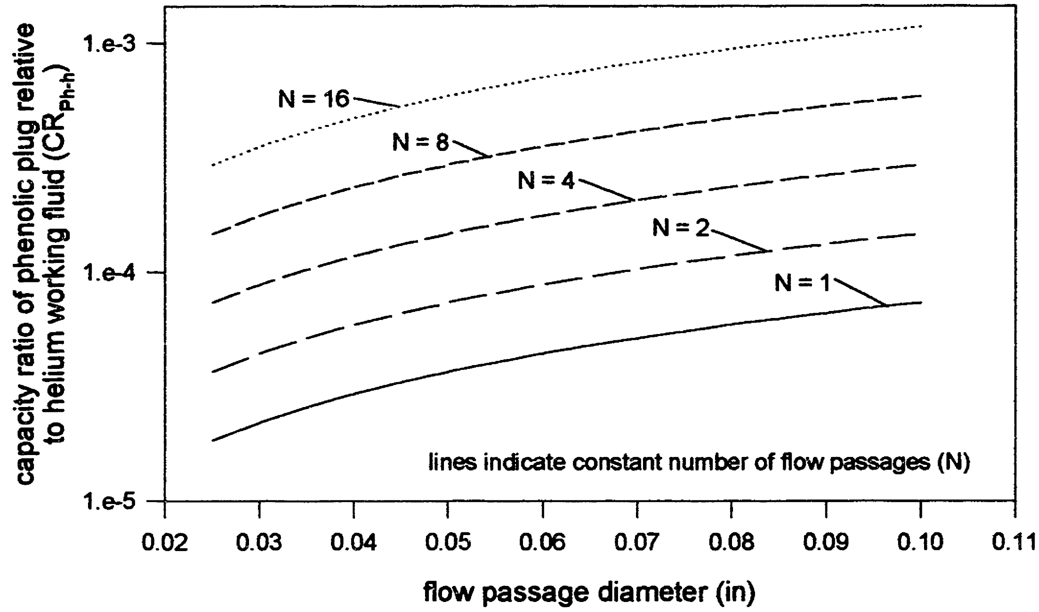

Figure 2-9. Ratio of effective capacity of phenolic plug used to fill ramped field section of superconducting solenoid to capacity of helium as a function of the flow passage diameter for several values of the number of flow passages

The friction factor associated with the flow through the phenolic plug is modeled as fully developed turbulent flow in a smooth tube [48].

$$f = (0.790 \cdot \ln\{Re\} - 1.64)^{-2} \tag{2.13}$$

The properties of phenolic are obtained using the program CRYOCOMP [49]. The length of the phenolic plug required to completely fill the ramped field section of the device is 2.25 inches. The resulting capacity ratio between the phenolic plug and the flowing helium as a function of the flow passage diameter is illustrated in Figure 2-9 for several values of number of tubes. The associated pressure drop is illustrated in Figure 2-10. The phenolic plug was made using 4 flow passages of diameter 0.055. The resulting effective capacity ratio under 1/100 and the pressure drop under 1 psi.

The bore of the solenoid is 4.2 cm (1.654 in) in diameter. The paramagnetic regenerator tube and vacuum jacket tube are selected to fit within this bore. This leads to a paramagnetic regenerator tube constructed of stainless steel with an inner diameter of 1.245 inches and a thickness of 0.065 inches. The resulting vacuum space is a 0.077 inch radial gap. Because the regenerator tube is a conductive element inside a time-varying magnetic field, it will be heated by the dissipation of induced currents.

The regenerator tube is modeled as an infinite cylindrical shell subjected to a sinusoidal applied field. The applied field is assumed to be spatially uniform and in the direction of the axis of the superconducting solenoid. The time averaged power (P) dissipated in the

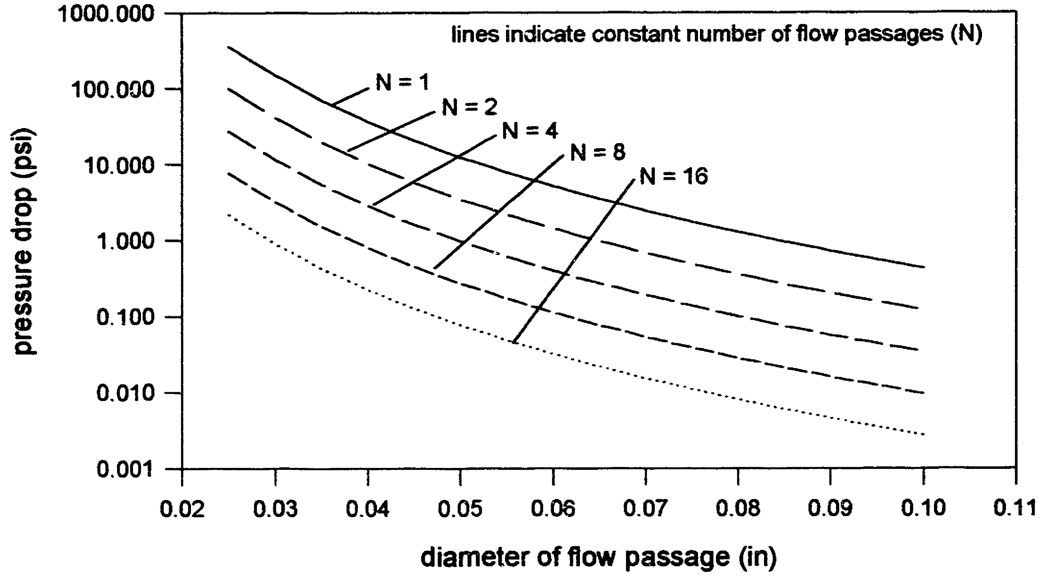

Figure 2-10. Pressure drop across phenolic plug used to fill ramped field section of superconducting solenoid bore as a function of the flow passage diameter for several values of the number of flow passages

cylindrical shell under these conditions is given below [50] (L indicates the tube length, D the diameter, δ the thickness, τ the half-cycle time, and ρ_e the electrical resistivity).

$$P = \frac{L \cdot \pi^3 \cdot \rho_e \cdot \left\{\mu_o H_{max}\right\}^2 \cdot D^3 \cdot \delta}{2 \cdot \tau^2 \cdot \left\{16 \cdot \rho_e^2 + \frac{\pi^2}{\tau^2} \cdot \mu_o^2 \cdot D^2 \cdot \delta^2\right\}} \tag{2.14}$$

For the conditions associated with the experimental apparatus, the regenerator tube is behaving in the insulator limit. In other words, the first term in the denominator is dominant for any reasonable value of tube thickness.

$$\frac{16 \cdot \rho_e^2 \cdot \tau^2}{\pi^2 \cdot \mu_o^2 \cdot D^2 \cdot \delta^2} >> 1 \tag{2.15}$$

Therefore, the power generation can be rewritten.

$$P = \frac{\pi^3 \cdot \left\{\mu_o H_{max}\right\}^2 \cdot D^3 \cdot \delta \cdot L}{32 \cdot \tau^2 \cdot \rho_e} \tag{2.16}$$

The eddy current heating in the regenerator tube is illustrated in Figure 2-11 as a function of half-cycle time for several values of tube thickness. As either the half cycle time decreases or the thickness increases the inductive heating of the regenerator tube tends to go up. The tube thickness used in the experimental apparatus is 0.065 inches and the half

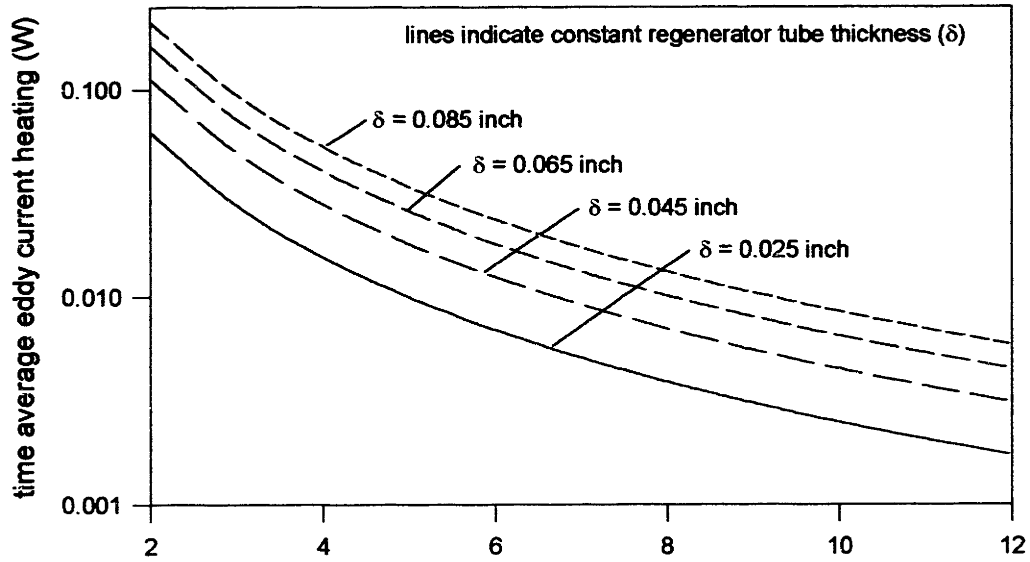

Figure 2-11. Eddy current heating of regenerator tube as a function of the half-cycle time for several values of the regenerator tube thickness

cycle time is approximately 6 seconds. The resulting eddy current heating is negligible (approximately 0.02 W) and the thick tube can easily be welded. Also, a thicker tube is required to support the packing forces imposed during the construction of the paramagnetic regenerator bed (as described in the next subsection).

2.3.2 Paramagnetic regenerator bed

This subsection describes the construction of the paramagnetic regenerator bed. The predictive model described in section 2.1 identifies void volume in the regenerator bed as the dominant loss mechanism in a GM/magnetic device. In order to reduce the porosity of the packed bed regenerator matrix, a fabrication technique was developed in which each layer of pre-crushed GGG particles are packed into the regenerator tube.

The appropriate packing pressure is critical to the success of this fabrication technique. If the pressure is too small, no significant improvement in porosity is realized. If the pressure is too large, the pressure drop across the matrix becomes large, favorable flow passages are produced, and, in the worst case, the matrix becomes completely occluded. In order to identify the appropriate packing pressure, several experiments were conducted using glass particles. Glass particles crush in a manner similar to GGG and are much less expensive.

The experiments involved pre-crushing the glass to a particle diameter which ranged from 0.42 mm to 0.60 mm. Enough glass particles to create 5 to 10 layers were poured into a tube and shaken using a vibrating shaker table. A controlled force was placed on a packing piston which slid in the regenerator bore. After the regenerator was filled in this fashion, the porosity and friction factor were measured.

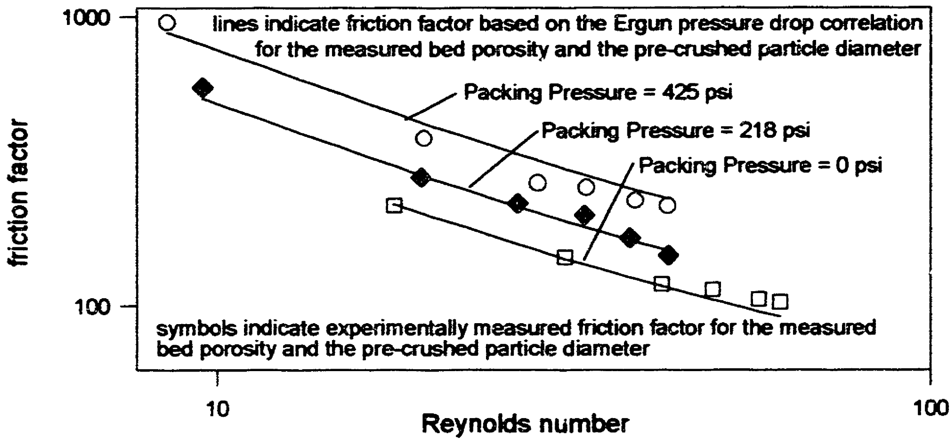

Figure 2-12 Friction factor based on experimental data and predicted by the Ergun correlation as a function of Reynolds number for several values of packing pressure

The internal characteristics of the packed bed could be examined using the friction factor. The Ergun correlation for pressure gradients within a packed bed can be generalized to any shape of particle by adding a correction factor called the shape factor (ϕ) [51]. The shape factor characterizes the irregularity of the packed bed particles and is defined as the ratio of the specific area of a bed of spherical particles to the specific area of the regenerator bed under consideration. The resulting pressure gradient correlation is given below in terms of the velocity which would exist in an unobstructed bed (v_o).

$$\frac{dP}{dx} = \frac{150 \cdot (1-\varepsilon)^2 \cdot \mu \cdot v_o}{\varepsilon^3 \cdot \phi^2 \cdot D_p^2} + \frac{7 \cdot (1-\varepsilon) \cdot \rho \cdot v_o^2}{4 \cdot \varepsilon^3 \cdot D_p} \tag{2.17}$$

Equation 2.17 may rewritten in terms of a friction factor, a Reynolds number, and the shape factor.

$$f_{D_p} \equiv \frac{\frac{dP}{dx} \cdot D_p}{\frac{1}{2} \cdot \rho \cdot v_o^2} = \frac{300 \cdot (1-\varepsilon)^2}{\varepsilon^3 \cdot \phi^2 \cdot Re_{D_p}} + \frac{15 \cdot (1-\varepsilon)}{4 \cdot \varepsilon^3 \cdot \phi} \tag{2.18}$$

Both the friction factor and the Reynolds number are defined in terms of the unobstructed bed velocity and the particle diameter.

$$Re_{D_p} \equiv \frac{v_o \cdot \rho \cdot D_p}{\mu} \tag{2.19}$$

Figure 2-12 illustrates the measured friction factor as a function of Reynolds number and the friction factor predicted by the Ergun pressure drop correlation based on the measured porosity and the average precrushed particle diameter. The shape factor of the particles was determined to be approximately 0.55 by fitting the zero packing pressure data to the

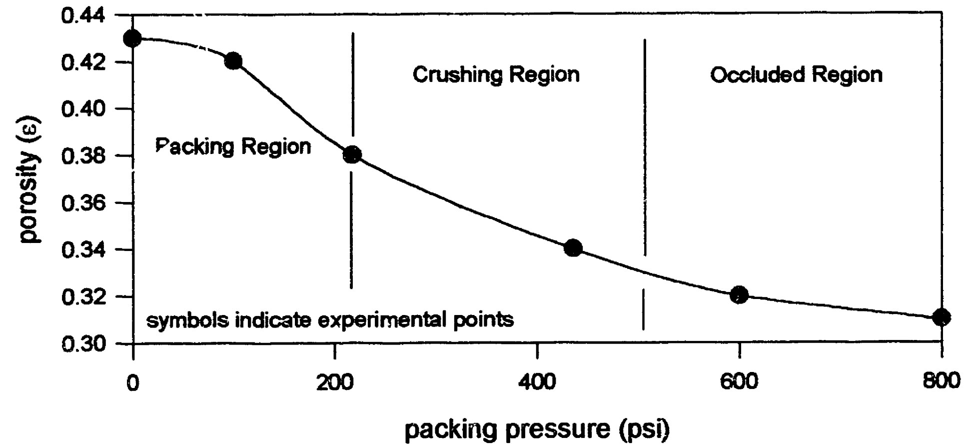

Figure 2-13. Porosity as a function of packing pressure

Ergun correlation. At low packing pressure, the Ergun correlation fits the data very well. As the packing pressure is increased above approximately 200 psi, the Ergun correlation does not fit the data as well. This indicates that the pre-crushed diameter is no longer appropriate when calculating the Reynolds number and friction factor because the particles have been further crushed during the packing process. Using this technique, it was possible to gain a qualitative idea of how the fabrication technique changes the internal character of the regenerator bed.

The porosity as a function of packing pressure is illustrated in Figure 2-13. Initially, packing pressure tends to reduce the porosity without crushing the particles any further (packing region). When the deviation from the Ergun correlation becomes large, the packing pressure is high enough to crush the particles to a smaller diameter (crushing region). Eventually, the packing pressure causes the matrix to become completely blocked to flow at reasonable pressures (occluded region).

Because it was feared that too much crushing of the particles within the regenerator tube might lead to favorable flow passages, the regenerator bed is constructed with a packing pressure of 200 psi. This leads to a porosity of 0.38 which is a significant improvement from the unpacked bed. The most important characteristics of the paramagnetic regenerator are listed in Table 2-5. The mass of GGG required to fill the uniform field section of the solenoid is approximately 1 kg. Multiplying the mass ratio associated with the design GM/magnetic cycle with the mass of GGG indicates that the mass of helium required per cycle is approximately 12.5 g. The flow characteristics within the paramagnetic regenerator are determined using the Ergun correlation and the resulting pressure drop across the regenerator bed is calculated to be approximately 1.3 psig.

The regenerator bed was constructed using the technique described above. A plunger which fit loosely into the regenerator tube was fashioned from aluminum. The force on the plunger could be regulated using a spring mechanism. The measured porosity of the regenerator is 0.392 which is slightly higher than that predicted by Figure 2-13. This is probably due to different crushing characteristics of GGG relative to glass.

Table 2-5. Characteristics of the paramagnetic regenerator

Parameter description	Symbol	Value	Units
packing pressure	P_{pack}	200	psi
regenerator porosity	ε	0.38	-
shape factor	ϕ	0.55	-
mass of GGG	M_G	1.013	kg
mass of helium (from MR)	M_h	12.7	g
Reynolds number	Re_{Dp}	600	-
friction factor	f	72	-
pressure drop	ΔP_{mag}	1.3	psig
particle diameter	D_p	0.0015	inch

2.3.3 Upper stage

This subsection describes the design and construction of the upper stage regenerator/heat exchanger. The subsection is divided into two parts. In the first part, a simple model of this type of device is developed and subsequently used to design the upper stage. The second part describes the construction of the upper stage device.

2.3.3.1 Design model

The upper stage device allows the working fluid to flow in contact with a conventional regenerator matrix material and a cooling stream. Throughout the entire cycle, the coolant stream enters the bottom of the device at a constant temperature ($T_{c,cold}$) which is the coldest temperature seen by the device. The working fluid flows in the top of the device during the first half of the cycle (the hot-to-cold blow portion of the magnetic stage cycle) at an elevated and constant temperature ($T_{w,hot}$) which is the highest temperature seen by the device. The working fluid flows in the bottom of the device during the second half of the cycle (the cold-to-hot blow portion of the magnetic stage cycle) at an intermediate temperature ($T_{w,in}$). The upper stage model is illustrated in Figure 2-14.

This model makes several simplifying assumptions. The mass flow rate of the working fluid and the coolant are assumed to be constant throughout the cycle (the working fluid mass flow rate simply changes direction half-way through the cycle). The properties and heat transfer coefficients are also assumed to be constant. The void volume of the regenerator is assumed to be zero. Finally, the change of phase associated with the vaporization of the liquid helium entering the coolant flow passages is neglected. It is hoped that this last assumption will lead to a design which is somewhat conservative.

The heat transfer coefficient and surface area between the matrix and the working fluid are denoted by U_{wr} and $A_{s,wr}$, respectively. The heat transfer coefficient and surface area between the working fluid and the coolant are denoted by U_{wc} and $A_{s,wc}$, respectively. The temperature of the working fluid, coolant, and regenerator are denoted by T_w, T_c, and T_r, respectively.

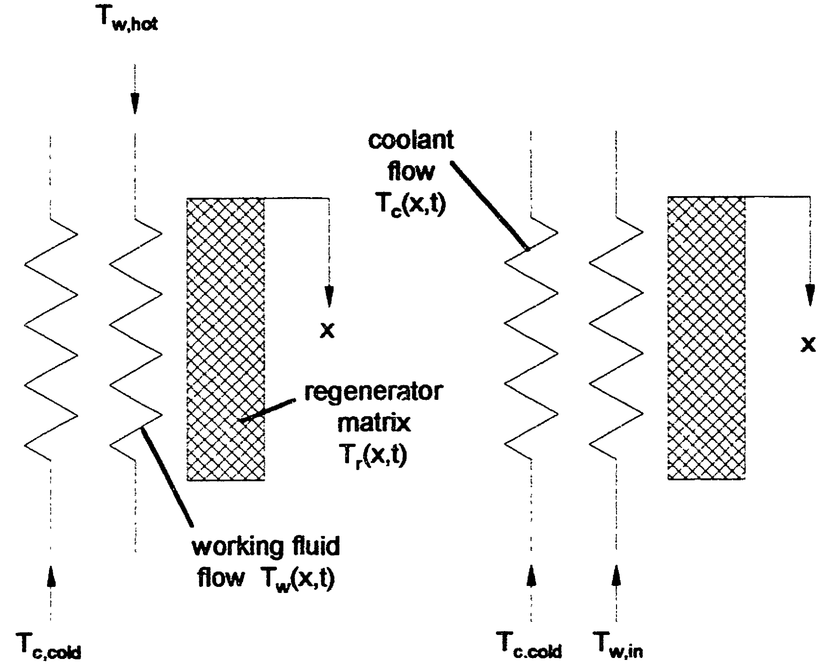

hot-to-cold blow process
$0 < t < \tau$

cold-to-hot blow process
$\tau < t < 2\tau$

Figure 2-14. Schematic of upper stage model

An energy balance on the working fluid flow passage during the hot-to-cold blow portion of the cycle balances energy storage in the fluid with heat flow to both the matrix and the coolant.

$$0 = m_w \cdot c_{P,w} \cdot \frac{\partial T_w}{\partial x} + \frac{U_{wr} \cdot A_{s,wr}}{L} \cdot \left(T_w - T_r\right) + \frac{U_{wc} \cdot A_{s,wc}}{L} \cdot \left(T_w - T_c\right) \tag{2.20}$$

During the cold-to-hot blow portion of the cycle, the working fluid mass flow switches direction.

$$m_w \cdot c_{P,w} \cdot \frac{\partial T_w}{\partial x} = \frac{U_{wr} \cdot A_{s,wr}}{L} \cdot \left(T_w - T_r\right) + \frac{U_{wc} \cdot A_{s,wc}}{L} \cdot \left(T_w - T_c\right) \tag{2.21}$$

An energy balance on the coolant stream balances energy storage in the coolant stream with heat transfer to the working fluid.

$$m_c \cdot c_c \cdot \frac{\partial T_c}{\partial x} = \frac{U_{wc} \cdot A_{s,wc}}{L} \cdot \left(T_c - T_w\right) \tag{2.22}$$

An energy balance on the regenerator matrix balances energy storage in the regenerator material with heat transfer to the working fluid.

$$0 = U_{wr} \cdot A_{s,wr} \cdot (T_r - T_w) + M_r \cdot c_r \cdot \frac{\partial T_r}{\partial t} \tag{2.23}$$

The boundary conditions associated with the device are that the working fluid enters the warm end of the device (x=0) during the hot-to-cold blow stroke (which lasts a time τ) at a constant temperature of $T_{w,hot}$.

$$T_w(0,t) = T_{w,hot} \quad \text{for } 0 < t \leq \tau \tag{2.24}$$

The working fluid enters the cold end of the device (x=L) during the cold-to-hot blow stroke at some constant temperature $T_{w,in}$.

$$T_w(L,t) = T_{w,in} \quad \text{for } \tau < t \leq 2 \cdot \tau \tag{2.25}$$

The coolant enters the cold end of the device at a constant temperature of $T_{c,cold}$.

$$T_c(L,t) = T_{c,cold} \quad 0 < t \leq 2 \cdot \tau \tag{2.26}$$

The device must undergo a steady-state cycle.

$$T_m(x,0) = T_m(x, 2 \cdot \tau) \tag{2.27}$$

The performance of the device can be quantified by dividing the heat transfer from the working fluid during the hot-to-cold blow process by the maximum possible heat transfer from the working fluid during the hot-to-cold blow process. This ratio is called the effectiveness and is defined below.

$$\alpha \equiv \frac{\frac{1}{\tau} \int_0^{\tau} (T_{w,hot} - T_w(L,t)) \cdot dt}{(T_{w,hot} - T_{c,cold})} \tag{2.28}$$

This problem statement can be nondimensionalized and solved in general using the definitions given below.

$$\text{dimensionless length}: \varepsilon \equiv \frac{x}{L} \tag{2.29}$$

$$\text{dimensionless time}: \varsigma \equiv \frac{t}{\tau} \tag{2.30}$$

$$\text{dimensionless temperature}: \Theta \equiv \frac{T - T_{c,cold}}{T_{w,hot} - T_{c,cold}} \qquad (2.31)$$

$$\text{number of transfer units, working fluid to regenerator}: NTU_{wr} \equiv \frac{U_{wr} \cdot A_{s,wr}}{m_w \cdot c_w} \qquad (2.32)$$

$$\text{number of transfer units, working fluid to coolant}: NTU_{wc} \equiv \frac{U_{wc} \cdot A_{s,wc}}{m_c \cdot c_c} \qquad (2.33)$$

$$\text{capacity ratio , working fluid to regenerator}: \Gamma_{wr} \equiv \frac{M_r \cdot c_r}{m_w \cdot c_w \cdot \tau} \qquad (2.34)$$

$$\text{capacity ratio , working fluid to coolant}: \Gamma_{wc} \equiv \frac{m_w \cdot c_w}{m_c \cdot c_c} \qquad (2.35)$$

$$\text{dimensionless working fluid inlet temperature}: \Theta_{w,in} = \frac{T_{w,in} - T_{c,cold}}{T_{w,hot} - T_{c,cold}} \qquad (2.36)$$

The dimensionless problem statement is given below.

$$0 = \frac{\partial \Theta_w}{\partial \varepsilon} + NTU_{wm} \cdot (\Theta_w - \Theta_r) + \frac{NTU_{wc}}{\Gamma_{wc}} \cdot (\Theta_w - \Theta_c) \quad \text{for } 0 < \varsigma \le 1 \qquad (2.37)$$

$$\frac{\partial \Theta_w}{\partial \varepsilon} = NTU_{wm} \cdot (\Theta_w - \Theta_r) + \frac{NTU_{wc}}{\Gamma_{wc}} \cdot (\Theta_w - \Theta_c) \quad \text{for } 1 < \varsigma \le 2 \qquad (2.38)$$

$$0 = NTU_{wm} \cdot (\Theta_r - \Theta_w) + \Gamma_{wr} \cdot \frac{\partial \Theta_r}{\partial \varsigma} \qquad (2.39)$$

$$\frac{\partial \Theta_c}{\partial \varepsilon} = NTU_{wc} \cdot (\Theta_c - \Theta_w) \qquad (2.40)$$

$$\Theta_w(0,\varsigma) = 1 \quad \text{for } 0 < \varsigma \le 1 \qquad (2.41)$$

$$\Theta_w(1,\varsigma) = \Theta_{w,in} \quad \text{for } 1 < \varsigma \le 2 \qquad (2.42)$$

$$\Theta_c(0,\varsigma) = 0 \quad \text{for } 0 < \varsigma \le 2 \qquad (2.43)$$

$$\Theta_m(\varepsilon,0) = \Theta_m(\varepsilon,2) \quad \text{for } 0 < \varepsilon \le 1 \qquad (2.44)$$

$$\alpha \equiv 1 - \int_{0}^{1} \Theta_w(1,\varsigma) \cdot d\varsigma \qquad \textbf{(2.45)}$$

The dimensionless problem is solved in a manner similar to the solution of the first order Stirling/magnetic model described in subsection 1.3.4. The partial differential equations are converted to finite difference equations. The entire position and time space are contained in one linear matrix. This matrix is solved to give the axial and temporal variation of dimensionless working fluid, coolant, and matrix temperatures. Since the equations are linear, only one inversion is required. The program used to carry out the solution technique is contained in appendix A.3.

The device behaves as a counterflow heat exchanger (during the hot-to-cold blow process) in the limit that there is no thermal communication between the matrix and the working fluid (i.e. as NTU_{wr} approaches zero). This characteristic of the device can be used to validate the solution technique. The effectiveness of the device predicted by the model for this situation is illustrated in Figure 2-15. The effectiveness is shown as a function of the number of transfer units between the coolant and the working fluid for various values of the capacity ratio between the working fluid and the coolant. These curves are nearly identical

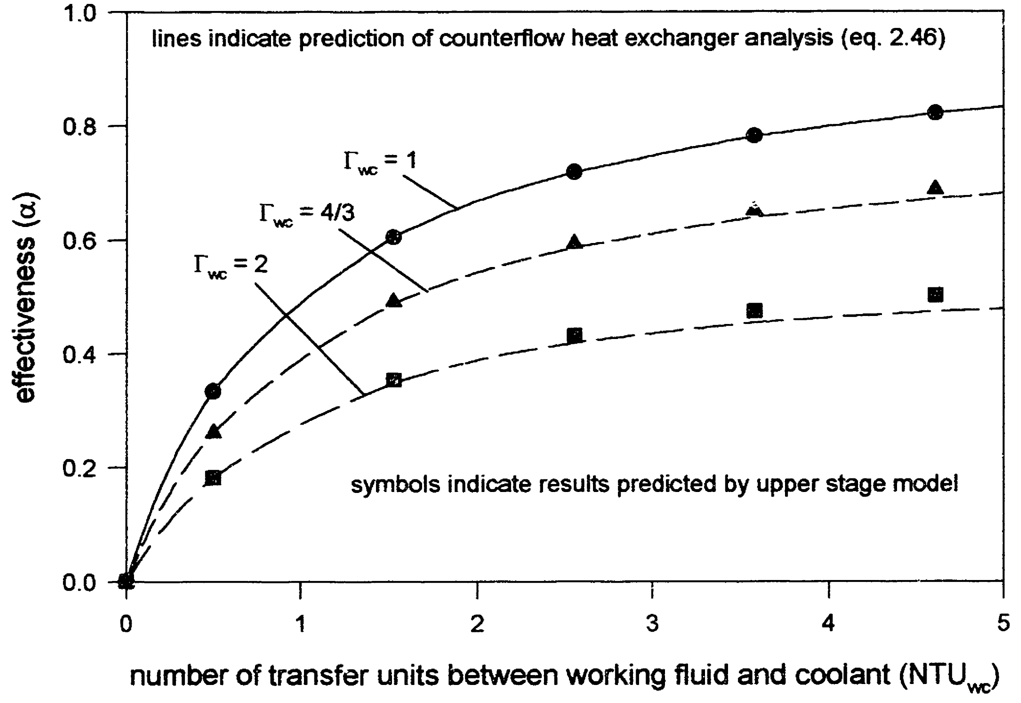

Figure 2-15. Effectiveness of regenerator/heat exchanger in the pure counterflow heat exchanger limit ($NTU_{wc} = 0$) as a function of the number of transfer units between the working fluid and the coolant for several values of the capacity ratio between the working fluid and the coolant

to those predicted by heat exchanger analysis applied to a counterflow heat exchanger [52]. The analytic solution for a counterflow heat exchanger is well known and given below in terms of the parameters defined in this problem (assuming that the capacity of the working fluid is always larger than the capacity of the coolant). This equation is shown in Figure 2-15 as a check of the finite difference program.

$$\alpha = \frac{1 - \exp\left(-\mathrm{NTU}_{wc} \cdot \{1 - 1/\Gamma_{wc}\}\right)}{\Gamma_{wc} \cdot \left[1 - \left(1/\Gamma_{wc}\right) \cdot \exp\left(-\mathrm{NTU}_{wc} \cdot \{1 - 1/\Gamma_{wc}\}\right)\right]} \tag{2.46}$$

The regenerator/heat exchanger limits to a balanced, counterflow regenerator when the thermal communication between the regenerator and the working fluid is removed (i.e. $\mathrm{NTU}_{wr} = 0$). This type of operation is illustrated in Figure 2-16. Again, the model may be checked against published effectiveness curves for this type of a device [53].

The advantage associated with adding the coolant flow to the regenerative device is that the effectiveness, as defined in equation 2.45, can be increased above unity since the working fluid has two places to transfer heat - the regenerator and the coolant. Figure 2-17 illustrates the effectiveness as a function of the number of transfer units between the working fluid and the coolant for several values of the capacity ratio between the working fluid and the coolant. As the amount of coolant increases (Γ_{wc} decreases) or the thermal communication between the working fluid and coolant increases (NTU_{wc} increases) the effectiveness increases.

For the design of the upper stage, the problem can be further specified. Since the coolant flow is taken directly from the boil-off of the magnet pool, the temperature at which the coolant enters the device will be liquid helium temperature at one atmosphere ($T_{c,cold} = 4.2$ K). The temperature of the working fluid as it enters the warm end of the experimental apparatus during the hot-to-cold blow portion of the cycle will not be signicantly different from room temperature ($T_{w,hot} = 300$ K). The average temperature of the helium which leaves the cold end of the upper stage is the warm reservoir temperature seen by the magnetic stage.

$$\frac{1}{\tau} \int_0^{\tau} T_w(L, t) \cdot dt = T_{\substack{H,\text{magnetic}\\ \text{stage}}} = 12 \text{ K} \tag{2.47}$$

These specifications set the required effectiveness of the device.

$$\alpha = \frac{300 - 12}{300 - 4.2} = 0.974 \tag{2.48}$$

The predictive model indicates that the GM/magnetic cycle will superheat the helium leaving the warm end of the magnetic stage by approximately 2 K ($T_{w,in} = 14$ K). This

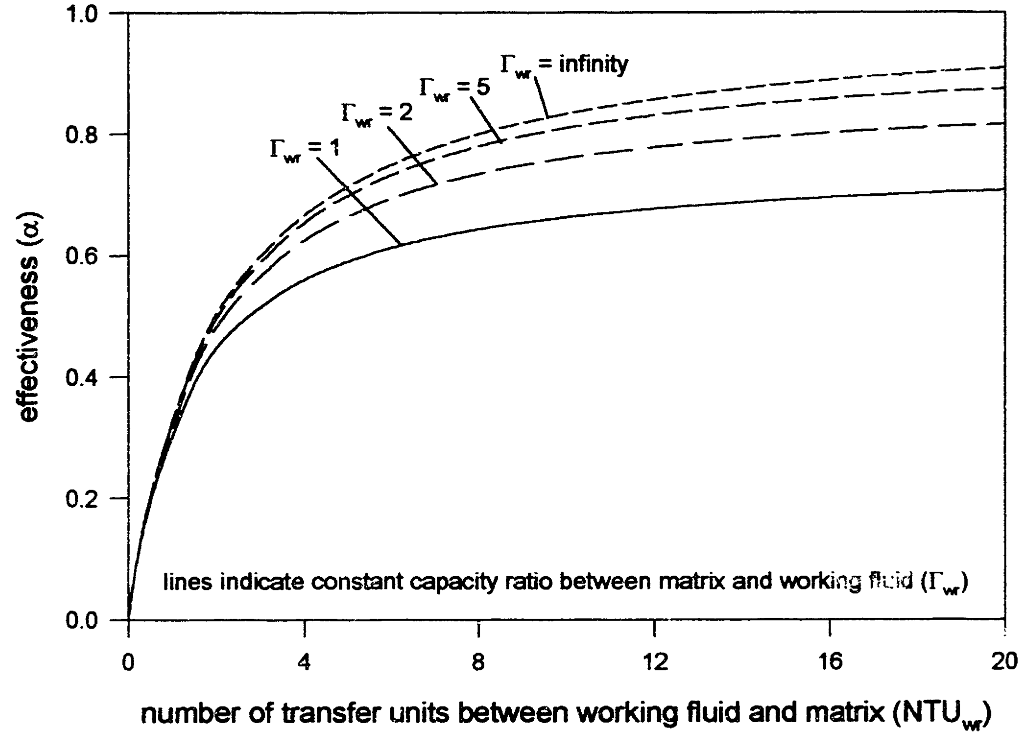

Figure 2-16. Effectiveness of the regenerator/heat exchanger in the balanced counterflow regenerator limit ($NTU_{wr} = 0$, $\Theta_{w,in} = 0$) as a function of the number of transfer units between the working fluid and the matrix for several values of the capacity ratio between the working fluid and the matrix

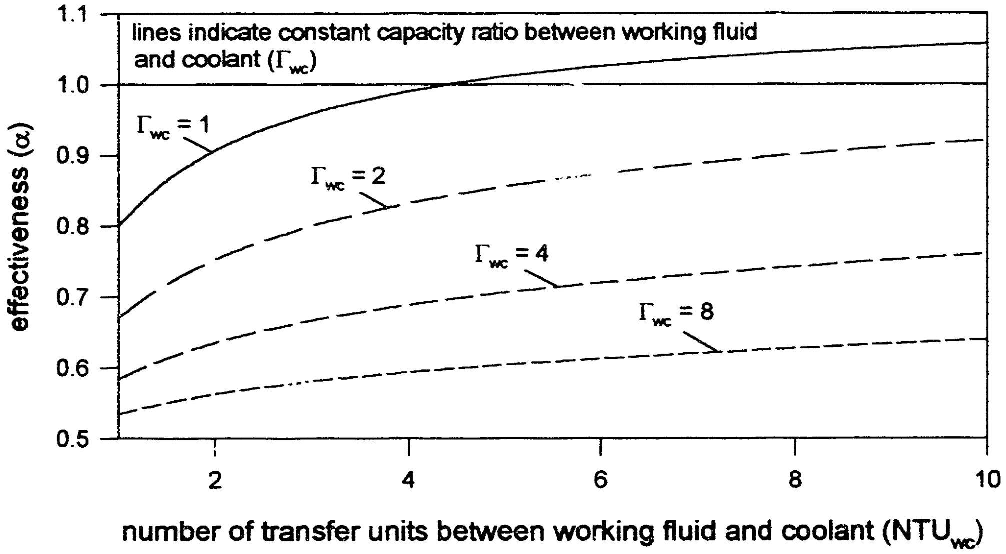

Figure 2-17. Effectiveness of regenerator/heat exchanger as a function of the number of transfer units between the working fluid and the coolant for several values of the capacity ratio between the working fluid and the coolant ($\Gamma_{wr} = 2$, $NTU_{wr} = 2$, $\Theta_{w,in} = 0.2$)

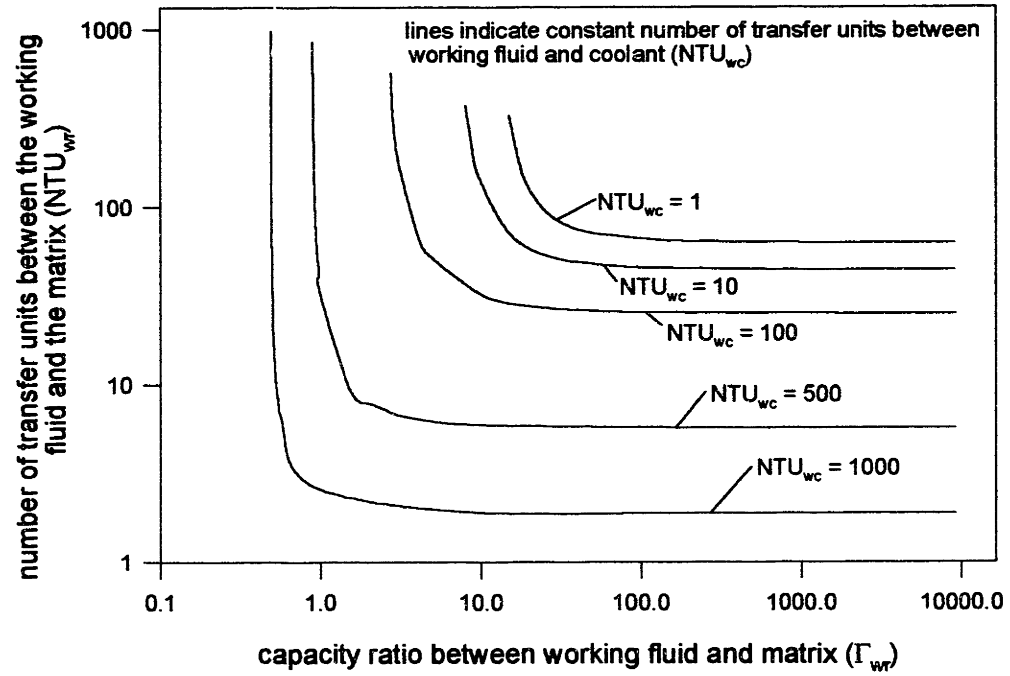

Figure 2-18. Number of transfer units between the working fluid and the matrix as a function of the capacity ratio between the working fluid and the matrix for several values of the number of transfer units between the working fluid and coolant for the design constraints associated with the experimental apparatus ($\Gamma_{wc} = 13$, $\alpha = 0.974$, $\Theta_{w,in} = 0.033$)

specifies the dimensionless inlet temperature of the working fluid during the cold-to-hot blow process.

$$\Theta_{w,in} = \frac{14-4.2}{300-4.2} = 0.033 \tag{2.59}$$

Another constraint is obtained by specifying a reasonable rate of liquid helium boiloff from the dewar (VF_{bo}). This constraint coupled with the design conditions for the GM/magnetic cycle leads to the required capacity ratio between the working fluid and the coolant.

$$\Gamma_{wc} = \frac{m_w \cdot c_w}{m_c \cdot c_c} = \frac{M_h}{\tau \cdot VF_{bo} \cdot \rho_{he}} = 13 \tag{2.50}$$

Having specified the required effectiveness, dimensionless working fluid inlet temperature, and capacity ratio between the working fluid and the coolant, the remaining three dimensionless quantities must be related.

$$NTU_{wr} = \Im\left(NTU_{wc}, \Gamma_{wr}\right) \tag{2.51}$$

The number of transfer units between the working fluid and regenerator required for the three constraints associated with equations 2.48 through 2.50 is illustrated in Figure 2-18 as a function of the capacity ratio between the working fluid and the regenerator at several values of the number of transfer units between the working fluid and the coolant. At very low values of the capacity ratio, the device cannot be made to provide the required effectiveness so the number of transfer units between the working fluid and the matrix goes to infinity. As the capacity ratio is increased, the number of transfer units between the working fluid and the matrix can be decreased. A similar trend is seen as the number of transfer units between the working fluid and the coolant is increased.

Another important performance characteristic of the upper stage device is the temperature swing at the cold end of the regenerator/heat exchanger during the hot-to-cold blow process (ΔT_{in}).

$$\Delta T_{in} = \max[T_w(L, 0 < t < \tau)] - \min[T_w(L, \tau < t \leq 2 \cdot \tau)] \qquad \textbf{(2.52)}$$

Because the upper stage device maintains the warm reservoir temperature on the magnetic stage, it is important that this temperature swing be minimized. The temperature swing is made dimensionless below.

$$\Delta\Theta_{in} \equiv \frac{\Delta T_{in}}{(T_{w,in} - T_{c,cold})} = \frac{\max[\Theta_w(1, 0 < \varsigma \leq 1)] - \min[\Theta_w(1, 1 < \varsigma \leq 2)]}{\Theta_{w,in}} \qquad \textbf{(2.53)}$$

The dimensionless temperature drift ($\Delta\Theta_{in}$) is plotted in Figure 2-19 as a function of the capacity ratio between the working fluid and the matrix for several values of the number of transfer units between the working fluid and the coolant. As the capacity ratio between the working fluid and the matrix goes up, the temperature drift decreases due to the increase in the heat capacity of the matrix. As the number of transfer units between the working fluid and the coolant goes up the temperature drift also decreases because the coolant is becoming a more effective thermal anchor at the cold end.

An achievable value of temperature drift is chosen to be 5 K. This leads to an additional design constraint corresponding to the dimensionless temperature drift.

$$\Delta\Theta_{in} = \frac{5K}{14K - 4.2K} = 0.5 \qquad \textbf{(2.54)}$$

This constraint allows one more dimensionless parameter to be eliminated. The number of transfer units between the working fluid and the coolant and the number of transfer units between the working fluid and the matrix are illustrated in Figure 2-20 as a function of the capacity ratio between the working fluid and the matrix. This figure can be thought of as the minimum number of each type of transfer unit required to achieve the desired thermal performance in the upper stage (as specified by the four constraints associated with equations 2.48, 2.49, 2.50, and 2.54). Any increase in either type of transfer units will result in an increase in the thermal performance of the device.

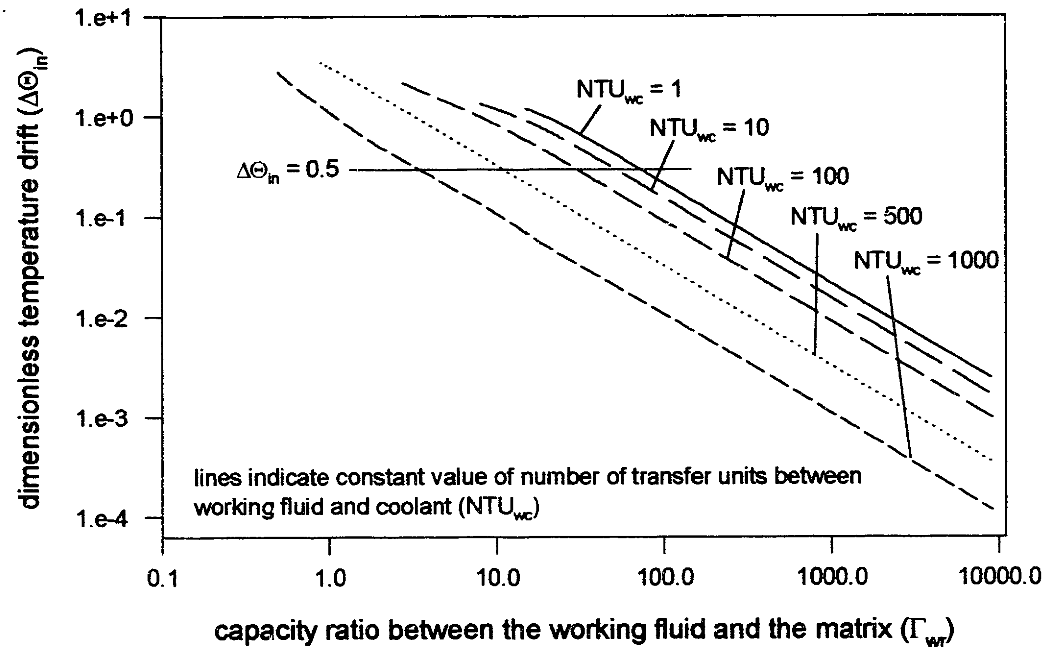

Figure 2-19. Dimensionless temperature drift as a function of the capacity ratio between the working fluid and the matrix for several values of the number of transfer units between the working fluid and the coolant for the design conditions associated with the experimental apparatus (Γ_{wc} = 13 , α = 0.974 , $\Theta_{w,in}$ = 0.033)

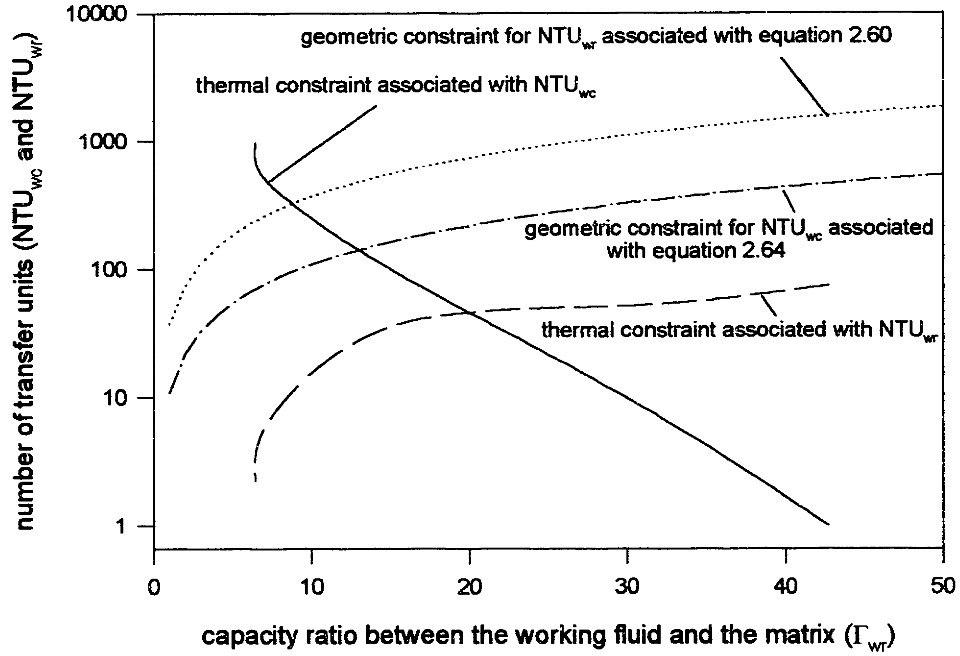

Figure 2-20. Minimum number of transfer units of each type required to achieve the thermal performance associated with the experimental apparatus and the required temperature drift (Γ_{wc} = 13, α = 0.974 , $\Theta_{w,in}$ = 0.033 , $\Delta\Theta_{in}$ = 0.51) as a function of the capacity ratio between the working fluid and the matrix, also shown are geometric constraints associated with the upper stage device

The upper stage device has a shell and tube heat exchanger geometry with one shell pass and one tube pass. The pressurized working fluid flows through the tubes which are filled with lead shot and the coolant flows through the shell. In order to increase the residence time of the coolant, the shell is constructed with a series of baffles that force the coolant to flow perpendicular to the tubes. This type of geometry is illustrated schematically in Figure 2-21.

Several aspects of the geometry are fixed by considering constraints associated with the size of the dewar. The diameter of the device must be approximately 4 inches in order to fit in the dewar while leaving room for a displacer. In order to facilitate the fabrication of the baffles, the tube array corresponds to a pattern associated with a standard size perforated metal sheet and a stock size of stainless steel tube. The perforated metal pattern is a 5/32 inch diameter hole pattern in a hexagonal close packed array with 3/16 inch centers. The corresponding stainless steel tube size is 9 guage thin wall stainless (0.148 inch OD and 0.128 inch ID). The number of stainless steel tubes which can feasibly fit into a 4 inch diameter using the pattern chosen is approximately 225 (a 15x15 array). The lead shot required for this device must be doped with Antimony in order to eliminate the possibility of cracking during operation. The lead shot most suitable for this application has a diameter of 7 mils and a chemical composition of 95% Pb and 5% Antimony.

The unspecified geometric parameters are the length of the device (L) and the number of baffles required (N_{baffle}). The capacity ratio between the working fluid and the regenerator may be written as a function of the length of the device.

$$\Gamma_{wr} = L \cdot \frac{\pi \cdot D_{tube,i}^2 \cdot (1-\varepsilon) \cdot N_{tube} \cdot \rho_{Pb} \cdot c_{Pb}}{4 \cdot M_h \cdot c_{p,he}} \approx 2.1 \cdot L \text{ where } L \text{ [inch]} \qquad \textbf{(2.55)}$$

The specific heat capacities in equation 2.55 (and all other material properties in this analysis) are evaluated at the mean temperature of the device and a representative pressure. The Reynolds number associated with the flow of the working fluid in the tubes is determined below.

$$Re_{D_p} = \frac{D_p \cdot M_h \cdot 4}{\pi \cdot D_{tube,i}^2 \cdot N_{tube} \cdot \mu \cdot \tau} \approx 16 \qquad \textbf{(2.56)}$$

The corresponding Nusselt number for a packed bed geometry can be computed using the correlation shown below.

$$Nu_{D_p} = 2 + Pr^{1/3} \cdot Re_{D_p}^{1/2} \qquad \textbf{(2.57)}$$

Because the diameter of the lead shot is small, the Biot number is much less than one for any reasonable value of heat transfer coefficient. Consequently, it is acceptable to ignore internal temperature gradients in the lead and take the overall heat transfer coefficient

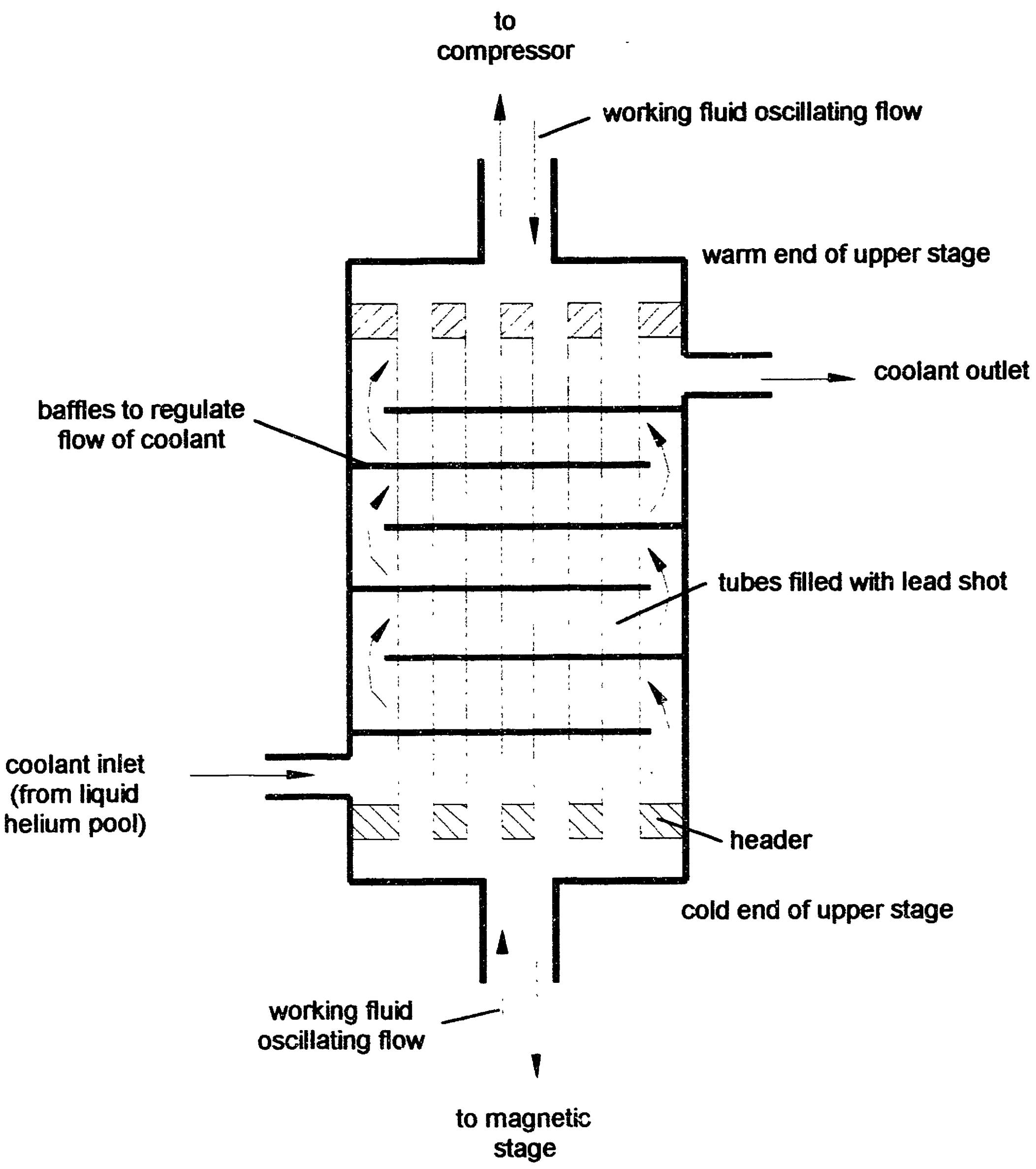

Figure 2-21. Schematic of upper stage geometry

between the working fluid and the regenerator to be the heat transfer coefficient associated with the thermal boundary layer in the flowing helium.

$$U_{wr} = \frac{k_h \cdot Nu_{D_p}}{D_p} \approx 3000\ W/m^2K \qquad (2.58)$$

The number of transfer units between the working fluid and the matrix can be expressed as a function of the length of the upper stage.

$$\mathrm{NTU}_{wr} = L \cdot \frac{U_{wr} \cdot \pi \cdot D_{tube,i}^2 \cdot N_{tube} \cdot \tau}{4 \cdot D_p \cdot M_h \cdot c_{p,h}} \approx 74 \cdot L \text{ where } L \text{ [inch]} \tag{2.59}$$

Equations 2.59 and 2.55 are combined to eliminate length and obtain an expression for the number of transfer units between the working fluid and the regenerator as a function of the capacity ratio between the working fluid and the regenerator.

$$\mathrm{NTU}_{wr} = 37 \cdot \Gamma_{wr} \tag{2.60}$$

This equation indicates one geometric contraint and is plotted in Figure 2-20. For every value of upper stage length, the number of transfer units between the working fluid and the matrix associated with the specific geometry is larger than the number of transfer units between the working fluid and the matrix required in order to ensure the proper thermal performance of the upper stage. This is because the large specific area and large heat transfer coefficient associated with the packed bed geometry yields good thermal communication between the regenerator and the working fluid.

It is somewhat more difficult to achieve the required number of transfer units between the working fluid and the coolant since the specific area and heat transfer coefficient associated with the tube bank are much smaller than those associated with the packed bed. Another equally important consideration when designing the coolant side of the upper stage is that the pressure drop within the coolant cannot exceed 3 psi. The inlet to the coolant circuit is connected to the magnet pool and the outlet is connected to atmosphere. Therefore, any pressure drop across the coolant circuit is equivalent to pressurizing the liquid helium pool which cools the magnet. Because boiling is required for effective cooling of the magnet, the vapor dome requires that the pressure of the liquid helium pool not be more than 3 psi above atmospheric pressure.

The distance between adjacent baffles ($L_{baffle} = L/N_{baffle}$) determines the Reynolds number associated with coolant flow across the tube bank.

$$\mathrm{Re}_{D_{tube}} = \frac{D_{tube,o} \cdot \left(M_h / \Gamma_{wc,req}\right)}{L_{baffle} \cdot N_{tube.across} \cdot \left(L_{center} - D_{tube,o}\right) \cdot \mu_h \cdot \tau} \approx \frac{63}{L_{baffle}} \quad \text{where } L_{baffle} \text{ [inch]} \tag{2.61}$$

The Nusselt number associated with a bank of tubes for the Reynolds numbers predicted by equation 2.61 and a feasible range of distance between baffles can be obtained by treating the tubes as isolated and using the low Reynolds number form of the Churchill correlation [54].

$$\mathrm{Nu}_{D_{tube}} = 0.3 + \frac{0.62 \cdot \mathrm{Re}_{D_{tube}}^{1/2} \cdot \mathrm{Pr}^{1/3}}{\left[1 + (0.4/\mathrm{Pr})^{2/3}\right]} \approx 0.3 + \frac{2.59}{L_{baffle}^{1/2}} \tag{2.62}$$

The thermal resistance associated with the tube wall and convection between the inside of the tube and the working fluid are dominated by the resistance of the thermal boundary layer between the outside of the tube and the coolant. Therefore the total heat transfer coefficient between the coolant and the working fluid can be taken to be the heat transfer coefficient between the coolant and the external surface of the tubes. The number of transfer units between the working fluid and the coolant is expressed as a function of the distance between adjacent baffles and the overall length of the device.

$$NTU_{wc} = \frac{Nu_{D_{tube}} \cdot k_h \cdot \pi \cdot L \cdot N_{tube} \cdot \tau \cdot \Gamma_{wc}}{M_h \cdot c_{P,h}} \approx 3 \cdot L \cdot \left(0.3 + \frac{2.59}{L_{baffle}^{1/2}}\right) \quad \textbf{(2.63)}$$

Equation 2.55 expresses the capacity ratio between the working fluid and the matrix as a function of the length. This equation is substituted into equation 2.63 to eliminate length and yield an expression for the number of transfer units between the working fluid and the coolant as a function of Γ_{wr} and the baffle separation distance.

$$NTU_{wc} = 1.43 \cdot \Gamma_{wr} \cdot \left(0.3 + \frac{2.59}{L_{baffle}^{1/2}}\right) \quad \textbf{(2.64)}$$

This equation is plotted in Figure 2-20 for a feasible baffle distance (5/32 inch) which does not produce a large pressure drop in the coolant. This equation is another geometric constraint for the device. The point where the thermal performance constraint intersects the geometric constraint specifies the length of the regenerator required for this baffle separation distance. The minimum length required for this baffle intersection is 7 inches according to Figure 2-20 and equation 2.55. A more conservative length of 11 inches is chosen for the design. The resulting number of baffles is 52 (taking into account the thickness of the punch plate).

All that remains is to calculate the pressure drop across the two streams. The pressure drop across the series of tube banks is given by the equation below [55].

$$\Delta P_c = N_{tube,across} \cdot N_{baffle} \cdot \chi \cdot f \cdot \frac{1}{2} \cdot \rho \cdot v_{max}^2 \quad \textbf{(2.65)}$$

The friction factor (f) is a function of the Reynolds number associated with the coolant given by equation 2.61 ($Re_{d,tube} = 400$) and is taken from a published chart ($f = 0.5$). The correction factor (χ) is based on the ratio of the transverse to lateral pitch of the tube bank and is also read from a chart ($\chi = 1.05$). The resulting pressure drop calculated with equation 2.65 and the geometry of the upper stage is 1.6 psi which is acceptable for this device. The pressure drop across the working fluid circuit is given by the packed bed correlation shown in equation 2.17. The resulting pressure drop is approximately 14 psi.

Table 2-6. Characteristics of the upper stage

Parameter description	Symbol	Value	Units
total number of tubes	N_{tube}	225	-
number of tubes in direction perpendicular to flow	$N_{tube,across}$	15	-
length	L	11	inch
distance between baffles	L_{baffle}	0.156	inch
number of baffles	N_{baffle}	52	-
outer diameter of tube	$D_{tube,o}$	0.148	inch
inner diameter of tube	$D_{tube,i}$	0.128	inch
particle diameter	D_p	0.007	inch
center distance between adjacent tubes	L_{center}	0.156	inch
capacity ratio between working fluid and matrix	Γ_{wr}	20	-
Reynolds number based on particle diameter	Re_{Dp}	16	-
number of transfer units between working fluid and regenerator	NTU_{wr}	810	-
Reynolds number based on tube diameter	$Re_{D,tube}$	400	-
number of transfer units between working fluid and coolant	NTU_{wc}	230	-
pressure drop across coolant	ΔP_c	1.5	psi
pressure drop across working fluid	ΔP_w	14	psi

The design parameters and important characteristics of the upper stage device are listed in Table 2-6.

2.3.3.2 Construction technique

This subsection describes the construction technique used to fabricate the upper stage. The most difficult part of constructing the upper stage device involved effectively sealing the high pressure working fluid side of the device from the low pressure coolant side. Two stainless steel headers were constructed into which the stainless steel tubes were brazed. The punch plate material was cut to the appropriate size and the tubes were passed through the baffles and into the header at each end. The baffle spacing was maintained during fabrication using spacers.

The brazing was accomplished by liberally fluxing the header assembly and placing small pieces of brazing alloy in every interstitial hole formed by the hexagonal close packed tube array. A copper piece was placed over the entire header and heated using an oxyacetylene torch. By heating the high conductivity copper piece rather than the low conductivity stainless steel, the entire header reached the melting temperature of the braze alloy at approximately the same time. This resulted in a reasonably uniform seal around each tube rather than preferential wetting of the hotter portions of the header which tends to occur

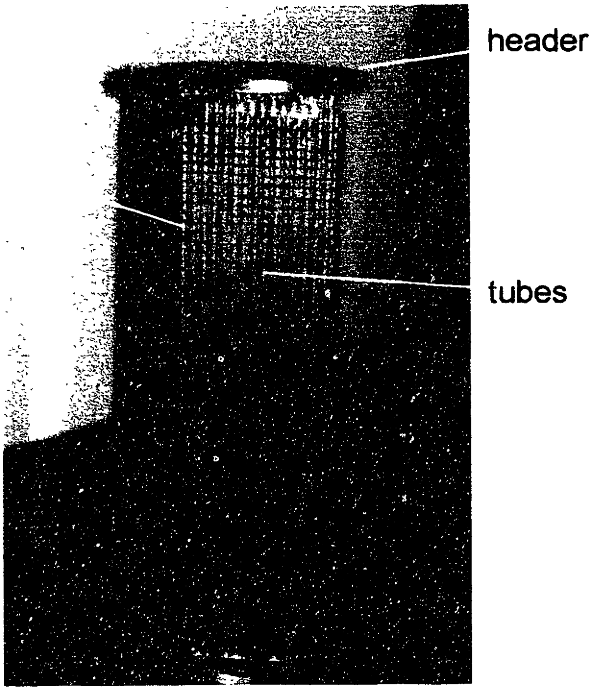

Figure 2-22. Assembled tube bank with headers and baffles

when large thermal gradients exist. The tube ends were subsequently removed and the resulting assembly is shown in Figure 2-22. The brazed tube pattern is shown in Figure 2-23.

The hole pattern used to construct the punch plate baffles leaves open holes at each end of the baffles. By closing or opening these holes, the flow can be directed from level to level. The hole pattern is illustrated in Figure 2-24, which is another view of the assembled tube

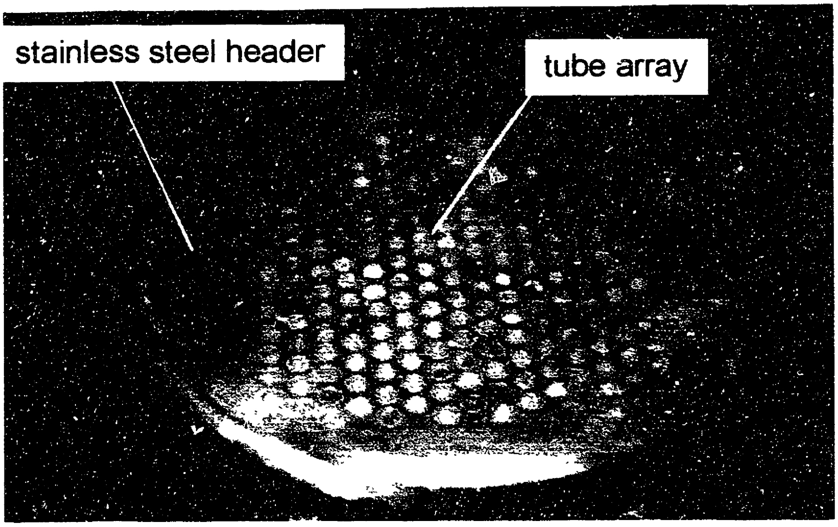

Figure 2-23. Brazed tubes in upper stage header

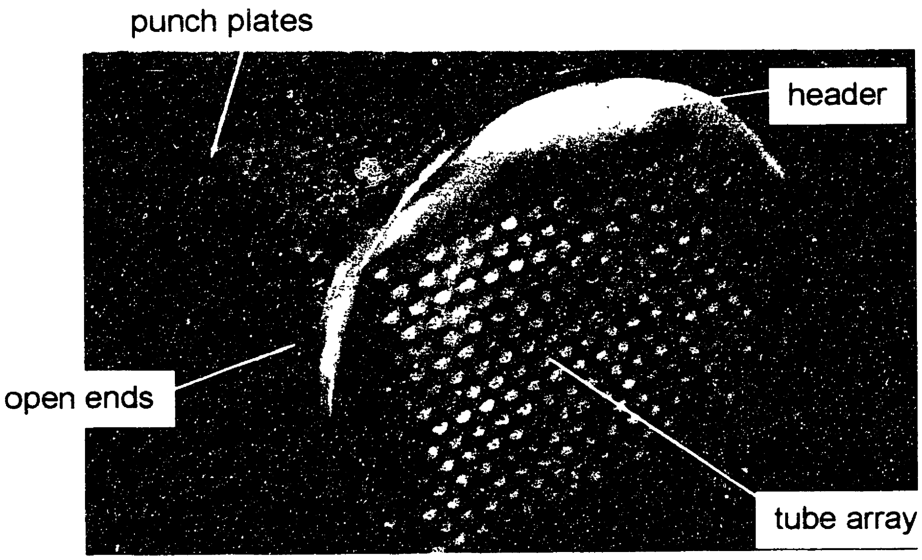

Figure 2-24. Assembled tube bank with header and punch plates

bank. Flow regulation is achieved using phenolic regulators. The phenolic flow regulators were machined so that their outer surface matched the circular contour of the header while the inner surface matched the tube bank profile. The side regulators simply close off any possibility of flow in this direction. The end regulators close off every other set of open

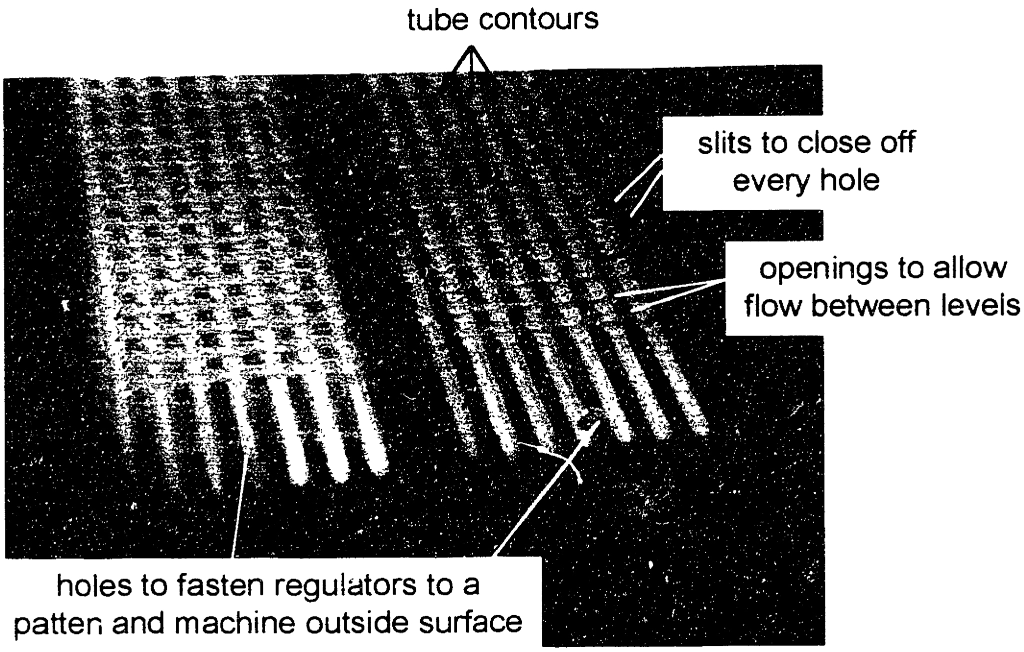

Figure 2-25. Phenolic end flow regulators prior to being cut to length

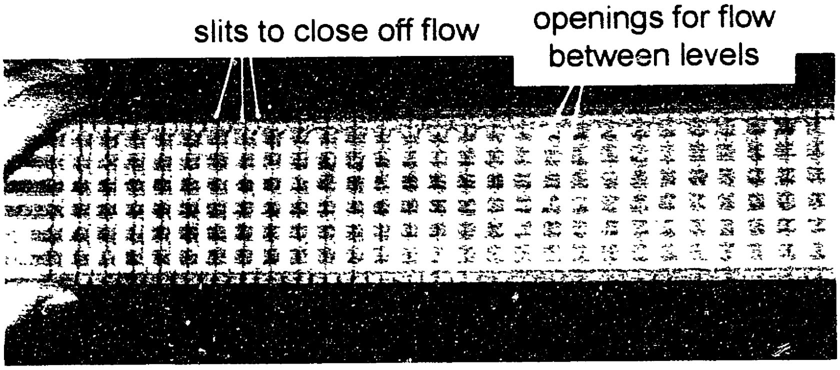

Figure 2-26. Phenolic end flow regulators prior to being cut to length

holes in order to allow the flow to pass between levels in the proper manner. This was accomplished by first cutting the contours of the tubes into the phenolic. Then, all of the openings were closed off by cutting appropriate slits into the phenolic using a jewelers saw of the same width as the punch plate thickness. Finally, every other set of holes was opened using an end mill. The finished end regulators before being cut to final length are shown in Figures 2-25 and 2-26.

The regulators were installed and a large stainless steel tube was welded around the headers. The coolant inlet and outlet passages were added and the resulting assembly is shown in Figure 2-27. The tubes were filled with lead shot which was captured by several layers of stainless steel screens of varying mesh sizes. These screens also act to diffuse the incoming working fluid and distribute it equally among all of the tubes.

2.3.4 Cold heat exchanger

The design and construction of the cold heat exchanger is described in this subsection. The cold heat exchanger provides thermal contact between the working fluid which passes to and from the cold space and the refrigeration load. The refrigeration load is simulated with a resistive Kapton heater.

The cold heat exchanger slides into the ramped field section of the superconducting solenoid. Consequently, the device is designed to minimize eddy current generation and void volume while keeping the required temperature difference between the working fluid and the heater and the pressure drop reasonable levels.

The cold heat exchanger is fashioned from a hollow cylinder and a solid cylinder. When the solid cylinder is placed within the hollow one, an annulus of thickness 20 mils is formed. The diameter of the annulus is such that when the flexible Kapton heater (of resistance 441 ohms at room temperature) is placed within the hollow cylinder, it expands and takes up the entire perimeter, as shown in Figure 2-28 a. The cylinders are aligned radially using the end caps, as shown in Figure 2-28 b. The Kapton heater has a thickness of approximately 10 mils so the working fluid flows in a uniform 10 mil gap. Because of the pattern of the

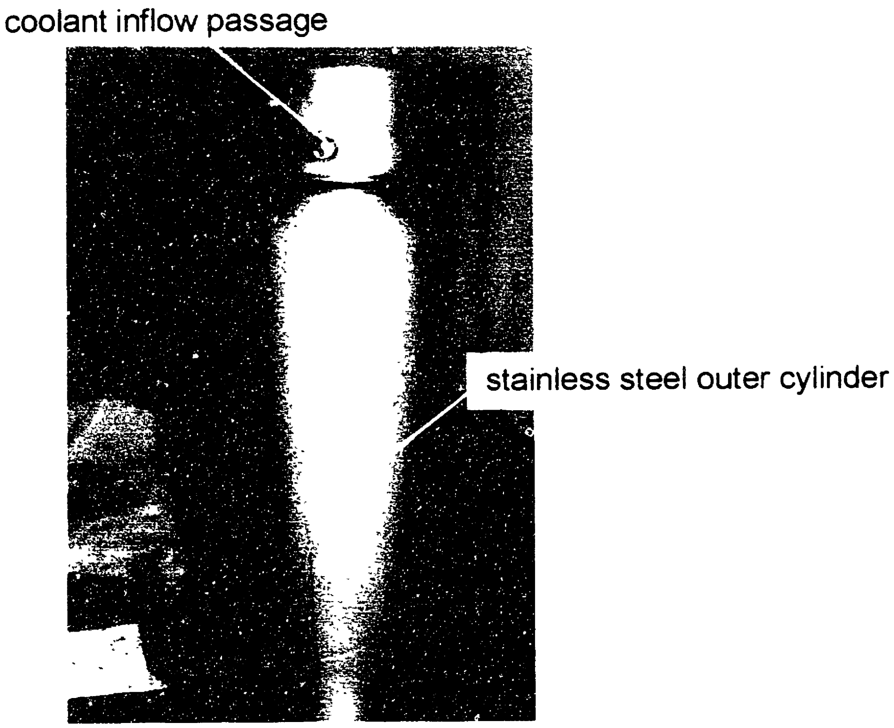

Figure 2-27. Assembled upper stage device

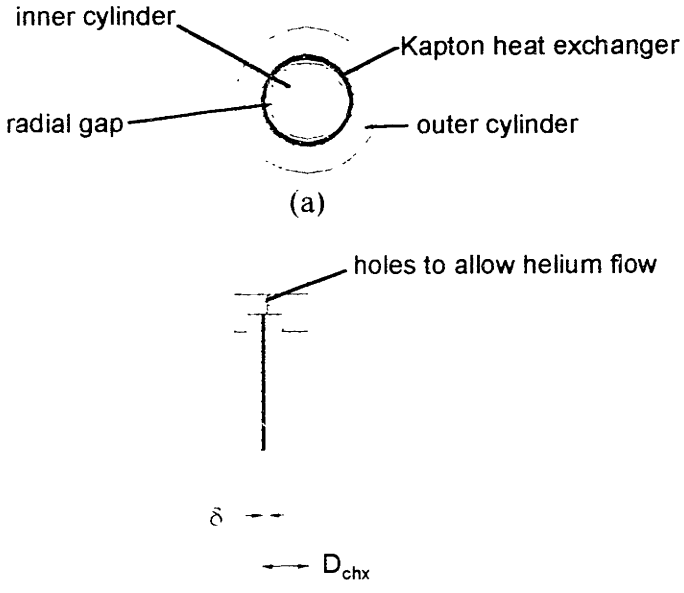

(a)

(b)

Figure 2-28. Diagram of cold heat exchanger heating element in the Kapton resistor, only one closed conduction path is formed. The induced voltage due to the applied field variation can be crudely estimated using Faraday's law [56].

$$V = \frac{d\phi}{dt} \approx \frac{\pi \cdot D_{chx}^2}{4} \cdot \frac{\mu_o H_{max}}{\tau} \approx 0.004\ V \qquad \textbf{(2.66)}$$

The eddy current heating associated with this induced voltage is negligible relative to the predicted refrigeration load.

The total void volume associated with the cold heat exchanger is approximately 1e-6 m^3 which is 1.2 % of the void volume contained in the regenerator bed. Therefore the void volume of the cold heat exchanger can be considered negligible.

The Reynolds number associated with flow through the cold heat exchanger is given below.

$$Re_t = \frac{2 \cdot M_h}{\tau \cdot D_{chx} \cdot \mu_h} \approx 8000 \qquad \textbf{(2.67)}$$

The associated friction factor is obtained using the correlation for turbulent flow in a smooth duct with the same hydraulic diameter and used to determine the approximate pressure drop across the cold heat exchanger.

$$\Delta P_{chx} = \frac{f_\delta}{2 \cdot \rho_h} \cdot \left(\frac{M_h}{\tau \cdot \pi \cdot D_{chx} \cdot \delta_{chx}} \right)^2 \approx 1000\ Pa \qquad \textbf{(2.68)}$$

This pressure drop is negligible relative to both the cyclic pressure variation imposed on the device and the pressure drop across the paramagnetic matrix.

The Nusselt number associated with the flow through the cold heat exchanger is also calculated using a correlation for turbulent flow in a smooth duct. The temperature difference required between the heater and the working fluid is determined below.

$$\Delta T_{chx} = \frac{Q_C \cdot 2 \cdot \delta_{chx}}{k_h \cdot Nu_\delta \cdot \pi \cdot D_{chx} \cdot L_{chx}} \approx 0.01\ K \qquad \textbf{(2.69)}$$

The entropy generation associated with the refrigeration load flowing through this temperature difference is negligible relative to other entropy flows associated with the experimental device.

The outer cylinder used in the cold heat exchanger is illustrated in Figures 2-29 and the flexible Kapton heater is illustrated in Figure 2-30. The important characteristics of the cold heat exchanger are listed in Table 2-7.

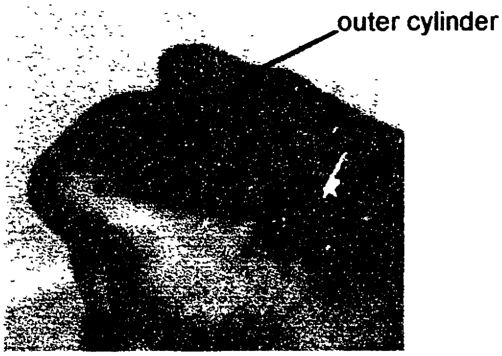

Figure 2-29. Cold heat exchanger outer cylinder

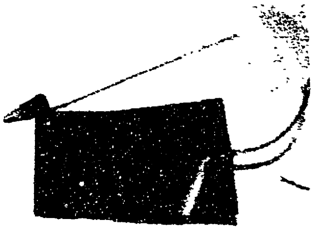

Figure 2-30. Cold heat exchanger Kapton heater

Table 2-7. Characteristics of cold heat exchanger

Description of parameter	Symbol	Value	Units
length of cylinder	L_{chx}	0.076	m
inner diameter of hollow cylinder	D_{chx}	0.016	m
thickness of flow passage	δ_{chx}	0.01	inch
void volume	$V_{dead,chx}$	1e-6	m^3
approximate Reynolds number	$Re_{t,chx}$	8000	-
approximate friction factor	f	0.04	-
approximate Nusselt number	Nu	24	-
approximate heat transfer coefficient	U	10000	W/m^2
approximate pressure drop	ΔP_{chx}	1000	Pa
approximate temperature difference between working fluid and heater	ΔT_{chx}	0.01	K

2.3.5 Displacer

This subsection describes the design and construction of the displacer. During the design of the displacer several effects are considered. Most importantly, the shuttle heat transfer is minimized. The void volume associated with the gap between the displacer and the displacer shell and conduction through the shell must be considered. Also, there can be no rubbing between the moving parts, particularly in the cold regions. Finally, the displacer has to be manufacturable using equipment and materials available at reasonable cost.

Shuttle heat transfer is associated with a 'bucket brigading' of heat down the temperature scale. The displacer moves upward and is exposed to a warmer portion of the shell where is absorbs heat. It subsequently moves downwards and transfers this heat to a colder portion of the shell. This is a more efficient mechanism for heat transfer than conduction under the conditions associated with the experimental apparatus.

A variety of models for shuttle heat transfer in displacer-cylinder systems have been proposed in the literature [57-59]. The model developed below is the most appropriate for the geometry specific to the experimental apparatus.

Figure 2-31 illustrates the model used to analyze shuttle heat transfer losses. The displacer shell can be modeled as having a quasi one-dimensional temperature profile in the z direction because the Biot number associated with the displacer shell thickness is fairly small throughout the displacer. The displacer is modeled as being semi-infinite in the x direction because the thermal penetration depth is much smaller than the diameter of the displacer. Axial conduction (i.e. conduction in the z direction) is neglected in this analysis.

The governing equations are derived using the coordinate system indicated in Figure 2-31, which is affixed to the displacer. The conduction equation governs the temperature distribution with the displacer (indicated with the subscript 1).

$$\frac{\partial^2 T_1}{\partial x^2} = \frac{1}{\alpha_1} \cdot \frac{\partial T_1}{\partial t} \qquad \textbf{(2.70)}$$

An energy balance on the displacer shell (subscript 2) yields the governing equation for the displacer shell temperature distribution. The first term indicates storage of energy, the second is related to the transfer of energy due to the velocity of the shell relative to the displacer, and the third terms is the convection of heat across the gas gap (U indicates the heat transfer coefficient between the displacer and the shell).

$$\frac{\partial T_2}{\partial t} + \frac{S \cdot \omega}{2} \cdot \sin(\omega \cdot t) \cdot \frac{\partial T_2}{\partial x} + \frac{U}{\rho_2 \cdot c_2 \cdot \delta_2} \cdot \left(T_2 - T_1\big|_{x=0} \right) = 0 \qquad \textbf{(2.71)}$$

The displacer temperature at the core of the displacer is assumed to be linear in the z direction.

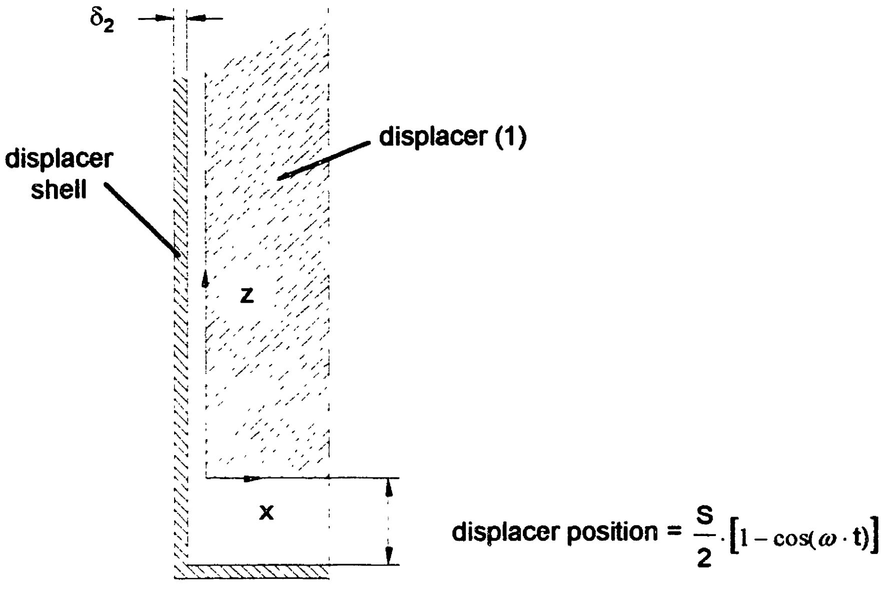

Figure 2-31. Shuttle heat transfer model

$$T_1\big|_{x\to\infty} = T_C + \frac{(T_H - T_C)}{L_{dis}}\cdot z \tag{2.72}$$

The heat flux into the displacer surface via convection must equal the conduction heat flux at the surface.

$$U\cdot\left(T_2 - T_1\big|_{x=0}\right) = k_1\cdot\left.\frac{\partial T_1}{\partial x}\right|_{x=0} \tag{2.73}$$

The shuttle heat transfer per cycle is obtained by integrating the enthalpy flux associated with the displacer wall moving relative to the displacer over a complete cycle.

$$Q_{shuttle} = -\int_0^{2\cdot\pi/\omega} \frac{\pi\cdot D_{dis}\cdot\delta_2\cdot\rho_2\cdot c_2\cdot\omega\cdot S}{2}\cdot\sin(\omega\cdot t)\cdot T_2(t)\cdot dt \tag{2.74}$$

This set of equations is made dimensionless using the definitions below. Also, by defining the dimensionless temperature in the manner shown below, the problem is transformed from a two dimensional, unsteady to a one dimensional, unsteady problem.

$$\text{dimensionless temperature}:\ \Theta \equiv \frac{T - T_C}{T_H - T_C} - \frac{z}{L_{dis}} \tag{2.75}$$

$$\text{dimensionless position} : \varepsilon \equiv x \cdot \sqrt{\frac{\omega}{\alpha_1}} \tag{2.76}$$

$$\text{dimensionless time} : \varsigma \equiv \omega \cdot t \tag{2.77}$$

$$\text{Biot number} : B \equiv \frac{U}{k_1} \cdot \sqrt{\frac{\alpha_1}{\omega}} \tag{2.78}$$

$$\text{dimensionless time constant} : \lambda \equiv \frac{U}{\rho_2 \cdot c_2 \cdot \delta_2 \cdot \omega} \tag{2.79}$$

$$\text{dimensionless stroke} : \beta \equiv \frac{S}{L_{dis}} \tag{2.80}$$

The dimensionless problem statement is given below.

$$\frac{\partial^2 \Theta_1}{\partial \varepsilon^2} = \frac{\partial \Theta_1}{\partial \varsigma} \tag{2.81}$$

$$\frac{\partial \Theta_2}{\partial \varsigma} + \frac{\beta}{2} \cdot \sin(\varsigma) + \lambda \cdot \left(\Theta_1 - \Theta_2 \big|_{\varepsilon=0} \right) = 0 \tag{2.82}$$

$$\Theta_1 \big|_{\varepsilon \to \infty} = 0 \tag{2.83}$$

$$\left(\Theta_1 \big|_{\varepsilon=0} - \Theta_2 \right) \cdot B = \left. \frac{\partial \Theta_1}{\partial \varepsilon} \right|_{\varepsilon=0} \tag{2.84}$$

Since only the steady-state periodic variation of the temperatures are of interest, the problem is solved by introducing complex temperatures for both the displacer and the wall (Ψ_1 and Ψ_2) [60]. This is accomplished by restating the problem in another set of variables (w_1 and w_2) in an identical manner (the same as equations 2.81 to 2.84) except that the sinusoidal term in equation 2.82 is changed to a cosine term. The complex temperatures are defined in terms of these variables.

$$\Psi_1 \equiv w_1 + i \cdot \Theta_1 \tag{2.85}$$

$$\Psi_2 \equiv w_2 + i \cdot \Theta_2 \tag{2.86}$$

Equations 2.81 through 2.84 are multiplied by i (the square root of negative one) and added to the equations associated with w_1 and w_2 to obtain the problem statement for the complex temperature.

$$\frac{\partial^2 \Psi_1}{\partial \varepsilon^2} = \frac{\partial \Psi_1}{\partial \varsigma} \tag{2.87}$$

$$\frac{\partial \Psi_2}{\partial \varsigma} + \frac{\beta}{2} \cdot \exp(i \cdot \varsigma) + \lambda \cdot \left(\Psi_1 - \Psi_2 \big|_{\varepsilon=0} \right) = 0 \tag{2.88}$$

$$\Psi_1 \big|_{\varepsilon \to \infty} = 0 \tag{2.89}$$

$$\left(\Psi_1 \big|_{\varepsilon=0} - \Psi_2 \right) \cdot B = \left. \frac{\partial \Psi_1}{\partial \varepsilon} \right|_{\varepsilon=0} \tag{2.90}$$

The time variation of the complex temperatures will be sinusoidal since that is the only driving force for the problem. The displacer complex temperature can be expressed as a product of a function in space and a sinusoidal function in time.

$$\Psi_1(\varepsilon, \varsigma) = E(\varepsilon) \cdot \exp(i \cdot \varsigma) \tag{2.91}$$

The wall temperature is simply a sinusoidal function of time.

$$\Psi_2(\varsigma) = C_3 \cdot \exp(i \cdot \varsigma) \tag{2.92}$$

Equations 2.87 and 2.89 yield the functional form of the spatial variation of the displacer complex temperature.

$$E(\varepsilon) = C_2 \cdot \exp(-\sqrt{i} \cdot \varepsilon) \tag{2.93}$$

Equations 2.90 through 2.92 are substituted into equations 2.88 and 2.90 to yield an algebraic set of equations which must be solved for the constants C_2 and C_3.

$$C_3 \cdot i + \frac{\beta}{2} + \lambda \cdot (C_3 - C_2) = 0 \tag{2.94}$$

$$(C_2 - C_3) \cdot B + C_2 \cdot \sqrt{i} = 0 \tag{2.95}$$

Equations 2.94 and 2.95 are solved for C_2 and C_3 and the results are substituted into equations 2.91 through 2.93 to obtain the complex temperatures. The imaginary part of the complex temperatures are the dimensionless temperatures which solve the original problem.

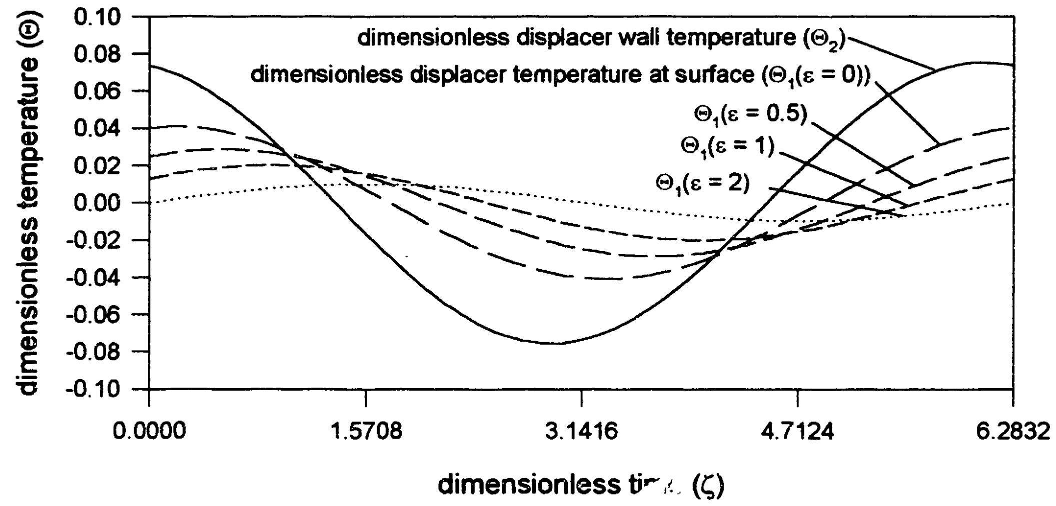

Figure 2-32. Dimensionless temperature variation predicted by shuttle heat transfer model as a function of time for several values of position (B = 1, λ = 1 , β = 0.2)

$$\Theta_1 = \frac{-\beta\cdot B}{\sqrt{2}\cdot F}\exp\left(-\frac{\varepsilon}{2}\right)\left[(\sqrt{2}\cdot B\cdot\lambda-1-\lambda)\sin(\varsigma-\frac{\varepsilon}{\sqrt{2}})-(\sqrt{2}\cdot B+\lambda+1)\cos(\varsigma-\frac{\varepsilon}{\sqrt{2}})\right] \quad \textbf{(2.96)}$$

$$\Theta_2 = \frac{-\beta\cdot B}{2\cdot F}\left[G\cdot\sin(\varsigma)+H\cdot\cos(\varsigma)\right] \quad \textbf{(2.97)}$$

where

$$F=\left[(\sqrt{2}\cdot B\cdot\lambda-1-\lambda)^2+(\sqrt{2}\cdot B+\lambda+1)^2\right]$$

$$G=\left[(\sqrt{2}\cdot B\cdot\lambda-1-\lambda)(\sqrt{2}\cdot B+1)+(\sqrt{2}\cdot B+\lambda+1)\right]$$

$$H=\left[(\sqrt{2}\cdot B\cdot\lambda-1-\lambda)-(\sqrt{2}\cdot B+\lambda+1)(\sqrt{2}\cdot B+1)\right]$$

The resulting dimensionless temperature variation of the displacer wall and the displacer at several values of dimensionless position is illustrated in Figure 2-32. The oscillations are largest in the displacer wall and decay as you approach the center of the displacer where the temperature is linear.

The shuttle heat transfer predicted by equation 2.74 is made dimensionless by comparing it with a convective heat transfer from the displacer to the displacer wall based on the same reference temperature difference.

$$\alpha \equiv \frac{Q_{shuttle}\cdot\omega}{U\cdot\pi\cdot D_{dis}\cdot L_{dis}\cdot(T_H-T_C)}=\frac{\beta}{2\cdot\lambda}\cdot\int_0^{2\cdot\pi}\Theta_2(\varsigma)\cdot\sin(\varsigma)\cdot d\varsigma \quad \textbf{(2.98)}$$

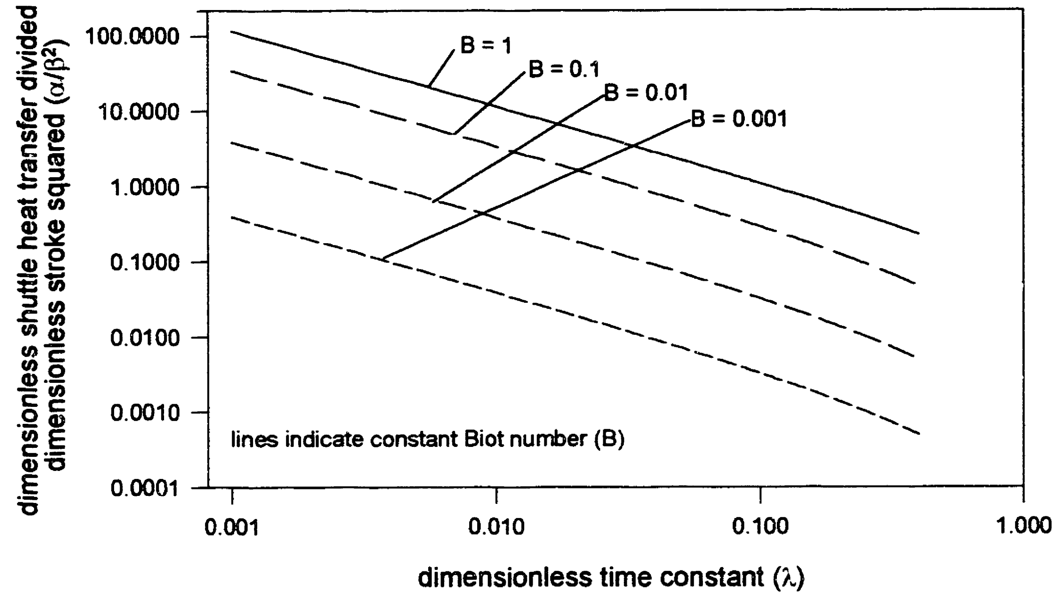

Figure 2-33. Dimensionless shuttle heat transfer divided by stroke squared as a function of the dimensionless time constant for several values of the Biot number

The solution for the displacer wall temperature obtained in equation 2.97 is substituted into equation 2.98 and integrated to yield an analytic expression for the dimensionless shuttle heat transfer.

$$\alpha = \frac{\beta^2 \cdot \left[\left(\sqrt{2}\cdot B\cdot\lambda - 1 - \lambda\right)\left(\sqrt{2}\cdot B + 1\right) + \left(\sqrt{2}\cdot B + \lambda + 1\right)\right]\cdot\pi}{4\cdot\lambda\cdot\left[\left(\sqrt{2}\cdot B\cdot\lambda - 1 - \lambda\right)^2 + \left(\sqrt{2}\cdot B + \lambda + 1\right)^2\right]} \tag{2.99}$$

Equation 2.99 indicates that the dimensionless shuttle heat transfer scales like the stroke squared. Figure 2-33 illustrates the dimensionless shuttle heat transfer divided by the stroke squared as a function of the dimensionless time constant for various values of the Biot number.

The shuttle heat transfer analysis of the displacer used in the experimental apparatus is carried out by dimensionalizing the results of the model explained above. The length and diameter of the displacer are restricted by geometric constraints ($L_{dis} \approx 1.27$ m and $D_{dis} =$ 1.25 inch). The stroke is obtained by determining the volume required by the helium mass at refrigeration temperature and low pressure. The resulting dimensionless stroke is given below.

$$\beta = \frac{4\cdot M_h}{\rho_h(4.2K, 3atm)\cdot\pi\cdot D_{dis}^2\cdot L_{dis}} \approx 0.07 \tag{2.100}$$

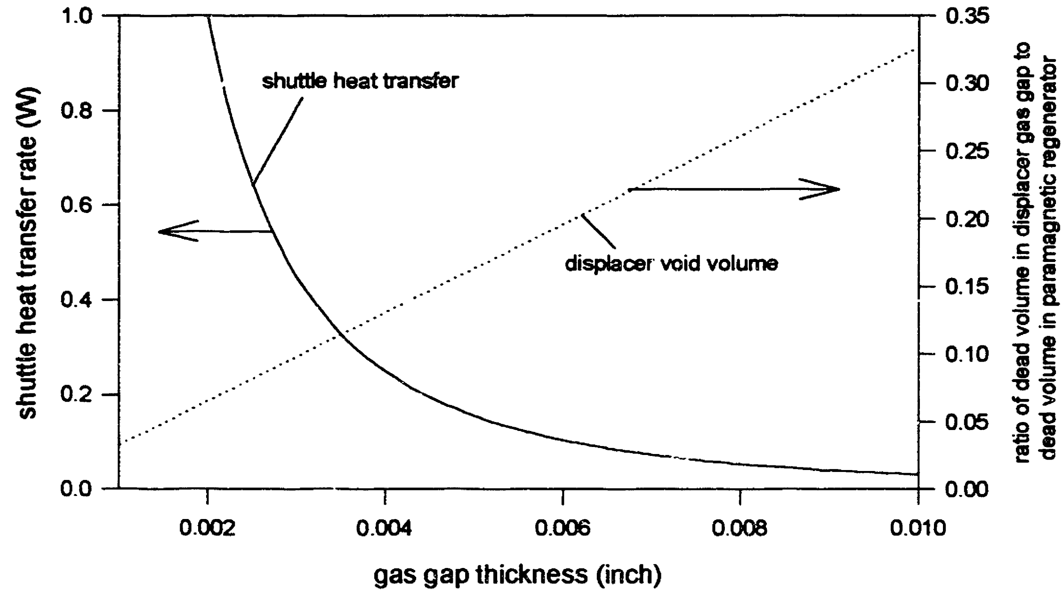

Figure 2-34 Shuttle heat transfer and displacer dead volume as a function of gas gap thickness for the design constraints

The heat transfer coefficient between the displacer and the displacer wall is approximated as a simple conduction resistance through the gas gap of thickness (δ_{gg}) which separates the two surfaces. The frequency of oscillation is dictated by the magnet time constant ($\omega = \pi/\tau$) and the temperature difference is from room temperature to the refrigeration temperature. The thickness of the displacer wall is taken to be 0.065 inch, since this is a standard tube size which is easy to weld and can be held in round over the required length. Using these constraints, the Biot number and dimensionless time constant are expressed as functions only of the gas gap thickness.

$$B = \frac{k_h}{\delta_{gg}\cdot k_{ph}}\cdot\sqrt{\frac{\alpha_{ph}}{\omega}} \approx \frac{0.0008}{\delta_{gg}} \quad \text{where } \delta_{gg} \text{ [inch]} \qquad \textbf{(2.101)}$$

$$\lambda = \frac{k_h}{\delta_{gg}\cdot\rho_{ss}\cdot c_{ss}\cdot\delta_2\cdot\omega} \approx \frac{0.002}{\delta_{gg}} \quad \text{where } \delta_{gg} \text{ [inch]} \qquad \textbf{(2.102)}$$

The shuttle heat transfer rate is obtained by dimensionalizing equation 2.99.

$$Q_{shuttle} = \alpha\cdot\frac{k_h\cdot L_{dis}\cdot\pi\cdot D_{dis}\cdot\left(T_H - T_C\right)}{\delta_{gg}} \approx \frac{50\cdot\alpha}{\delta_{gg}} \quad \text{where } \delta_{gg} \text{ [inch]} \qquad \textbf{(2.103)}$$

This function is illustrated in Figure 2-34 as a function of the gas gap thickness. As the gas gap thickness is increased, the wall is more effectively insulated from the displacer and the shuttle heat transfer losses become less significant. Also illustrated in Figure 2-34 is the

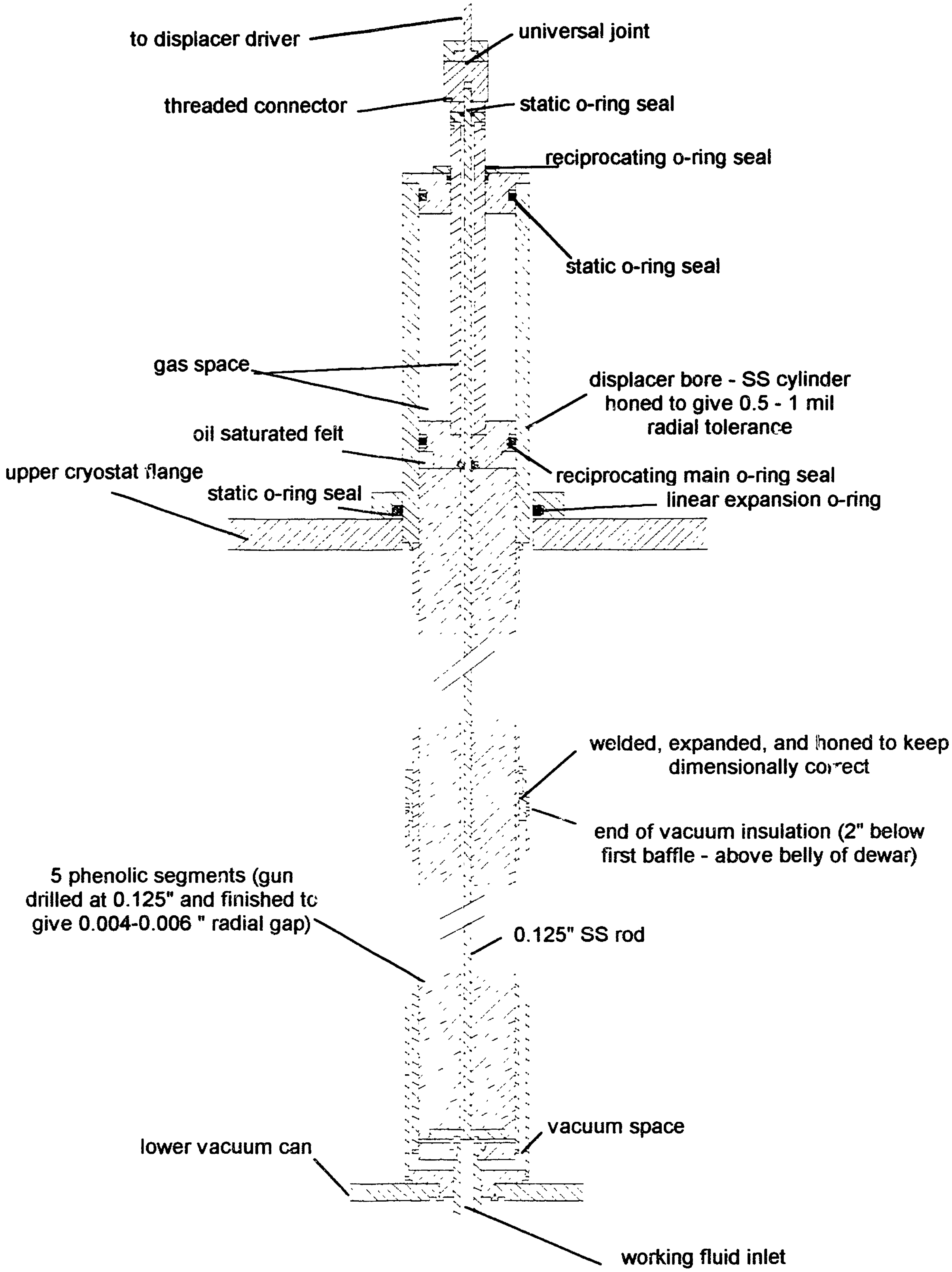

Figure 2-35. Displacer drawing

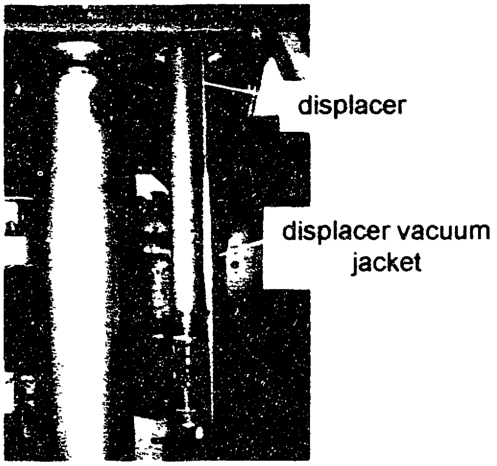

Figure 2-36. Displacer picture

ratio of the dead volume associated with the gas gap in the displacer (nearly all of the gas gap will be 'active' since the cycle time is so long) to the dead volume in the regenerator. A gas gap of approximately 5 mils is chosen since that reduces both the shuttle heat transfer loss and the dead volume to a reasonable level. This gas gap is also achievable using machine tools available and should preclude any rubbing at the cold end.

The articulated displacer consists of five segments. Each segment is a solid piece of spirally wrapped linen based phenolic approximately a foot long. A 0.125 inch hole is gun drilled down the center of the phenolic piece. The displacer segment is then finished on the lathe to achieve a uniform 5 mil gap relative to the displacer tube. A small (10-20 mil) nub is machined onto the center of the ends of the phenolic pieces in order to allow some bending between adjacent pieces so that the overall displacer can conform to the tube.

The displacer is vacuum insulated from the bottom almost all of the way to the warm end. The displacer tube protrudes from the top of the cryostat flange through an o-ring seal to allow for contraction during cool down. The displacer is sealed at the warm end with a sliding o-ring seal. The seal is made to a honed piece of thick wall (one half inch) stainless stell tube. The entire displacer assembly can be removed from the apparatus. The space above the displacer seal is connected to the working fluid inlet conduit. A drawing of the displacer is shown in Figure 2-35. Figure 2-36 illustrates a photograph of the displacer tube in relation to the rest of the experimental apparatus. Table 2-8 lists some of the important characteristics of the displacer.

2.3.6 Current leads

This subsection describes the design model used to analyze the current leads. The general design model is described and then applied to the situation corresponding to the experimental apparatus.

Table 2-8. Characteristics of the displacer

Parameter description	Symbol	Value	Units
length	L_{dis}	1.27	m
diameter	d_{dis}	1.25	inch
gas gap thickness	δ_{gg}	0.005	inch
dimensionless time constant	λ	0.4	-
stroke	S	0.09	m
Biot number	B	0.16	-
shuttle heat transfer rate	$Q_{shuttle}$	0.18	W
dead volume	$V_{dead,dis}$	5e-6	m^3

The current leads which connect the superconducting magnet to the power supply must be able to carry up to 100 amps of current from room temperature to liquid helium temperature. The leads each run through a separate conduit and are convectively cooled with helium vapor vented from the liquid helium pool cooling the magnet. The design of these leads primarily involves balancing the conductive heat leak through the high conductivity leads with resistive heating.

The governing differential equation for the magnet leads are obtained by considering a differential energy balance on the lead (designated with subscript l) and the coolant (designated with subscript c). The axial coordinate is taken to be zero at the magnet and run towards the warm end. The resistivity (ρ_e) and thermal conductivity (k) are very strong functions of temperature. Since these material properties are related to the primary effects being studied, the temperature dependence cannot be neglected in this analysis.

$$\frac{4 \cdot I^2 \cdot \rho_e(T)}{\pi \cdot N_{ml} \cdot D_{ml}^2} = -\frac{d}{dx}\left[k(T) \cdot \frac{\pi \cdot N_{ml} \cdot D_{ml}^2}{4} \cdot \frac{dT_l}{dx}\right] + U \cdot \pi \cdot N_{ml} \cdot D_{ml} \cdot (T_l - T_c) \qquad \textbf{(2.104)}$$

$$m_{c,ml} \cdot c_p \cdot \frac{dT_c}{dx} + U \cdot \pi \cdot N_{ml} \cdot D_{ml} \cdot (T_c - T_l) = 0 \qquad \textbf{(2.105)}$$

The heat transfer rate from the magnet lead into the liquid helium pool is purely conductive.

$$Q_{ml} = k(T_C) \cdot \frac{\pi \cdot N_{ml} \cdot D_{ml}^2}{4} \cdot \left.\frac{dT_l}{dx}\right|_{x=0} \qquad \textbf{(2.106)}$$

The boundary conditions for the problem are associated with the temperature of the magnet lead at the cold and warm ends, and the temperature of the coolant entering the conduit from the liquid helium pool.

$$T_l(0) = T_{LHe} \qquad \textbf{(2.107)}$$

$$T_l(L) = T_{rm} \tag{2.108}$$

$$T_c(0) = T_{LHe} \tag{2.109}$$

This problem can be made dimensionless using the definitions shown below.

$$\text{dimensionless thermal conductivity } \bar{k} \equiv \frac{k(T)}{k(T_H)} \tag{2.110}$$

$$\text{dimensionless electrical resistivity } \bar{\rho}_e \equiv \frac{\rho_e(T)}{\rho_e(T_H)} \tag{2.111}$$

$$\text{dimensionless position } \varepsilon \equiv \frac{x}{L} \tag{2.112}$$

$$\text{dimensionless temperature } \Theta \equiv \frac{T - T_L}{T_H - T_L} \tag{2.113}$$

$$\text{number of transfer units } NTU \equiv \frac{U \cdot N_{ml} \cdot \pi \cdot D_{ml} \cdot L}{m_{c,ml} \cdot c_P} \tag{2.114}$$

$$\text{ratio of generation to conduction } \beta \equiv \frac{I^2 \cdot \rho_e(T_H) \cdot L^2}{\left(\frac{N_{ml} \cdot \pi \cdot D_{ml}^2}{4}\right)^2 \cdot k(T_H) \cdot (T_H - T_C)} \tag{2.115}$$

$$\text{ratio of convection to conduction } \chi \equiv \frac{4 \cdot m_{c,ml} \cdot c_P \cdot L}{k(T_H) \cdot N_{ml} \cdot \pi \cdot D_{ml}^2} \tag{2.116}$$

The dimensionless problem statement is shown below.

$$\beta \cdot \bar{\rho}_e(\Theta_l) = -\frac{d}{dx}\left[\bar{k}(\Theta_l) \cdot \frac{d\Theta_l}{dx}\right] + \chi \cdot NTU \cdot (\Theta_l - \Theta_c) \tag{2.117}$$

$$\frac{d\Theta_c}{dx} + NTU \cdot (\Theta_c - \Theta_l) = 0 \tag{2.118}$$

$$\Theta_l(0) = 0 \tag{2.119}$$

$$\Theta_l(1) = 1 \tag{2.120}$$

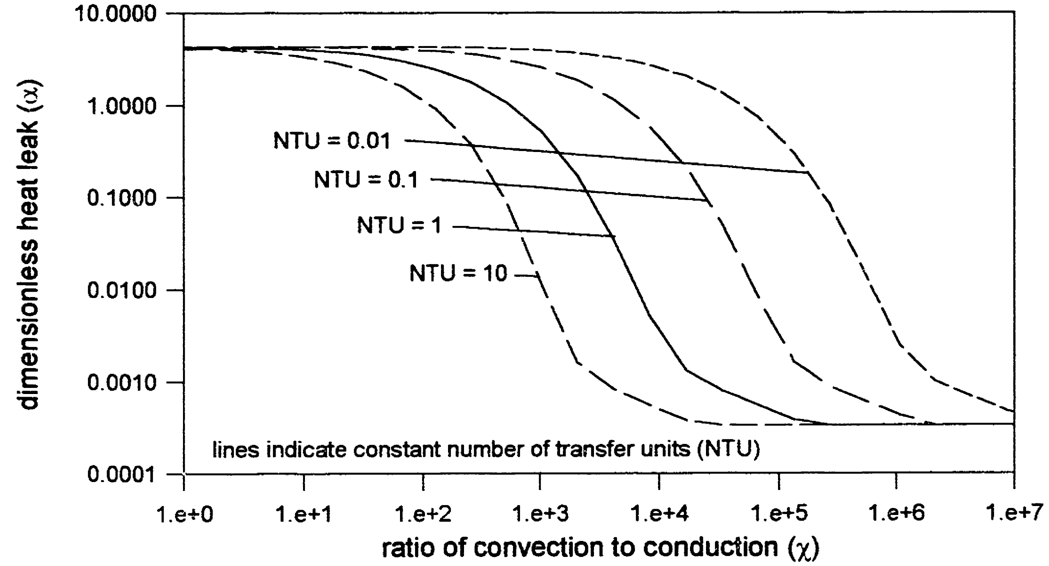

Figure 2-37. Dimensionless magnet lead heat leak as a function of the ratio of convection to conduction for several values of the number of transfer units (β=1)

$$\Theta_c(0) = 0 \tag{2.121}$$

The heat leak is made dimensionless by comparing it with a reference generation rate.

$$\alpha \equiv \frac{Q_{ml}}{\dfrac{I^2 \cdot \bar{\rho}_e(T_H) \cdot 4 \cdot L}{N_{ml} \cdot \pi \cdot D_{ml}^2}} = \frac{\bar{k}(0) \cdot \left.\dfrac{d\Theta_l}{d\varepsilon}\right|_{\varepsilon=0}}{\beta} \tag{2.122}$$

The dimensionless electrical resistivity is simulated using a linear fit for copper resistivity between room temperature and liquid helium temperatures. The thermal conductivity is related to the electrical resistivity by the Weidemann-Franz-Lorenz Law [61].

$$\frac{\bar{k}(\Theta_l) \cdot \bar{r}(\Theta_l)}{\Theta_l} = \text{constant} \tag{2.123}$$

The problem is solved by dividing the second order ordinary differential equation for the lead temperature into two first order equations. The resulting three first order differential equations are stepped from the cold end to the warm end. The warm end boundary condition is met using a shooting technique which varies the first derivative of the lead temperature at the cold end. The code used to affect this solution is listed in appendix A.4.1. Figure 2-37 illustrates the dimensionless heat leak as a function of the ratio of convection to conduction for several values of the number of transfer units with the ratio of generation to conduction set to unity. The heat leak is decreasing in both number of transfer units and ratio of convection to conduction. Changing the ratio of generation to conduction changes the level of these curves but does not affect their qualitative shape.

The magnet leads associated with the experimental apparatus are further constrained. The boil-off from the liquid helium pool which fills the dewar is generated due to heat leaks through the structural supports (Q_{str}), heat leaks through the magnet leads (Q_{ml}), and generation due to imperfect magnet windings (Q_{gen}). The boil-off can only leave the dewar through the coolant side of the upper stage regenerator/heat exchanger device or through the magnet lead conduits. An energy balance on the dewar yields an additional constraint which must be satisfied.

$$h_{fg,h} \cdot \left(m_{c,us} + m_{c,ml}\right) = Q_{ml} + Q_{str} + Q_{gen} \qquad \textbf{(2.124)}$$

The most important design parameter associated with the convectively cooled leads is the diameter. The length of the magnet leads is specified by the geometry of the dewar (L_{ml} = 0.75 m). A reasonable heat transfer coefficient is assumed (U = 100 W/m^{2}K). Once a magnet lead diameter (D_{ml}) is specified, all of the dimensionless characteristics of the magnet leads become functions only of the mass flow rate of coolant. Therefore, equation 2.124 can be thought of as an implicit equation which specifies the mass flow rate of coolant for a given magnet lead diameter since the heat leak into the liquid helium pool can be calculated for a given diameter and mass flow rate of coolant. When equation 2.124 is satisfied, the conditions associated with the given magnet lead diameter have been determined. The results of this calculation include the overall heat leak into the dewar and the total liquid helium boil-off rate, which is directly related to the amount of time available for a set of experimental runs. Figure 2-38 illustrates the total magnet heat leak as a

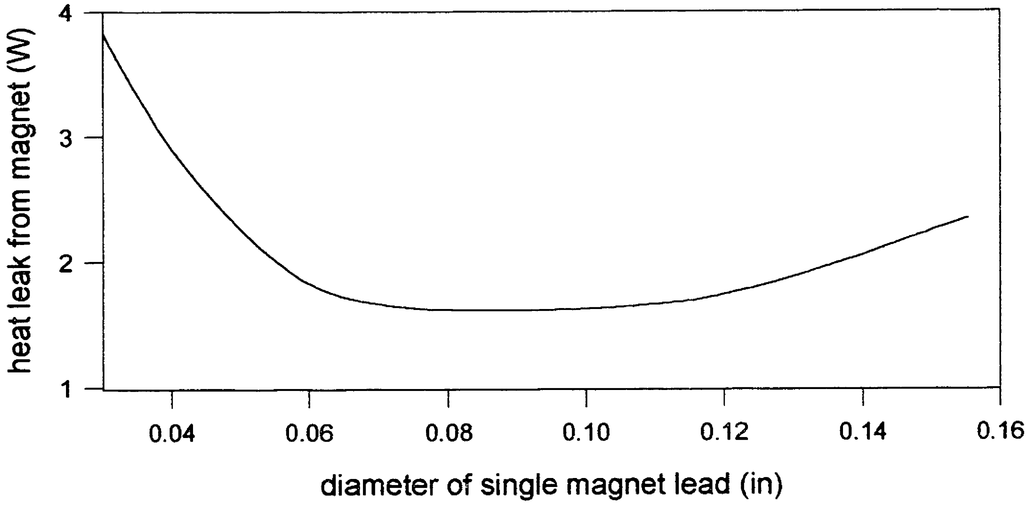

Figure 2-38. Magnet heat leak as a function of magnet lead diameter

Table 2-9. Characteristics of magnet leads

Parameter description	Symbol	Value	Units
heat transfer coefficient	U	100	W/m^2K
length	L_{ml}	0.75	m
current	I	100	amp
diameter of magnet leads	D_{ml}	0.065	inch
heat leak through magnet leads	Q_{ml}	1.7	watt
mass flow rate in magnet lead conduits	$m_{c,ml}$	0.1	g/s
liquid helium boil-off rate	VF_{LHe}	15	L/hr
capacity of belly of dewar	V_{dewar}	10	L
approximate run time	τ_{rim}	36	minutes

function of the diameter of the leads. At very low diameters, the resistive heating becomes large and at very large diameters the conduction heat leak becomes large. The additional code required to perform the design iteration associated with equation 2.124 is listed in appendix A.4.2.

Copper wire of diameter of 65 mils was chosen for the magnet leads based on Figure 2-38. The wire runs through phenolic flow conduits with valves at the cryostat flange which can be used to regulate the flow of coolant. A type T thermocouple was mounted at the warm end of each magnet lead in order to ensure that the temperature did not exceed safe levels.

Some of the most important characteristics of the magnet leads are listed in Table 2-9. The liquid helium consumption associated with this design coupled with the capacity of the dewar to store liquid helium above the magnet yields a run time of nearly 36 minutes for the experiment.

2.4 Instrumentation of Experimental Apparatus

This section describes how the experimental apparatus is instrumented for data acquisition. The section is divided into three subsections. The first subsection describes how temperature is measured. The second subsection describes how pressure measurements are obtained. The final subsection describes the system used to acquire data.

2.4.1 Temperature instrumentation

This subsection describes how temperature measurements are made throughout the experimental apparatus. The subsection is divided into two parts corresponding to the two types of temperature sensors used. The first part describes the carbon resistor sensors which are used in the magnetic stage of the device. The second subsection describes the thermocouples used in the warmer portions of the device.

2.4.1.1 Allen Bradley resistors

The temperature sensors used in the magnetic stage of the experimental apparatus have to be sensitive at temperatures below 15 K. They also have to be insensitive to magnetic fields, since they are mounted within the bore of the superconducting magnet. Carbon resistors are cheap and have both of the characteristics described above [62].

Several 47 ohm Allen Bradley carbon resistors were obtained and individually calibrated. Before calibration, the resistors were thermally cycled in order to eliminate any hysteresis and make future temperature measurements repeatable [63]. The calibration was accomplished by mounting the resistors on an OHFC copper block. The temperature of the block was nearly uniform due to the high conductivity and could be measured precisely using pre-calibrated silicon diodes. The temperature of the block was varied from liquid helium temperature at atmospheric pressure (4.2 K) to room temperature (300 K) by moving it up and down inside the neck of a liquid helium dewar.

Resistance measurements were made using four wire readings. Two of the wires were used to excite individual resistors with 10 micro amps of direct current. The other two wires measured the voltage across the resistors. The voltage was amplified with a DC amplifier and read with a voltmeter. The polarity of the excitation current was reversed at each temperature level in order to eliminate any thermal voltages.

A typical resistance vs temperature curve for an Allen Bradley resistor is illustrated in Figure 2-39. Rather than fit a mathematical function to the entire temperature region, it is more convenient to fit a distinct function for each of three regions. The high temperature region goes from approximately 17 K (depending on the resistor) to 100 K. Above 100 K, carbon resistors are not sensitive enough to give any useful information. A simple polynomial of the form shown below was used for the high temperature region.

$$T = \sum_{i=-2}^{2} a_i \cdot R^i \tag{2.125}$$

The mid range of temperatures spans liquid helium temperature to approximately 17 K. A slightly more complex polynomical is used in this region.

$$T = \sum_{i=-3}^{2} b_i \cdot R^i \tag{2.126}$$

Below liquid helium temperature no measurements were taken during the calibration. However, in a previous PhD project at the Cryogenics Lab, several 47 ohm Allen Bradley resistors were calibrated from 4.2 K to 1.8 K by pumping on liquid helium [64]. When the data associated with these calibrations is normalized by dividing the resistance with the resistance of the same sensor at 4.2 K, it is observed that the resistance-temperature curves collapse to a single curve. The function shown below was fit to this normalized data.

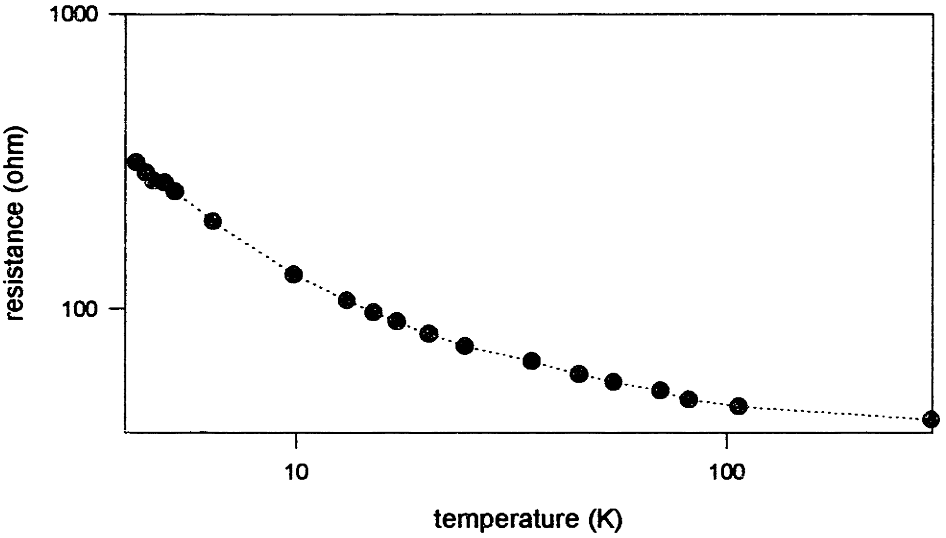

Figure 2-39. Resistance as a function of temperature for a typical AB 47 ohm resistor

$$T = \frac{1}{0.2363392 + 0.40868312 \cdot \log(R/R|_{4.23K}) + 0.064788889 \cdot \left(\log(R/R|_{4.23K})\right)^2} \tag{2.127}$$

Figure 2-40 illustrates this low temperature extrapolation curve and also indicates the standard deviation of the reported calibrations at each temperature level.

The sensitivity (S) of the carbon resistors is defined below.

$$S \equiv \frac{dR}{dT} \tag{2.128}$$

The sensitivity is obtained by implicitly differentiating each of the three curve fits described above. Figure 2-41 illustrates the sensitivity of a typical carbon resistor as a function of temperature. The sensitivity becomes very small at temperatures above approximately 15 K, indicating that the resistor is unsuitable for making precise temperature measurements at these temperatures.

The resistors are all mounted in the apparatus with four leads. Two of the leads are used for the excitation current, which is provided by a 10 microamp current source. The remaining two leads are used to measure the voltage across the resistor. The voltage is read by a 16 bit Acro 900 data acquisition card with an internal amplifier. The uncertainty in the temperature measurement can be attributed to uncertainty in the resistance measurement.

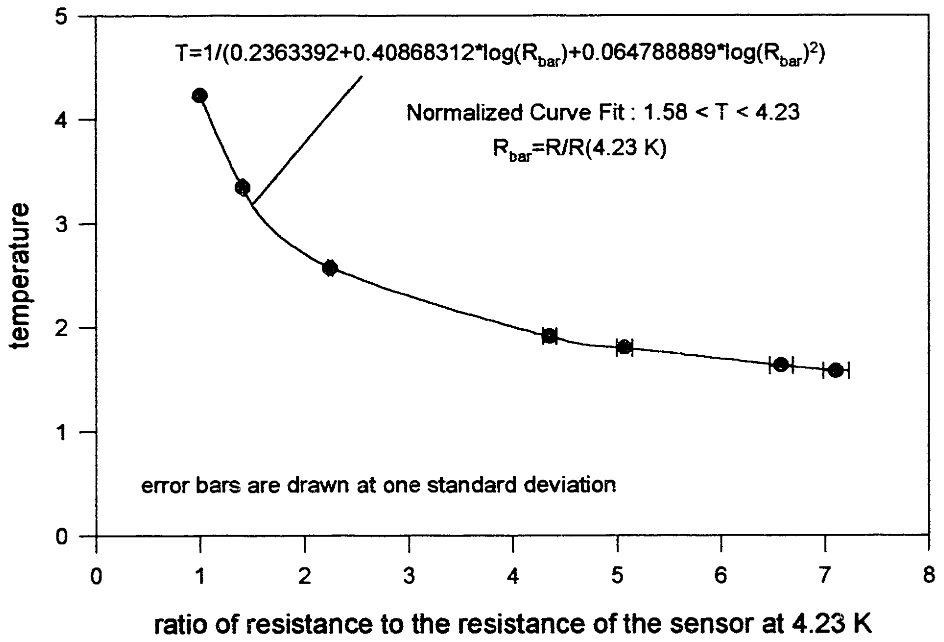

Figure 2-40. Low temperature extrapolation based on reported calibrations

$$\Delta T = \frac{\Delta R}{S} \tag{2.129}$$

The error in the resistance measurement may be attributed to either uncertainty in the voltage measurement or uncertainty in the excitation current [65].

$$\frac{\Delta R}{R} = \sqrt{\left|\frac{\Delta V}{V}\right|^2 + \left|\frac{\Delta I}{I}\right|^2} \tag{2.130}$$

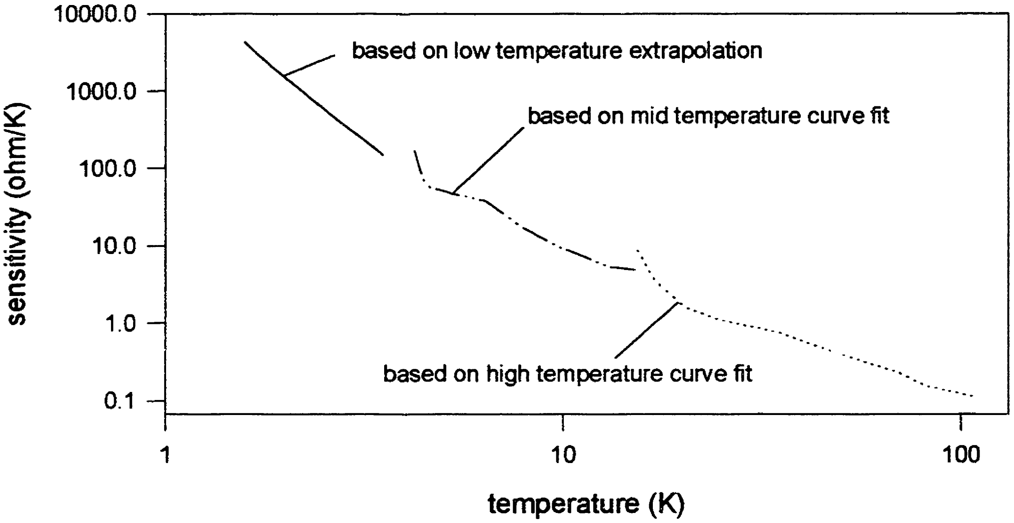

Figure 2-41. Sensitivity of a typical carbon resistor

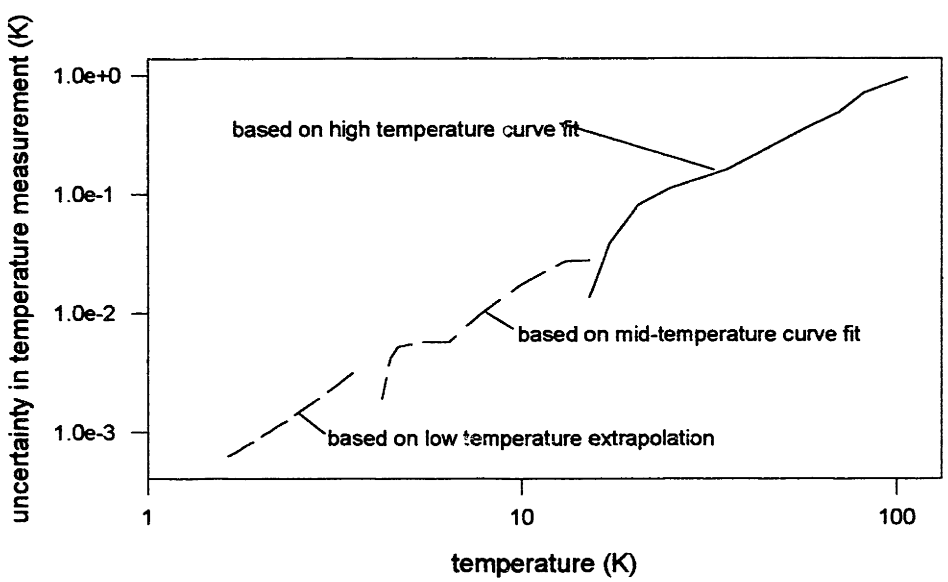

Figure 2-42. Estimated uncertainty in temperature measurement made with a typical carbon resistor as a function of temperature

Combining equations 2.129 and 2.130 leads to an estimate for the temperature error.

$$\Delta T = \frac{R}{S} \cdot \sqrt{\left|\frac{\Delta V}{V}\right|^2 + \left|\frac{\Delta I}{I}\right|^2} \qquad \textbf{(2.131)}$$

The uncertainty in the voltage measurement is estimated based on the resolution of the A/D converter and the uncertainty in the excitation current is obtained from the manual for the current source. The resulting estimate of the error in a temperature measurement as a function of temperature is illustrated in Figure 2-42 for a typical carbon resistor. The uncertainty in a temperature measurement made below 20 K is less than 20 mK and below 10 K is less than 10 mK.

The carbon resistors are mounted in the magnetic stage of the device. The positions of the resistors and the numbers which are subsequently used to refer to individual resistors are illustrated in Figure 2-43. The resistors are wired with 38 guage teflon insulated copper wire. The four wires for each resistor are wound together to create one wire braid. The wire braid is wrapped several times around the resistor to prevent temperature errors due to thermal gradients within the leads. Also, the main mode of thermal equilibration of the resistors is through the leads.

The resistors at the warm end (above and below the phenolic plug) and the cold end (above and below the heat exchanger) are mounted with epoxy in small divits in the phenolic piece. The resistors along the axis of the paramagnetic regenerator are mounted within a phenolic rod. A picture of the axial resistor array is shown in Figure 2-44.

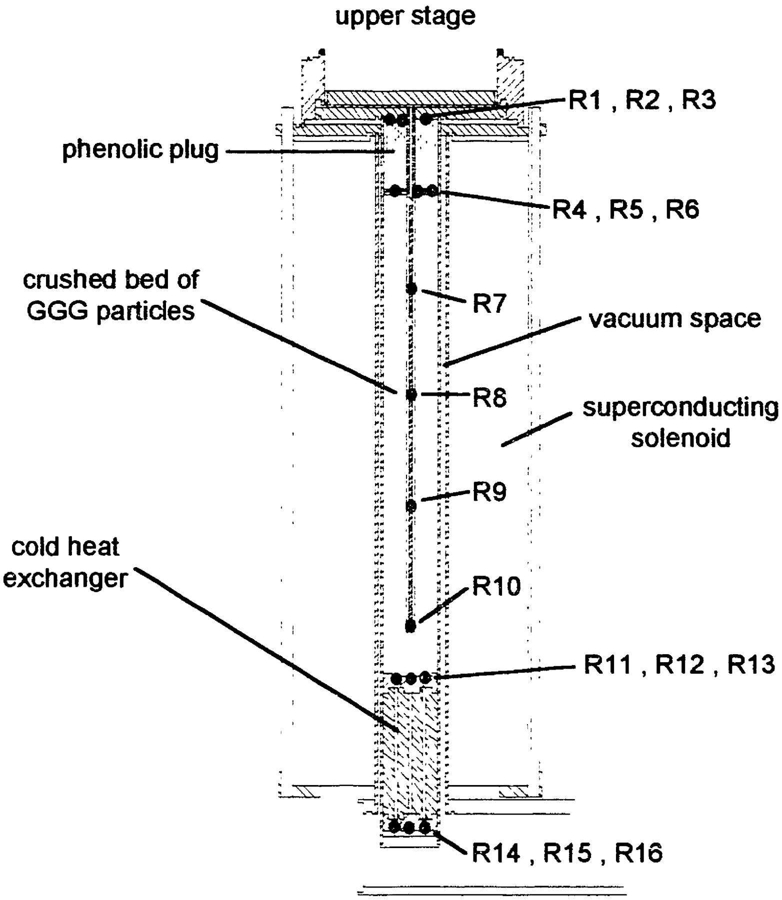

Figure 2-43. Positions of carbon resistors in magnetic stage

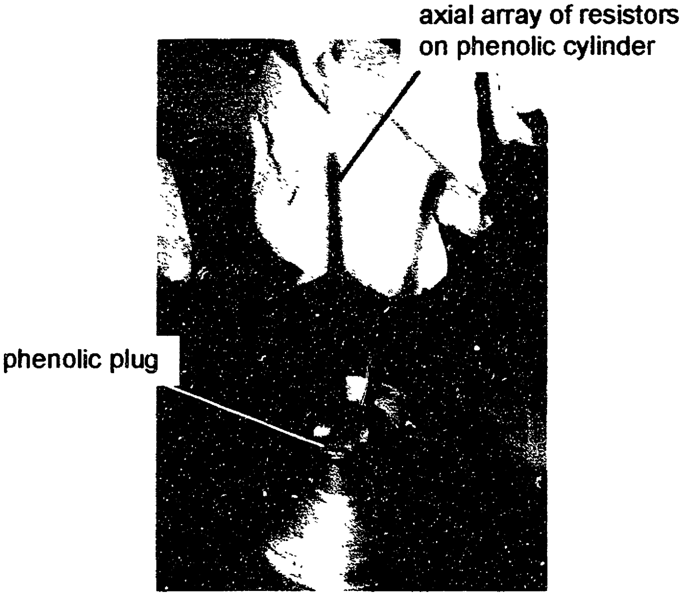

Figure 2-44. Axial array of resistors

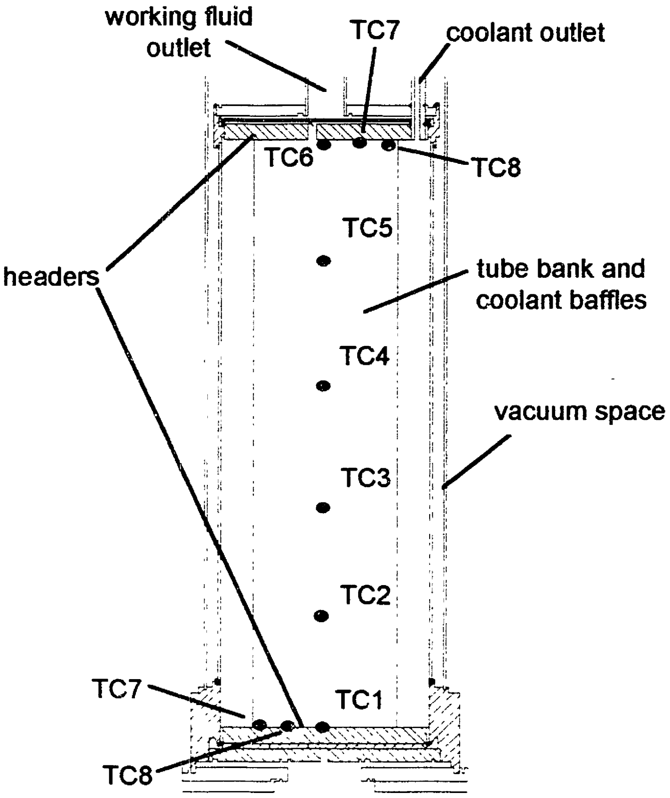

Figure 2-45. Positions of thermocouples in upper stage

Four or fewer resistors at approximately the same temperature level can be wired in series and excited with a 10 microamp current source. The excitation current is very small in order to prevent self-heating of the resistor sensors. Two current sources are used during the experimental runs. The polarity of the current sources is alternated to prevent errors due to thermal voltages.

2.4.1.2 Thermocouples

Temperatures in the upper stage are measured with type E thermocouples. The thermocouple wire is 36 guage teflon insulated. The locations of the various thermocouples in the upper stage regenerator/heat exchanger are illustrated in Figure 2-45. Thermocouples at the same axial location are positioned to obtain a radial temperature profile. The thermocouples are mounted by running them into a stainless steel upper stage tube to the desired location and subsequently packing the lead spheres around the junctions. The temperatures associated with the thermocouple sensors are measured using a cold junction compensated Acro 900 data acquisition card.

2.4.2 Pressure Instrumentation

This section describes the construction of the pressure taps used to measure the pressure at two locations in the device. The pressure taps must be designed carefully, particularly in the cold space because significant losses can occur as flow oscillates into and out of the pressure tap due to the pressurization of the void volume associated with the device. Reducing the void volume tends to lead to measurement errors associated with attenuation and phase lag between the pressure at the cold end (which is the pressure of interest) and the pressure at the warm end (which is where the pressure is actually measured). A good pressure tap will balance these effects. A simple model of the flow conditions in the pressure tap is presented and then used to design the pressure taps for the experimental apparatus.

The pressure tap is a conduit of some arbitrary shape which allows pressure variations in the working space of the experimental apparatus to be communicated to room temperature pressure sensors. The pressure taps extend from approximately liquid helium temperature to room temperature. This model assumes that the temperature of the wall of the conduit varies linearly and that the thermal communication between the wall and the gas is perfect so that the gas temperature also varies linearly in space. This assumption is justified by the small hydraulic diameter of any reasonable channel. The temperature profile is given below (x measures distance from the cold end).

$$T(x) = T_C + \frac{(T_H - T_C) \cdot x}{L} \tag{2.132}$$

The gas in the conduit is assumed to behave as an ideal gas (with ideal gas constant R) and the pressure at the cold end is assumed to vary sinusoidally. This is the pressure that is to be measured at the warm end.

$$P(0,t) = P_L + \frac{(P_H - P_L)}{2} \cdot \left[1 - \cos\left(\frac{\pi \cdot t}{\tau} \right) \right] \tag{2.133}$$

It is also assumed that there is no void volume in the room temperature pressure sensor (i.e. the mass flow rate must go to zero at x = L). A continuity equation on a differential piece of the conduit (where the mass flow rate is taken to be positive towards the warm end) is shown below.

$$\frac{\partial m}{\partial x} + A_c \cdot \frac{\partial \rho}{\partial t} = 0 \tag{2.134}$$

The ideal gas law is substituted into equation 2.134.

$$\frac{\partial m}{\partial x} + \frac{A_c}{R \cdot T} \cdot \frac{\partial P}{\partial t} = 0 \tag{2.135}$$

It is assumed that the momentum equation reduces to a balance between wall friction and pressure forces (i.e. all unsteady momentum effects are neglected). It is also assumed that the flow is fully developed and laminar. The friction factor for a circular pipe with the same hydraulic diameter is used.

$$f = \frac{64}{\mathrm{Re}_{Dh}} \tag{2.136}$$

After some manipulation, the momentum equation is shown below (where pe represents the wetted perimeter of the conduit).

$$\frac{\partial P}{\partial x} = -\frac{2 \cdot m \cdot pe^2 \cdot \mu \cdot R \cdot T}{P \cdot A_c^3} \tag{2.137}$$

There are three quantities which are of interest in the design of the pressure tap. From a measurement standpoint, the attenuation and phase shift of the pressure variation measured at the warm end of the conduit relative to the actual pressure variation at the cold end are important.

$$\text{attenuation}: \alpha \equiv \frac{\max[P(L,t)] - \min[P(L,t)]}{P_H - P_L} \tag{2.138}$$

$$\text{phase lag}: \phi \equiv \frac{t_{max}}{\tau} \cdot \pi \text{ where } P(t_{max}, L) = \max[P(L,t)] \tag{2.139}$$

From a cycle performance standpoint, the entropy flux into the apparatus due to mass flowing into and out of the conduit is important, especially for the cold end pressure tap. This entropy flux directly reduces the total amount of entropy which is pumped up the temperature scale through the paramagnetic regenerator and therefore diminishes the performance of the cycle.

The lost refrigeration associated with the pressure tap (Q_{loss}) is proportional to the entropy flux and the temperature level of the pressure tap.

$$\text{lost refrigeration}: Q_{loss} = -\frac{T_C}{\tau} \cdot \int_0^{2 \cdot \tau} m(0,t) \cdot s(P(0,t), T_C) \cdot dt \tag{2.140}$$

The problem can be made dimensionless by defining the following parameters.

$$\text{dimensionless time}: \varsigma \equiv \frac{t}{\tau} \tag{2.141}$$

$$\text{dimensionless position}: \varepsilon \equiv \frac{x}{L} \tag{2.142}$$

$$\text{dimensionless pressure : } \Pi \equiv \frac{P}{P_L} \tag{2.143}$$

$$\text{dimensionless temperature : } \Theta \equiv \frac{T}{T_C} \tag{2.144}$$

$$\text{dimensionless pressure variation : } \Delta\Pi \equiv \frac{P_H - P_L}{P_L} \tag{2.145}$$

$$\text{dimensionless tempeature variation : } \Delta\Theta \equiv \frac{T_H - T_C}{T_C} \tag{2.146}$$

$$\text{dimensionless mass flow rate : } \sigma \equiv \frac{m \cdot R \cdot T_C \cdot \tau}{A_c \cdot L \cdot P_L} \tag{2.147}$$

$$\text{ratio of mass storage to friction effects : } \lambda \equiv \frac{2 \cdot pe^2 \cdot \mu \cdot L^2}{A_c^2 \cdot \tau \cdot P_L} \tag{2.148}$$

The dimensionless problem statement is given below.

$$\frac{\partial \Pi}{\partial \varsigma} = -(1 + \varepsilon \cdot \Delta\Theta) \cdot \frac{\partial \sigma}{\partial \varepsilon} \tag{2.149}$$

$$\frac{\partial \Pi}{\partial \varepsilon} = -\lambda \cdot \frac{(1 + \varepsilon \cdot \Delta\Theta)}{\Pi} \cdot \sigma \tag{2.150}$$

$$\sigma(1, \varsigma) = 0 \tag{2.151}$$

$$\Pi(0, \varsigma) = 1 + \frac{\Delta\Pi}{2} \cdot (1 - \cos(\pi \cdot \varsigma)) \tag{2.152}$$

The attenuation and phase lag can be expressed in terms of the dimensionless parameters defined above.

$$\alpha = \frac{\max[\Pi(1, \varsigma)]}{1 + \Delta\Pi} \tag{2.153}$$

$$\phi = \pi \cdot \varsigma_{max} \text{ where } \Pi(\varsigma_{max}, 1) = \max[\Pi(1, \varsigma)] \tag{2.154}$$

The lost refrigeration is made dimensionless as shown below.

$$\text{dimensionless lost refrigeration}: \Omega \equiv \frac{Q_{loss} \cdot \tau}{P_L \cdot A_c \cdot L} = \int_0^{2\pi} \ln[\Pi(0,\varsigma)] \cdot \sigma(0,\varsigma) \cdot d\varsigma \quad (2.155)$$

When equation 2.150 is substituted into equation 2.149, a single second order nonlinear partial differential equation in nondimensional pressure is obtained.

$$\left(\frac{\partial \Pi}{\partial \varepsilon}\right)^2 + \Pi \cdot \frac{\partial^2 \Pi}{\partial \varepsilon^2} - \frac{\Pi \cdot \Delta\Theta}{(1+\varepsilon \cdot \Delta\Theta)} \cdot \frac{\partial \Pi}{\partial \varepsilon} = \lambda \cdot \frac{\partial \Pi}{\partial \varsigma} \quad (2.156)$$

The mass flow boundary condition (equation 2.151) can be expressed in terms of the pressure gradient. The mass flow can be backed out of the pressure variation using equation 2.150. The problem is solved using an implicit technique in space and an explicit technique in time. The linearized, finite difference version of equation 2.156 is put in matrix form and solved for a given time step. The nonlinear coefficients are estimated based on the conditions at the previous time step. This stepping technique in time is continued until a steady state cycle is reached. The code required to solve this problem is listed in appendix A.5.

Figure 2-46 illustrates the dimensionless pressure as a function of time at various values of the axial position for a given set of dimensionless paramaters. The dimensionless mass flow

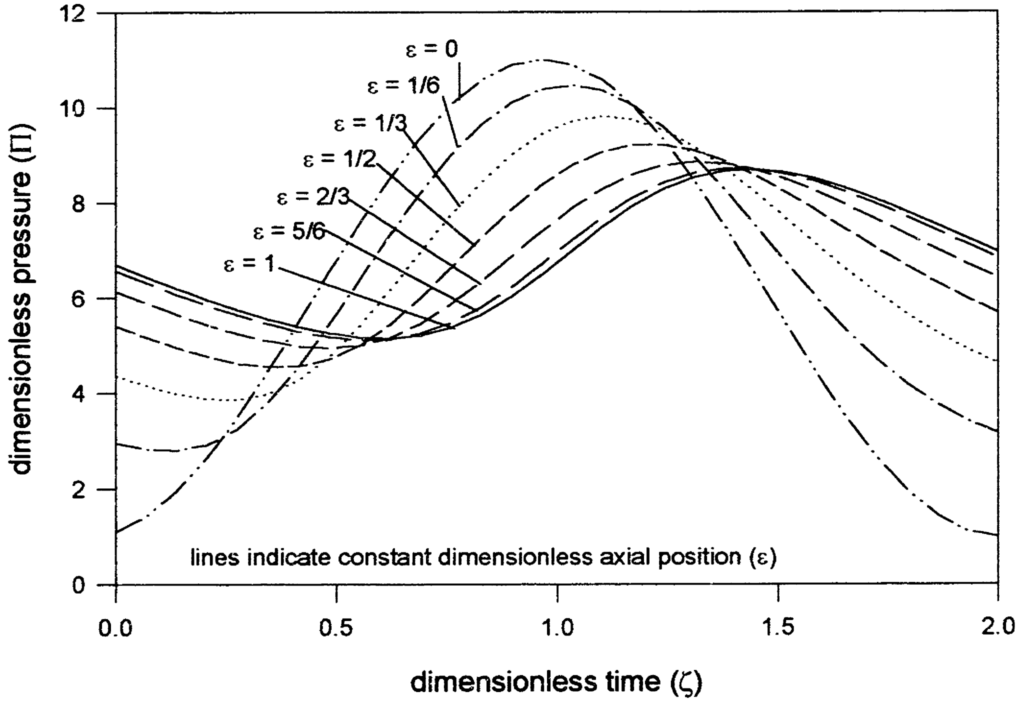

Figure 2-46. Dimensionless pressure as a function of time for several values of dimensionless axial position (λ = 10 , ΔΠ = 10 , ΔΘ = 10)

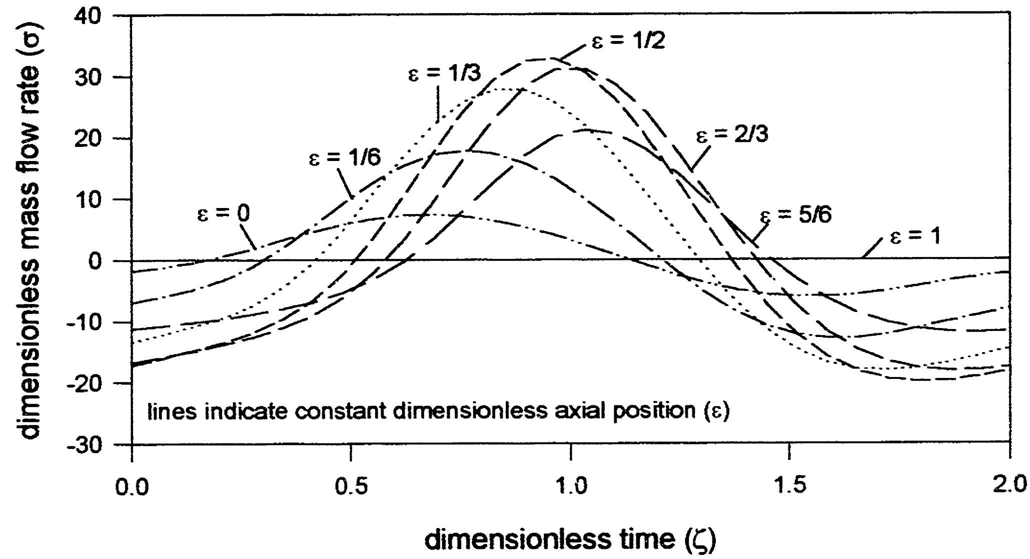

Figure 2-47. Dimensionless mass flow rate as a function of time for several values of dimensionless axial position ($\lambda = 10$, $\Delta\Pi = 10$, $\Delta\Theta = 10$)

rate for the same set of dimensionless conditions is illustrated in Figure 2-47. The lost refrigeration as a function of the ratio of mass storage to friction effects for various values of the dimensionless temperature drop is illustrated in Figures 2-48 for a dimensionless pressure drop of 10. The attenuation is illustrated in Figure 2-49.

The pressure taps used in the experimental apparatus consists of a stainless steel tube of 0.065 inch inner diameter. The void volume associated with the tube is reduced by inserting a stainless steel rod through the tube. The radial gap between the rod and the

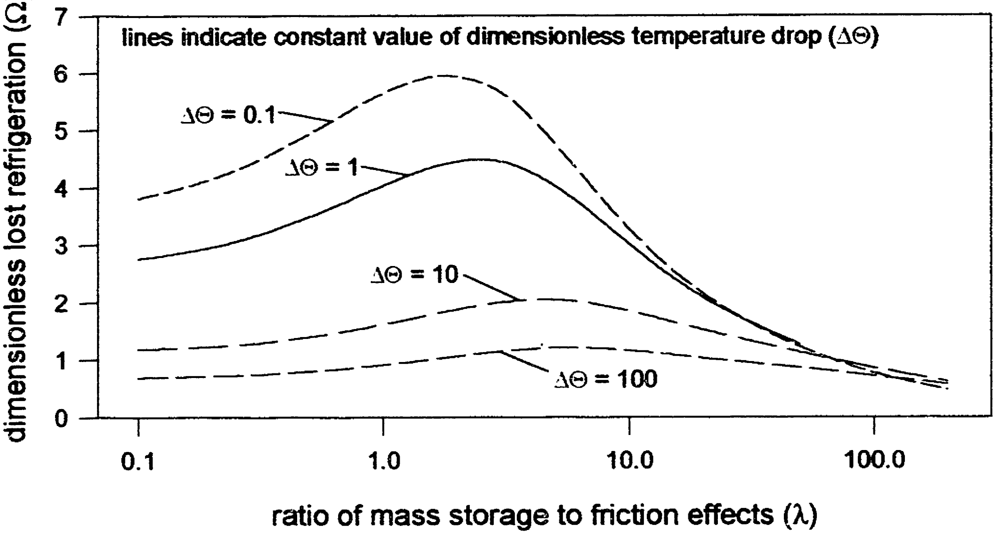

Figure 2-48 Dimensionless lost refrigeration as a function of the ratio of mass storage to friction effects for various values of dimensionless temperature drop ($\Delta\Pi = 10$)

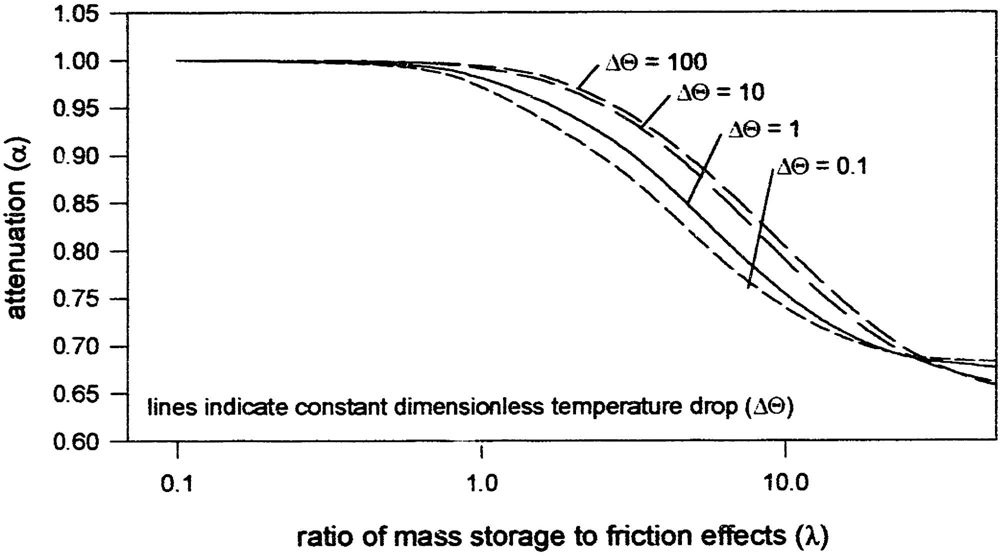

Figure 2-49. Attenuation as a function of the ratio of mass storage to friction effects for various values of dimensionless temperature drop ($\Delta\Pi = 10$)

tube forms the flow conduit of the pressure tap. The main design parameter is the thickness of the radial gap (δ_{pt}) which dictates the diameter of the filler rod to use. The dimensionless pressure difference and temperature drop can be specified from the refrigeration cycle.

$$\Delta\Pi \approx 2 \tag{2.157}$$

$$\Delta\Theta \approx 70 \tag{2.158}$$

The ratio of mass storage to pressure gradient effects can be expressed in terms of the radial gap.

$$\lambda = \frac{8 \cdot \mu_h \cdot L^2}{\delta_{pt}^2 \cdot \tau \cdot P_L} \approx \frac{6e-8}{\delta_{pt}^2} \quad \text{where } \delta_{pt} \text{ [inch]} \tag{2.159}$$

The lost refrigeration can be obtained from the dimensionless lost refrigeration for this set of design constraints.

$$Q_{lost} = \frac{\Omega \cdot P_L \cdot \pi \cdot D_{pt} \cdot \delta_{pt} \cdot L}{\tau} \approx 4 \cdot \Omega \cdot \delta_{pt} \;\; \text{[J/s] where } \delta_{pt} \text{ [inch]} \tag{2.16}$$

The attenuation, phase shift, and lost refrigeration are illustrated in Figure 2-50 as functions of the radial gap. A radial gap of 5 mils is chosen for the experimental apparatus to keep the lost refrigeration at a negligible level and minimize the measurement errors associated with attenuation and phase shift. The room temperature pressure transducers are Omega

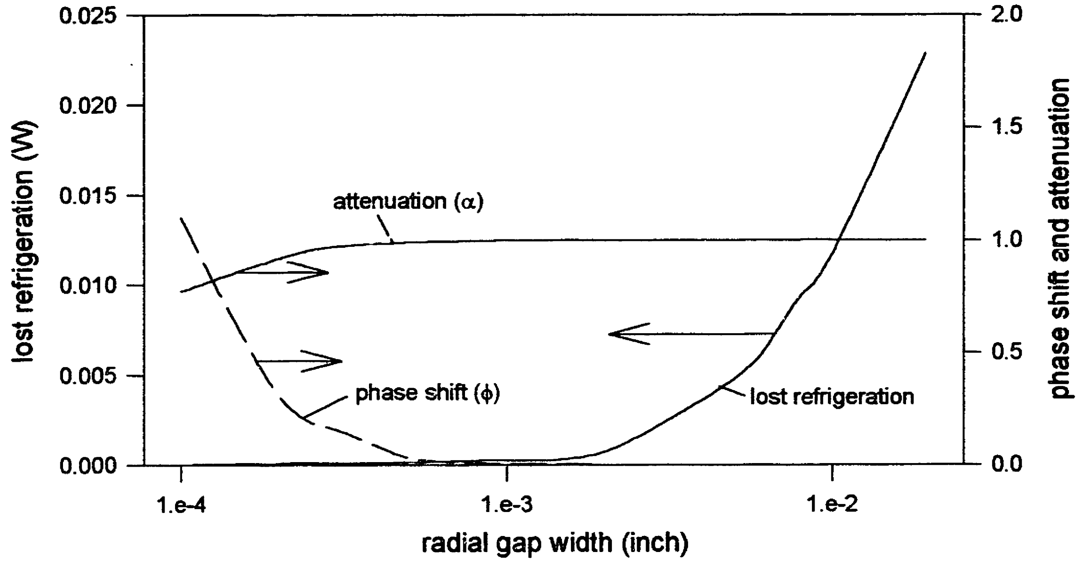

Figure 2-50. Lost refrigeration, phase shift, and attenuation as a function of radial gap for design constraints

PX304 transducers. The approximate time constant for these transducers is 1 millisecond which is on the same order of magnitude as the lag caused by the phase shift for the 0.005 inch radial gap. This time scale is four orders of magnitude less than the time scale of the cycle.

2.4.3 Data acquisition

This subsection describes the data acquisition system used during an experimental run. One of the two Dell 286 computers available for the experiment is designated the data acquisition computer. This computer interfaces with the Acro 900 system through an RS-232 port. The computer is also equipped with an internal data acquisition card. The internal data acquisition card does not have a functional A/D converter due to an accidental current overload. However, the binary inputs and outputs are functional.

The internal data acquisition card binary inputs and outputs are used to recognize user switches to start and stop taking data. They are also used to pick up top-dead-center and bottom-dead-center of the displacer motion. The analog data signals are fed to the Acro system. Three pressure transducers, the magnet current, three thermocouples, and five carbon resistor sensors are read during a typical experimental run. The data is written to a file on the hard drive. Several channels are also graphically represented on the screen to aid in adjusting the cycle parameters.

The system is set up so that the Acro system continuously performs 16 bit A/D conversions and stores the last conversion in a buffer which can be read externally by the computer. In this way, the time between readings performed on the same channel is reduced to approximately 0.25 seconds. This is sufficiently fast relative to the total cycle time. The BASIC program used to run the data acquisition computer is contained in appendix A.6.

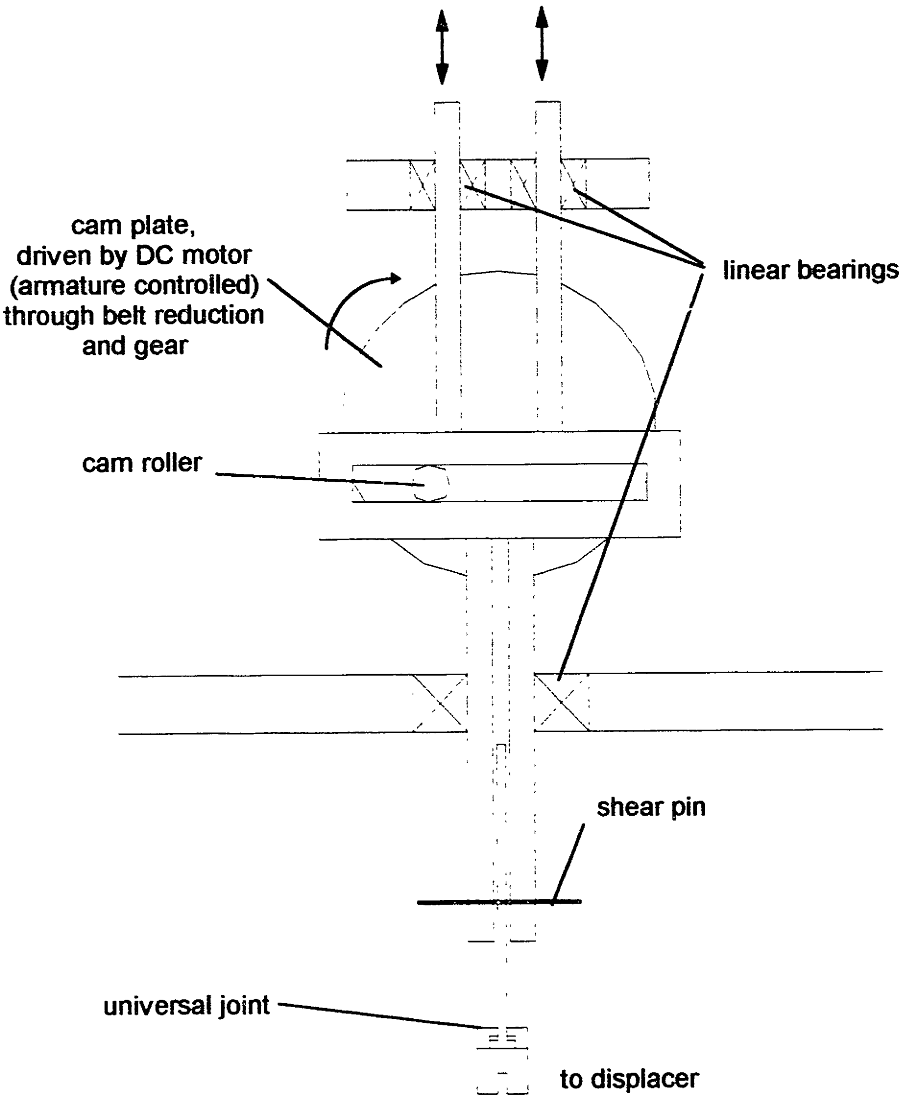

Figure 2-51. Displacer drive mechanism

2.5 Cycle control

This section describes the subsystems associated with controlling the cycle parameters. The section is divided into three parts. The first part describes the mechanical mechanism used to control the displacer motion. This subsystem also sets the overall cycle timing used by the cycle control computer. The second subsection describes the compressor, valves, and related plumbing which is used to control the pressure in the experimental apparatus. The third subsection describes the power supply used to control the current in the solenoid and therefore the applied field in the paramagnetic material. The final subsection describes the computer code used to coordinate these subsystems and the resulting GM/magnetic cycle imposed on the paramagnetic regenerator bed.

2.5.1 Displacer drive mechanism

The displacer is driven by a scotch yoke mechanism powered with an armature controlled DC electric motor. The displacer driver mechanism is illustrated schematically in Figure 2-51. The cam plate is driven by the motor through a v-belt and a double gear box. The speed of rotation is controlled by varying the armature voltage with a variac. Two stationary mechanical switches are mounted at the top and bottom of the cam plate. These switches are tripped by a toggle which is mounted at the same angular position as the cam.

The stroke of the displacer can be varied by changing the radial position of the cam. The position of the shear pin must be changed in order to ensure that when the cam reaches bottom dead center the displacer reaches the bottom of its tube. The angular position of the toggle must also be adjusted to match the new position of the cam. The cam can be mounted at radii ranging from 0.5 inches to 1.75 inches with positions at every quarter inch. This corresponds to displacer strokes ranging from 1 inch to 3.5 inches in half inch increments.

2.5.2 Pressure control

The room temperature compressor used to affect the compression of the helium working fluid is a four stage Ingersoll Rand modified air compressor. The most important components used to interface the compressor with the working space of the experimental apparatus are illustrated in Figure 2-52.

The pressure of the helium entering the compressor is maintained at approximately 3 psig using the compressor inlet pressure regulator. The compressor increases the helium pressure to approximately 1800 psig and expels it through the high pressure check valve (which prevents back flow from the high pressure regulator when the compressor is not operating) into the high pressure reservoir. The helium flows through a cold trap which removes any impurities. The pressure in the high pressure accumulator must be maintained at the high pressure level seen by the cycle. This is accomplished by the high pressure regulator. The high pressure accumulator ensures that the pressure does not change dramatically when the apparatus is pressurized. The compression solenoid opens when the apparatus is to be pressurized. The time constant of the compression process can be controlled with the compression throttle. The expansion solenoid opens when the apparatus is to be de-pressurized. The pressure in the low pressure accumulator is controlled with the low pressure regulator. The low pressure accumulator ensures that the pressure will not change dramatically during the depressurization process.

The compressor is turned on and off using a pressure activated latching circuit. When the pressure in the high pressure reservoir drops to a preset start-up level, the compressor turns on and pumps helium from the low pressure to the high pressure reservoir. This continues until the pressure in the high pressure reservoir reaches a preset shut-down level. This control system operates independently of the experimental apparatus.

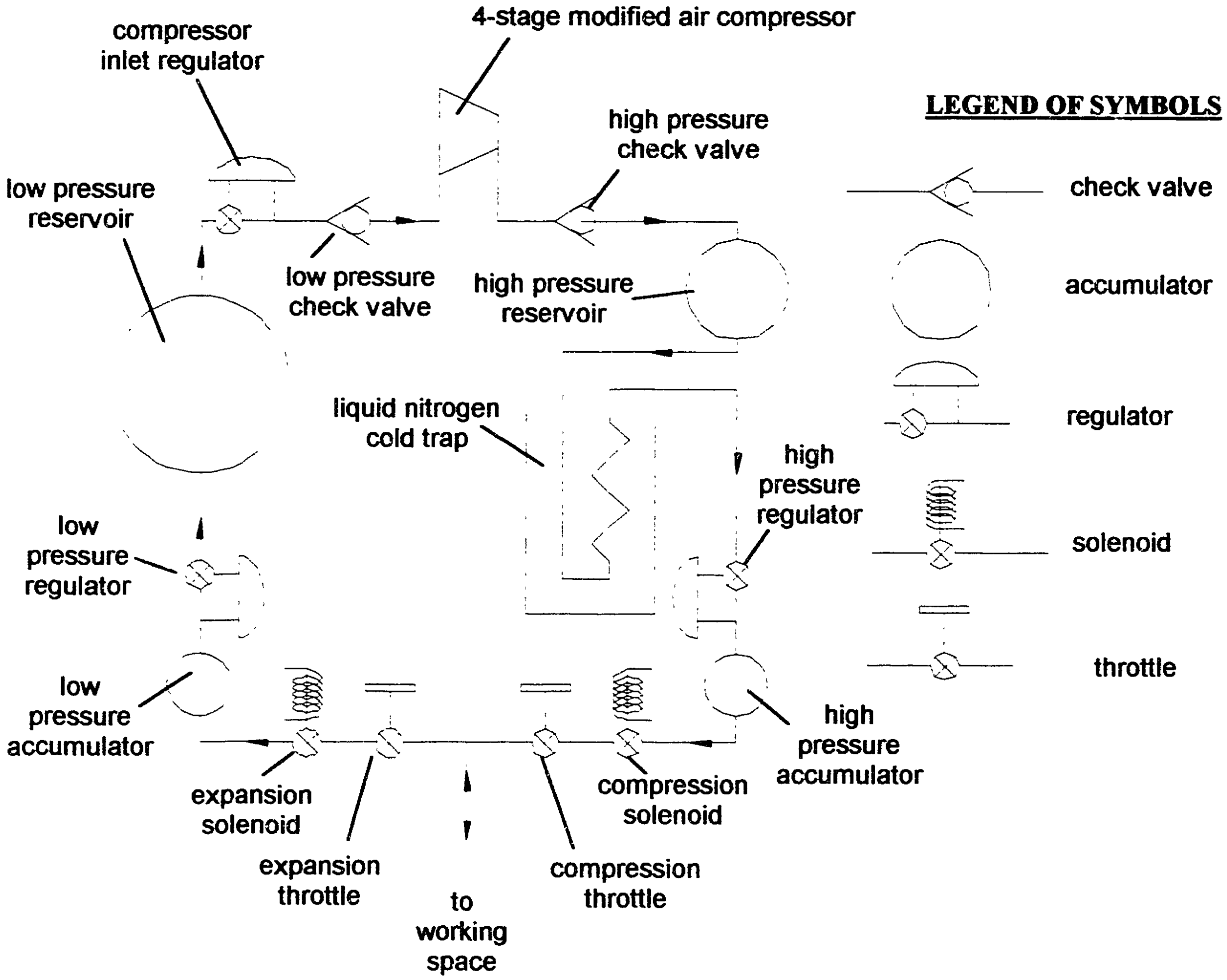

Figure 2-52. Schematic of pressure control system

2.5.3 Magnet power supply

The current in the magnet is controlled using a Lakeshore MPS 622 power supply. This power supply is a true four quadrant direct current power supply. The MPS 622 supplies power to the magnet during the charging process and accepts power from the magnet during the discharging process. This is in contrast to power supplies used in previous magnetic refrigerators which were forced to accomplish the discharging process with a shunt resistor.

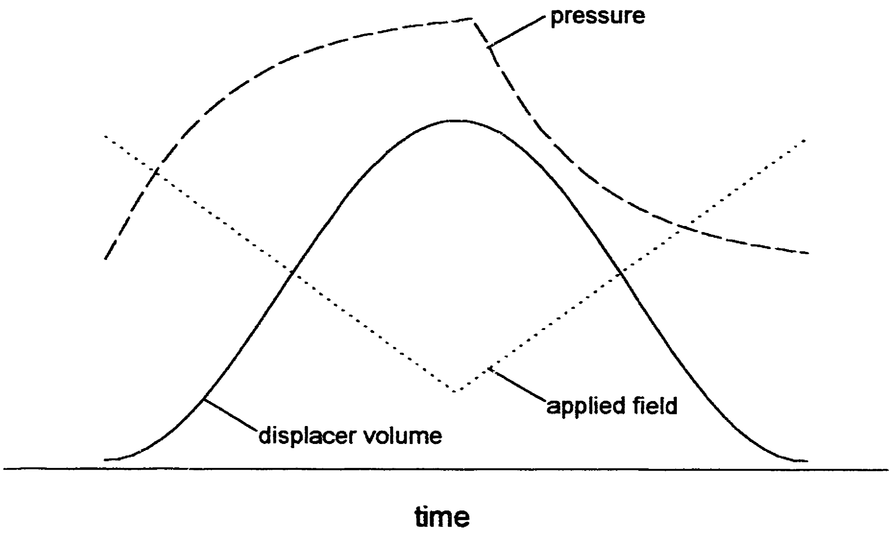

Figure 2-53. Qualitative pressure, displacer volume, and applied field profiles resulting from cycle control system

The four quadrant power supply allows the magnet voltage to be constant causing the current to linearly increase and decrease. The maximum charging rate can be achieved in this way since the magnet voltage can be kept just under the quench voltage. When a shunt resistor is used, the voltage is largest at the start of the discharge process and quickly decreases. Since the initial discharge voltage must be kept below the quench voltage, the voltage throughout the majority of the discharge process is significantly less than the magnet quench voltage and the discharge time is increased.

2.5.4 Total cycle control

The second Dell 286 computer available for the experiment was designated the cycle control computer. This computer interfaces with the MPS 622 system using a RS-232 port. It also has an internal data acquisition card with binary inputs and outputs. The internal card is used to determine when the displacer reaches top-dead-center and bottom-dead-center. At top-dead-center, the expansion solenoid is activated and instructions are sent to the MPS 622 to charge the magnet. At bottom-dead-center, the compression solenoid is activated and instructions are sent to the MPS 622 to discharge the magnet.

The applied field imposed by the magnet starts at 1 Tesla and increases as much as possible (up to 4 Tesla). Therefore, the magnetic field swing is proportional to the total cycle time, which is set by the speed of the displacer driver motor. The pressure levels are controlled by the high and low pressure regulators. The low pressure regulator is typically kept at approximately 35 psig (in order to avoid the two phase region in the experimental apparatus) and the high pressure level is adjusted to achieve the desired pressure ratio. The cold heat exchanger heater voltage (and thus the refrigeration load) is controlled with a separate DC power supply.

The pressure, displacer volume, and magnetic field profiles resulting from this cycle control system are illustrated qualitatively in Figure 2-53. The BASIC program used to affect the cycle control is listed in appendix A.7.

EXPERIMENTAL PROCEDURE AND RESULTS

This chapter describes the procedure used to obtain the experimental results. The data which was collected is also described. This chapter is divided into three sections. The first section describes the general experimental procedure used to operate the experimental apparatus. The second section chronologically lists the experimental runs which were performed and describes the type of data taken during each run. Some general notes regarding problems with equipment and related modifications are also presented. The final section describes the type of data taken and presents some of the raw results.

3.1 Experimental Procedure

This section describes the experimental procedure which is used each time the apparatus is run. The procedure presented here evolved as the author became more familiar with the apparatus.

There are three distinct gas spaces within the experimental apparatus: the working space contains the high pressure helium which is used as the working fluid of the cycle, the dewar space contains the liquid helium used to cool the superconducting magnet, and the vacuum space refers to the evacuated space used to isolate the working space from the dewar space. These spaces are connected through valves to various external equipment including a vacuum pump, a pressurized tank of helium, and the compressor system. The plumbing associated with the experimental apparatus is illustrated schematically in Figure 3-1.

The procedure used to prepare for an experimental run is described below.

Night before experiment

1. The vacuum space and dewar space are evacuated.
2. The working space is filled with helium from the pressurized helium tank. A pressure regulator is used to maintain the pressure at approximately 5 psig despite leakage from the upper stage warm header.
3. The radiation shield of the dewar is filled with liquid nitrogen.
4. The vacuum space is filled with helium gas to a pressure of 1 psig.
5. The dewar space is filled with liquid nitrogen and the vent is opened. The experimental apparatus is allowed to 'thermally soak' overnight to bring it to liquid nitrogen temperature.

Day of experiment

6. The dewar space is purged of liquid nitrogen. This is accomplished by closing the vent and opening the purge valve. The dewar is then pressurized with helium gas to approximately 3 psig, forcing liquid nitrogen through the bottom purge tube.
7. The liquid nitrogen purge heater is turned on for several hours. This ensures that there is no residual liquid nitrogen in the bottom of the dewar space. Liquid nitrogen

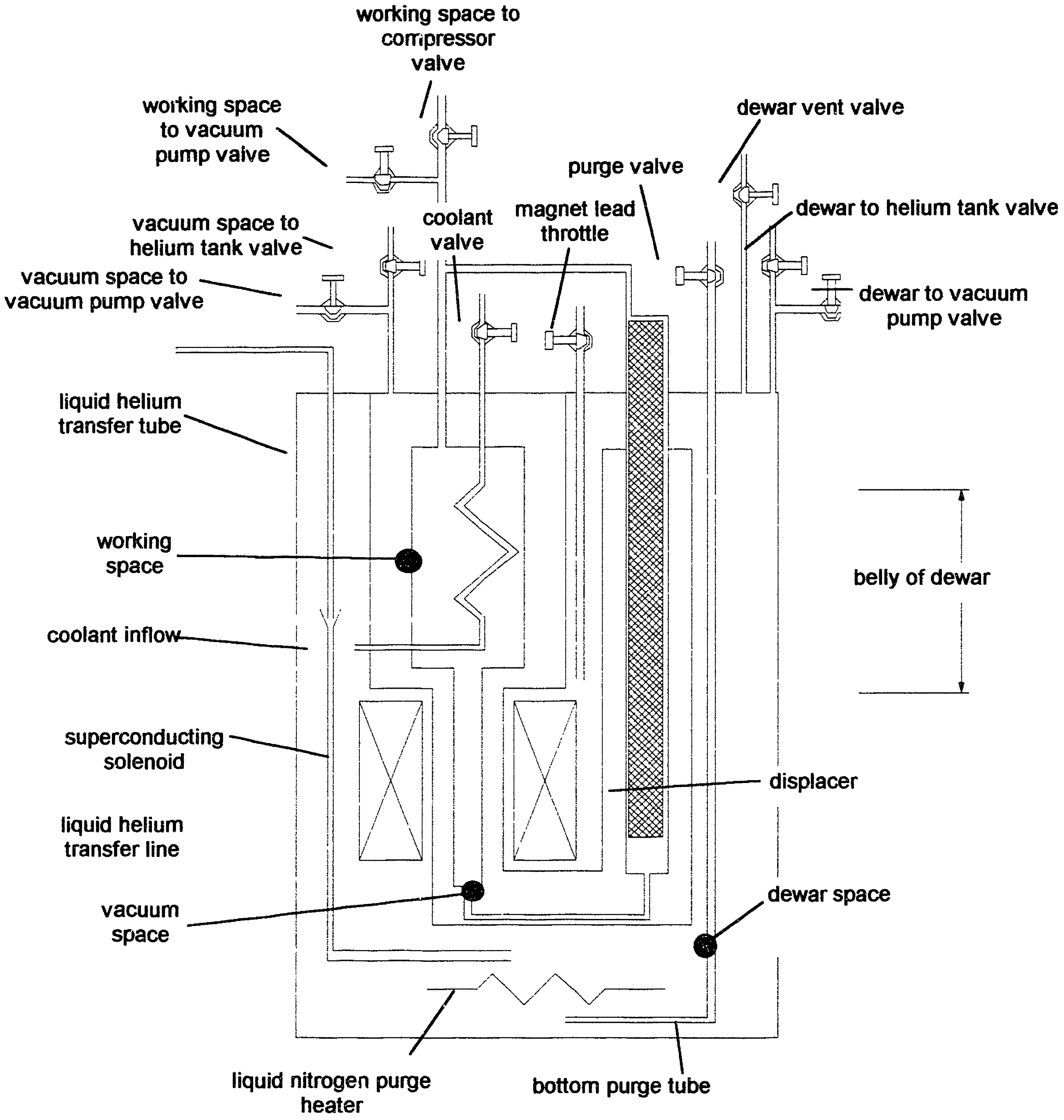

Figure 3-1. Schematic of experimental apparatus plumbing

remaining in the dewar space has a very large heat capacity (both sensible and latent) and greatly increases the amount of liquid helium required to cool down the apparatus.

8. The vacuum space is evacuated to approximately 40 millitorr and closed off. The ultimate vacuum in the vacuum space is less than 3 millitorr due to cryopumping.
9. Liquid helium is slowly transferred to the dewar space. The end of the liquid helium transfer tube which enters the dewar is placed in the liquid helium transfer line. In this way, the liquid helium enters the dewar below the experimental apparatus and more of the sensible heat capacity is used. Typically, about 30 liters of liquid helium are required to bring the temperature of the apparatus below 10 K. The temperature of the experiment can be monitored with two Allen Bradley resistors or by measuring the resistance of the superconducting magnet.
10. The transfer pressure is increased so that liquid helium is transferred more rapidly. The dewar space is filled up to the first radiation shield with liquid helium. The level of the liquid helium in the dewar can be monitored with two separate superconducting level indicators. Typically 30 liters are required to fill the dewar the first time.
11. The lines connecting the compressor to the working space are evacuated and purged repeatedly to ensure that there are no pockets of air which can be sucked into the working space. Any air in the helium will collect in the flow passages of the regenerators, blocking flow. Also, air in the working space can result in freezing of the displacer.

The procedure used to carry out an experimental run is described below.

1. The displacer cam is placed in the position to yield the desired displacer stroke. The shear pin must be adjusted so that the bottom-dead-center position of the driver plate coincides with the bottom of the displacer in the displacer tube. The toggle pin must also be adjusted so that it is at the same angular position as the cam.
2. The voltage to the cold heat exchanger heater is adjusted to yield the desired refrigeration load.
3. The pressure ratio is adjusted using the high pressure regulator.
4. The magnet lead throttle and the coolant valve are opened. All other vents from the dewar space are closed.
5. The displacer drive motor is started and the armature voltage is adjusted until the desired cycle time is achieved.
6. The data acquisition computer is started.
7. The working space is connected to the compressor space.
8. The cycle control computer is started.
9. The time constant of the expansion and compression processes are adjusted with the expansion and compression throttles by observing the pressure variation on the data acquisition computer screen.
10. The flow rate of liquid helium boil-off through the magnet lead conduits is adjusted with the magnet lead throttle. The flow rate should be increased until the temperature at the warm end of the leads reaches a safe level. This temperature is monitored with a pair of type T thermocouples affixed to the magnet lead.

11. The pressure level within the dewar must be monitored. If the pressure exceeds approximately 3 psig then the vent is opened.
12. The apparatus is allowed to run until the temperature variation at the warm and cold ends of the paramagnetic regenerator reach steady state. This is determined qualitatively by examining the temperature variation on the screen of the data acquisition computer. Typically, at least 10 to 15 cycles are required. Several cycles of steady state data are recorded and the files saved. The experimental parameters are changed and the apparatus is allowed to reach a new steady state.
13. Step 12 may be repeated until the belly of the dewar runs out of liquid helium (the liquid helium level is monitored with the superconducting level meter). When the belly of the dewar is empty, the liquid helium level is just above the superconducting magnet and the experiment must be stopped. Typically, this occurs after approximately 4 experimental runs are accomplished which requires 20 minutes of operation. This is somewhat less than the 35 minutes predicted in subsection 2.3.6 because leakage through the upper stage warm header tends to pressurize the dewar space and increase the level of liquid helium consumption.
14. The belly of the dewar is refilled with liquid helium if further experimental runs are required. This requires approximately 20 liters of liquid helium.

3.2 Summary of Experimental Runs and Modifications

This section describes the experimental runs which were achieved with the apparatus. Some of the major experimental obstacles are also described. The experimental apparatus was modified several times in response to various difficulties. These modifications and some general notes regarding the qualitative performance of the device are detailed. The experimental apparatus was cooled down on four separate occasions. On three of these occasions, data was successfully taken. The data taken and problems encountered during these runs are listed chronologically below.

August 1, 1996

The experimental apparatus was precooled to liquid nitrogen temperatures and the liquid nitrogen purged from the dewar space. The device could not be cooled to liquid helium temperatures due to incomplete purging of the liquid nitrogen and the use of a flexible liquid helium transfer tube with a high flow resistance.

As a result of experience gained during this run, a rigid liquid helium transfer tube with a smaller flow resistance was obtained. Also, the liquid nitrogen purge heater described in section 3.1 was installed in the bottom of the dewar to ensure complete purging of the liquid nitrogen.

August 16, 1996

The experimental apparatus was successfully cooled to liquid helium temperatures and the dewar space was filled with liquid helium. The magnet superconducted and all subsystems successfully operated. The device was allowed to cycle for approximately 100 cycles with no refrigeration load, a pressure ratio of 1.75, a displacer stroke of 3.5 inches, and a cycle time of 12 seconds. After approximately 100 cycles, the magnet leads melted at the point where they left the cryostat, causing an open circuit. The resulting current overload damaged the MPS 622 power supply and the data acquisition system. The experimental run had to be terminated.

As a result of the damage sustained during this run the MPS 622 had to be repaired and the data acquisition system had to be modified to more fully utilize the Acro 900 system. The magnet lead conduits were modified to better cool the magnet leads at the warm end. Also, two thermocouples were affixed to the magnet leads in order to monitor their temperature during the experimental run.

September 5, 1996

The experiment was cooled to liquid helium temperatures and the dewar was filled with liquid helium. All systems operated and data was taken for refrigeration loads ranging from 0 to 1 watt and cycle times ranging from 10 to 16 seconds (i.e. applied field swings ranging from 1.2 to 2.6 tesla). Also, the pressure ratio was varied from 1.75 to 2.6. The displacer stroke was maintained at 3.5 inches for all runs.

Examination of the data from this set of runs revealed that some improvement might be realized using smaller displacer strokes and a longer expansion time constant.

September 10, 1996

The experiment was cooled to liquid helium temperatures and the dewar was filled with liquid helium. All systems operated and data was taken for refrigeration loads ranging from 0 to 0.5 watt and displacer strokes ranging from 1 to 2 inch. The pressure ratio was maintained at 2 and the cycle time was maintained at 20 second (applied field change of 3 tesla). The expansion time constant was adjusted to yield a more gentle expansion process.

3.3 Raw Results

This section details the type of data taken directly from the experimental apparatus and describes qualitatively some of the important trends observed in the data. The section is divided into three subsections. The first subsection describes the temperature measurements which were taken within the magnetic stage of the device. The second subsection describes the pressure measurements which were collected. In the third subsection, the temperature measurements associated with the upper stage are detailed.

Some results not reported in this section but used in Chapter 4 are the displacer volume and applied field. The displacer volume is sinusoidal in time. The time at which top-dead-center and bottom-dead-center are reached are recorded for each cycle. This data, together with knowledge of the void volume at bottom-dead-center, is used to infer the displacer volume as a function of time by disregarding any backlash in the displacer drive. The applied field can be measured using a shunt resistor in line with the superconducting magnet together with knowledge of the characteristics of the magnet. More commonly, the applied field is taken to be simply linear between a maximum and minimum value of applied field which is recorded for each cycle.

3.3.1 Temperature of the GGG bed

The temperature of the magnetic stage can be measured in 16 locations as shown in Figure 2-43. All of the resistors were initially examined in order to cross check one another. However, the resistors which were most commonly read during an experimental run are listed below:

resistor R1 : warm end of phenolic plug
resistor R5 : warm end of paramagnetic matrix
resistor R8: near midpoint of paramagnetic matrix
resistor R12 : cold end of paramagnetic matrix
resistor R16 : cold end of cold heat exchanger

The temperature as a function of time at each of the locations listed above is illustrated for a typical cycle in Figure 3-2. The temperature of the helium entering the regenerator during the hot-to-cold blow portion of the cycle (i.e. R1 during the first half) increases dramatically. The regenerative nature of the upper stage device coupled with the fact that the regenerator material at the cold end of the upper stage device has very little heat capacity contributes to this temperature increase. Also, the demagnetization, which tends to decrease the temperature of the magnetic matrix, is not a very strong effect above 10 K since the magneto-caloric effect of the GGG decreases with temperature. The temperatures in the colder regions of the paramagnetic regenerator do not exhibit the same degree of temperature rise because the magnetic effect is much stronger at lower temperature.

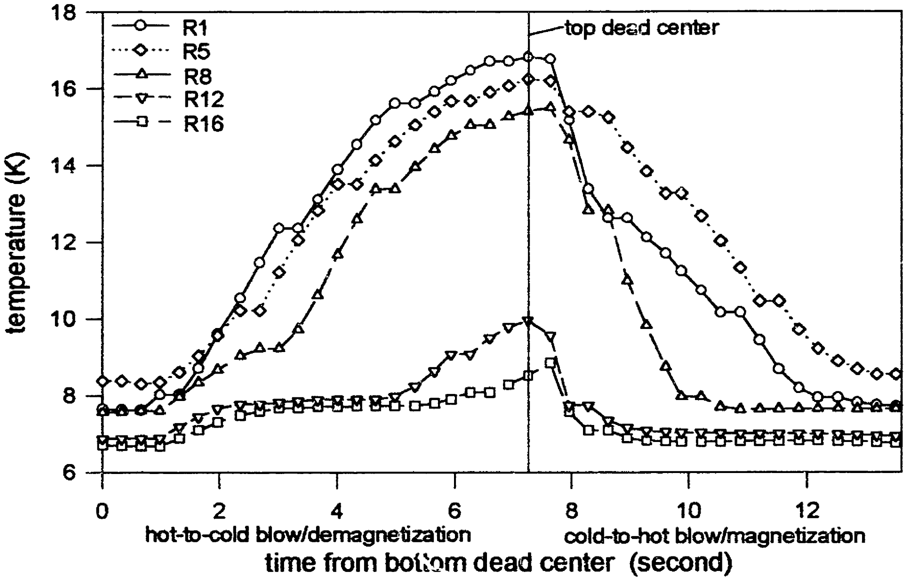

Figure 3-2. Temperature measurements in magnetic stage for a typical cycle (applied field swing = 2.2 Tesla, pressure ratio = 1.75, refrigeration load = 0.25 W, displacer stroke = 3.5 inch)

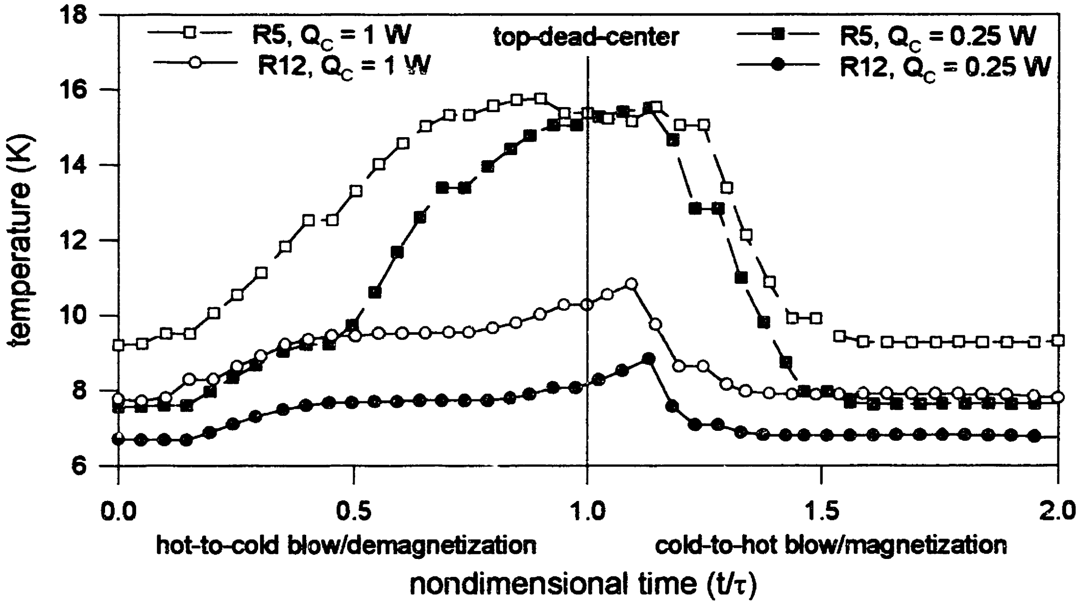

Figure 3-3. Temperature in the magnetic stage for different levels of refrigeration load (applied field swing = 2.2 Tesla , pressure ratio = 1.75 , displacer stroke = 3.5 inch)

The temperature of the fluid entering the warm end of magnetic stage is fairly accurately represented by resistor R1 because this resistor is isolated from the magnetic matrix during the hot-to-cold blow process by the phenolic plug. This temperature is slightly higher than the temperature of the magnetic regenerator at the warm end, which is fairly accurately measured by resistor R5. This temperature difference between the two resistors is exaggerated by the delay in the data acquisition system. The fluid is slightly warmer than the regenerator during the hot-to-cold blow process because the regenerator is absorbing entropy from the fluid. The opposite is true during the cold-to-hot blow portion of the cycle (i.e. the second half). The temperature of the regenerator is slightly higher than the temperature of the fluid leaving the regenerator because the regenerator is rejecting entropy to the fluid.

The parameters which were varied during the experimental runs include the magnetic field swing, pressure ratio, refrigeration load, and displacer stroke. Figure 3-3 shows the temperature at the hot and cold ends of the magnetic regenerator bed for two different values of refrigeration load with all other parameters held constant. The time is nondimensionalized with respect to the half cycle time in order to display temperatures at the same point in the cycle at the same location on the x-axis and allow easier comparison between cycles. Figure 3-3 shows that increasing the level of refrigeration tends to raise the temperature level in the magnetic regenerator, particularly at the low end. At the warm end the temperature level increases, but not as much since the temperature at the warm end is constrained more by the upper stage operation than the conditions in the magnetic regenerator. The upper stage operation is affected by the level of refrigeration, but this is a small effect relative to other processes.

It is difficult to separate the effect of changing the refrigeration load from significant secondary effects which are caused by changing this parameter. The most important secondary effect is

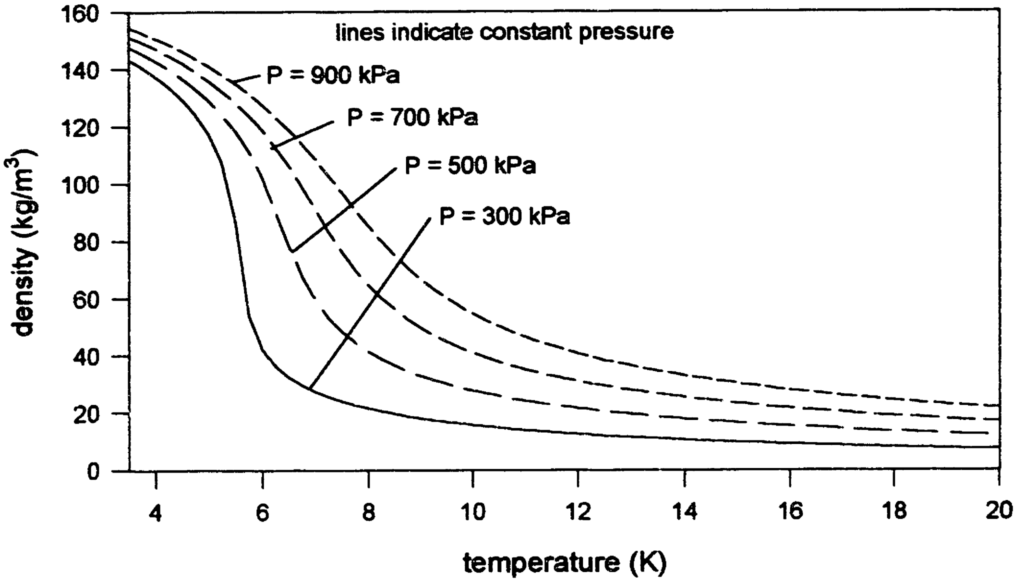

Figure 3-4. Density of helium as a function of temperature for several different pressure levels

changing the mass ratio of the device. Increasing the refrigeration load tends to increase the refrigeration temperature of the device. This, in turn, tends to decrease the mass of helium which is pulled through the magnetic regenerator during the hot-to-cold blow process because the swept volume of the displacer is held constant and the density of helium is decreasing rapidly. The density of helium as a function of temperature for several levels of pressure is illustrated in Figure 3-4. This decreasing mass ratio tends to make the regenerator operate more effectively, as the

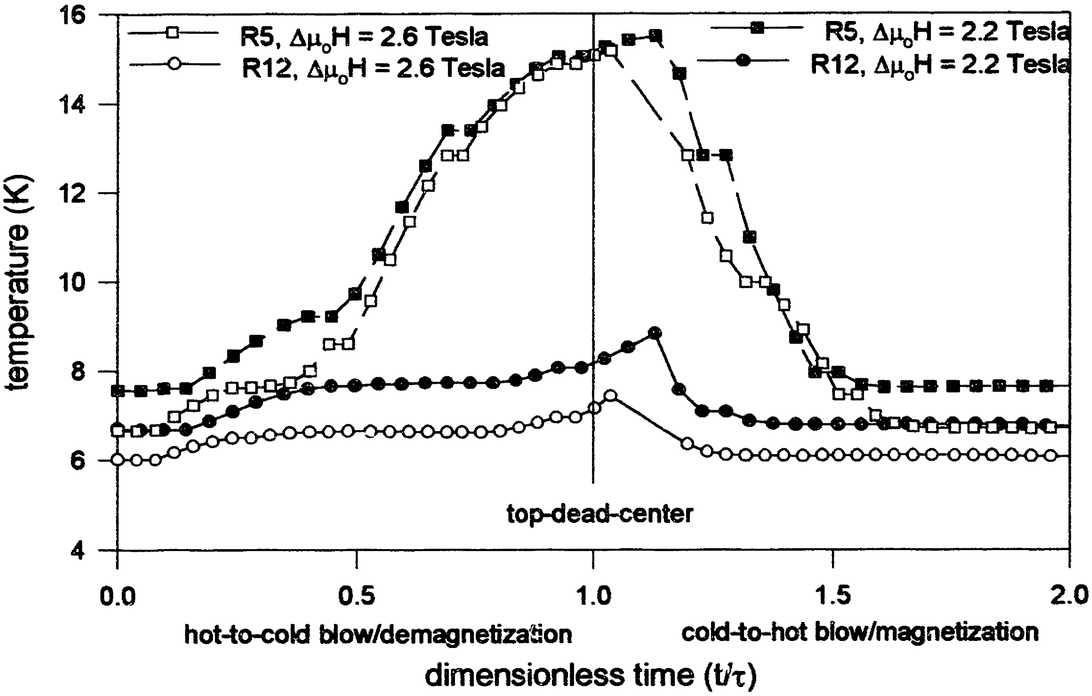

Figure 3-5. Temperature of magnetic bed for different levels of applied field swing (refrigeration load = 0.25 watt , pressure ratio = 1.75 , displacer stroke = 3.5 inch)

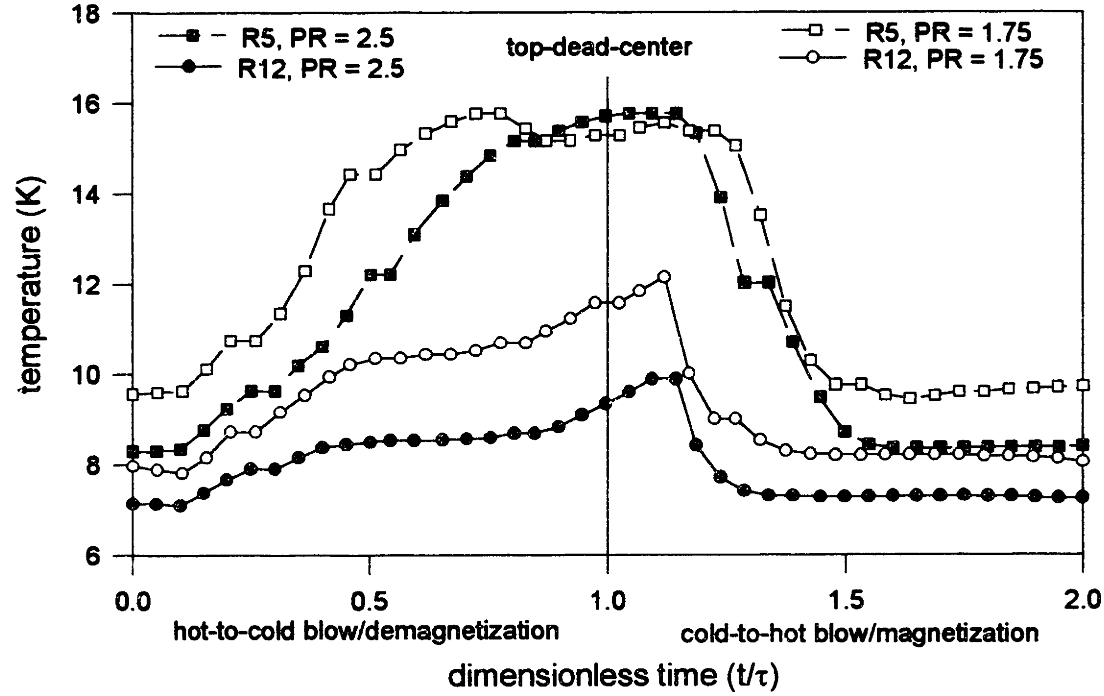

Figure 3-6. Temperature in magnetic stage for different pressure ratios at high value of refrigeration load (refrigeration load = 0.5 watt, applied field swing = 2.2 Tesla, displacer stroke = 3.5 inch)

GM/magnetic cycle is operating on the right hand side of the curves shown in Figure 2-1 (i.e. the refrigeration is decreasing with mass ratio). Another secondary effect is associated with the decrease in the magneto-caloric effect as the temperature increases.

Figure 3-5 shows the temperature at the warm and cold ends of the magnetic regenerator bed for two values of applied field swing. The increase in the applied field swing tends to reduce the temperature level, particularly in the cold regions of the regenerator where the magneto-caloric effect is the strongest. This effect is again confounded with changing mass ratio as described above. Also, the change in the level of applied field swing is accomplished by lengthening the total cycle time. Consequently the losses associated with heat leaks down the temperature scale are increased and the total refrigeration per cycle is also increased.

The effect of pressure ratio is not as apparent as the effect of the two parameters discussed above. The effect of pressure ratio depends on the temperature level of the device because the losses associated with the void volume of the regenerator depend heavily on the density of helium which, in turn, depends on temperature.

Figure 3-6 illustrates the effect of pressure ratio for a high value of refrigeration load (and consequently a comparably warmer regenerator). The increase in the pressure ratio increases the expansion effect and improves the performance of the device, as seen by the decrease in the temperature at the cold end. The increase in pressure level also increases losses associated with the void volume, but for a high refrigeration load this effect is less than the improvement associated with more expansion.

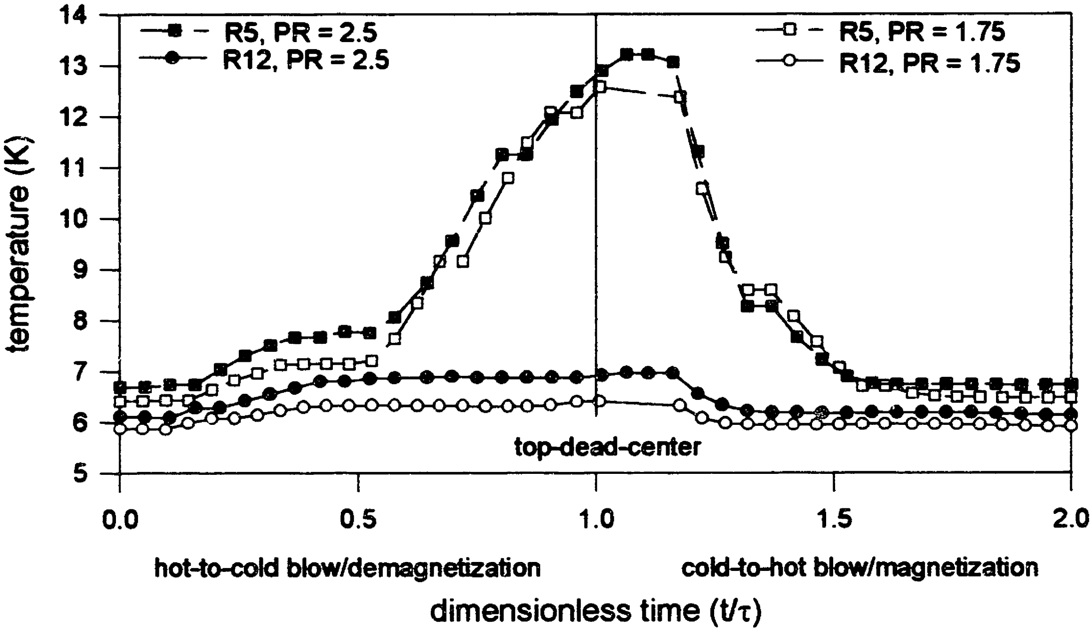

Figure 3-7. Temperature in magnetic stage for different pressure ratios at low value of refrigeration load (refrigeration load = 0 watt, applied field swing = 2.2 Tesla, displacer stroke = 3.5 inch)

Figure 3-7 illustrates the effect of pressure ratio at a low value of refrigeration load (and consequently a colder regenerator). Because the regenerator matrix is colder, the density of the helium entrained in the void volume is much larger and the losses associated with the void volume overcome the gains associated with increasing the expansion effect. The temperature at the cold end of the regenerator is actually warmer in the run with the larger pressure ratio.

The effect of displacer stroke can be seen in Figure 3-8. It is obvious that decreasing the displacer stroke causes a dramatic increase in the performance of the device. As was mentioned earlier, this is because the magnetic stage is operating in the region where a decreasing mass ratio tends increase the performance. The effect of changing the displacer stroke is again confounded by the change in density of helium as the low temperature end of the device gets colder.

3.3.2 Pressure

The pressure in the experimental apparatus could be measured at three locations: the room temperature inlet to the working space (PT1), the interface between the upper stage and the magnetic stage (PT2), and the cold space (PT3). Typically only the pressures in the cold region of the device were recorded during an experimental run (PT2 and PT3). The analysis in subsection 2.4.2 indicates that the attenuation and phase lag associated with the pressure tap are negligible. Therefore no correction is applied to the pressure readings taken by the computer.

The pressure as a function of time at each of these locations is shown in Figure 3-9 for a typical cycle. During the hot-to-cold blow process, the pressure at the interface between the upper stage is somewhat greater than the pressure in the cold space due to the flow resistance of the magnetic

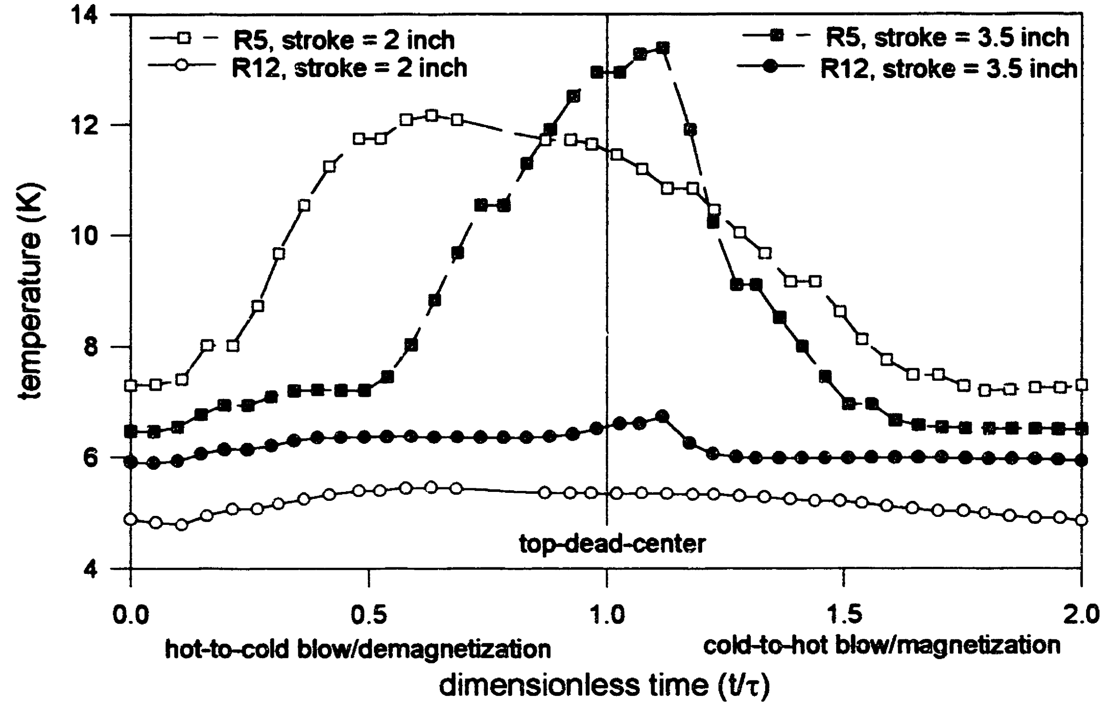

Figure 3-8. Temperature of magnetic stage at different levels of displacer stroke (refrigeration load = 0 watt, pressure ratio = 1.75, applied field swing = 2.6 Tesla)

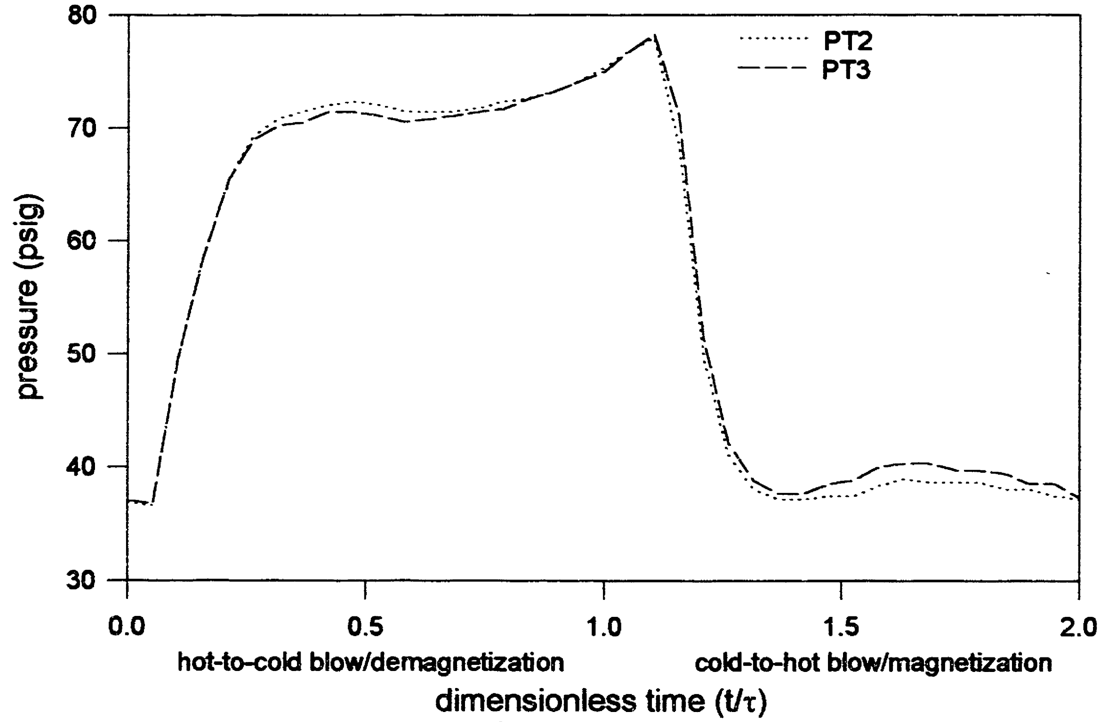

Figure 3-9. Pressure measurements for a typical cycle as a function of time at the warm and cold ends of the regenerator (stroke = 3.5 inch, applied field swing = 1.4 Tesla, pressure ratio = 2, refrigeration load = 0 watt)

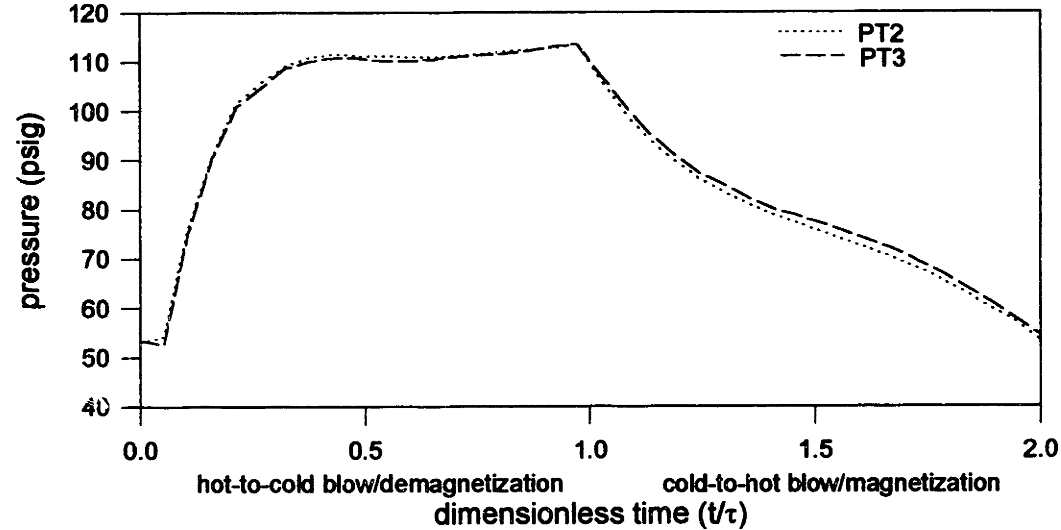

Figure 3-10. Pressures as function of time for a cycle with a long expansion time constant (stroke = 2 inch, applied field swing = 2.8 Tesla , pressure ratio = 2 , refrigeration load = 0 watt)

matrix. This pressure drop is on the order of a few psi, which agrees well with the calculated pressure drop reported in Table 2-5. The pressure difference switches direction during the cold-to-hot blow process as the flow reverses itself. The gradual increase in pressure at the end of the hot-to-cold blow process and the gradual decrease in pressure at the end of the cold-to-hot blow process are caused by the recharging of the accumulators through the pressure regulators.

The expansion process illustrated in Figure 3-9 has a very short time constant. Consequently, a large mass of helium leaves the cold space immediately when the displacer hits top-dead-center. This spike in the mass flow rate degrades the performance of the device. When later cycles were run, the expansion throttle was adjusted so that the time constant associated with the expansion process is longer and the mass flow rate more uniform throughout the cold-to-hot blow process. Figure 3-10 illustrates the pressure variation with the expansion throttle adjusted to yield a longer expansion time constant.

3.3.3 Temperature of upper stage

The temperature of the upper stage could be measured at 10 separate locations with Type E thermocouples, as indicated in Figure 2-45. Typically only three of these thermocouples were read during experimental runs : two thermocouples at the cold end and one at the midpoint. However, during cool-down and certain cycles, the data acquisition system can be rewired (by means of a plug) so that all of the resistor measurements are replaced by thermocouple measurements. In this way, a qualitative measure of the temperature variation in the upper stage can be obtained.

Figure 3-11 indicates the temperature as a function of time measured in the upper stage at several axial locations. The measurements in the cold region of the apparatus are at too low of a temperature for thermocouples to be accurate. Furthermore, they are in the presence of a time-

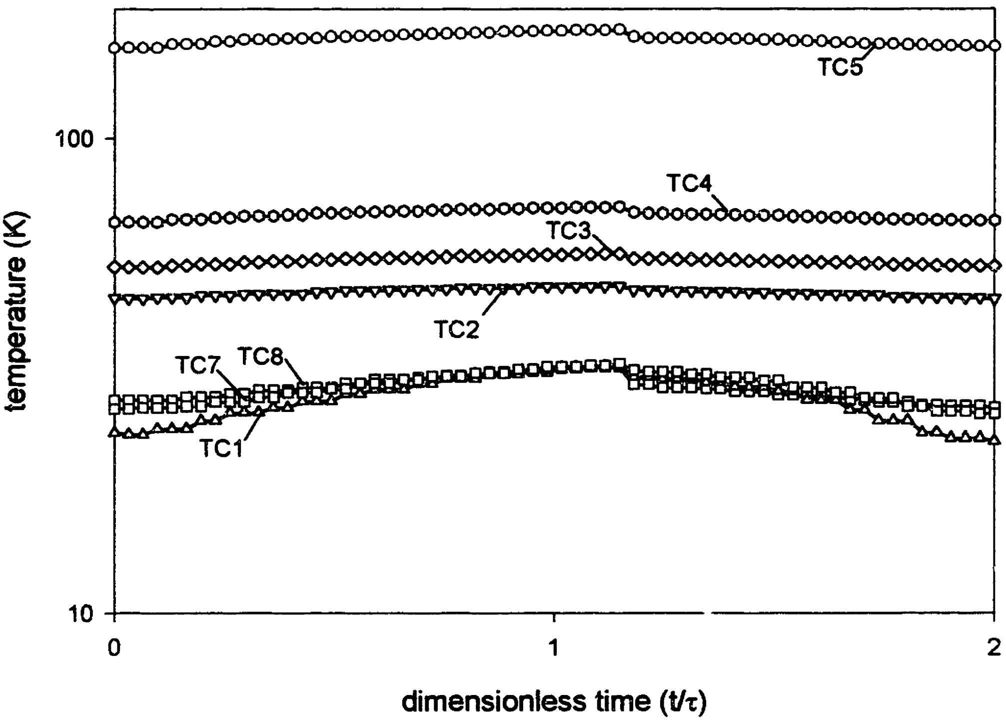

Figure 3-11. Temperature measurements in upper stage for a typical cycle

varying fringing magnetic field. Consequently, the cold measurements should be taken as only a qualitative indication of the temperature variation.

Figure 3-11 illustrates that the three temperature measurements made at the cold end of the device do not deviate from one another dramatically. This indicates that the working fluid flow is fairly evenly distributed among the upper stage tubes. Also, the temperature variation over the course of a cycle is much larger at the cold end of the device because of the relatively low specific heat capacity of lead in this temperature range.

ANALYSIS OF EXPERIMENTAL DATA

This chapter describes how the raw data described in chapter 3 is interpreted to yield meaningful results. Also, the experimental results are compared to the results obtained from theoretical models of the GM/magnetic cycle.

This chapter is divided into three sections. The first section explains the techniques used to infer data quantities not directly measured in the experimental apparatus and describes how the data is used to characterize the cycle. The second section presents the performance curves associated with the experimental apparatus. A figure of merit for the refrigeration cycle is defined and used to identify the most critical parameters which could not directly be controlled. In the final section, the experimental results are compared with the predictive model. Discrepancies observed during this comparison motivate the modification of the predictive model.

4.1 Characterization of data

This section explains how the time based data taken during the experimental runs are used to infer quantities which were not measured and to characterize the data in a quantitative manner. The techniques described in this section are applied to a typical steady state cycle for demonstration purposes. This section is divided into three subsections. The first subsection describes how the mass flow rate at the cold end and the temperature in the cold space of the device are inferred from pressure, temperature, and displacer volume data. The second subsection describes how temperature measurements made at specific axial locations are used to infer axial profiles of temperature and mass flow rate. The third subsection describes how the refrigeration and warm reservoir temperature of the magnetic stage are defined.

4.1.1 Displacer temperature and cold end mass flow rate

The magnetic stage of the device is illustrated schematically in Figure 4-1. All directly measured (such as temperatures or pressures) or known (such as the cold end dead volume) quantities are indicated in bold. The known quantities can be combined with mass and energy balances on the cold space in order to determine the displacer temperature (i.e. the temperature of the helium contained in the cold space which is the volume swept by the displacer and the dead volume) and the mass flow rate at the interface between the magnetic stage and the cold space. The characterization technique assumes that all of the cold space is at a uniform temperature, that there is no leakage of helium from the cold space, and that the only heat transfer to or from the cold space is the refrigeration load. In addition, the characterization technique assumes that the pressure everywhere in the magnetic stage is uniform and that the temperature of the GGG and the helium at every position are the same.

A mass balance on the cold space is shown below.

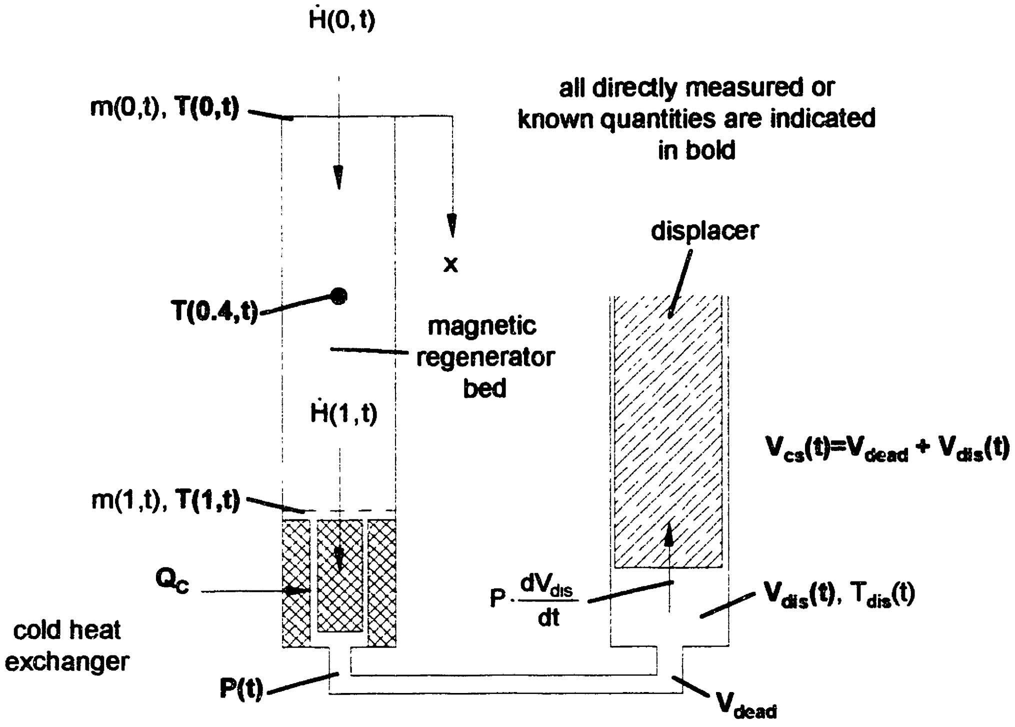

Figure 4-1. Magnetic stage schematic used to infer cold end mass flow rate and displacer temperature

$$m(L,t) = \frac{\partial(\rho \cdot V_{cs})}{\partial t} \tag{4.1}$$

This equation can be expanded, as shown below.

$$m(1,t) = \rho(T_{dis},P) \cdot \frac{dV_{cs}}{dt} + V_{cs} \cdot \left(\frac{\partial \rho}{\partial P}\right)_T \cdot \frac{dP}{dt} + V_{cs} \cdot \left(\frac{\partial \rho}{\partial T}\right)_P \cdot \frac{dT_{dis}}{dt} \tag{4.2}$$

The energy balance will differ depending on whether the flow is into or out of the cold space. When the flow is into the cold space (i.e. the mass flow rate is positive) the enthalpy of the flow term in the energy balance is associated with the temperature at the cold end of the magnetic regenerator bed.

$$m(L,t) \cdot h(T(L,t),P) = P \cdot \frac{dV_{cs}}{dt} + \frac{\partial(\rho \cdot V_{cs} \cdot u)}{\partial t} \quad \text{for } m(L,t) > 0 \tag{4.3}$$

If equation 4.2 is substituted into equation 4.3 and expanded, an equation in terms of only the displacer temperature is obtained.

$$\begin{aligned}
&m(L,t) > 0 \text{ (i.e. downflow)}\\
&\frac{dT_{dis}}{dt}\left[\{h(T(L,t),P)-u(T_{dis},P)\}\cdot V_{cs}\cdot\left(\frac{\partial\rho}{\partial T}\right)_P-\rho(T_{dis},P)\cdot V_{cs}\cdot\left(\frac{\partial u}{\partial T}\right)_P\right]=\\
&\qquad -Q_C+\frac{dV_{cs}}{dt}\left[P-\rho(T_{dis},P)\cdot\{h(T(L,t),P)-u(T_{dis},P)\}\right]+\\
&\frac{dP}{dt}\left[\rho(T_{dis},P)\cdot V_{cs}\cdot\left(\frac{\partial u}{\partial P}\right)_T-\{h(T(L,t),P)-u(T_{dis},P)\}\cdot V_{cs}\cdot\left(\frac{\partial\rho}{\partial P}\right)_T\right]
\end{aligned}\tag{4.4}$$

When the flow is out of the cold space (i.e. the mass flow rate is negative), the enthalpy is associated with the temperature in the cold space.

$$m(L,t)\cdot h(T_{dis},P)=P\cdot\frac{dV_{cs}}{dt}+\frac{\partial(\rho\cdot V_{cs}\cdot u)}{\partial t}\quad \text{for } m(L,t)<0 \tag{4.5}$$

Again the equation may be rearranged in order to obtain an expression in terms of only the unknown displacer temperature.

$$\begin{aligned}
&m(L,t) < 0 \text{ (i.e. upflow)}\\
&\frac{dT_{dis}}{dt}\left[\frac{P}{\rho(T_{dis},P)}\cdot V_{cs}\cdot\left(\frac{\partial\rho}{\partial T}\right)_P-\rho(T_{dis},P)\cdot V_{cs}\cdot\left(\frac{\partial u}{\partial T}\right)_P\right]=\\
&-Q_C+\frac{dP}{dt}\left[\rho(T_{dis},P)\cdot V_{cs}\cdot\left(\frac{\partial u}{\partial P}\right)_T-\frac{P}{\rho(T_{dis},P)}\cdot V_{cs}\cdot\left(\frac{\partial\rho}{\partial P}\right)_T\right]
\end{aligned}\tag{4.6}$$

These equations are stepped forward in time using a finite difference approach to determine the mass flow rate at the cold end of the magnetic regenerator bed and the temperature in the cold space. The program used to accomplish this, as well as the other characterization procedures described in this section, is listed in appendix A.8.

Figure 4-2 illustrates the estimated cold end mass flow rate for a typical cycle. An indication of the accuracy of the estimation technique is the equality of the areas above and below the axis in Figure 4-2 (i.e. if the cycle is steady state then the mass entering the cold space must equal the mass leaving the cold space).

Figure 4-3 illustrates the temperature measured at several positions in the magnetic regenerator and the estimated temperature of the cold space. During the cold-to-hot blow portion of the cycle, the temperature in the displacer should closely agree with the temperature at the cold end of the magnetic regenerator. The discrepancy between the two temperature variations during the second half of the cycle is an indication in the error either of the characterization technique described above or of the measurement of the cold end temperature.

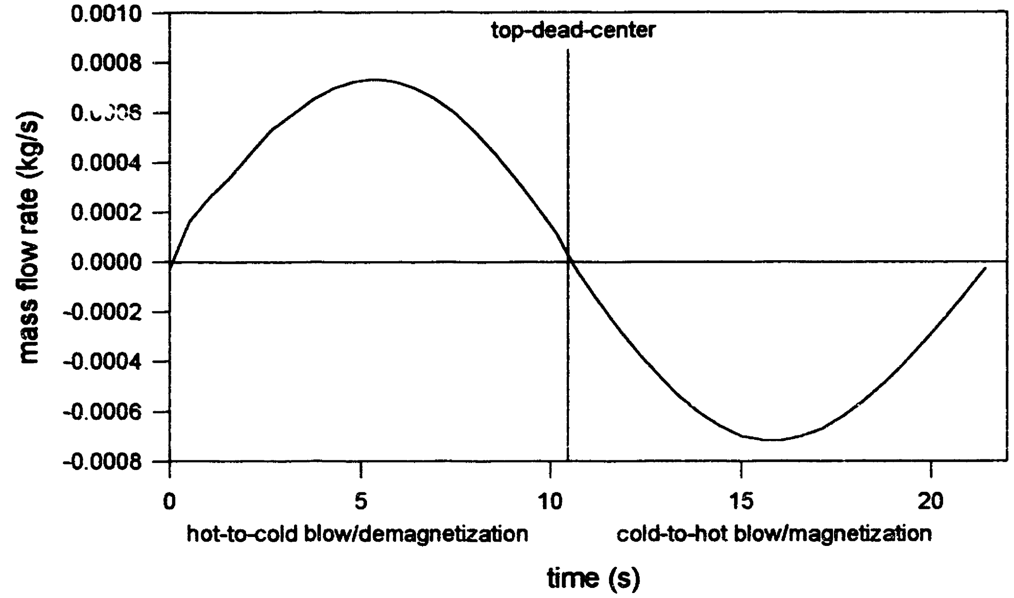

Figure 4-2. Estimated mass flow rate at the cold end of the magnetic regenerator as a function of time for a typical cycle (stroke = 1 inch, applied field swing = 3 Tesla, pressure ratio = 2.5, refrigeration load = 0.36 watt)

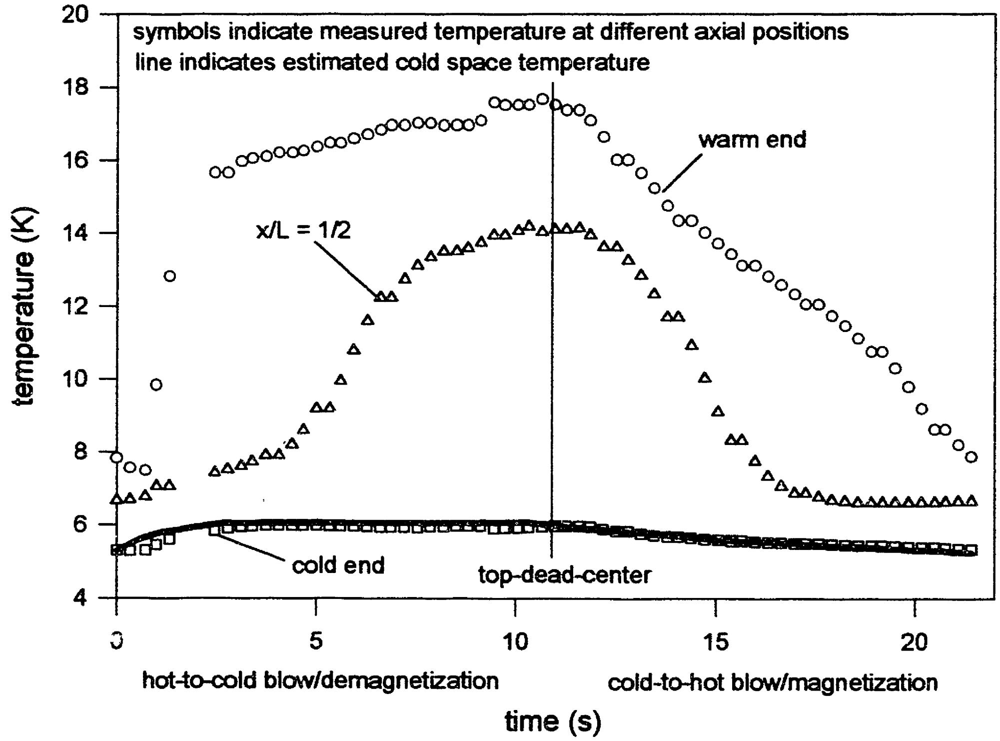

Figure 4-3. Esimated cold space temperature and measured temperature as a function of time at several axial locations for a typical cycle (stroke = 1 inch, applied field swing = 3 Tesla, pressure ratio = 2.5, refrigeration load = 0.36 watt)

4.1.2 Quantities at other axial positions

The procedure described in subsection 4.1.1 estimates the mass flow rate at the cold end of the magnetic stage. In order to properly characterize the experimental cycles, it is necessary to estimate the conditions along the entire axis of the magnetic regenerator. This requires an interpolation scheme to estimate the temperature between measured points and further analysis to estimate the mass flow rate along the entire axis.

The temperature at any axial position and time are estimated using two dimensional cubic interpolation between adjacent axial positions and times. The pressure at any time is estimated using one dimensional linear interpolation between adjacent times. The displacer volume and applied field variations are estimated as sinusoidal and linear, respectively.

The mass flow rate at any axial position can be obtained by performing a mass balance around the regenerator void volume between that axial position and the cold end of the device.

$$m(x,t) = m(L,t) + \frac{V_{reg} \cdot \varepsilon}{L} \cdot \int_{x'}^{L} \left[\left(\frac{\partial \rho}{\partial T} \right)_P \cdot \frac{\partial T(x',t)}{\partial t} + \left(\frac{\partial \rho}{\partial P} \right)_T \cdot \frac{dP}{dt} \right] \cdot dx' \qquad \textbf{(4.7)}$$

The mass flow rate as a function of time for various axial positions is illustrated in Figure 4-4. The mass flow rate at the warm end of the device is always of greater magnitude than at the cold end due to the void volume of the matrix. Also, there is a 'spike' in the mass flow rate when the compression solenoid is initially opened at the warmer end of the device due to the rapid pressurization of the void volume. The expansion process is much smoother at all axial locations because the expansion throttle is adjusted to smooth out the de-pressurization process.

The mass flow rate as a function of space and time is used to estimate the net entropy and enthalpy flux through any axial position. If the refrigerator is viewed as an entropy processing device, it is clear that the entropy associated with the refrigeration load must be convected up the temperature scale through the regenerator [66]. The net entropy flux must be equal to or greater than the entropy associated with the refrigeration load and must increase or (in the limit of a reversible device) remain constant in the direction of the entropy flow. The enthalpy flux does not have to be monotonically increasing with temperature because there is a magnetic work input at every axial location which may affect the enthalpy flux. The entropy and enthalpy fluxes are taken to be positive in the direction of increasing temperature and are calculated below.

$$S_{flux}(x) = -\int_{0}^{2\tau} m(x,t) \cdot s(T(x,t),P(t)) \cdot dt \qquad \textbf{(4.8)}$$

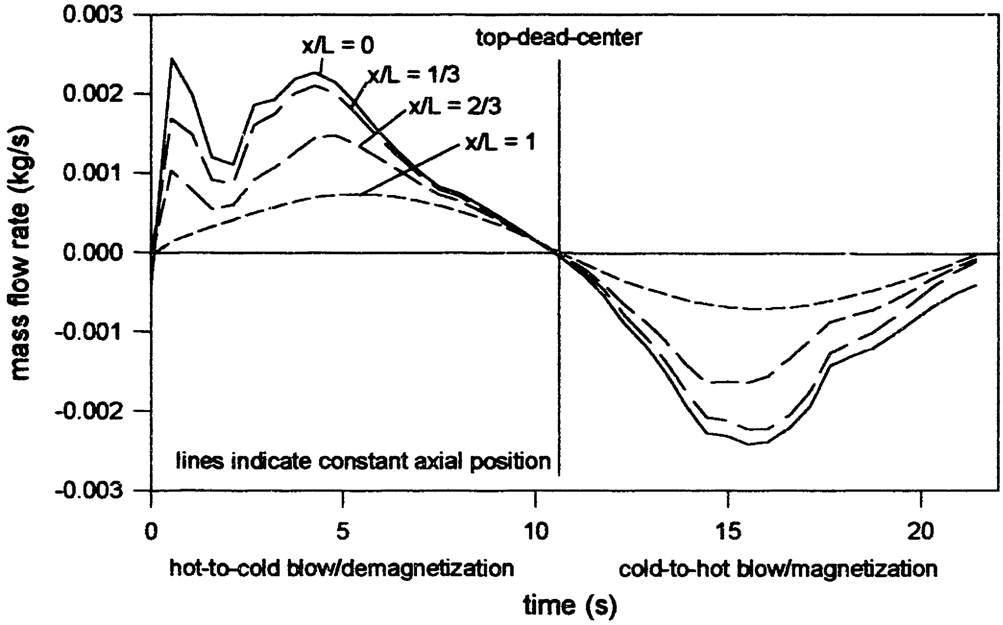

Figure 4-4. Estimated mass flow rate as a function of time at several axial locations for a typical cycle (stroke = 1 inch, applied field swing = 3 Tesla, pressure ratio = 2.5, refrigeration load = 0.36 watt)

$$H_{flux}(x) = -\int_0^{2\tau} m(x,t)\cdot h(T(x,t),P(t))\cdot dt \tag{4.9}$$

The entropy and enthalpy flux for a typical cycle are illustrated in Figure 4-5. Notice that the entropy flux is monotonically increasing in the negative x direction (i.e. towards the warm end of the device). The increase in the entropy flux indicates that there is a significant amount of entropy being generated within the regenerator bed.

When the enthalpy flux increases in temperature (i.e. near the cold end), the magnetic work must be into the device. An effective magnetic cycle uses this magnetic work input to pump heat up the temperature scale. It is obvious from Figure 4-5 that the magnetic regenerator is operating effectively in the cold region (i.e. as x/L approaches 1) but is less effective in the warm region. This is due to the nature of the magneto-caloric effect in GGG. At very cold temperatures, the GGG is an effective magnetic refrigerant but above about 9 K the GGG loses most of its magneto-caloric effect. This is illustrated clearly by calculating the net magnetic work per unit length into the apparatus as a function of axial position. The net magnetic work per unit length is calculated by taking the derivative of enthalpy flux with respect to axial position.

$$W'_{mag} = -\frac{dH_{flux}}{dx} \tag{4.10}$$

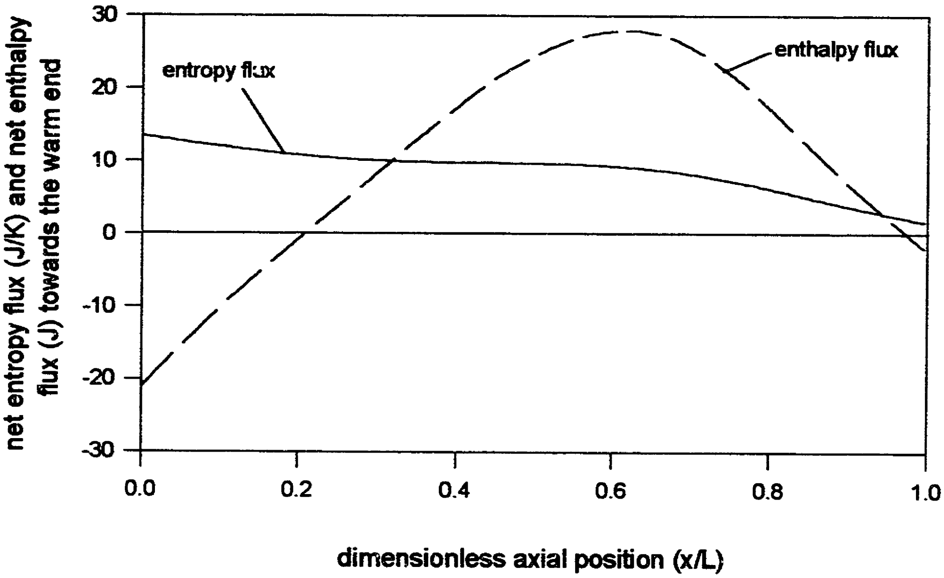

Figure 4-5. Entropy and enthalpy flux for a typical cycle as a function of axial position (stroke = 1 inch, applied field swing = 3 Tesla, pressure ratio = 2.5, refrigeration load = 0.36 watt)

The entropy generation per unit length is determined by taking the derivative of the entropy flux with respect to axial position.

$$S'_{gen} = -\frac{dS_{flux}}{dx} \tag{4.11}$$

The entropy generation and magnetic work per unit length are illustrated in Figure 4-6 as a function of axial position for a typical cycle.

Another method of analyzing the cycle is to generate the temperature-entropy diagrams for the GGG at any axial positions. Such a diagram is illustrated in Figure 4-7 for a typical cycle. The temperature-entropy diagrams at the cold end of the device are quite wide and flat. Also, the temperature-entropy diagrams at the cold end are in a counter-clockwise direction which indicates that the GGG absorbs heat at a cold temperature and rejects it to a slightly warmer temperature. This is the manner in which an effective magnetic regenerator bed operates and again indicates that the bed works well at lower temperatures. At higher temperatures, the temperature entropy diagrams are more vertical and are clockwise. This indicates that the GGG is actually operating as a heat engine, which is not an effective method of operation.

The characterizations described in this section are all accomplished using the code listed in appendix A.8.

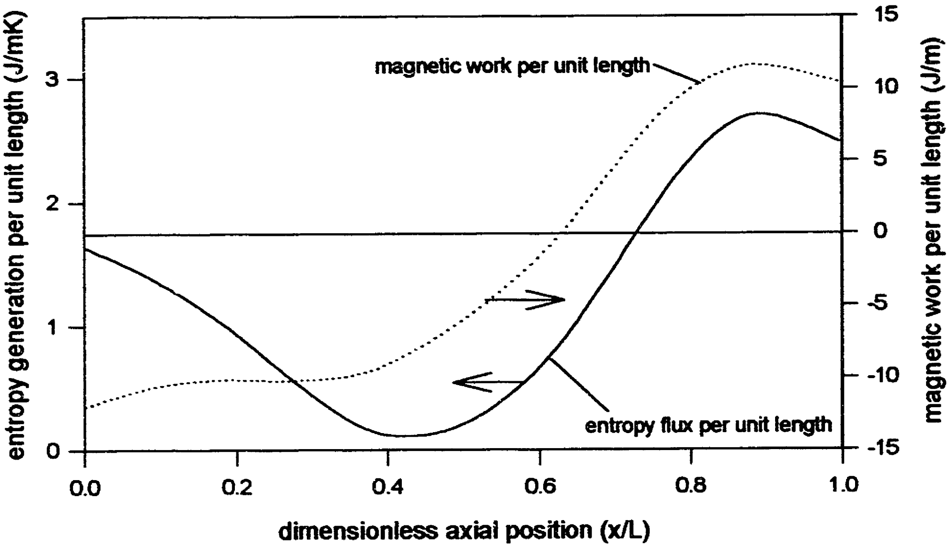

Figure 4-6. Entropy generation and magnetic work per unit length as a function of axial position for a typical cycle (stroke = 1 inch, applied field swing = 3 Tesla, pressure ratio = 2.5, refrigeration load = 0.36 watt)

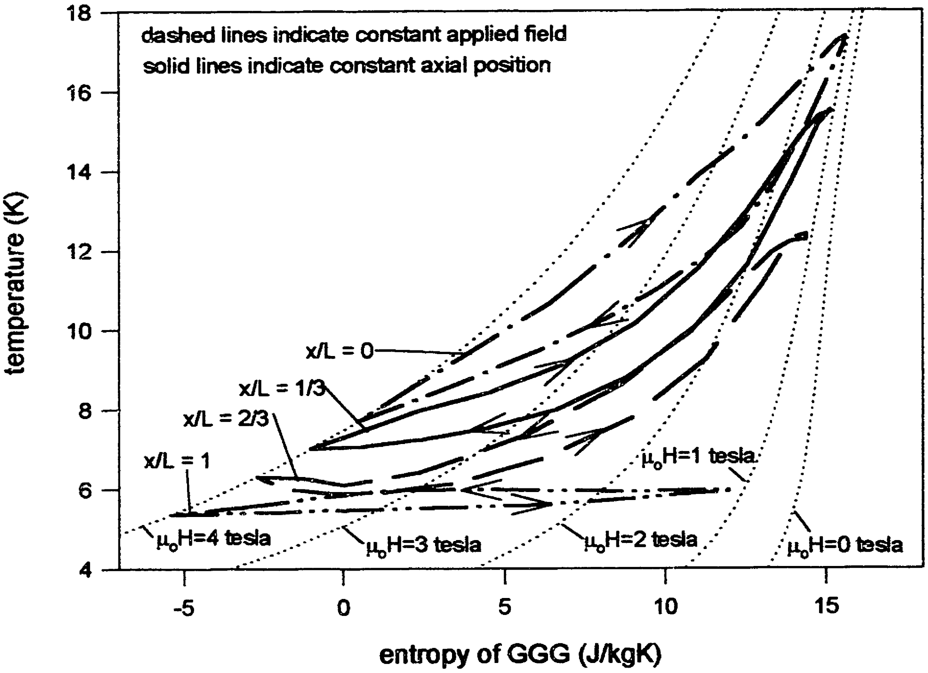

Figure 4-7. Temperature entropy diagrams for GGG at various axial positions for a typical cycle (stroke = 1 inch, applied field swing = 3 Tesla, pressure ratio = 2.5, refrigeration load = 0.36 watt)

4.1.3 Refrigeration temperature and warm reservoir temperature

The temperature at the warm and cold ends of the magnetic regenerator bed vary with time, making it difficult to identify the appropriate refrigeration and warm reservoir temperature associated with a particular cycle.

The warm reservoir temperature is taken to be the temperature associated with the mass average enthalpy and entropy of the flow into warm end of the regenerator during the hot-to-cold blow portion of the cycle.

$$\bar{h}_{df}(0) = \frac{1}{M_{df}(0)} \cdot \int m(0,t) \cdot h(T(0,t),P(t)) \cdot dt \quad \text{for all t such that } m(0,t) > 0$$

$$\bar{s}_{df}(0) = \frac{1}{M_{df}(0)} \cdot \int m(0,t) \cdot s(T(0,t),P(t)) \cdot dt \quad \text{for all t such that } m(0,t) > 0 \qquad \textbf{(4.12)}$$

$$M_{df}(0) = \int m(0,t) \cdot dt \quad \text{for all t such that } m(0,t) > 0$$

$$T_H \equiv T(\bar{h}_{df}(0), \bar{s}_{df}(0))$$

The refrigeration temperature is taken to be the temperature associated with the mass average enthalpy and entropy of the flow into the cold end of the regenerator during the cold-to-hot blow portion of the cycle.

$$\bar{h}_{uf}(L) = \frac{1}{M_{uf}(L)} \cdot \int m(L,t) \cdot h(T(L,t),P(t)) \cdot dt \quad \text{for all t such that } m(L,t) < 0$$

$$\bar{s}_{uf}(L) = \frac{1}{M_{uf}(L)} \cdot \int m(L,t) \cdot s(T(L,t),P(t)) \cdot dt \quad \text{for all t such that } m(L,t) < 0 \qquad \textbf{(4.13)}$$

$$M_{uf}(L) = \int m(L,t) \cdot dt \quad \text{for all t such that } m(L,t) < 0$$

$$T_C \equiv T(\bar{h}_{uf}(L), \bar{s}_{uf}(L))$$

Applying this technique to the typical cycle used in subsections 4.1.1 and 4.1.2 leads to a refrigeration temperature of 5.6 K and a warm reservoir temperature of 14.0 K. The

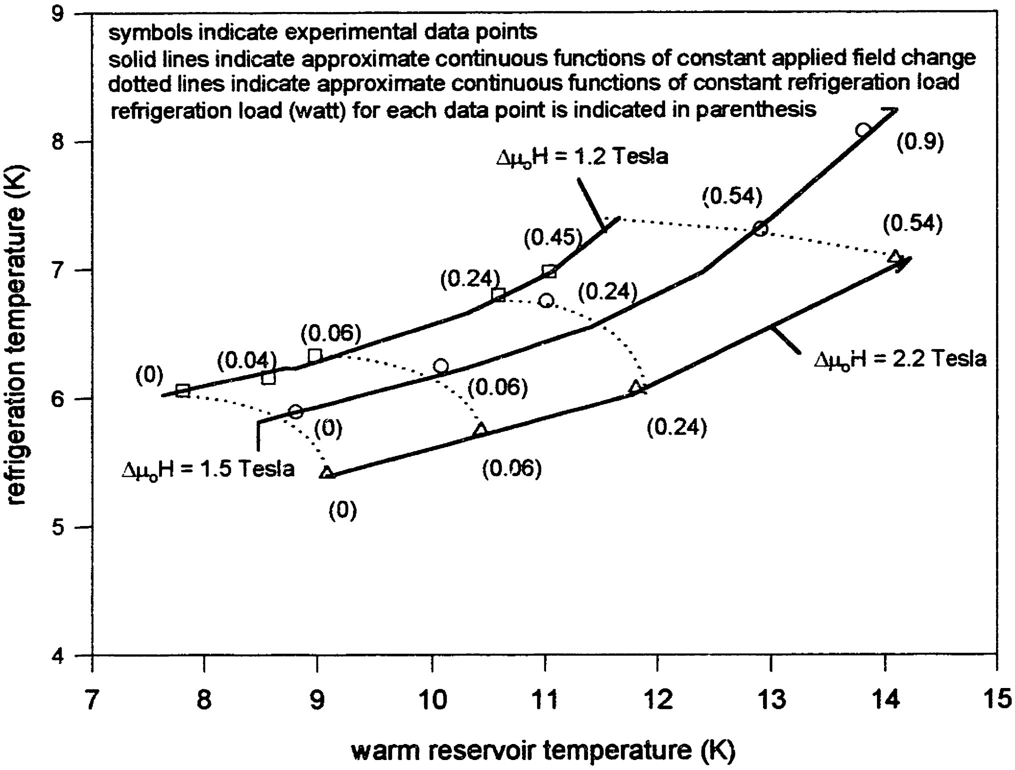

Figure 4-8. Variation of refrigeration temperature as a function of warm reservoir temperature as refrigeration load is changed for various values of applied field swing (stroke = 3.5 inch, pressure ratio = 2)

characterization of the refrigeration and warm reservoir temperature is accomplished with the code listed in appendix A.8.

4.2 Performance of Experimental Apparatus

In this section, the characterization techniques developed in section 4.1 are applied to the data obtained using the experimental apparatus.

The most important aspects of any refrigeration system are the refrigeration load, refrigeration temperature, and warm reservoir temperature. Figure 4-8 illustrates the variation in refrigeration temperature as a function of the warm reservoir temperature as the refrigeration load is changed. Several values of applied magnetic field swings are illustrated. Any point to the right of and below other points at the same level of refrigeration in Figure 4-8 represents better performance (higher warm reservoir temperature and/or lower refrigeration temperature). Therefore, Figure 4-8 indicates that as the applied magnetic field swing is increased the device operates more effectively. The

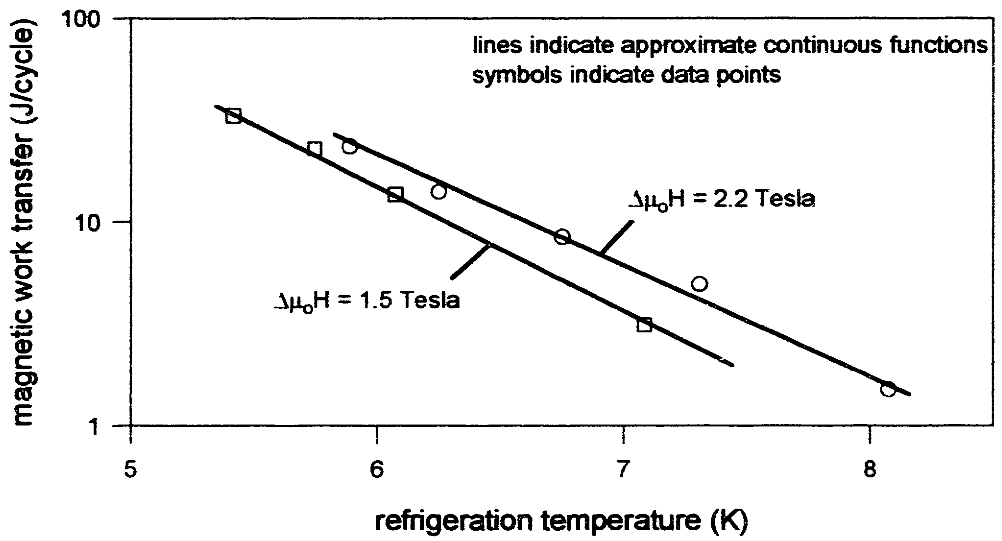

Figure 4-9. Variation of magnetic work transfer as a function of refrigeration temperature as refrigeration load is changed for two values of applied field swing (stroke = 3.5 inch, pressure ratio = 2)

improvement is remarkable since the increase in applied field swing comes only by increasing the total cycle time a proportional amount. Consequently, the total refrigeration per cycle supplied by a cycle with a higher applied field swing will be much larger than one with a lower applied field swing even if the refrigeration rates are the same.

Figure 4-9 illustrates the variation in the magnetic work transfer (as calculated by the increase in the enthalpy flux through the regenerator) as a function of refrigeration temperature as the refrigeration load is changed for two different values of applied field variation. The magnetic work transfer tends to increase as the applied magnetic field swing is increased. This causes the increase in the performance of the device. It is also interesting that the magnetic work transfer tends to increase as the temperature decreases. This is because the magneto-caloric effect in the GGG gets stronger at lower temperatures.

Figure 4-10 illustrates the variation of the refrigeration temperature as a function of the warm reservoir temperature as the refrigeration load is changed for two values of the pressure ratio. At a high pressure ratio, the device operates more effectively in the warmer temperature region and less effectively when it is colder. This is because the pressurization of the entrained helium degrades the cycle more as the temperature is decreased.

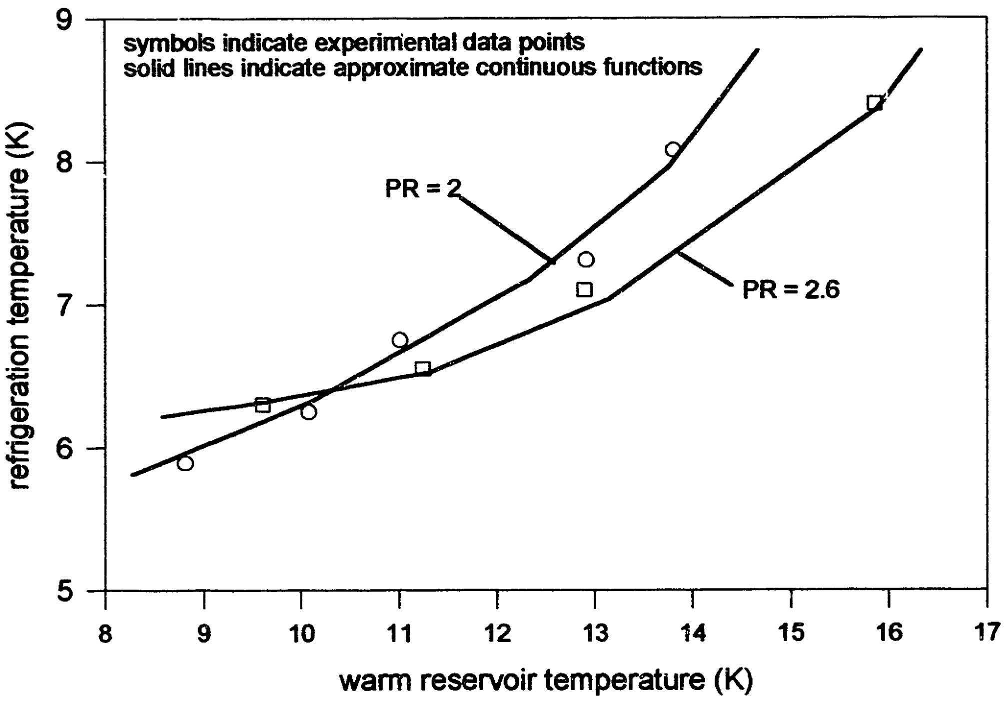

Figure 4-10. Variation of refrigeration temperature as a function of warm reservoir temperature as refrigeration load is changed for two values of pressure ratio (stroke = 3.5 inch, applied field swing = 1.5 Tesla)

Figure 4-11 illustrates the variation of the refrigeration temperature as a function of the warm reservoir temperature as the refrigeration load is changed for two values of the stroke. As the stroke is decreased, the mass of helium which the regenerator must process is lowered. Since the device is operating at a relatively high mass ratio (i.e. on the right hand side of the performance curves illustrated in Figure 2-1), lowering the helium mass improves the performance of the device.

When examining the figures presented above, it must be remembered that the effect of varying the parameter of interest is always confounded by several factors. Most importantly, if the refrigeration temperature changes then the mass of helium changes drastically due to temperature related density variations. This occurs even if the pressure ratio and displacer stroke are not varied. A performance curve which would be analogous to the predicted performance curve illustrated in Figure 2-1 cannot be constructed because the only parameter which can be exactly controlled is the refrigeration load.

One method of gaining at least a qualitative idea as to what parameters are most important in terms of determining the performance of the device is to develop a figure of merit

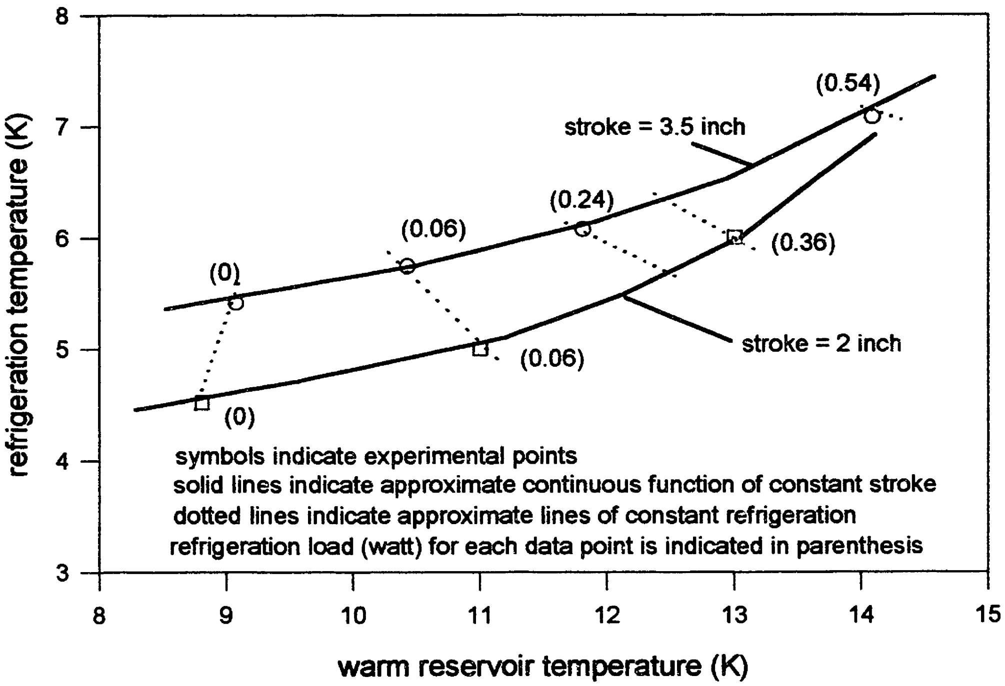

Figure 4-11. Variation of refrigeration temperature as a function of warm reservoir temperature as refrigeration load is changed for two values of stroke (applied field swing approximately 2.8 Tesla, pressure ratio = 2)

(FOM) for a cycle. The figure of merit is defined as the temperature ratio spanned by the cycle multiplied by the heat load in the cold space and divided by the refrigeration temperature. The heat load in the cold space is taken to be the refrigeration load plus the estimated heat leak associated with the shuttle heat transfer loss (as estimated in subsection 2.3.5) and conduction through the structural members leading to the cold space.

$$\mathrm{FOM} \equiv \frac{\mathrm{TR}}{\mathrm{T_C}} \cdot (\mathrm{Q_C} + 0.2\ \mathrm{watt}) \qquad \textbf{(4.14)}$$

Figure 4-12 shows the figure of merit as a function of the mass of helium which enters the cold space for all of the experimental runs. Also indicated on Figure 4-12 is the result of a single regression of the figure of merit against the mass of helium. The scatter in the data is due to the effect of other parameters which are being varied (e.g. pressure ratio, applied field change, etc.). Figure 4-12 indicates that the mass ratio between the helium and the GGG is of critical importance to the performance of the device. This agrees with the results of the predictive model described in subsection 2.1.2. For the operating region

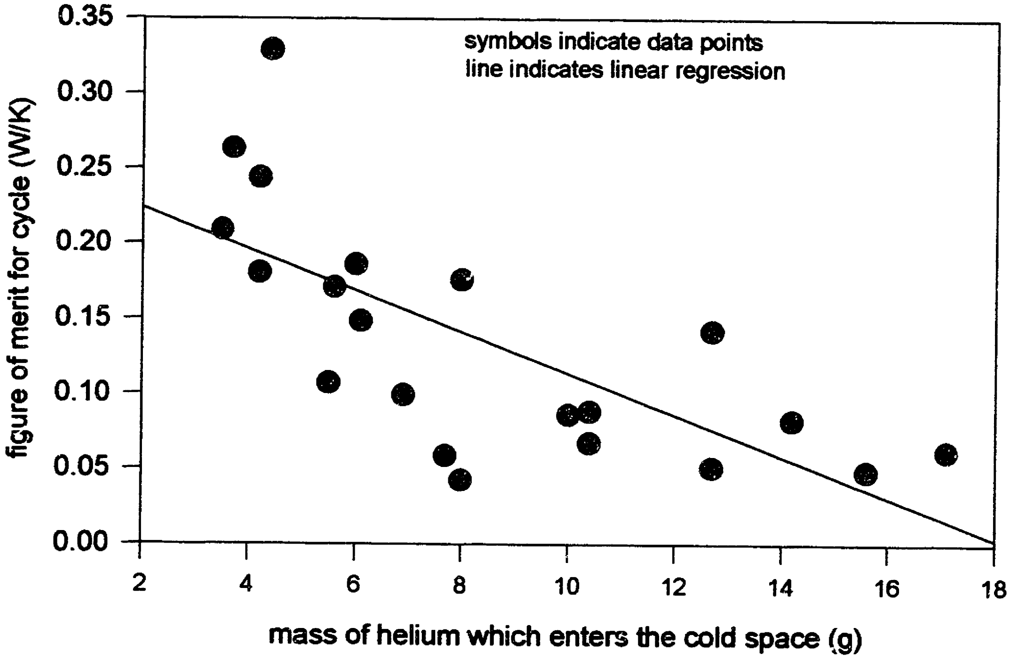

Figure 4-12. Figure of merit as a function of mass of helium which enters the cold space

associated with the experimental apparatus, a smaller mass ratio generally is more desirable.

The total magnetic effect is another parameter which was anticipated to be important to the performance of the device. In section 2.1, the magnetic effect was defined in order to nondimensionalize the refrigeration. The magnetic effect (ME) is defined again below.

$$ME \equiv \frac{M_G}{(T_H - T_C)} \cdot \int_{T_C}^{T_H} T \cdot \left\{ s_G(\mu_o H_{min}, T) - s_G(\mu_o H_{max}, T) \right\} \cdot dT \qquad \textbf{(4.15)}$$

Figure 4-13 illustrates the variation of the figure of merit as a function of the magnetic effect. Increasing the magnetic effect does tend to increase the figure of merit although the scatter associated with the other parameters obscures this relation. The single regression of figure of merit against magnetic effect is also indicated in Figure 4-13.

In order to separate the effects, a multiple regression is run on the figure of merit with three explanatory variables : the mass of helium which enters the cold space, the magnetic effect, and the mass of inactive helium. The mass of inactive helium is defined as the mass of helium which enters the warm end of the device and never passes into the cold space.

$$M_{ia} \equiv M_{df}(0) - M_{uf}(L) \qquad \textbf{(4.16)}$$

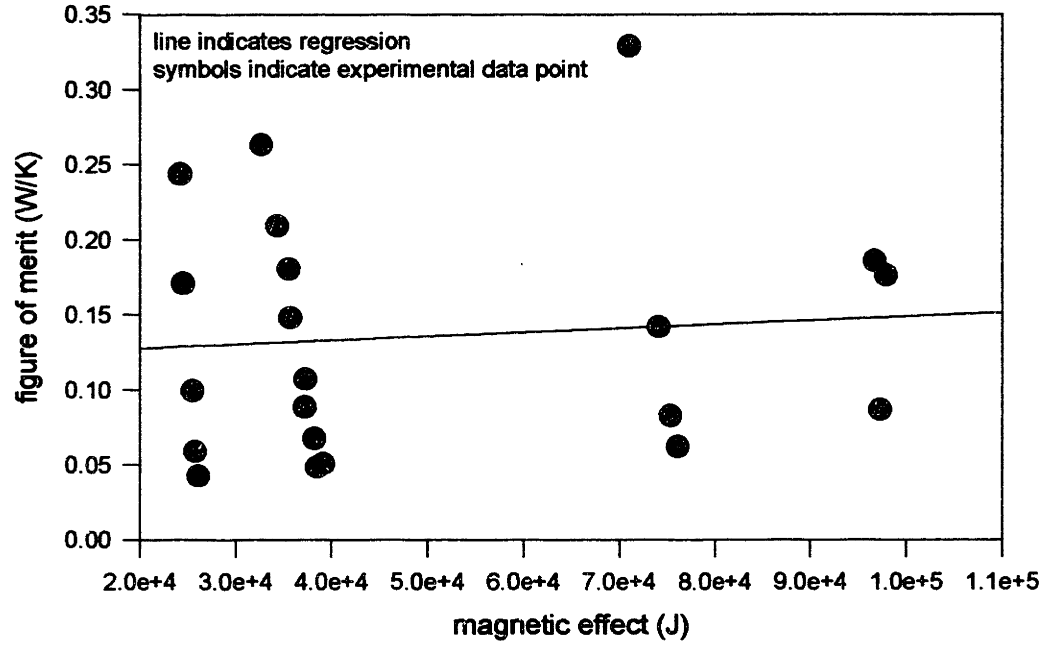

Figure 4-13. Figure of merit as a function of magnetic effect

The result of the regression analysis is reported in Table 4-1. The mass of helium which enters the cold space and the magnetic effect are both found to be significant. The mass of inactive helium is not found to be significant. However, the mass of inactive helium and the mass of helium which enters the cold space are possibly jointly determined since they both depend on similar factors.

4.3 Comparison of experimental results with theoretical models

This section describes how the experimental results are compared with theoretical models of a GM/magnetic cycle. This section is divided into three subsections. In the first subsection, the results are compared with the predictive model described in section 2.1.

Table 4-1. Results of regression analysis of experimental data

regression is of the form: $FOM = b_0 + b_1 M_{uf}(0) + b_2 M_{ia} + b_3\ ME + \varepsilon$

Description of parameter	Value	Units
coefficient for mass of helium in cold space (b_1)	-0.0143	W/Kg
coefficient for mass of inactive helium (b_2)	-0.0148	W/Kg
coefficient for magnetic effect (b_3)	1.73e-6	W/K J
level of significance of mass of helium in cold space (p-value)	0.000307	-
level of significance of mass of entrained helium (p-value)	0.171	-
level of significance of magnetic effect (p-value)	0.016711	-
R-squared statistic for regression	0.65	-

The second subsection describes how the model is modified in order to more accurately represent the boundary conditions imposed on the experimental device. The final subsection presents the comparison of the modified model with the experimental data.

4.3.1 Comparison with predictive model

The predictive model described in section 2.1 contains the important effects associated with a GM/magnetic cycle and should be capable of predicting the behavior of the magnetic regenerator bed. Unfortunately, the model assumes boundary conditions which are inconsistent with the boundary conditions seen by the experimental apparatus. The model assumes isothermal warm and cold heat exchangers, linear displacer volume variation, and linear pressure variations. The actual experimental apparatus sees very non-uniform temperatures in the incoming flows of helium, a sinusoidal displacer volume variation, and nearly exponential pressure variation. Consequently it is difficult to identify whether discrepancies between the predicted and experimental results are due to incomplete modeling or the disparate boundary condtions.

While it might be feasible to make some of the boundary conditions more accurate, the relaxation of the isothermal cold heat exchanger assumption cannot be accomplished using the explicit time and space modeling technique described in section 2.1. When all of the helium contained in the cold space can be assumed to be at one constant temperature, the mass flow at the interface between the magnetic regenerator and the cold heat exchanger is determined only by the pressure and displacer volume variation. Consequently the mass flow rate is unambiguously positive (towards the cold end) during the hot-to-cold blow portions of the cycle and unambiguously negative (towards the warm end) during the cold-to-hot blow portions. If the cold space is modeled as being adiabatic except for the constant refrigeration load, then the temperature in the cold space varies with time. The density variations induced by these temperature changes may cause a negative mass flow rate even as the displacer volume and pressure are increasing. This effect is particularly strong near bottom-dead-center since the apparatus has very low cold end dead volume. To accurately model the magnetic regenerator bed coupled to the cold space, the modeling technique must be implicit in space. This model (subsequently referred to as the modified model) is described in the remaining subsections.

Although the predictive model does not do a good job of quantitatively predicting the performance of the experimental device, it does qualitatively show the same general cycles as were experimentally observed. Figure 4-14 illustrates the temperature-entropy diagrams experimentally observed for a typical cycle and those associated with the predictive model at the same warm reservoir temperature and refrigeration temperature. The shapes of the cycles agree very well in the cold regions of the device. The agreement is much worse at the warm end because the regenerative upper stage of the experimental apparatus imposes a time varying temperature at the warm end while the predictive model assumes a constant warm reservoir temperature.

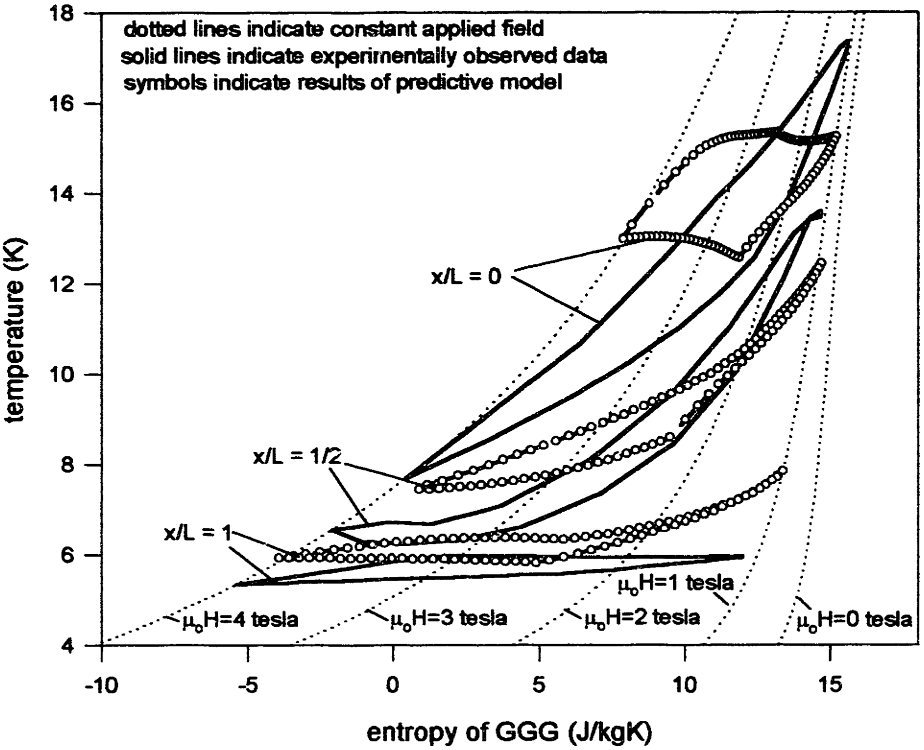

Figure 4-14. Temperature entropy diagrams for GGG observed using experimental apparatus and predicted using predictive model for a typical cycle (stroke = 1 inch, applied field swing = 3 Tesla, pressure ratio = 2.5, refrigeration load = 0.36 watt)

4.3.2 Modification of predictive model

The modified model imposes boundary conditions on the magnetic regenerator that agree more closely with those associated with the experimental apparatus. The displacer volume is assumed to vary sinusoidally, the pressure is assumed to vary linearly, and the applied field is assumed to vary linearly. The temperature of the fluid entering the warm end of the magnetic stage during the hot-to-cold blow process is curve fit to the experimentally observed temperature variation during this portion of the cycle.

Two effects which were modeled in the predictive model and subsequently found to be of limited importance are the friction induced pressure gradients and the variation in the heat transfer coefficient due to flow conditions. These effects are not modeled in the modified model. The pressure is assumed to be spatially uniform and the heat transfer coefficient is assumed to be constant in time and space.

The cold space is modeled as being adiabatic except for the refrigeration load. The resulting uncertaintly regarding the direction of the mass flow rate requires an implicit technique in space rather than the explicit technique associated with the predictive model.

The governing equations within the magnetic regenerator are shown below.

$$\frac{\partial m_h}{\partial x} + A_c \cdot \varepsilon \cdot \left\{ \left(\frac{\partial \rho_h}{\partial P} \right)_T \frac{\partial P}{\partial t} + \left(\frac{\partial \rho_h}{\partial T} \right)_P \frac{\partial T_h}{\partial t} \right\} = 0 \tag{4.17}$$

$$\begin{aligned} & m_h \cdot c_{P,h} \cdot \frac{\partial T_h}{\partial x} + A_c \cdot \varepsilon \cdot \left\{ \rho_h \cdot \left(\frac{\partial u_h}{\partial P} \right)_T - \frac{P}{\rho_h} \cdot \left(\frac{\partial \rho_h}{\partial P} \right)_T \right\} \cdot \frac{\partial P}{\partial t} \\ & + A_c \cdot \varepsilon \cdot \left\{ \rho_h \cdot \left(\frac{\partial u_h}{\partial T} \right)_P - \frac{P}{\rho_h} \cdot \left(\frac{\partial \rho_h}{\partial T} \right)_P \right\} \cdot \frac{\partial T_h}{\partial t} + U \cdot a \cdot A_c \cdot (T_h - T_G) = 0 \end{aligned} \tag{4.18}$$

$$\begin{aligned} & T_G \cdot (1-\varepsilon) \cdot A_c \cdot \rho_G \cdot \left(\frac{\partial s_G}{\partial \mu_o H} \right)_T \cdot \frac{d\mu_o H}{dt} + T_G \cdot (1-\varepsilon) \cdot A_c \cdot \rho_G \cdot \left(\frac{\partial s_G}{\partial T} \right)_{m_o H} \cdot \frac{\partial T_G}{\partial t} \\ & + U \cdot a \cdot A_c \cdot (T_G - T_h) = 0 \end{aligned} \tag{4.19}$$

These equations are put into finite difference form and solved implicitly for the mass flow rate, helium temperature, and GGG temperature at each node. At the same time, a mass and energy balance on the cold space are solved to yield the displacer temperature. The coefficients are determined using the conditions at the previous time step.

The convective term in the helium energy balance is nonlinear due to the mass flow rate multiplying the spatial temperature derivative. This is linearized using a 'guess' value of the mass flow rate as the coefficient. The temperature induced storage term in the GGG entropy balance is also nonlinear due to the temperature multiplying the temporal temperature derivative. This is linearized using a 'guess' value of the temperature as the coefficient. When the finite difference matrix is solved for the new mass flow rates and temperatures, these results are used to improve the 'guess' values and the matrix is reconstructed. This iteration process is continued until the solution converges. The solution technique described above is continued until a steady state cycle is obtained. The code used to carry out this simulation is contained in appendix A.9. The helium properties are obtained using two dimensional interpolation of property tables which were constructed using the program HEPAK [67].

4.3.3 Comparison with modified model

The modified model agrees much better with the experimentally observed results. Figure 4-15 indicates the experimentally observed temperature variation at several axial locations. Also shown are the temperature variations at the same axial positions predicted by the modified model under the same conditions.

The modified model was also used to simulate a series of cycles corresponding to a series of experimental runs for a given stroke, applied field swing, and pressure ratio with an

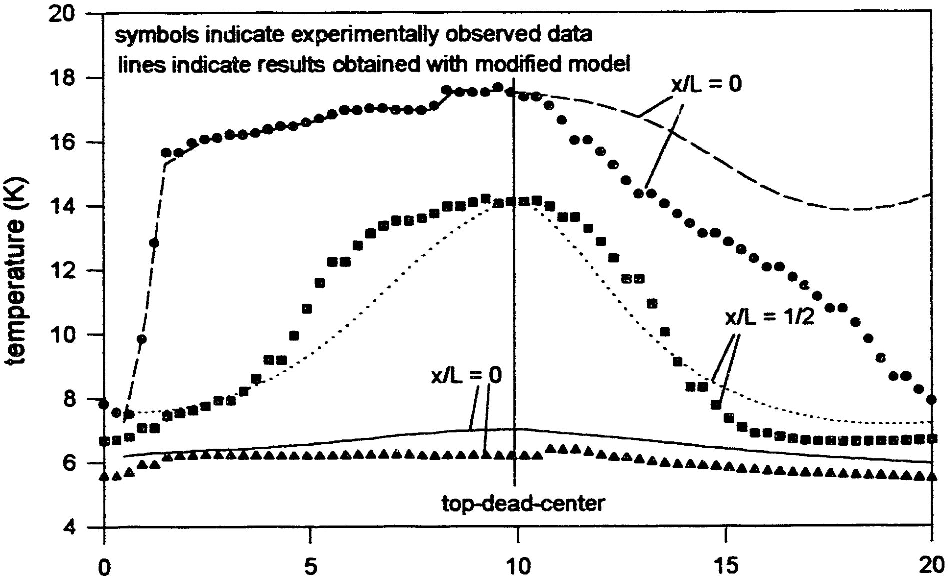

Figure 4-15. Experimentally measured temperature and temperature predicted by modified model as a function of time for a typical cycle (stroke = 1 inch, applied field swing = 3 Tesla, pressure ratio = 2.5, refrigeration load = 0.36 watt)

increasing amount of refrigeration load. The performance curve predicted by the modified model and characterized using the experimental data are both is illustrated in Figure 4-16. The agreement between the two curves is with 10% when compared using the temperature ratio.

The agreement between the modified model and the experimentally measured data indicates that the partial differential equations and property routines used to simulate the GM/magnetic cycle are adequate for the conditions associated with the experimental apparatus. If the cycle time became significantly smaller, more care would have to be taken to accurately simulate the momentum and heat transfer effects. If the cycle time became larger, the axial conduction could become significant.

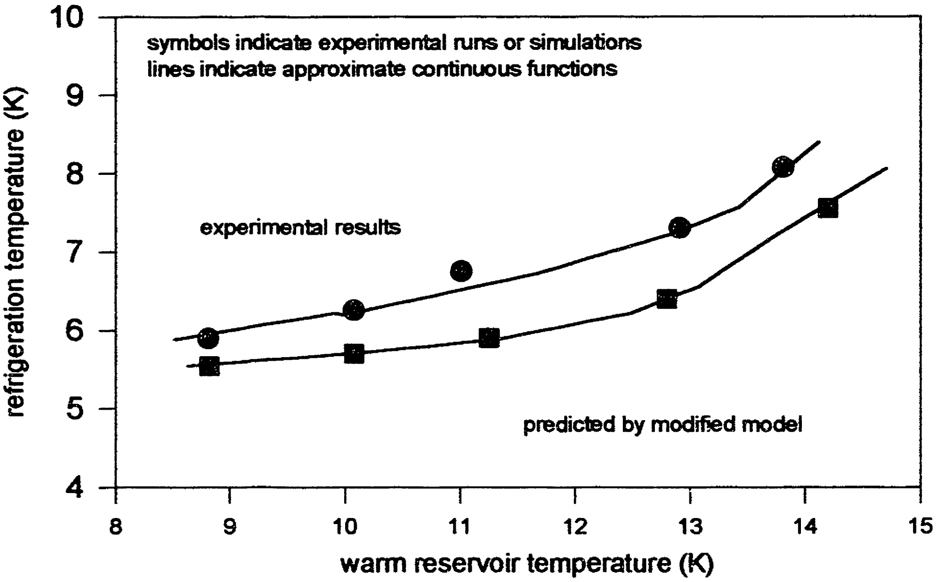

Figure 4-16. Refrigeration temperature as a function of warm reservoir temperature for an increasing rate of refrigeration load predicted by the modified model and measured experimentally (stroke = 3.5 inch , applied field swing = 1.5 Tesla , pressure ratio = 2)

CONCLUSIONS

This chapter summarizes the work which has been accomplished during this project. This chapter is divided into three sections. In the first section the work done for the Stirling/magnetic cryocooler project is summarized. The second section describes some of the major conclusions which resulted from this work. The final section suggests future work.

5.1 Summary of work

The Stirling/magnetic cryocooler is the first refrigeration cycle to use the thermodynamic coupling which exists in a paramagnetic material and a compressible fluid simultaneously. This type of cycle is capable of producing more refrigeration than those which are limited to a single thermodynamic working fluid.

Because this cycle concept has not been studied before, considerable time was spent developing a fairly simple model of a Stirling/magnetic cycle which is presented in section 1.3. This model is used to gain insight into the fundamental physical processes occurring during a Stirling/magnetic cycle. The important dimensionless groups that govern the performance of such a cycle are identified and some trade-offs are studied. The simple model is used to illustrate the advantages associated with a Stirling/magnetic cycle over a regenerative magnetic cycle or a Stirling cycle in the temperature range of interest.

The simple model is not used for design purposes due to the gross simplifications used to formulate the model. Consequently, a predictive model is developed which accounts for the non-ideal GGG and helium properties and the pressurization of the void volume in the regenerator. The predictive model is developed elsewhere, but is described in section 2.1. The predictive model is used to identify the appropriate operating conditions required for an effective GM/magnetic cycle (a slight variation of the Stirling/magnetic cycle). Also, the predictive model identified that the key loss mechanism in a practical GM/magnetic device is the pressurization of the void volume.

The theoretical studies of the Stirling/magnetic cycle indicate that it can be used to construct a practical refrigeration device. An experimental prototype was constructed which can impose a GM/magnetic cycle on a GGG bed in the presence of helium-4. The goals for the experimental prototype are to demonstrate that a GM/magnetic device is practical and to verify the theoretical models.

Having identified the appropriate design conditions for the GM/magnetic cycle, the rest of the experimental apparatus is designed around the magnetic bed, as described in chapter 2. Simple models of several critical subsystems are created. Some of the most interesting models include the upper stage regenerator/heat exchanger (subsection 2.3.3.1), the displacer shuttle heat transfer (subsection 2.3.5), the convectively cooled current leads (subsection 2.3.6), and the pressure tap (subsection 2.4.2). Whenever possible, these models are constructed nondimensionally in order to increase their generality.

The prototype GM/magnetic device has been built and tested. The magnetic stage of the device proved to be an effective refrigeration stage, providing 0.36 watts at a refrigeration temperature of 5.6 K while rejecting heat at 15.5 K. Further results and analysis of the experimental apparatus are described in chapters 3 and 4. The theoretical models were modified to more accurately reflect the experimental boundary conditions and subsequently found to be quite accurate when compared to the experimental data.

5.2 General conclusions

Some of the more important conclusions associated with the GM/magnetic cycle in general and this project in particular are listed below.

- The GM/magnetic cycle has been experimentally and theoretically shown to be an effective refrigeration cycle. This dual working fluid cycle has definite advantages over either a Stirling or a regenerative magnetic cycle.

- Gadolinium Gallium Garnet is not a particularly effective paramagnetic refrigeration material at temperatures above approximately 10 K. The magneto-caloric effect exhibited by GGG decreases rapidly in this temperature range, resulting in a regenerator which is only marginally more effective than a conventional lead regenerator above 10 K.

- The void volume which is unavoidably present in any real regenerator matrix has a particularly large effect on a GM/magnetic cycle. Not only does the entrained helium prevent the magnetic material from undergoing true adiabatic processes, but the pressurization of this helium acts as an additional heat load on the regenerator.

- The time constant associated with the discharge of the superconducting magnet was the limiting time constant for the experimental apparatus. The cycle could be made more effective if the voltage restriction associated with quenching the magnet could be overcome and the cycle time reduced.

- The large temperature swing associated with the regenerative upper stage device used to impose the warm reservoir temperature on the magnetic stage of the experimental apparatus degrades the GM/magnetic cycle. If the warm reservoir temperature were more precisely controlled, the resulting GM/magnetic cycles would be more effective.

- The magnetic aspect of this cycle requires a sophisticated power supply and a superconducting solenoid. These subsystems complicate the overall device and add to the expense of the cryocooler. Also, the paramagnetic material is significantly more expensive than a conventional regenerator material such as lead. The performance increase associated with these subsystems is significant, even for the prototype described in this work. However, this performance increase must be balanced against the costs described above.

5.3 Suggestions for future work

Further advancement of the GM/magnetic cycle should initially take place on three different fronts simultaneously. These areas include: (1) the economic justification of the GM/magnetic cycle in the light of new low temperature regenerator materials, (2) the improvement and simplification of the magnetic aspects of the GM/magnetic device, and (3) the selection of a more appropriate paramagnetic material for use in the high temperature portions of the GM/magnetic device. After accomplishing these goals, a practical refrigeration device should be constructed in which the benefits of a GM/magnetic cycle can clearly be demonstrated relative to a GM cycle.

As mentioned in section 5.2, the GM/magnetic cycle is considerably more complex and expensive than a conventional Gifford-McMahon or Stirling type device. The refrigeration range and power are improved as a result of this complexity and expense. Recent advances in the development of erbium based regenerator materials [68,69] have significantly improved the low temperature performance of GM type devices. The magnitude of the performance increase which can be expected using a GM/magnetic cycle relative to a GM device operating with an advanced regenerator material must be investigated and quantified.

The cost associated with the magnetic aspects of the GM/magnetic cycle is concentrated in the sophisticated power supply. If the power supply could be simplified, the GM/magnetic cycle would become more attractive from an economic standpoint. Some possible solutions could include building a natural oscillator to accomplish the current variation, physically moving the regenerator bed in and out of the magnetic field (this type of arrangement would require only a persistent switch with minimal make-up power), or improving the magnet design in order to generate the required magnetic fields with smaller currents.

The improvement in the performance of the GM/magnetic cycle could be dramatically increased if a more effective paramagnetic material was used. This is particularly true in the warm regions of the regenerator. Possible paramagnetic materials could be selected for more extensive study using the results of the ideal Stirling/magnetic model presented in section 2.1. The magnetic to thermal capacity ratio identified in this model indicates the important dimensionless material characteristic of the regenerator substance. Further study of such a material could be accomplished through experimental measurement of the magnetic properties of likely candidates. The magnetic properties could subsequently be used to formulate self-consistent entropy functions. The predictive model described in section 4.1 could then be used to evaluate the practical cycles associated with the regenerator material. Layered regenerators should also be studied. This would involve putting several different types of paramagnetic materials at the temperature regions where they are the most effective.

With the insight gained during the studies described above, an informed economic comparison of the GM/magnetic cycle relative to a GM cycle with an advanced regenerator material can be carried out. If such a comparison indicates that the GM/magnetic cycle is an economically attractive technology for low temperature refrigeration then the next step is to construct a practical experimental apparatus which can implement a GM/magnetic cycle. Ideally, a commercially available multi-stage GM device with well known performance characteristics would be purchased. By replacing the lowest temperature stage with a paramagnetic matrix, the practical improvement in the refrigeration power and temperature range could be quantitatively demonstrated.

REFERENCES

1. K. D. Timmerhaus, "Recent Trends in Cryocooler Development", *Proceedings of the XVII'th International Congress of Refrigeration*, **1** : 233, (1991).

2. J. L. Smith, Jr., "Cryogenic refrigeration for space exploration - a challenge for the future", *Proceedings of the XVII'th International Congress of Refrigeration*, **1** : 2, (1991).

3. G. Walker and E. R. Bingham, "Low-Capacity Cryogenic Refrigeration", Clarendon Press, Oxford (1994).

4. G. Walker, "Stirling Engines", Clarendon Press, Oxford, (1980).

5. J. A. Barclay, "Magnetic refrigeration for low-temperature applications", *Proceedings of the Third Cryocooler Conference*, **1**:20, (1984).

6. G. F. Nellis, "Magnetically augmented cryogenic refrigeration", M. I. T. (M.S. Thesis), Cambridge, (1995).

7. G. F. Nellis and J. L. Smith, Jr. , "Investigation of a magnetically augmented cryogenic refrigerator", *Proceedings of the Eighth Cryocooler Conference*, **1**:647, (1995).

8. E. G. Cravalho and J. L. Smith, Jr., "Engineering Thermodynamics", reprinted by Authors, M.I.T., Cambridge, (1992).

9. E. A. Guggenheim, "Thermodynamics, and Advanced Treatment for Chemists and Physicists", North Holland, Amsterdam, (1967),.

10. F. W. Sears, "An Introduction to Thermodynamics, the Kinetic Theory of Gases, and Statistical Mechanics", Addison-Wesley, Reading, (1953).

11. G. R. Ghallagher, "Analysis of a Magnetically Active Regnerator", M.I.T. (M.S. Thesis), Cambridge, (1986).

12. R.A. Fisher, G. E. Brodale, E. W. Hornung, and W. F. Giauque, "Magnetothermodynamics of gadolinium gallium garnet. I. Heat capacity, entropy, magnetic moment from 0.5 to 4.2 K, with fields to 90 kG along the [100] axis", *J. Chem. Phys.* , **59** : 4652, (1972).

13. E. W. Hornung, R. A. Fisher, G. E. Brodale, And W. F. Giauque, "Magnetothermodynamics of gadolinium gallium garnet. II. Heat capacity, entropy, magnetic moment from 0.5 to 4.2 K, with fields to 90 kG along the [111] axis", *J. Chem. Phys.* , **61** : 282 (1974).

14. G. E. Brodale, E. W. Hornung, R. A. Fisher, and W. F. Giauque, "Magnetothermodynamcis of gadolinium gallium garnet. III. Heat capacity, entropy, magnetic moment from 0.5 to 4.2 K, with fields to 90 kG along the [110] axis", *J. Chem. Phys.*, **62** : 4041, (1975).

15. R. A. Fisher, *et. al.*

16. J. L. Smith, G. Y. Robinson, and Y. Iwasa, "Survey of the State of the Art of Miniature Cryocoolers for Superconductive Devices", Office of Naval Research Contract No. N0001483K0327, Cryogenic Engineering Lab, MIT, Cambridge, (1984).

17. G. Walker, "Cryocoolers", Plenum, New York, (1983).

18. W. P. Pratt, Jr. , S. S. Rosenblum, W. A. Steyert, and J. A. Barclay, "A continuous demagnetization refrigerator operating near 2 K and a study of magnetic refrigerants", *Cryogenics*, **17**:689, (1977).

19. W. A. Steyart, "Rotating Carnot-cycle magnetic refrigerators for use near 2 K", *Journal of Applied Physics*, **49**:1227, (1978).

20. J. A. Barclay, O. Moze, and L. Paterson, "A reciprocating magnetic refrigerator for 2 - 4 K operation - initial results", *Journal of Applied Physics,* **50**: 5870, (1979).

21. D. L. Johnson, "Reciprocating Magnetic Refrigerator", *Proceedings of the Third Cryocooler Conference,* **1**:33, (1984).

22. G. Patton, G. Green, J. Stevens, and J. Humphrey, "Reciprocating magnetic refrigerator", *Proceedings of the Fourth Cryocooler Conference,* **1**:65, (1986).

23. A. F. Lacaze, A. A. Lacaze, R. Beranger, and G. Bon Mardion, "Thermodynamic analysis of a double acting reciprocating magnetic refrigerator", *Proceedings of the Ninth Cryocooler Conference,* **1**:14, (1982).

24. J. E. Zimmerman, J. D. McNutt, and H. V. Bohm, " A magnetic refrigerator employing superconducting solenoids", *Cryogenics,* **2**:3, (1962).

25. Y. Hakuraku and H. Ogata, "Thermodynamic analysis of a magnetic refrigerator with static heat switches", *Cryogenics,* **26**:171, (1986).

26. A. Kashani, B. P. M. Helvensteijn, J. J. McCormack, A. L. Spivak, and P. Kittel, "Development of a magnetic refrigeration operating between 2 K and 10 K", *Proceedings of the Eighth Cryocooler Conference,* **1**:637, (1995).

27. S. Jeong, "Development of the regenerative magnetic refrigerator operating from 4.2 K to 1.8 K", M. I. T. (Ph.D. Thesis), Cambridge, (1992).

28. K. Matsumoto and T. Hashimoto, "Thermodynamic analysis of magnetically active regenerator", *Proceedings of the International Congress of Cryogenics and Refrigeration,* **1**:110, (1989).

29. C. B. Zimm, A. G. Jastrab, and J. W. Johnson, "Design of active magnetic regenerative stage interfacing to a G-M cryocooler", *Proceedings of the Eighth Cryocooler Conference*, **1**:657, (1995).

30. C. P. Taussing, G. R. Gallagher, J. L. Smith, Jr. , and Y. Iwasa, "Magnetic refrigeration based on magnetically active regeneration", *Proceedings of the Fourth International Cryocoolers Conference,* **1**:79, (1986).

31. F. J. Cogswell, "Cycle Control of a Regenerative Magnetic Refrigerator Operating Between 4.2 K to 15 K", M.I.T. (Ph.D. Thesis), Cambridge, (1989).

32. P. Seyfert, P. Bredy, and G. Claudet, "Construction and testing of a magnetic refrigeration device for the temperature range of 5 to 15 K", *Proceedings of the Twelfth International Cryogenic Engineering Conference*, **1**:607, (1988).

33. S. Jeong and J. L. Smith, Jr. , "Magnetically augmented regereneration in Stirling Cryocooler", *Advances in Cryogenic Engineering,* **39B**:1399, (1994).

34. G. F. Nellis, *et. al.*

35. R. H. Fowler and E. A. Guggenheim, "Statistical Thermodynamics", Cambridge University Press, (1965).

36. E. P. Gyftopoulos and G. P. Beretta, "Thermodynamics : Foundations and Applications", Macmillan, New York, (1991).

37. G. F. Nellis, *et. al.*

38. G. R. Ghallagher

39. R. D. McCarty, "NBS Standard Reference Database 12", National Bureau of Standards Center for Chemical Engineering, Gaithersburg, (1986), interactive FORTRAN Program.

40. W. M. Rohsenow, J. P. Hartnett, and E. N. Ganic, "Handbook of Heat Transfer Applications, Second Edition", McGraw Hill, New York, (1973).

41. S. Ergun, "Fluid flow through packed columns", *Chem Eng Prog* , **48**:89, (1952).

42. G. F. Nellis and J. L. Smith, Jr, "Entropy based modification of finite difference approximations", accepted for publication in the *Journal of Numerical Heat Transfer : Applications*, (1996).

43. C. P. Taussig, "Magnetically Active Regeneration", M.I.T. (Ph.D. Thesis), Cambridge, (1986).

44. W. W. Chin, "Construction and Testing of an AC Superconducting Magnet for a Magnetic Refrigerator", M.I.T. (B.S. Thesis), Cambridge, (1985).

45. F. J. Cogswell *et. al.*

46. W. W. Chin *et. al.*

47. A. F. Mills "Heat Transfer", Irwin, Boston, (1992).

48. A. F. Mills *et. al.*

49. "Cryocomp: an interactive routine providing cryogenic properties of typical construction materials", Cryodata, Florence, (1994), FORTRAN program.

50. Y. Iwasa, "Case Studies in Superconducting Magnets: Design and Operational Issues", Plenum, New York, (1994).

51. W. M. Rohsenow *et. al.*

52. F. P. Incropera and D. P. DeWitt, "Fundamentals of heat and mass transfer", Wiley, New York, (1990).

53. F. W. Schmidt and A. J. Willmott, "Thermal Energy Storage and Regeneration", McGraw-Hill, New York, (1981).

54. J. H. Lienhard, "A Heat Transfer Textbook", Prentice-Hall, New Jersey, (1987).

55. F. P. Incropera *et. al.*

56. H. W. Jackson, "Introduction to electric circuits", Prentice-Hall, New Jersey, (1981).

57. F. J. Zimmerman and R. C. Longthworth, "Shuttle heat transfer", *Advances in Cryogenic Engineering*, **16**:342, (1970).

58. P. A. Rios, "An approximate solution to the shuttle heat transfer losses in a reciprocating machine", *ASME J of Eng for Power*, **4**:177, (1971).

59. H. M. Chiang and J. H. Baik, "An exact expression for shuttle heat transfer", *Advances in Cryogenic Engineering*, **41**:1535, (1996).

60. V. S. Arpaci, "Conduction Heat Transfer", Abridged Edition, Ginn Press, (1991).

61. Y. Iwasa *et. al.*

62. R. Radebaugh and E. Marquardt, "Cryogenic Instrumentation", *Recent Advances in Cryogenic Engineering*, **267**:13, (1993).

63. S. Jeong and D. H. Smith (an internal report, Cryogenic Engineering Laboratory, MIT, unpublished 1990).

64. S. Jeong, *et. al.*

65. Y. Iwasa, *et. al.*

66. J. L. Smith, Jr. , "Entropy flow and generation in energy conversion systems", Symposium proceedings of the ASME Winter Annual Meetings, Symposium on Thermodynamics and the Design, Analysis, and Improvement of Energy Systems, **266**:181, (1993).

67. V. Arp, R. D. McCarty, and B. A. Hands, "HEPAK 3.30: Thermodynamic, transport, superfluid, and lambda lineproperties of helium for temperatures from 0.8 to 1500 K with pressures to 20000 bars including liquid-vapor mixtures", Cryodata, Florence, (1994), FORTRAN program.

68. T. Hashimoto, T. Tsukagoshi, H. Nitta, M. Yabuki, T. Kuriyama, and H. Nakagome, "Excellent Character of Multi-Layer Type Magnetic Regenerator near 4.2 K", *Proceedings of the Eighth International Cryocooler Conference*, **1**:677, (1994).

69. K. A. Gschneider, Jr., V. K. Pecharsky, and M. Gailloux, "New Ternary Magnetic Lanthanide Regenerator Materials for the Low-Temperature Stage of a Gifford-McMahon (G-M) Cryocooler", *Proceedings of the Eighth International Cryocooler Conference*, **1**:685, (1994).

APPENDIX

This appendix contains some of the computer codes referred to within this thesis. The appendix is divided into nine sections. In the first section, the Matlab function used to determine the properties of GGG as described in subsection 1.2.2 is listed. In the second section, the Matlab program used to simulate the first order Stirling/magnetic cycle described in subsection 1.3.4.1 is listed. The third section contains the Matlab program used to simulate the regenerator/heat exchanger device described in subsection 2.3.3.1. The fourth section contains the Matlab functions used to simulate the magnet leads, as described in subsection 2.3.4. The fifth subsection contains a listing of the Matlab code used to simulate the pressure tap which was described in subsection 2.4.2. The sixth section contains a listing of the BASIC code used for data acquisition, as described in subsection 2.4.3. The seventh section contains the BASIC code used to control the cycle, as described in subsection 2.5.4. The eighth section contains the Matlab code which was used to analyze and characterize the raw data, as described in section 4.1 The final section contains the Matlab code used to carry out the simulation of the GM/magnetic cycle under experimentally determined boundary conditions, as described in subsection 4.3.2.

A.1 Matlab function for computation of GGG properties

This function is written in Matlab language. The function requires the temperature and applied field. The function returns the entropy and the first partial derivatives of entropy. This function is translated from a FORTRAN program written in 1986 by Gregory R. Ghallagher for his Master of Science Thesis.

```
function[sg,dsgdTuoH,dsgduoHT]=GGG(T,uoH)

% [sg,dsgdTuoH,dsgduoHT]=GGG(T,uoH)
% calculates the properties of GGG in SI units
% translated from a FORTRAN program written by G. Ghallagher
% T = temperature [K]    uoH = applied field [tesla]
% sg = specific entropy [J/kgK]    dsgdtuoH = partial derivative of entropy with
% respect to temperature at constant applied field [J/kgK^2]    dsgduoHT = partial derivative
% of entropy with respect to applied field at constant temperature [J/kg tesla]

eta(1)=0.1252334085;
eta(2)=0.3678314990;
eta(3)=0.5873179543;
eta(4)=0.7699026742;
eta(5)=0.9041172564;
eta(6)=0.9815606342;
W(1)=0.2491470458;
W(2)=0.2334925365;
W(3)=0.2031674267;
W(4)=0.1600783285;
W(5)=0.1069393260;
W(6)=0.0471753364;
C0= 13.67388+2.718523*T+0.1278728*T*T-0.0025072373*T*T*T;
C1= -2.890799+0.9144735*T- 0.073461875*T*T+0.0011088194*T*T*T
```

```
        +0.0000098684995*T*T*T*T;
C2= 3.166695-0.6364962*T+0.048334930*T*T-0.0010940200*T*T*T
        +0.0000043787923*T*T*T*T;
C3= -0.3461423+0.090944469*T-0.0069979527*T*T+0.00013868879*T*T*T;
C4= 0.013560383-0.0041968897*T+0.00033840450*T*T-0.0000068436516*T*T*T;
vM= uoH/(C0+uoH*C1+uoH*uoH*C2+uoH*uoH*uoH*C3+uoH*uoH*uoH*uoH*C4);
dvMduoH= (C0-C2*(uoH*uoH)-2*C3*(uoH*uoH*uoH)-
        3*C4*(uoH*uoH*uoH*uoH))/((C0+C1*uoH+C2*(uoH*uoH)
        +C3*(uoH*uoH*uoH)+C4*(uoH*uoH*uoH*uoH))*(C0+C1*uoH
        +C2*(uoH*uoH)+C3*(uoH*uoH*uoH)+C4*(uoH*uoH*uoH*uoH)));
dC0dT= 2.718523+2*0.1278728*T-3*0.0025072373*T*T;
dC1dT= 0.9144735-2*0.073461875*T+3*0.0011088194*T*T
        +4*0.0000098684995*T*T*T;
dC2dT= -0.6364962+2*0.04833493*T-3*0.0010840200*T*T
        +4*0.0000043787923*T*T*T;
dC3dT= 0.090944469-2*0.0069979527*T+3*0.00013868879*T*T;
dC4dT= -0.0041968897+2*0.00033840450*T-3*0.0000068436516*T*T;
d2C0dT2= 2*0.12787728-6*0.0025072373*T;
d2C1dT2= -2*0.073461875+6*0.0011088194*T+12*0.0000098684995*T*T;
d2C2dT2= 2*0.048334930-6*0.0010840200*T+12*0.0000043787923*T*T;
d2C3dT2= -2*0.0069979527+6*0.00013868879*T;
d2C4dT2= 2*0.00033840450-6*0.0000068436516*T;
DEN= C0+C1*uoH+C2*uoH*uoH+C3*uoH*uoH*uoH+C4*uoH*uoH*uoH*uoH;
dDENdT= dC0dT+dC1dT*uoH+dC2dT*uoH*uoH+dC3dT*uoH*uoH*uoH
        +dC4dT*uoH*uoH*uoH*uoH;
d2DENdT2= d2C0dT2+d2C1dT2*uoH+d2C2dT2*uoH*uoH+d2C3dT2*uoH*uoH*uoH;
d2DENdT2=d2DENdT2+d2C4dT2*uoH*uoH*uoH*uoH;
dsgduoHT = -uoH*dDENdT/(DEN*DEN);
dsgduoHT=1000*dsgduoHT;
vd2MdT2= uoH*(2*dDENdT*dDENdT-DEN*d2DENdT2)/(DEN*DEN*DEN);
s0= 0.00000023*T*T*T-0.031925/(T*T)+0.01699/(T*T*T)
        -(0.00000023-0.031925+0.01699);
ds0dT= 0.00000069*T*T+0.06385/(T*T*T)-0.05096/(T*T*T*T);
sSUM= 0.0;
dsdTSUM= 0.0;
for i=1:6
  x1= uoH/2*(1+eta(i));
  x2= uoH/2*(1-eta(i));
  DEN= C0+C1*x1+C2*x1*x1+C3*x1*x1*x1+C4*x1*x1*x1*x1;
  dDENdT= dC0dT+dC1dT*x1+dC2dT*x1*x1+dC3dT*x1*x1*x1
        +dC4dT*x1*x1*x1*x1;
  d2DENdT2= d2C0dT2+d2C1dT2*x1+d2C2dT2*x1*x1+d2C3dT2*x1*x1*x1
        +d2C4dT2*x1*x1*x1*x1;
  vdMdT1= -x1*dDENdT/(DEN*DEN);
  vd2MdT21= x1*(2*dDENdT*dDENdT-DEN*d2DENdT2)/(DEN*DEN*DEN);
  DEN= C0+C1*x2+C2*x2*x2+C3*x2*x2*x2+C4*x2*x2*x2*x2;
  dDENdT= dC0dT+dC1dT*x2+dC2dT*x2*x2+dC3dT*x2*x2*x2
        +dC4dT*x2*x2*x2*x2;
  d2DENdT2= d2C0dT2+d2C1dT2*x2+d2C2dT2*x2*x2+d2C3dT2*x2*x2*x2
        +d2C4dT2*x2*x2*x2*x2;
  vdMdT2= -x2*dDENdT/(DEN*DEN);
  vd2MdT22= x2*(2*dDENdT*dDENdT-DEN*d2DENdT2)/(DEN*DEN*DEN);
  sSUM= sSUM+W(i)*(vdMdT1+vdMdT2);
  dsdTSUM= dsdTSUM+W(i)*(vd2MdT21+vd2MdT22);
```

```
end
sg = s0+uoH/2*sSUM;
sg=1000*sg;
dsgdTuoH = ds0dT+uoH/2*dsdTSUM;
dsgdTuoH=1000*dsgdTuoH;
```

A.2 Matlab code to simulate first order Stirling/magnetic cycle

This function is written in the Matlab programming language. The function simulates the partial differential equations and boundary conditions associated with an ideal Stirling/magnetic cycle, as derived in subsection 1.3.4.1. The function uses a full matrix inversion of a set of linearized differential equations in conjunction with a Newton-Raphson iteration until the nonlinearity dies away.

The function requires the dimensionless characteristics of a first order Stirling/magnetic cycle : number of transfer units (NTU), magnetic capacity ratio (lb), sensible heat capacity ratio (Gm), temperature ratio (TR), volume ratio (VR), ratio of ideal gas specific heat capacities (k). The function also requires the number of time steps in a half cycle (m) and the number of axial steps (n).

The function returns the dimensionless temperatures (Qr and Qf), dimensionless entropy (beta), dimensionless applied field profile (sg), dimensionless length and time coordinates (e and z), and the resulting dimensionless refrigeration (psi).

```
function[Qr,Qf,beta,sg,e,z,psi]=smag(NTU,lb,Gm,TR,VR,k,m,n)

%[Qr,Qf,beta,sg,e,z,psi]=smag(NTU,lb,Gm,TR,VR,k,m,n)
%
% This function calculates the dimensionless regenerator and fluid temperature variation in
% space and time (Qr and Qf) associated with a first order Stirling/magnetic cycle. The
% dimensionless regenerator entropy is also calculated (beta). The dimensionless applied
% field, axial position, and time coordinates (sg, e, and z) are also returned. The resulting
% dimensionless refrigeration is returned (psi).
%
% The function requires:
% NTU : number of transfer units
% lb : magnetic capacity ratio
% Gm : sensible heat capacity ratio
% TR : temperature ratio
% VR : volume ratio
% k : ratio of ideal gas specific heat capacities
% m : number of half cycle time steps
% n : number of length steps

Ntot=(4*m+1)*(n+1);
A=sparse(zeros(Ntot,Ntot));
b=sparse(zeros(Ntot,1));
Qrl=zeros(n+1,2*m+1);
F=Qrl;
G=Qrl;
```

```
for i = 1:n+1
  for j = 1:2*m+1
    Qrl(i,j)=TR-(i-1)*(TR-1)/n;
  end
end
for j=0:m
  sg(j+1,1)=1-j/m;
end
for j=1:m
  sg(m+j+1,1)=j/m;
end

done=0;
while done==0
  for i=1:n+1
    for j=1:m+1
      dsdb=-1;
      F(i,j)=Gm+lb*sg(j,1)*sg(j,1)/(Qrl(i,j)*Qrl(i,j));
      G(i,j)=lb*sg(j,1)*dsdb/Qrl(i,j);
    end
    for j=m+2:2*m+1
      dsdb=1;
      F(i,j)=Gm+lb*sg(j,1)*sg(j,1)/(Qrl(i,j)*Qrl(i,j));
      G(i,j)=lb*sg(j,1)*dsdb/Qrl(i,j);
    end
  end
  for j=1:2*m
    for i=0:n
      A(j*(n+1)+1+i,j*(n+1)+1+i)=NTU+F(i+1,j+1)*m;
      A(j*(n+1)+1+i,(2*m+1)*(n+1)+(j-1)*(n+1)+1+i)=-NTU;
      A(j*(n+1)+1+i,(j-1)*(n+1)+1+i)=-F(i+1,j+1)*m;
      b(j*(n+1)+1+i,1)=G(i+1,j+1);
    end
  end
  for i=0:n
    A(1+i,1+i)=1;
    A(1+i,2*m*(n+1)+1+i)=-1;
  end
  for i=1:n
    for j=1:m
      A((2*m+1)*(n+1)+(j-1)*(n+1)+1+i,(2*m+1)*(n+1)+(j-1)*(n+1)+1+i)=NTU+n;
      A((2*m+1)*(n+1)+(j-1)*(n+1)+1+i,j*(n+1)+1+i)=-NTU;
      A((2*m+1)*(n+1)+(j-1)*(n+1)+1+i,(2*m+1)*(n+1)+(j-1)*(n+1)+1+i-1)=-n;
    end
  end
  for j=1:m
    A((2*m+1)*(n+1)+(j-1)*(n+1)+1,(2*m+1)*(n+1)+(j-1)*(n+1)+1)=1;
    b((2*m+1)*(n+1)+(j-1)*(n+1)+1,1)=TR;
  end
  for i=0:n-1
    for j=m+1:2*m
      A((2*m+1)*(n+1)+(j-1)*(n+1)+1+i,(2*m+1)*(n+1)+(j-1)*(n+1)+1+i)=NTU+n;
      A((2*m+1)*(n+1)+(j-1)*(n+1)+1+i,j*(n+1)+1+i)=-NTU;
      A((2*m+1)*(n+1)+(j-1)*(n+1)+1+i,(2*m+1)*(n+1)+(j-1)*(n+1)+1+i+1)=-n;
```

```
    end
  end
  for j=m+1:2*m
    A((2*m+1)*(n+1)+(j-1)*(n+1)+1+n,(2*m+1)*(n+1)+(j-1)*(n+1)+1+n)=1;
    b((2*m+1)*(n+1)+(j-1)*(n+1)+1+n,1)=1;
  end
  x=A\b;
  for i=0:n
    for j=0:2*m
      Qr(i+1,j+1)=x(j*(n+1)+1+i,1);
    end
    for j=1:2*m
      Qf(i+1,j+1)=x((2*m+1)*(n+1)+(j-1)*(n+1)+1+i,1);
    end
  end
  for i=0:n
    Qf(i+1,1)=Qf(i+1,2*m+1);
  end
  ss=sum(abs(Qr-Qrl));
  ss=sum(ss')/((n+1)*(2*m+1))
  if ss<0.01
    done=1;
  else
    Qrl=0.5*(Qr+Qrl);
  end
end
int=0;
for j=1:m
  int=int+(Qf(n+1,j)-1)/m;
end
psi=1-k*int/((k-1)*log(VR));
e=linspace(0,1,n+1)';
z=linspace(0,2,2*m+1)';
for i=1:n+1
  for j=1:2*m+1
    beta(i,j)=log(Qr(i,j))-0.5*lb*sg(j,1)*sg(j,1)/(Gm*Qr(i,j)*Qr(i,j));
  end
end
```

A.3 Matlab code used to simulate regenerator/heat exchanger

This function is written in the Matlab programming language. The function simulates the partial differential equations and boundary conditions associated with a regenerator/heat exchanger, as derived in subsection 2.3.3.1. The function uses a full matrix inversion of a set of linear differential equations.

The function requires the dimensionless characteristics of a regenerator/heat exchanger device : number of transfer units between the matrix and working fluid (NTUwm), number of transfer units between the coolant and the working fluid (NTUwc), the capacity ratio between the matrix and the working fluid (Crwm), the capacity ratio between the working fluid and the coolant (Crwc), the dimensionless temperature of the working fluid which enters the device during the cold-to-hot blow process (Qwin), the number of time steps in a half cycle (m), and the number of length steps (n). The function returns the dimensionless temperatures of the working fluid, matrix, and coolant (Qw, Qm, and Qc), effectiveness (eff).

```
function[Qw,Qm,Qc,eff]=ustg(NTUwm,NTUwc,Crwm,Crwc,Qwin,m,n)

% [Qw,Qm,Qc]=ustg(NTUwm,NTUwc,Crwm,Crwc,Qwin,m,n)

Nt=n+1;
A=sparse(zeros((6*m+1)*Nt,(6*m+1)*Nt));
b=sparse(zeros((6*m+1)*Nt,1));

% hot to cold blow working fluid energy balances
for i=1:n
  for j=1:m
    A(Nt*(3*j-1)+1+i,Nt*(3*j-1)+1+i)=n+NTUwm+NTUwc/Crwc;
    A(Nt*(3*j-1)+1+i,Nt*(3*j-1)+1+i-1)=-n;
    A(Nt*(3*j-1)+1+i,3*Nt*j+1+i)=-NTUwm;
    A(Nt*(3*j-1)+1+i,Nt*(3*j-2)+1+i)=-NTUwc/Crwc;
  end
end

% cold to hot blow working fluid energy balances
for i=0:n-1
  for j=m+1:2*m
    A(Nt*(3*j-1)+1+i,Nt*(3*j-1)+1+i)=n+NTUwm+NTUwc/Crwc;
    A(Nt*(3*j-1)+1+i,Nt*(3*j-1)+1+1+i)=-n;
    A(Nt*(3*j-1)+1+i,3*Nt*j+1+i)=-NTUwm;
    A(Nt*(3*j-1)+1+i,Nt*(3*j-2)+1+i)=-NTUwc/Crwc;
  end
end

% matrix energy balances
for i=0:n
  for j=1:2*m
    A(3*Nt*j+1+i,3*Nt*j+1+i)=NTUwm/Crwm+m;
    A(3*Nt*j+1+i,3*Nt*(j-1)+1+i)=-m;
    A(3*Nt*j+1+i,Nt*(3*j-1)+1+i)=-NTUwm/Crwm;
  end
end

% coolant energy balances
for i=0:n-1
  for j=1:2*m
    A(Nt*(3*j-2)+1+i,Nt*(3*j-2)+1+i)=NTUwc+n;
    A(Nt*(3*j-2)+1+i,Nt*(3*j-2)+1+i+1)=-n;
    A(Nt*(3*j-2)+1+i,Nt*(3*j-1)+1+i)=-NTUwc;
  end
end
```

```
% boundary conditions
for j=1:m
  A(Nt*(3*j-1)+1,Nt*(3*j-1)+1)=1;
  b(Nt*(3*j-1)+1,1)=1;
end
for j=m+1:2*m
  A(Nt*(3*j-1)+1+n,Nt*(3*j-1)+1+n)=1;
  b(Nt*(3*j-1)+1+n,1)=Qwin;
end
for j=1:2*m
  A(Nt*(3*j-2)+1+n,Nt*(3*j-2)+1+n)=1;
  b(Nt*(3*j-2)+1+n,1)=0;
end
for i=0:n
  A(1+i,1+i)=1;
  A(1+i,3*Nt*2*m+1+i)=-1;
end
x=A\b;
for j=1:2*m
  for i=0:n
    Qw(i+1,j)=x(Nt*(3*j-1)+1+i,1);
    Qc(i+1,j)=x(Nt*(3*j-2)+1+i,1);
  end
end
for j=0:2*m
  for i=0:n
    Qm(i+1,j+1)=x(3*Nt*j+1+i,1);
  end
end
full(A);
e=0;
for j=1:m
  e=e+Qw(n+1,j);
end
e=e/m;
eff=(1-e)/(1-Qwin);
```

A.4 Matlab code used to simulate magnet leads

This appendix describes the models used to design the magnet leads. The appendix is split into two sections. The first section contains the code used to simulate the general magnetic lead problem. The second section further constrains the problem by requiring that the boil-off rate match the heat leak.

A.4.1 General dimensionless problem

These functions are written in the Matlab programming language. The functions simulates the ordinary differential equations and boundary conditions associated with the magnet lead, as derived in subsection 2.3.6. The functions divides the second order ordinary differential equation for the lead temperature into two first order equations. A first order stepping technique simulates the resulting three first order equations from the cold end to the warm end. A shooting technique is used to match the warm end boundary condition.

The function requires the number of transfer units (NTU), the ratio of generation to conduction (b), the ratio of convection to conduction (Y), and the number of length steps to use in the simulation (n). The function returns the dimensionless temperature profile in the lead and the coolant (Qw and Qc), the first derivative of the temperature profile in the lead (Qwp), and the dimensionless heat leak through the magnet (qbar).

```
function[Qw,Qc,Qwp,qbar]=lead(NTU,b,Y,n)

% [Qw,Qc,Qwp,qbar]=lead(NTU,b,Y,n)

% This function simulates the magnet lead in a dimensionless manner.
% The function requires :
%       NTU : number of transfer units
%       b : ratio of generation to conduction
%       Y : ratio of convection of conduction
%       n : number of length steps
% The function returns
%       Qw : dimensionless temperature profile in lead
%       Qc : dimensionless coolant profile
%       Qwp : first derivative of temperature profile in lead
%       qbar : dimensionless heat leak

t1=[NTU;b;Y;n];
save t1 t1;
Qwp0=fzero('f1',1);
[Qw,Qc,Qwp]=derivs(NTU,b,Y,Qwp0,n);
qbar=kbar(Qw(1))*Qwp(1)/Y

function[f]=f1(Qwp0)

% [f]=f1(Qwp0)
% This is the dummy function which is zeroed in order to match the warm end
% boundary condition using the first derivative at the cold end (Qwp0).
% The dimensionless characteristics of the lead (NTU,b,Y) and the number of length
```

```
% steps (n) are passed to this function indirectly via the vector t1.

load t1;
NTU=t1(1);
b=t1(2);
Y=t1(3);
n=t1(4);
[Qw,Qc,Qwp]=derivs(NTU,b,Y,Qwp0,n);
f=Qw(n+1)-1;

function[Qw,Qc,Qwp]=derivs(NTU,b,Y,Qwp0,n)

% [Qw,Qc,Qwp]=derivs(NTU,b,Y,Qwp0,n)
% This function performs the numerical stepping of the two ODE's
% The function is given the dimensionless characteristics of the lead (NTU,b,Y)
% , the first derivative at the cold end (Qwp0) , and the number of length steps (n).
% The function returns the temperature profiles (Qw,Qc) and the first derivative of the
% lead temperature profile (Qwp)

Qw=zeros(n+1,1);
Qc=zeros(n+1,1);
Qwp=zeros(n+1,1);
Qwp(1)=Qwp0;
for i=2:n+1
   Qw(i) = Qw(i-1)+Qwp(i-1)/n;
   Qc(i) = Qc(i-1)-NTU*(Qc(i-1)-Qw(i-1))/n;
   t=-b*rbar(Qw(i-1));
   t=t-dkbardQw(Qw(i-1))*Qwp(i-1)*Qwp(i-1);
   t=t+Y*NTU*(Qw(i-1)-Qc(i-1));
   Qwp(i)=Qwp(i-1)+t/(n*kbar(Qw(i-1)));
end

function[rb]=rbar(Qw)

% rbar(Qw)
% This function gives the dimensionless electrical resistivity as a function of
% dimensionless temperature.  A linear profile is used.  More complex profiles can be
% used

rb=0.1+0.9*Qw;

function[kb]=kbar(Qw)

% kbar(Qw)

% kbar(Qw)
% This function gives the dimensionless thermal conductivity as a function of
% dimensionless temperature.  The functional dependence is inversely related to the
% dimensionless electrical resistivity

kb=1/(0.1+0.9*Qw);

function[dkdQ]=dkbardQw(Qw)
```

```
% dkbardQw(Qw)
% This function gives the first derivative of the dimensionless thermal conductivity
% with respect to dimensionless temperature

dkdQ=-0.99/(0.1+0.9*Qw)^2;
```

A.4.2 Design problem

This subsection contains the additional Matlab code required to satisfy the additional boundary condition for the magnet leads associated with the energy balance on the dewar, as derived in subsection 2.3.6.

This function requires (all in SI units) : the diameter of the magnet leads (d), the heat transfer coefficient between the magnet lead and the coolant (h), the length of the magnet leads (L), the reference thermal conductivity (ko), the reference electrical resistivity (ro), the design current (i), the temperature difference (DT), the mass flow rate through the upper stage coolant circuit (mc), and the heat leak into the dewar not associated with the magnet leads (qo). The function returns the temperature profile of the lead (Tw) and the coolant (Tc), the heat leak associated with the magnet leads (q), and the total volumetric liquid helium boil-off rate (qf).

```
function[Tw,Tc,q,qf]=design(d,h,L,ko,ro,i,DT,mc,qo)

% [Tw,Tc,q,qf]=design(d,h,L,ko,ro,i,DT,mc,qo)
%
% This function matches the additional design boundary conditions associated with the
% overall energy balance on the dewar.
% The function requires:
%       d : diameter of magnet leads [m]
%       h : heat transfer coefficient [W/m^2K]
%       L : length of leads [m]
%       ko : reference k [W/mK]
%       ro : reference r [ohm m]
%       i : current [amp]
%       DT : temperature difference [K]
%       mc : coolant mass flow rate [kg/s]
%       qo : heat leak not due to magnet leads [W]
% The function returns
%       Tw : temperature profile in lead [K]
%       Tc : temperature profile in coolant [K]
%       q : magnet heat leak
%       qf : boil-off rate [L/hr]

t2=[d;h;L;ko;ro;i;DT;mc;qo];
save t2 t2;
mw=fzero('f2',0.01);
cp=5192;
hfg=20900;
rho=125;
A=2*3.1416*d*d/4;
P=2*3.1416*d;
```

```
b=i*i*ro*L*L/(ko*A*A*DT);
Y=mw*cp*L/(ko*A);
NTU=h*P*L/(mw*cp);
[Qw,Qc,Qwp,qb]=lead(NTU,b,Y,20);
q=qb*ko*A*DT/L;
qf=3600*1000*(mw+mc)/rho;
Tw=4.2+Qw.*DT;
Tc=4.2+Qc.*DT;

function[f]=f2(mw)

% f2(mw)
% This is a dummy function used to satisfy the energy balance constraint.  The geometric
% characteristics of the magnet leads are passed to this function indirectly through the
% vector t2

load t2;
d=t2(1);
h=t2(2);
L=t2(3);
ko=t2(4);
ro=t2(5);
i=t2(6);
DT=t2(7);
mc=t2(8);
qo=t2(9);
cp=5192;
hfg=20900;
A=2*3.1416*d*d/4;
P=2*3.1416*d;
b=i*i*ro*L*L/(ko*A*A*DT);
Y=mw*cp*L/(ko*A);
NTU=h*P*L/(mw*cp);
[Qw,Qc,Qwp,qb]=lead(NTU,b,Y,20);
qw=qb*ko*A*DT/L;
f=(mw+mc)*hfg-qw-qo;
```

A.5 Matlab code to simulate pressure tap

This appendix contains the Matlab code used to simulate the dimensionless problem associated with the pressure tap, as described in subsection 2.4.2. The function simulates the second order nonlinear partial differential equation associated with dimensionless pressure by setting up an implicit matrix for the spatial profile at each time step. The nonlinear portions of this matrix are simulated based on the conditions at the previous timestep. The matrix is stepped forward in time until the cycle reaches steady state.

The function requires the number of time steps (m), the number of length steps (n), the dimensionless pressure variation (DP), the dimensionless temperature difference (DT), the ratio of mass storage to pressure effects (I), and the initial pressure profile to start the iteration (Pi - will have no effect on the final answer other than how long it takes to converge).

The function returns the dimensionless pressure variation (P), the dimensionless lost refrigeration (Qloss), the attenuation (att), and the phase shift (phi).

```
function[P,Qloss,att,phi]=Ptap(m,n,DP,DT,l,Pi)

% [P,Qloss,att,phi]=Ptap(m,n,DP,DT,l,Pi)
%
% This function simulates the dimensionless pressure tap problem
%  The function requires:
%         m : number of time steps
%         n : number of length steps
%         DP : dimensionless pressure change
%         DT . dimensionless temperature difference
%         l : ratio of mass storage to pressure drop effects
%         Pi : initial pressure profile

Pt=zeros(n+1,1);
P=zeros(n+1,m);
A=zeros(n,n);
b=zeros(n,1);
x=zeros(n,1);
essn=999;
Pinitial=Pi;
Pt=Pi;
while essn>0.0001;
  for j=1:m
    P0=1+DP*(1-cos(2*3.1416*j/m))/2;
    essj=999;
    while essj>0.0001
      for i=1:(n-1)
        A(i,i)= -Pt(i+1,1)*(1+1/((n/DT)+i))-2*Pt(i,1)-l*m/(n^2);
        b(i,1)= -l*m*Pi(i+1,1)/(n^2);
        if i>1
          A(i,i-1)=Pt(i,1)+Pt(i+1,1)*(1+1/((n/DT)+i));
        else
```

```
               b(i,1)=b(i,1)-P0*(Pt(i,1)+Pt(i+1,1)*(1+1/((n/DT)+i)));
            end
            A(i,i+1)=Pt(i+1,1);
         end
         A(n,n)=1;
         A(n,n-1)=-1;
         x=A\b;
         Ptl=Pt;
         Pt(1,1)=P0;
         for i=1:n
            Pt(i+1,1)=x(i,1);
         end
         essj=sum(abs(Pt-Ptl))/n;
      end
      P(:,j)=Pt;
      Pi=Pt;
   end
   essn=sum(abs(Pt-Pinitial));
   essn=sum(essn)/(n*m);
   Pinitial=Pt;
end
Qloss=0;
Pmax=0;
for j=1:m
   Qloss=Qloss-(n/(l*m))*(P(1,j)*(P(2,j)-P(1,j))*log(P(1,j)));
   if P(n+1,j)>Pmax
      Pmax=P(n+1,j);
      jmax=j;
   end
end
att=Pmax/(1+DP);
phi=(jmax-(m/2))*3.1416/m;
```

A.6 Basic program for data acquisition

This appendix contains the basic code used to take data during an experimental run. The program interfaces with both the Acro 900 system which performs continuous A/D conversions and with an internal data acquisition card. The program prompts the user for various aspects of the data acquisition setup which can change for various experimental runs. The data is stored to a file in both its raw and converted form. Several of the channels are also graphically shown on the screen.

```
DECLARE FUNCTION BDCM! (H!)
DECLARE FUNCTION TDCM! (H!)
DECLARE FUNCTION BPLOT! (FST!, LST!, Y1!, Y2!, H!)
DECLARE FUNCTION TPLOT! (FST!, LST!, Y1!, Y2!, H!)
DECLARE FUNCTION AXLBL! (FST!, LST!, FSB!, LSB!)
DECLARE FUNCTION TMPRST! (NUM!, MV!)
DECLARE SUB SCRN ()

   ' OPEN PORT TO ACRO SYSTEM'
OPEN "COM1:9600,N,8,2,CS,DS" FOR RANDOM AS #1
```

```
10 IF NOT EOF(1) THEN X$ = INPUT$(1, #1): GOTO 10
    ' TURN OFF COLD JUNCTION COMPENSATION TO RESISTORS'
PRINT #1, "#4,CJR1,2,3,4,5,6,7=0"
    ' TURN ON COLD JUNCTION COMPENSATION TO THERMOCOUPLE'
PRINT #1, "#4,CJR8=1"
    ' SET UP DATA TO BE DISPLAYED - OPEN DEFAULT FILE OF RESISTOR #'S'
PRINT " "
OPEN "RN" FOR INPUT AS #3
INPUT #3, RN1
INPUT #3, RN2
INPUT #3, RN3
INPUT #3, RN4
INPUT #3, RN5
INPUT #3, RN6
INPUT #3, RN7
CLOSE #3

12 PRINT " "
PRINT "CURRENT RESISTOR CHANNEL SETTINGS"
PRINT "  CHANNEL 1 = "; RN1
PRINT "  CHANNEL 2 = "; RN2
PRINT "  CHANNEL 3 = "; RN3
PRINT "  CHANNEL 4 = "; RN4
PRINT "  CHANNEL 5 = "; RN5
PRINT "  CHANNEL 6 = "; RN6
PRINT "  CHANNEL 7 = "; RN7
INPUT "ENTER RESISTOR SETTING TO CHANGE (0=NONE)"; G1
IF G1 = 0 GOTO 14
PRINT "ENTER NEW RESISTOR SETTING FOR CHANNEL #"; G1
INPUT G2
IF G1 = 1 THEN RN1 = G2
IF G1 = 2 THEN RN2 = G2
IF G1 = 3 THEN RN3 = G2
IF G1 = 4 THEN RN4 = G2
IF G1 = 5 THEN RN5 = G2
IF G1 = 6 THEN RN6 = G2
IF G1 = 7 THEN RN7 = G2
INPUT "CHANGE ANOTHER CHANNEL SETTING (1=YES)"; G1
IF G1 = 1 THEN GOTO 12
OPEN "RN" FOR OUTPUT AS #3
PRINT #3, RN1
PRINT #3, RN2
PRINT #3, RN3
PRINT #3, RN4
PRINT #3, RN5
PRINT #3, RN6
PRINT #3, RN7
CLOSE #3
    'SET UP SCALES - OPEN DEFAULT FILE OF FULL AND LOW SCALES'
14 OPEN "SCL" FOR INPUT AS #3
INPUT #3, FS1, LS1
INPUT #3, FS2, LS2
CLOSE #3
PRINT " "
```

```
PRINT "CURRENT SCALE SETTINGS"
PRINT " RESISTOR TEMPERATURES: "; LS1; " TO "; FS1
PRINT " COLD END PRESSURE/MAGNET CURRENT: "; LS2; " TO "; FS2
PRINT " "

INPUT "CHANGE SCALES (1=YES)"; G1
IF G1 <> 1 THEN GOTO 20

15 PRINT " "
PRINT "ENTER SCALE TO CHANGE"
PRINT "  (1) RESISTOR TEMPERATURES"; LS1; FS1
PRINT "  (2) COLD END PRESSURE"; LS2; FS2
INPUT G1
PRINT " "
INPUT "ENTER FULL SCALE"; G2
INPUT "ENTER LOW SCALE"; G3
IF G1 = 1 THEN FS1 = G2
IF G1 = 1 THEN LS1 = G3
IF G1 = 2 THEN FS2 = G2
IF G1 = 2 THEN LS2 = G3
INPUT "CHANGE ANOTHER SCALE (1=YES)"; G1
IF G1 = 1 GOTO 15
OPEN "SCL" FOR OUTPUT AS #3
PRINT #3, FS1, LS1
PRINT #3, FS2, LS2
CLOSE #3
20 PRINT " "

' SET UP FILE FOR DATA'
INPUT "ENTER NAME FOR DATA FILE (N=NONE)"; FILE$
IF (FILE$ <> "N") THEN INPUT "FORWARD (1) OR REVERSE (0) CURRENT";      CDIR
IF (FILE$ <> "N") THEN OPEN FILE$ + "C.DAT" FOR OUTPUT AS #2
IF (FILE$ <> "N") THEN OPEN FILE$ + "R.DAT" FOR OUTPUT AS #4
IF (FILE$ <> "N") THEN PRINT #2, RN1, RN2, RN3, RN4, RN5, RN6, RN7, CDIR
IF (FILE$ <> "N") THEN PRINT #4, RN1, RN2, RN3, RN4, RN5, RN6, RN7, CDIR
INPUT "ENTER NUMBER OF SECONDS BETWEEN DATA PTS (0=MINIMUM)";   TD
    ' WAIT FOR START DTQN SIGNAL'
PRINT #1, "#1,DOUT1=1"
PRINT #1, "#1,DIN1"
INPUT #1, D1
WHILE (D1 = 0)
   PRINT #1, "#1,DIN1"
   INPUT #1, D1
WEND
    ' START A/D CONVERSIONS ON A CONTINUOUS BASIS - STORE LATEST'
    ' READING IN BUFFER'
PRINT #1, "#4,CONV=65535"
PRINT #1, "#1,CONV=65535"
    ' SET UP SCREEN FOR DATA'
SCRN
FST = FS1
LST = LS1
FSB = FS2
LSB = LS2
```

```
G = AXLBL(FST, LST, FSB, LSB)
    ' GET BASE TIME FOR TIME MEASUREMENT '
BTIME = TIMER
TDATA = TD
H = 60
    ' TAKE DATA UNTIL SWITCH IS FLIPPED'
BDCO = 0
TDCO = 0
WHILE (D1 = 1)
  TLAPSE = TIMER - BTIME
  PRINT #1, "#4,MVIN1,2,3,4,5,6,7,8"
  INPUT #1, MVR1, MVR2, MVR3, MVR4. MVR5, MVR6, MVR7, MVR8
  R1 = ABS(MVR1) / (1000 * 10 ^ -5)
  R2 = ABS(MVR2) / (1000 * 10 ^ -5)
  R3 = ABS(MVR3) / (1000 * 10 ^ -5)
  R4 = ABS(MVR4) / (1000 * 10 ^ -5)
  R5 = ABS(MVR5) / (1000 * 10 ^ -5)
  R6 = ABS(MVR6) / (1000 * 10 ^ -4)
  R7 = ABS(MVR7) / (1000 * 10 ^ -4)
    'CONVERT RESISTANCE TO TEMPERATURE'
  T1 = TMPRST(RN1, R1)
  T2 = TMPRST(RN2, R2)
  T3 = TMPRST(RN3, R3)
  T4 = TMPRST(RN4, R4)
  T5 = TMPRST(RN5, R5)
  T6 = TMPRST(RN6, R6)
  T7 = TMPRST(RN7, R7)
    ' READ PRESSURE TRANSDUCERS'
  PRINT #1. "#1,VIN1,2"
  INPUT #1. VPC, VPW
  VPC = VPC + .27
  VPW = VPW + .27
  PC = -30.5577 + 29.9647 * VPC - .017 * VPC ^ 2
  PW = -28.8186 + 29.711 * VPW + .0137 * VPW ^ 2
     ' READ TOP AND BOTTOM DEAD CENTER SWITCHES'
  PRINT #1, "#1,DIN1,2"
  INPUT #1, D1, TDC
  IF (TDC = 1) AND (TDCO = 0) THEN G = TDCM(H)
  IF (TDC = 1) AND (TDCO = 0) THEN BDCO = 0
  IF (TDC = 1) AND (TDCO = 0) THEN TDCO = 1
  IF (TDC = 0) AND (BDCO = 0) THEN G = BDCM(H)
  IF (TDC = 0) AND (BDCO = 0) THEN TDCO = 0
  IF (TDC = 0) AND (BDCO = 0) THEN BDCO = 1
  IF TLAPSE < TDATA THEN GOTO 40
  IF (FILE$ <> "N") THEN PRINT #2. TLAPSE, T1, T2, T3, T4, T5, T6, T7, MVR8. PC, PW, TDC
  IF (FILE$ <> "N") THEN PRINT #4, TLAPSE. R1, R2, R3, R4, R5, R6, R7, MVR8,          VPC.
VPW. TDC
  TDATA = TLAPSE + TD
    ' PLOT READINGS ON SCREEN'
  G = TPLOT(FST, LST, T2, T1, H)
  G = BPLOT(FSB, LSB, PC, IM, H)
  H = H + 8
  IF H > 630 THEN SCRN
  IF H > 630 THEN G = AXLBL(FST, LST, FSB, LSB)
```

```
   IF H > 630 THEN H = 60
40  ' DONE TAKING DATA'
WEND
   ' STOP A/D CONVERSIONS'
PRINT #1, "#4,CONV=0"
PRINT #1, "#1,CONV=0"
   ' CLOSE FILES AND PORTS'
CLOSE #1
IF FILE$ <> "N" THEN CLOSE #2
IF FILE$ <> "N" THEN CLOSE #4

FUNCTION AXLBL (FST, LST, FSB, LSB)

' THIS FUNCTION LABELS THE AXES ON THE SCREEN'
' THE FUNCTION REQUIRES THE TOP AND BOTTOM FULL SCALE AND'
' LOW SCALE LABELS'

PRINT FST; "K"
FOR I = 1 TO 10
  PRINT " "
NEXT I
PRINT LST; "K"
PRINT FSB; "PSI,A"
FOR I = 1 TO 9
  PRINT " "
NEXT I
PRINT LSB; "PSI,A"

END FUNCTION

FUNCTION BDCM (H)

  ' THIS FUNCTION PAINTS A VERTICAL DOTTED LINE WHEN THE'
  ' BOTTOM DEAD CENTER SWITCH IS HIT'
  ' THE FUNCTION REQUIRES THE CURRENT HORIZONTAL POSITION'

  FOR I = 1 TO 90 STEP 4
    PSET (H, I)
    PSET (H, 100 + I)
  NEXT
END FUNCTION

FUNCTION BPLOT (FST, LST, Y1, Y2, H)

' THIS FUNCTION PLOTS TO THE BOTTOM GRAPH ON THE SCREEN'
' THE FUNCTION REQUIRES THE BOTTOM SCALE. THE READINGS TO BE'
' PLOTTED AND THE CURRENT HORIZONTAL POSITION'

V1 = (Y1 - LST) / (FST - LST)
IF V1 > 1 THEN CIRCLE (H, 100), 3
IF V1 < 0 THEN CIRCLE (H, 190), 3
IF (V1 < 1) AND (V1 > 0) THEN CIRCLE (H, INT(190 - V1 * 90)), 3
V2 = (Y2 - LST) / (FST - LST)
IF V2 > 1 THEN GOTO 9000
```

```
IF V2 < 0 THEN GOTO 9100
V2 = INT(190 - V2 * 90)
CIRCLE (H, V2), 2
GOTO 9500
9000 'V2 OUT OF RANGE HIGH'
CIRCLE (H, 100), 2
GOTO 9500
9100 'V2 OUT OF RANGE LOW'
CIRCLE (H, 190), 2
CIRCLE (H, 190). 2
BPLOT = V2
9500 'END OF PLOT FUNCTION'

END FUNCTION

SUB SCRN

  ' THIS FUNCTION SETS UP THE SCREEN FOR PLOTTING'

  ' CLEAR SCREEN'
  SCREEN 1
  SCREEN 2
  'DRAW AXES'
  LINE (60, 0)-(60, 90)
  LINE (60, 100)-(60, 190)
  LINE (60, 90)-(640, 90)
  LINE (60. 190)-(640, 190)
  FOR I = 1 TO 144
    PSET (60 + 4 * I, 0)
    PSET (60 + 4 * I, 22)
    PSET (60 + 4 * I, 45)
    PSET (60 + 4 * I, 68)
    PSET (60 + 4 * I, 100)
    PSET (60 + 4 * I, 122)
    PSET (60 + 4 * I, 145)
    PSET (60 + 4 * I. 168)
  NEXT
END SUB

FUNCTION TDCM (H)

  ' THIS FUNCTION PAINTS A SOLID VERTICAL LINE WHEN TOP'
  ' DEAD CENTER IS HIT'
  ' THIS FUNCTION REQUIRES THE CURRENT HORIZONTAL POSITION'

  LINE (H, 0)-(H, 90)
  LINE (H. 100)-(H. 190)
END FUNCTION

FUNCTION TMPRST (NUM. R)

'THIS FUNCTION CHANGES RESISTANCE MEASUREMENTS TO THE'
' CORRESPONDING TEMPERATURE'
  ' THE FUNCTION REQUIRES THE NUMBER OF THE RESISTOR AND'
```

```
  ' THE RESISTANCE MEASUREMENT'

IF R < 40 THEN GOTO 6950
IF NUM = 28 THEN GOTO 6100
IF NUM = 9 THEN GOTO 6200
IF NUM = 10 THEN GOTO 6300
IF NUM = 24 THEN GOTO 6400
IF NUM = 27 THEN GOTO 6500
IF NUM = 1 THEN GOTO 6600
IF NUM = 2 THEN GOTO 6700
IF NUM = 5 THEN GOTO 6800
IF NUM = 8 THEN GOTO 6900
6100 'R28 - RB33'
  IF (R < 94.237) THEN T = 5209080.8# * R ^ -2 - 250608.8 * R ^ -1 + 4744.8865# -   40.15199 * R +
.1270273# * R ^ 2
  IF (R >= 94.237) AND (R < 299.845) THEN T = -185683172.4# * R ^ -3 +   5615772.2# * R ^ -2 -
61709.994# * R ^ -1 + 332.4384 - .837836 * R +      .000816617# * R ^ 2
  IF (R >= 299.845) THEN T = 1 / (.2363392# + .408683128# * LOG(R / 316) +         .0647888898# *
(LOG(R / 316)) ^ 2)
  GOTO 7000
6200 'R9 - RC11'
  IF (R < 94.734) THEN T = 6953933.85# * R ^ -2 - 374278.92# * R ^ -1 + 7778.1362#           -
71.892216# * R + .24784555# * R ^ 2
  IF (R >= 94.734) AND (R < 283.057) THEN T = -117714642.2# * R ^ -3 +   3382375.051# * R ^ -2 -
34581.39668# * R ^ -1 + 178.9278334# - .4216927799#       * R + .0003828716362# * R ^ 2
  IF (R >= 283.057) THEN T = 1 / (.2363392# + .408683128# * LOG(R / 356) +         .0647888898# *
(LOG(R / 356)) ^ 2)
  GOTO 7000
6300 'R10 - RC6'
  IF (R < 103.55) THEN T = 3330896.1599# * R ^ -2 - 154557.2424# * R ^ -1 +          2886.41# -
24.4320634# * R + .0784666# * R ^ 2
  IF (R >= 103.55) AND (R < 361.55) THEN T = -23095576.297# * R ^ -3 +   794046.8624# * R ^ -2 -
6841.466109# * R ^ -1 + 34.50885207# -    .05952785992# * R + .00003404659413# * R ^ 2
  IF (R >= 361.55) THEN T = 1 / (.2363392# + .408683128# * LOG(R / 346.54) +       .0647888898# *
(LOG(R / 346.54)) ^ 2)
  GOTO 7000
6400 'R24 - RC1'
  IF (R < 90.188) THEN T = 3232369.1# * R ^ -2 - 164405.57# * R ^ -1 + 3322.5392# -
          30.0060491# * R + .10149211# * R ^ 2
  IF (R >= 90.188) AND (R < 317.508) THEN T = -110531875.8# * R ^ -3 +   3600942.483# * R ^ -2 -
41967.265# * R ^ -1 + 242.45749# - .643405102# * R +       .0006539844# * R ^ 2
  IF (R >= 317.508) THEN T = 1 / (.2363392# + .408683128# * LOG(R / 313.4) +       .0647888898# *
(LOG(R / 313.402)) ^ 2)
  GOTO 7000
6500 'R27 - RC9'
  IF (R < 96.756) THEN T = 3016117.31# * R ^ -2 - 133286.4 * R ^ -1 + 2389.8046# - 19.5031664# * R
+ .0607388275# * R ^ 2
  IF (R >= 96.756) AND (R < 342.443) THEN T = 23299620.203# * R ^ -3 -   470215.065# * R ^ -2 +
5288.05728# * R ^ -1 - 17.8102 + .041332516# * R -          .0000360749# * R ^ 2
  IF (R >= 342.443) THEN T = 1 / (.2363392# + .408683128# * LOG(R / 331.0324) +  .0647888898# *
(LOG(R / 3331.0324#)) ^ 2)
  GOTO 7000
6600 'R1 - RC8'
```

```
  IF (R < 96.376) THEN T = 3067095.73# * R ^ -2 - 137430.51# * R ^ -1 + 2470.9293#          -
20.107286# * R + .06225981# * R ^ 2
  IF (R >= 96.376) AND (R < 321.005) THEN T = 24463927.98# * R ^ -3 -    373738.073# * R ^ -2 +
2182.5242# * R ^ -1 + 11.41252# - .06772746# * R +          .000103673935# * R ^ 2
  IF (R >= 321.005) THEN T = 1 / (.2363392# + .408683128# * LOG(R / 324.5493) +  .0647888898# *
(LOG(R / 324.5493)) ^ 2)
  GOTO 7000
6700 ' R2 - RC10'
  IF (R < 110.52) THEN T = 4600814.992# * R ^ -2 - 205669.453# * R ^ -1 +  3626.8856# - 28.705445#
* R + 8.55754855000001D-02 * R ^ 2
  IF (R >= 110.52) AND (R < 286.501) THEN T = -18696777.83# * R ^ -3 +   749965.5828# * R ^ -2 -
7157.932998# * R ^ -1 + 41.69100334# -   9.07146964400001D-02 * R + .0000757837205# * R ^ 2
  IF (R >= 286.501) THEN T = 1 / (.2363392# + .408683128# * LOG(R / 375) +         .0647888898# *
(LOG(R / 375)) ^ 2)
  GOTO 7000
6800 'R5 - RC14'
  IF (R < 94.103) THEN T = 3130079.355# * R ^ -2 - 153049.5477# * R ^ -1 +          3053.251441# -
27.70935157# * R + 9.52920688200001D-02 * R ^ 2
  IF (R >= 94.103) AND (R < 273.898) THEN T = -111234167.8# * R ^ -3 +   3106653.764# * R ^ -2 -
30076.12856# * R ^ -1 + 146.6787699# - .3205891394#       * R + .0002695971557# * R ^ 2
  IF (R >= 273.898) THEN T = 1 / (.2363392# + .408683128# * LOG(R / 349.7237) +  .0647888898# *
(LOG(R / 349.7237)) ^ 2)
  GOTO 7000
6900 'R8 - RC2'
  IF (R < 102.683) THEN T = 3405695.24# * R ^ (-2) - 150080.17# * R ^ (-1) +          2648.50534# -
21.1465013# * R + .0641227987# * R ^ 2
  IF (R >= 102.683) AND (R < 333.048) THEN T = 15705565.2# * R ^ -3 - 96933.086#          * R ^ -2
- 839.6144508# * R ^ -1 + 26.3244352# - .0987198# * R +   0001240915# * R ^ 2
  IF (R >= 333.048) THEN T = 1 / (.2363392# + .408683128# * LOG(R / 335.4072) +  0647888898# *
(LOG(R / 335.4072)) ^ 2)
  GOTO 7000
6950 'ERROR - CURRENT SOURCE PROBABLY NOT TURNED ON'
  T = 300
7000 TMPRST = T

END FUNCTION

FUNCTION TPLOT (FST, LST, Y1, Y2, H)

' THIS FUNCTION PLOTS READINGS TO THE UPPER GRAPH ON THE SCREEN'
' THE FUNCTION REQUIRES THE SCALE OF THE UPPER GRAPH, THE'
' READINGS TO BE PLOTTED AND THE CURRENT HORIZONTAL POSITION'

V1 = (Y1 - LST) / (FST - LST)
IF V1 > 1 THEN CIRCLE (H, 1), 3
IF V1 < 0 THEN CIRCLE (H, 90), 3
IF (V1 < 1) AND (V1 > 0) THEN CIRCLE (H, INT(90 - V1 * 90)), 3
V2 = (Y2 - LST) / (FST - LST)
IF V2 > 1 THEN GOTO 8000
IF V2 < 0 THEN GOTO 8100
V2 = INT(90 - V2 * 90)
CIRCLE (H, V2), 2
CIRCLE (H, V2), 2
GOTO 8500
```

```
8000 'V2 OUT OF RANGE HIGH'
CIRCLE (H, 1), 2
CIRCLE (H, 1), 2
GOTO 8500
8100 'V2 OUT OF RANGE LOW'
CIRCLE (H, 90), 2
CIRCLE (H, 90), 2
TPLOT = V2
8500 'END OF PLOT FUNCTION'
END FUNCTION
```

A.7 Basic code used for cycle control

This appendix contains the basic code used to control the experimental prototype. The program interfaces with both the MPS 622 superconducting solenoid power supply and with an internal data acquisition card.

```
0 ' PCLAB BASIC definition file (short names)
10 ' This file has been MERGEd with the cycle control
20 ' to define routine offsets and establish the PCLAB
30 ' segment.
40 XAV=3 : XAOT=6 : XSA=9 : XAS=12 : XBAD=15 : XTAD=18
50 XWAD=21  :  XDV=24 : XDOT=27 : XSD=30 :  XDS=33 : XBDD=36
60 XTDD=39 : XWDD=42 : XSCD=45 : XSSC=48 : XSCF=51 : XSCP=54
70 XEFI=57 : XEFO=60 : XIDV=63 : XODV=66 : XIDOT=69 : XODOT=72
80 XSECW=75 : XGEC=78 : XSB=81 : XSBA=84 : XSDC=87 : XSAR=90
90 XSAC=93 : XSDR=96 : XSLF=99 : XSTG=102 : XST=105
100 XGDE=108 : XRD=111 : XGDS=114 : XCWFC=117 : XCWFO=120 : XCWFI=123
110 XSAD=126 : XSDD=129 : XCAD=132 : XCDD=135
120 XDLY=138 :  XSTB=141 :  XWD=144 : XGC=147 : XCEV=150 : XREV=153
130 XGF=156 : XSC=159 : XINIT=162 : XTERM=165 : XIXR=168 : XIXW=171
140 XFDL=174 : XESC=177 : XDSC=180
150 DEF SEG=&H0  ' get the PCLAB segment
160 PCLSEG = PEEK ( &H4FE ) + 256*PEEK ( &H4FF )
170 DEF SEG=PCLSEG ' REM address the PCLAB segment
180 'OPEN RS232 INTERFACE TO MPS 622 MAGNET POWER SUPPLY
190 OPEN "COM1:9600.O.7.1.RS" AS #1
200 TERM$=CHR$(13)+CHR$(10)
210 PRINT #1. "VSET 11"+TERM$
205 'ALL COMMANDS TO THE MPS MUST BE FOLLOWED BY A DELAY'
220 DLY=0
230 IF DLY>100 THEN GOTO 260
240 DLY=DLY+1
250 GOTO 230
260 PRINT #1."ISET0"+TERM$
270 IPORT%=0
280 CALL XEFI(IPORT%)
290 OPORT%=1
300 CALL XEFO(OPORT%)
310 'INITIALIZE ALL OUTPUT BITS TO ZERO'
320 MASK%=255
330 BVO%=0
340 CALL XODV(OPORT%.MASK%.BVO%)
350 'OUTPUT 1 ON PORT 1. BIT 0 FOR USE IN SWITCHING'
360 MASK%=1
370 BVO%=1
380 CALL XODV(OPORT%.MASK%.BVO%)
390 BVI%=0
400 MASK%=4
410 PRINT " "
420 PRINT #1. "ISET0"+TERM$
430 PRINT #1. "VSET9"+TERM$
440 PRINT " "
```

```
450 PRINT "WAITING FOR CYCLE START SWITCH"
460 'WAIT UNTIL CYCLE START SWITCH IS FLIPPED'
470 CALL XIDV(IPORT%,MASK%,BVI%)
480 IF BVI%=0 THEN GOTO 460
490 PRINT " "
500 PRINT " *********************** "
510 TDC%=0
520 BDC%=0
530 BTIME=TIMER
540 'BEGIN CYCLE'
550 MASK%=3
560 BVI%=0
570 'CHECK DISPLACER SWITCHES'
580 CALL XIDV(IPORT%,MASK%,BVI%)
590 IF BVI%=2 THEN GOTO 620
600 IF BVI%=1 THEN GOTO 890
610 IF BVI%=0 THEN GOTO 1130
620 'TOP DEAD CENTER SWITCH IS HIT'
630 'CHECK IF WE HAVE ALREADY SEEN THAT TDC WAS HIT'
640 IF TDC%=1 THEN GOTO 1130
650 TDC%=1
660 BDC%=0
670 'SEND SIGNAL TO DATA ACQUISITION COMPUTER'
680 MASK%=6
690 BVO%=2
700 CALL XODV(OPORT%,MASK%,BVO%)
710 'ACTIVATE EXPANSION SOLENOID'
720 MASK%=24
730 BVO%=16
740 CALL XODV(OPORT%,MASK%,BVO%)
750 'ACTIVATE POWER SUPPLY'
760 PRINT #1,"RAMP1 25 100 14"+TERM$
770 DLY=0
780 IF DLY>100 THEN GOTO 810
790 DLY=DLY+1
800 GOTO 780
810 PRINT #1,"RMP1"+TERM$
820 CALL XODV(OPORT%,MASK%,BVO%)
830 ETIME=TIMER
840 CYCTIME=ETIME-BTIME
850 PRINT " "
860 PRINT "CYCLE TIME ";CYCTIME;" SECONDS"
870 BTIME=ETIME
880 GOTO 1130
890 'BOTTOM DEAD CENTER SWITCH IS HIT'
900 'CHECK IF WE HAVE ALREADY SEEN THAT BDC WAS HIT'
910 IF BDC%=1 THEN GOTO 1130
920 BDC%=1
930 TDC%=0
940 'SEND SIGNAL TO DATA ACQUISITION COMPUTER'
950 MASK%=6
960 BVO%=4
970 CALL XODV(OPORT%,MASK%,BVO%)
980 'ACTIVATE COMPRESSION SOLENOID'
```

```
990 MASK%=24
1000 BVO%=8
1010 CALL XODV(OPORT%,MASK%,BVO%)
1020 'DEACTIVATE POWER SUPPLY'
1030 PRINT #1,"RAMP1 100 25 14"+TERM$
1040 DLY=0
1050 IF DLY>100 THEN GOTO 1080
1060 DLY=DLY+1
1070 GOTO 1050
1080 PRINT #1,"RMP1"+TERM$
1090 CALL XODV(OPORT%,MASK%,BVO%)
1100 PRINT "HIT BOTTOM DEAD CENTER"
1110 GOTO 1130
1120 ''
1130 'CHECK IF CYCLE START SWITCH IS STILL ON'
1140 ''
1150 MASK%=4
1160 BVI%=0
1170 CALL XIDV(IPORT%,MASK%,BVI%)
1180 IF BVI%=4 THEN GOTO 540
1190 CLOSE #1
```

A.8 Matlab code used to analyze and characterize data

This appendix contains the Matlab code used to analyze and characterize the data associated with a steady state experimental cycle, as described in section 4.1. The function determines the cold end mass flow rate and cold space temperature, as described in subsection 4.1.1. The mass flow rate is also calculated at other axial positions and the entropy and enthalpy fluxes are determined, as described in subsection 4.1.2. The warm reservoir and refrigeration temperature are characterized, as described in subsection 4.1.3. Finally, the 'ideal' work transfers and heat rejection are determined, as described in subsection 4.1.4.

The function requires the data points which will be used to characterize the cycle. This data includes the temperature at three axial positions and the pressure as a function of time and is contained in the matrix data. The function also requires the displacer stroke (stroke), the maximum applied field (uoHmax), the dead volume contained in the cold space (Vdead), the refrigeration load (Qc), the porosity of the magnetic regenerator (e), the total volume of the regenerator (Vreg), the number of time steps required (m), and the number of length steps required (n).

The function returns the displacer temperature and cold end mass flow rate as functions of time (Td and mc). The mass flow rate throughout the regenerator (mf), the interpolated temperature variation (T), the entropy flux (sflx), the enthalpy flux (hflx), the 'ideal' magnetic work transfer (Wmag), the 'ideal' mechanical work transfer (Wc), the mass of helium which passes through the warm end of the device (M0), the mass of helium which passes through the cold end of the device (ML), the warm reservoir temperature (Twarm), the refrigeration temperature (Tcold), the heat rejection (Qrej), the actual COP of the device (nact), the carnot efficiency (ncarn), the entropy of the GGG (sg), and interpolated time and space vectors for use in plotting (ti and xi).

```
function[Td,mc,mf,T,sflx,hflx,Wmag,Wc,M0,ML,Twarm,Tcold,Qrej,nact,ncarn,sg,ti,xi]=a
        nls1(data,stroke,uoHmax,Vdead,Qc,e,Vreg,m,n)

% [Td,mc,mf,T,sflx,hflx,Wmag,Wc,M0,ML,Twarm,Tcold,Qrej,nact,ncarn,sg,ti,xi]
%       =anls1(data,stroke,uoHmax,Vdead,Qc,e,Vreg,m,n)

% This function analyzes and characterizes the data obtained with the experimental
% GM/magnetic apparatus
%
% The function requires:
%       data - the data obtained with the apparatus
%       stroke - the displacer stroke
%       uoHmax - the maximum applied field
%       Vdead -  the cold space dead volume
%       Qc - the refrigeration load
%       e - the regenerator porosity
%       Vreg - the volume of the regenerator
%       m - the number of time steps
%       n - the number of length steps
%
% The function returns:
%       Td - the displacer temperature
%       mc - the cold end mass flow rate
%       mf - the mass flow rate at all positions
%       T- the temperature
%       sflx - the entropy flux
%       hflx - the enthalpy flux
%       Wmag - the ideal magnetic work transfer
%       Wc - the ideal mechanical work transfer
%       M0 - the helium mass which passes through the warm end
%       ML - the helium mass which passes through the cold end
%       Twarm - the warm reservoir temperature
%       Tcold - the refrigeration temperature
%       Qrej - the heat rejection
%       nact - the COP of the device
%       ncarn - the carnot efficiency of the device
%       sg - the entropy of the GGG
%       ti - the interpolated time vector
%       xi - the interpolated space vector

[ndata,g]=size(data);
timedata=data(:,1);
Tdata=data(:,2:4);
Pdata=data(:,5);
tau=timedata(ndata,1)/2-0.01;
Td=zeros(1,2*m+1);
mc=Td;
% characterize cold space
% hot-to-cold blow
Tdin=Tdata(1,3);
```

```
Tdl=Tdin;
done=0;
while done==0
  Td(1,1)=Tdin;
  for j=1:m
    t=tau*j/m;
    [TLt,dTLdt]=Tint(Tdata,timedata,1,t);
    [Pt,dPdtt]=Pint(Pdata,timedata,t);
    [Vdist,dVdisdtt]=Vdis(Vdead,stroke,tau,t);
    [u,dudTP,dudPT,hL,cp,dhdPT,r,drdTP,drdPT,s,dsdTP,dsdPT]=heprop(TLt,Pt,3);
    [u,dudTP,dudPT,h,cp,dhdPT,r,drdTP,drdPT,s,dsdTP,dsdPT]=heprop(Tdl,Pt,1);
    dTddt=-Qc+dVdisdtt*(Pt-r*(hL-u))+dPdtt*(r*Vdist*dudPT-(hL-u)*Vdist*drdPT);
    dTddt=dTddt/((hL-u)*Vdist*drdTP-r*Vdist*dudTP);
    mct=r*dVdisdtt+Vdist*drdPT*dPdtt+Vdist*drdTP*dTddt;
   % if flow reversed
    if mct<0
      dTddt=-Qc+dPdtt*(r*Vdist*dudPT-(Pt/r)*Vdist*drdPT);
      dTddt=dTddt/((Pt/r)*Vdist*drdTP-r*Vdist*dudTP);
      mct=r*dVdisdtt+Vdist*drdPT*dPdtt+Vdist*drdTP*dTddt;
    end
    Tdl=Tdl+dTddt*tau/m;
    mc(1,j+1)=mct;
    Td(1,j+1)=Tdl;
    [t,mct,Tdl]
  end
  % cold-to-hot blow process
  for j=1:m
    t=tau+tau*j/m;
    [TLt,dTLdt]=Tint(Tdata,timedata,1,t);
    [Pt,dPdtt]=Pint(Pdata,timedata,t);
    [Vdist,dVdisdtt]=Vdis(Vdead,stroke,tau,t);
    [u,dudTP,dudPT,h,cp,dhdPT,r,drdTP,drdPT,s,dsdTP,dsdPT]=heprop(Tdl,Pt,1);
    dTddt=-Qc+dPdtt*(r*Vdist*dudPT-(Pt/r)*Vdist*drdPT);
    dTddt=dTddt/((Pt/r)*Vdist*drdTP-r*Vdist*dudTP);
    mct=r*dVdisdtt+Vdist*drdPT*dPdtt+Vdist*drdTP*dTddt;
   % if flow reversed
    if mct>0
      [u,dudTP,dudPT,hL,cp,dhdPT,r,drdTP,drdPT,s,dsdTP,dsdPT]=heprop(TLt,Pt,3);
      dTddt=-Qc+dVdisdtt*(Pt-r*(hL-u))+dPdtt*(r*Vdist*dudPT-(hL-u)*Vdist*drdPT);
      dTddt=dTddt/((hL-u)*Vdist*drdTP-r*Vdist*dudTP);
      mct=r*dVdisdtt+Vdist*drdPT*dPdtt+Vdist*drdTP*dTddt;
    end
    Tdl=Tdl+dTddt*tau/m;
    mc(1,m+j+1)=mct;
    Td(1,m+j+1)=Tdl;
    [t,mct,Tdl]
  end
  mc(1,1)=mct;
  % check if displacer variation is steady state
  error=abs(Tdl-Tdin)
  if error<0.1
    done=1;
  else
    Tdin=Tdl;
```

```
  end
end
% create interpolated time vector
for j=1:2*m+1
  ti(1,j)=(j-1)*tau/m;
end
mf=zeros(n+1,2*m+1);
mf(n+1,:)=mc;
sflx=zeros(n+1,1);
hflx=zeros(n+1,1);
% determine entropy and enthalpy fluxes and mass flow rates
for j=1:2*m
  sum=0;
  tt=tau*j/m;
  [Pt,dPtdt]=Pint(Pdata,timedata,tt);
  j
  [Tx,dTxdt]=Tint(Tdata,timedata,1,tt);
  [u,dudTP,dudPT,h,cp,dhdPT,r,drdTP,drdPT,s,dsdTP,dsdPT]=heprop(Tx,Pt,2);
  sflx(n+1,1)=sflx(n+1,1)-mf(n+1,j+1)*s*tau/m;
  hflx(n+1,1)=hflx(n+1,1)-mf(n+1,j+1)*h*tau/m;
  for i=1:n
    it=n+1-i;
    xt=it/(n+1);
    [Tx,dTxdt]=Tint(Tdata,timedata,xt,tt);
    [u,dudTP,dudPT,h,cp,dhdPT,r,drdTP,drdPT,s,dsdTP,dsdPT]=heprop(Tx,Pt,2);
    sum=sum+(e*Vreg/n)*(drdTP*dTxdt+drdPT*dPtdt);
    mf(it,j+1)=mf(n+1,j+1)+sum;
    sflx(it,1)=sflx(it,1)-mf(it,j+1)*s*tau/m;
    hflx(it,1)=hflx(it,1)-mf(it,j+1)*h*tau/m;
  end
end
% determine entropy of GGG
for j=1:2*m+1
  j
  tt=2*tau*j/(2*m+1);
  [uoHt,duoHdt]=uoHv(uoHmax,tau,tt);
  for i=1:n+1
    xt=i/(n+1);
    [Tx,dTdt]=Tint(Tdata,timedata,xt,tt);
    [sgt,dsgdTuoH,dsgduoHT]=GGG(Tx,uoHt);
    T(i,j)=Tx;
    sg(i,j)=sgt;
  end
end
mf(:,1)=mf(:,2*m+1);
% determine ideal magnetic work transfer
Wmag=hflx(1,1)-hflx(n+1,1);
% characterize warm reservoir and refrigeration temperature
Stdf0=0;
Htdf0=0;
Mtdf0=0;
StufL=0;
HtufL=0;
MtufL=0;
```

```
Stuf0=0;
Htuf0=0;
for j=1:2*m
  j
  tt=j*tau/m;
  [Pt,dPdt]=Pint(Pdata,timedata,tt);
  if mf(1,j+1)>0
    T0t=T(1,j+1);
    [u,dudTP,dudPT,h,cp,dhdPT,r,drdTP,drdPT,s,dsdTP,dsdPT]=heprop(T0t,Pt,2);
    Stdf0=Stdf0+mf(1,j+1)*tau*s/m;
    Htdf0=Htdf0+mf(1,j+1)*tau*h/m;
    Mtdf0=Mtdf0+mf(1,j+1)*tau/m;
  end
  if mf(1,j+1)<0
    T0t=T(1,j+1);
    [u,dudTP,dudPT,h,cp,dhdPT,r,drdTP,drdPT,s,dsdTP,dsdPT]=heprop(T0t,Pt,2);
    Stuf0=Stuf0+mf(1,j+1)*tau*s/m;
    Htuf0=Htuf0+mf(1,j+1)*tau*h/m;
  end
  if mf(n+1,j)<0
    TLt=T(n+1,j+1);
    [u,dudTP,dudPT,h,cp,dhdPT,r,drdTP,drdPT,s,dsdTP,dsdPT]=heprop(TLt,Pt,2);
    StufL=StufL+mf(n+1,j+1)*tau*s/m;
    HtufL=HtufL+mf(n+1,j+1)*tau*h/m;
    MtufL=MtufL+mf(n+1,j+1)*tau/m;
  end
end
ML=abs(MtufL);
M0=abs(Mtdf0);
SufL=StufL/MtufL;
Sdf0=Stdf0/Mtdf0;
HufL=HtufL/MtufL;
Hdf0=Htdf0/Mtdf0;
[HufL,SufL]
'input cold reservoir temperature as Tcold, type return'
keyboard
[Hdf0,Sdf0]
'input warm reservoir temperature as Twarm, type return'
keyboard
% determine Qrej , Wc , and efficiencies
Qrej=Twarm*sflx(1,1);
Wc=-hflx(1,1)+Qrej;
nrev=1/(Twarm/Tcold-1);
nact=2*tau*Qc/(Wc+Wmag);
ncarn=nact/nrev;
% create interpolated space vector
for i=1:n+1
  xi(i,1)=(i-1)/n;
end

function[u,dudTP,dudPT,h,cp,dhdPT,r,drdTP,drdPT,s,dsdTP,dsdPT]=heprop(T,P,type)

% [u,dudTP,dudPT,h,cp,dhdPT,r,drdTP,drdPT,s,dsdTP,dsdPT]=heprop(T,P,type)
```

```
%
% This function determines the properties of helium-4 between 3.5 K - 35 K and
% 220 - 1100 kPa by interpolating using a set of property tables generated with
% the HEPAK program
%
% The function requires:
%        T - the temperature
%        P - the pressure
%        type - the set of properties to be determined
%                 1=all, 2 = drdTP, drdPT,s,h , 3=h
%
% The function returns:
%        u, dudTP, dudPT - the specific internal energy and its partial derivatives
%        h, cp, dhdPT - the specific enthalpy and its partial derivatives
%        r, drdTP, drdPT - density and its partial derivatives
%        s, dsdTP, dsdPT - the specific entropy and its partial derivatives

load Ti.tab;
Pii=[220000,300000,500000,700000,900000,1100000];
if type==1
  load ri.tab;
  load cpi.tab;
  load dudTPi.tab;
  load dudPTi.tab;
  load drdTPi.tab;
  load drdPTi.tab;
  load hi.tab;
  load si.tab;
  dudTP=interp2(Pii',Ti,dudTPi,P,T,'linear');
  dudPT=interp2(Pii',Ti,dudPTi,P,T,'linear');
  drdTP=interp2(Pii',Ti,drdTPi,P,T,'linear');
  drdPT=interp2(Pii',Ti,drdPTi,P,T,'linear');
  cp=interp2(Pii',Ti,cpi,P,T,'linear');
  r=interp2(Pii',Ti,ri,P,T,'linear');
  h=interp2(Pii',Ti,hi,P,T,'linear');
  s=interp2(Pii',Ti,si,P,T,'linear');
  u=h-P/r;
elseif type==2
  load drdTPi.tab;
  load drdPTi.tab;
  load hi.tab;
  load si.tab;
  drdTP=interp2(Pii',Ti,drdTPi,P,T,'linear');
  drdPT=interp2(Pii',Ti,drdPTi,P,T,'linear');
  h=interp2(Pii',Ti,hi,P,T,'linear');
  s=interp2(Pii',Ti,si,P,T,'linear');
elseif type==3
  load hi.tab;
  h=interp2(Pii',Ti,hi,P,T,'linear');
end
```

A.9 Matlab code used to simulate modified GM/magnetic cycle

This appendix contains the Matlab code used to simulate the modified GM/magnetic cycle described in section 4.3.2. The modified GM/magnetic cycle uses the hot-to-cold blow temperature boundary conditions obtained with the experimental apparatus. The model uses an implicit technique in space and an explicit technique in time. The cold space is taken to be a separate node and is modeled as being adiabatic except for the refrigeration load.

The function requires initial guesses for the GGG, helium, and cold space temperatures (Tgin, Thin, and Tdin), the time constant (tau), the number of time steps (m), the number of length steps (n), the refrigeration load (Qr), the displacer stroke (stroke), the maximum applied field (uoHhigh), the high pressure (Ph), the low pressure (Pl), vectors containing the time and temperature observed at the hot end of the device during the hot-to-cold blow process (hbtm and hbtmp), and the number of cycles to simulate (ncyc).

The function returns the helium and GGG temperature variations (Th and Tg), the mass flow variation (mf), the displacer temperature variation (Tdspl), and the cold reservoir temperature based on the mass average pressure rather than entropy (Tcr).

```
function[Th,Tg,mf,Tdspl,Tcr]=gmag3(Tgin,Thin,Tdin,tau,m,n,Qr,stroke,uoHhigh,Ph,Pl,h
         btm,hbtmp,ncyc)

% [Th,Tg,mf,Tdspl,Tcr]
%        =gmag3(Tgin,Thin,Tdin,tau,m,n,Qr,stroke,uoHhigh,Ph,Pl,hbtm,hbtmp,ncyc)
%
% This function simulates a modified GM/magnetic cycle
%
% The function requires:
%        Tgin - the initial GGG profile
%        Thin - the initial helium profile
%        Tdin - the initial displacer temperature
%        tau - the time constant
%        m - the number of time steps
%        n - the number of length steps
%        Qr - the refrigeration load
%        stroke - the displacer stroke
%        uoHhigh - the maximum applied field
%        Ph - the maximum pressure
%        Pl - the minimum pressure
%        hbtm - the time vector associated with observed warm end b.c.
%        hbtmp - the temperature vector associated with observed warm end b.c.
%        ncyc - the number of cycles
%
% The function requires:
%        Th - the helium temperature
%        Tg - the GGG temperature
%        mf - the mass flow
%        Tdspl - the displacer temperature
```

```
%       Tcr - the cold reservoir


Th=zeros(n+1,2*m*ncyc);
Tg=Th;
mf=Th;
Tdspl=zeros(1,2*m*ncyc);
Tcr=zeros(1,ncyc);
ss=0;
Tgl=Tgin;
Thl=Thin;
Dt=tau/m;
Tco=Tdin;
Vmax=stroke*1.25*1.25*3.1416/4;
Vmax=Vmax*0.0254*0.0254*0.0254;
Vdead=0.0000005;
for cyc=1:ncyc
  Hdf=0;
  Mdf=0;
  for j=1:m
    j
    t=j*tau/m;
    uoH=uoHhigh-(uoHhigh-1)*j/m;
    duoHdt=-(uoHhigh-1)/tau;
    P=Pl+(Ph-Pl)*t/tau;
    dPdt=(Ph-Pl)/tau;
    V=Vdead+0.5*Vmax*(1-cos(t*3.1416/tau));
    dVdt=Vmax*3.1416*sin(3.1416*t/tau)/(2*tau);
    Th0=spline(hbtm,hbtmp,j/m)
    [u,dudTP,dudPT,hh,cp,dhdPT,r,drdTP,drdPT,s,dsdTP,dsdPT]=heprop(Tco,P);
    if j==1
      mt=ones(n+1,1)*(r*dVdt+V*drdPT*dPdt);
    else
      mt=mfi;
    end
    Tgt=Tgl;
    done2=0;
    while done2==0
      [Thi,Tgi,mfi,Tdi]=df2(Tgl,Thl,Tgt,mt,Th0,uoH,duoHdt,P,dPdt,V,dVdt,Tco,tau,Qr,m,n);
      mss=sum(abs(mt-mfi))/(n+1)
      if mss<0.001
        done2=1;
      else
        mt=0.5*(mfi+mt);
      end
    end
    Tgl=Tgi;
    Thl=Thi;
    [Thi,Tgi,mfi]
    Tco=Tdi
    Th(:,(cyc-1)*2*m+j)=Thi;
    Tg(:,(cyc-1)*2*m+j)=Tgi;
    mf(:,(cyc-1)*2*m+j)=mfi;
```

```
      Tdspl(1,(cyc-1)*2*m+j)=Tdi;
      [u,dudTP,dudPT,hh,cp,dhdPT,r,drdTP,drdPT,s,dsdTP,dsdPT]=heprop(Thi(n+1,1),P);
    end
    for j=1:m
      j
      t=j*tau/m;
      uoH=1+(uoHhigh-1)*j/m;
      duoHdt=(uoHhigh-1)/tau;
      P=Ph-(Ph-Pl)*t/tau;
      dPdt=-(Ph-Pl)/tau;
      V=Vdead+0.5*Vmax*(1-cos((t+tau)*3.1416/tau));
      dVdt=Vmax*3.1416*sin(3.1416*(t+tau)/tau)/(2*tau);
      [u,dudTP,dudPT,hh,cp,dhdPT,r,drdTP,drdPT,s,dsdTP,dsdPT]=heprop(Tco,P);
      if j==1
        mt=(-ones(n+1,1)*(r*dVdt+V*drdPT*dPdt));
      else
        mt=mfi;
      end
      Tgt=Tgl;
      done2=0;
      while done2==0
        [Thi,Tgi,mfi,Tdi]=uf2(Tgl,Thl,Tgt,mt,uoH,duoHdt,P,dPdt,V,dVdt,Tco,tau,Qr,m,n);
        mss=sum(abs(mt-mfi))/(n+1)
        if mss<0.001
          done2=1;
        else
          mt=0.5*(mt+mfi);
        end
      end
      Tgl=Tgi;
      Thl=Thi;
      [Thi,Tgi,mfi]
      Tco=Tdi
      Th(:,(cyc-1)*2*m+m+j)=Thi;
      Tg(:,(cyc-1)*2*m+m+j)=Tgi;
      mf(:,(cyc-1)*2*m+m+j)=-mfi;
      Tdspl(1,(cyc-1)*2*m+m+j)=Tdi;
      Hdf=Hdf+mfi(n+1,1)*hh;
      Mdf=Mdf+mfi(n+1,1);
    end
    Tcr(1,cyc)=ThP(Hdf/Mdf,(Ph+Pl)/2);

    css=sum(abs(Tgin-Tgi))/(n+1)
    if css<0.1
      ss=1;
    else
      Tgin=Tgi;
    end
    Tgin=Tgi;
  end

  function[u,dudTP,dudPT,h,cp,dhdPT,r,drdTP,drdPT,s,dsdTP,dsdPT]=heprop(T,P)

  % [u,dudTP,dudPT,h,cp,dhdPT,r,drdTP,drdPT,s,dsdTP,dsdPT]=heprop(T,P)
```

```
%
% This function determines the properties of helium-4 between 3-35 K and 220 - 1100
% kPa using 2-d interpolation on a set of property tables constructed using the
% HEPAK program
%
% The function requires:
%        T - the temperature
%        P - the pressure
%
% The function returns:
%        u, dudTP, dudPT - the specific internal energy and its partial derivatives
%        h, cp, dhdPT - the specific enthalpy and its partial derivatives
%        r, drdPT, drdTP - the density and its partial derivatives
%        s, dsdPT, dsdTP - the specific entropy and its partial derivatives

load Ti.tab;
Pii=[220000,300000,500000,700000,900000.1100000];
load ri.tab;
load cpi.tab;
load dudTPi.tab;
load dudPTi.tab;
load drdTPi.tab;
load drdPTi.tab;
load hi.tab;
if T>35
  Tt=T;
  T=35;
  'error'
end
if T<3
  Tt=T;
  T=3;
  'error'
end
if P<220000
  P=220000;
  'error'
end
if P>1100000
  P=1100000;
  'error'
end
dudTP=interp2(Pii',Ti,dudTPi,P,T,'linear');
dudPT=interp2(Pii',Ti.dudPTi,P,T,'linear');
drdTP=interp2(Pii',Ti.drdTPi,P,T,'linear');
drdPT=interp2(Pii',Ti,drdPTi,P,T,'linear');
cp=interp2(Pii',Ti,cpi,P,T,'linear');
r=interp2(Pii',Ti,ri,P,T,'linear');
h=interp2(Pii',Ti.hi,P,T,'linear');
u=h-P/r;

function[Thi,Tgi,mfi,Tdi]=df2(Tgl.Thl.Tgt,mt,Th0,uoH,duoHdt.P.dPdt,Ve,dVdt,Tco,tau,           Qr,m,n)

% [Thi,Tgi,mfi,Tdi]
```

```
%	=mtrx(Tgl,Thl,Tgt,mt,Th0,uoH,duoHdt,P,dPdt,Ve,dVdt,Tco,tau,Qr,m,n)
%
% This function simulates one downflow timestep (at the warm end) of the cycle
%
% This function requires :
%	Tgl - the last timestep GGG temperature
%	Thl - the last timestep helium temperature
%	Tgt - the guess value of the GGG temperature
%	mt - the guess value of the mass flow rate
%	Th0 - the inlet helium temperature
%	uoH - the applied field
%	duoHdt - the applied field change rate
%	P - the pressure
%	dPdt - the pressure change rate
%	Ve - the volume in the cold space
%	 dVdt - the cold space volume change rate
%	Tco - the last timestep cold space temperature
%	tau - the time constant
%	Qr - the refrigeration rate
%	m - the number of time steps
%	n - the number of length steps
%
% The function returns:
%	Thi - the helium temperature
%	Tgi - the GGG temperature
%	mfi - the mass flow
%	Tdi - the cold space temperature

Mg=1;
h=75;
As=5.7;
V=0.00024132;
L=0.3048;
e=0.3;
Dt=tau/m;
Dx=L/n;
A=zeros(3*(n+1),3*(n+1));
b=zeros(3*(n+1),1);

% displacer energy + mass balance
[u,dudTP,dudPT,ho,cp,dhdPT,r,drdTP,drdPT,s,dsdTP,dsdPT]=heprop(Thl(n+1,1),P);
[u,dudTP,dudPT,hh,cp,dhdPT,r,drdTP,drdPT,s,dsdTP,dsdPT]=heprop(Tco,P);
dTcdt=(-Qr+dVdt*(P-r*(ho-u)+dPdt*(r*Ve*dudPT-(ho-u)*Ve*drdPT)));
dTcdt=dTcdt/((ho-u)*Ve*drdTP-Ve*r*(dudTP));
dTcdt
%displacer mass balance
A(1,1+3*n)=1;
b(1,1)=r*dVdt+Ve*drdPT*dPdt+Ve*drdTP*dTcdt;
% given inlet temperature
A(2,2)=1;
b(2,1)=Th0;
% matrix entropy balance at inlet
[sg,dsgdTuoH,dsgduoHT]=GGG(Tgl(1,1),uoH);
A(3,3)=Mg*Tgt(1,1)*dsgdTuoH/Dt;
```

```
A(3,3)=A(3,3)+h*As;
A(3,2)=-h*As;
b(3,1)=Tgl(1,1)*Mg*Tgt(1,1)*dsgdTuoH/Dt;
b(3,1)=b(3,1)-Mg*Tgt(1,1)*dsgduoHT*duoHdt;
for i=1:n
  [u,dudTP,dudPT,hh,cp,dhdPT,r,drdTP,drdPT,s,dsdTP,dsdPT]=heprop(Thl(i+1,1),P);
  [sg,dsgdTuoH,dsgduoHT]=GGG(Tgl(i+1,1),uoH);
  % helium mass balance
  A(1+3*i,1+3*i)=1/Dx;
  A(1+3*i,1+3*(i-1))=-1/Dx;
  A(1+3*i,2+3*i)=e*V*drdTP/(Dt*L);
  b(1+3*i,1)=Thl(i+1,1)*e*V*drdTP/(L*Dt);
  b(1+3*i,1)=b(1+3*i,1)-e*V*drdPT*dPdt/L;
  % helium energy balance
  A(2+3*i,2+3*i)=mt(i+1,1)*cp/Dx+h*As/L;
  A(2+3*i,2+3*i)=A(2+3*i,2+3*i)+e*V*dudTP*r/(Dt*L);
  A(2+3*i,2+3*(i-1))=-mt(i+1,1)*cp/Dx;
  A(2+3*i,1+3*i)=P/(r*Dx);
  A(2+3*i,1+3*(i-1))=-P/(r*Dx);
  A(2+3*i,3+3*i)=-h*As/L;
  b(2+3*i,1)=-e*V*dudPT*dPdt*r/L;
  b(2+3*i,1)=b(2+3*i,1)+Thl(i+1,1)*r*e*V*dudTP/(L*Dt);
  %GGG entropy balance
  A(3+3*i,3+3*i)=Mg*Tgt(i+1,1)*dsgdTuoH/Dt+h*As;
  A(3+3*i,2+3*i)=-h*As;
  b(3+3*i,1)=Tgl(i+1,1)*Mg*Tgt(i+1,1)*dsgdTuoH/Dt;
  b(3+3*i,1)=b(3+3*i,1)-Mg*Tgt(i+1,1)*dsgduoHT*duoHdt;
end
x=A\b;
for i=0:n
  Thi(i+1,1)=x(2+3*i,1);
  Tgi(i+1,1)=x(3+3*i,1);
  mfi(i+1,1)=x(1+3*i,1);
end
Tdi=Tco+dTcdt*Dt;

function[Thi,Tgi,mfi,Tdi]=uf2(Tgl,Thl,Tgt,mt,uoH,duoHdt,P,dPdt,Ve,dVdt,Tco,tau,Qr,m,n)

% [Thi,Tgi,mfi,Tdi]=uf2(Tgl,Thl,Tgt,mt,uoH,duoHdt,P,dPdt,Ve,dVdt,Tco,tau,Qr,m,n)
%
% This function simulates one upflow timestep (at the warm end) of the cycle
%
% This function requires :
%       Tgl - the last timestep GGG temperature
%       Thl - the last timestep helium temperature
%       Tgt - the guess value of the GGG temperature
%       mt - the guess value of the mass flow rate
%       uoH - the applied field
%       duoHdt - the applied field change rate
%       P - the pressure
%       dPdt - the pressure change rate
%       Ve - the volume in the cold space
%        dVdt - the cold space volume change rate
%       Tco - the last timestep cold space temperature
```

```
%         tau - the time constant
%         Qr - the refrigeration rate
%         m - the number of time steps
%         n - the number of length steps
%
% The function returns:
%         Thi - the helium temperature
%         Tgi - the GGG temperature
%         mfi - the mass flow
%         Tdi - the cold space temperature

Mg=1;
h=75;
As=5.7;
V=0.00024132;
L=0.3048;
e=0.3;
Dt=tau/m;
Dx=L/n;
A=zeros(3*(n+1),3*(n+1));
b=zeros(3*(n+1),1);

% displacer energy + mass balance
[u,dudTP,dudPT,ho,cp,dhdPT,r,drdTP,drdPT,s,dsdTP,dsdPT]=heprop(Thl(n+1,1),P);
[u,dudTP,dudPT,hh,cp,dhdPT,r,drdTP,drdPT,s,dsdTP,dsdPT]=heprop(Tco,P);
dTcdt=Qr-dPdt*(r*Ve*dudPT-P*Ve*drdPT/r);
dTcdt=dTcdt/(r*Ve*dudTP-P*Ve*drdTP/r);
dTcdt

%displacer mass balance
A(1+3*n,1+3*n)=1;
b(1+3*n,1)=-r*dVdt-Ve*drdPT*dPdt-Ve*drdTP*dTcdt;
% given inlet temperature
A(2+3*n,2+3*n)=1;
b(2+3*n,1)=Tco;
% matrix entropy balance at outlet
[sg,dsgdTuoH,dsgduoHT]=GGG(Tgl(1,1),uoH);
A(3+3*n,3+3*n)=Mg*Tgt(n+1,1)*dsgdTuoH/Dt+h*As;
A(3+3*n,2+3*n)=-h*As;
b(3+3*n,1)=Tgl(n+1,1)*Mg*Tgt(n+1,1)*dsgdTuoH/Dt;
b(3+3*n,1)=b(3+3*n,1)-Mg*Tgt(n+1,1)*dsgduoHT*duoHdt;
for i=0:(n-1)
  [u,dudTP,dudPT,hh,cp,dhdPT,r,drdTP,drdPT,s,dsdTP,dsdPT]=heprop(Thl(i+1,1),P);
  [sg,dsgdTuoH,dsgduoHT]=GGG(Tgl(i+1,1),uoH);
  % helium mass balance
  A(1+3*i,1+3*i)=1/Dx;
  A(1+3*i,1+3*(i+1))=-1/Dx;
  A(1+3*i,2+3*i)=e*V*drdTP/(Dt*L);
  b(1+3*i,1)=Thl(i+1,1)*e*V*drdTP/(L*Dt);
  b(1+3*i,1)=b(1+3*i,1)-e*V*drdPT*dPdt/L;
  % helium energy balance
  A(2+3*i,2+3*i)=mt(i+1,1)*cp/Dx+h*As/L;
  A(2+3*i,2+3*i)=A(2+3*i,2+3*i)+e*V*dudTP*r/(Dt*L);
  A(2+3*i,2+3*(i+1))=-mt(i+1,1)*cp/Dx;
```

```
  A(2+3*i,1+3*i)=P/(r*Dx);
  A(2+3*i,1+3*(i+1))=-P/(r*Dx);
  A(2+3*i,3+3*i)=-h*As/L;
  b(2+3*i,1)=-e*V*dudPT*dPdt*r/L;
  b(2+3*i,1)=b(2+3*i,1)+Thl(i+1,1)*r*e*V*dudTP/(L*Dt);
  %GGG entropy balance
  A(3+3*i,3+3*i)=Mg*Tgt(i+1,1)*dsgdTuoH/Dt+h*As;
  A(3+3*i,2+3*i)=-h*As;
  b(3+3*i,1)=Tgl(i+1,1)*Mg*Tgt(i+1,1)*dsgdTuoH/Dt;
  b(3+3*i,1)=b(3+3*i,1)-Mg*Tgt(i+1,1)*dsgduoHT*duoHdt;
end
x=A\b;
for i=0:n
  Thi(i+1,1)=x(2+3*i,1);
  Tgi(i+1,1)=x(3+3*i,1);
  mfi(i+1,1)=x(1+3*i,1);
end
Tdi=Tco+dTcdt*Dt;
```

THESIS PROCESSING SLIP

FIXED FIELD: ill ______ name ______

index ______ biblio ______

► COPIES [✓ Archives] Aero Dewey [✓ Eng] Hum

Lindgren Music Rotch Science

TITLE VARIES ►☐

NAME VARIES ►☑ Gregory Francis

IMPRINT (COPYRIGHT) ______

► COLLATION: 198p

► ADD. DEGREE: ______ ► DEPT.: ______

SUPERVISORS: ______

NOTES:

cat'r: date:

page: ► F.53

► DEPT: M.E

► YEAR: 1997 ► DEGREE: Ph.D

► NAME: NELLIS, Greg